

UNIVERSIDADE FEDERAL DO PARANÁ

LEANDRO JOSÉ LEMES STIVAL

LARGE EDDY SIMULATION OF THE ATMOSPHERIC FLOW
AROUND WIND TURBINES WITH THE USE OF AN
IMMERSED BOUNDARY METHOD

CURITIBA

2022

LEANDRO JOSÉ LEMES STIVAL

LARGE EDDY SIMULATION OF THE ATMOSPHERIC FLOW
AROUND WIND TURBINES WITH THE USE OF AN
IMMERSED BOUNDARY METHOD

Tese de Doutorado apresentada ao Programa de Pós-Graduação em Engenharia de Recursos Hídricos e Ambiental, Setor de Tecnologia da Universidade Federal do Paraná, como requisito à obtenção do grau de Doutor.

Orientador: Prof. Dr. Fernando Oliveira de Andrade

Co-orientador: Prof. Dr. João Marcelo Vedovotto

CURITIBA

2022

DADOS INTERNACIONAIS DE CATALOGAÇÃO NA PUBLICAÇÃO (CIP)
UNIVERSIDADE FEDERAL DO PARANÁ
SISTEMA DE BIBLIOTECAS – BIBLIOTECA CIÊNCIA E TECNOLOGIA

Stival, Leandro José Lemes

Lange eddy simulation of the atmospheric flow around wind turbines
with the use of an immersed boundary method. / Leandro José Lemes
Stival. – Curitiba, 2022.

1 recurso on-line : PDF.

Tese (Doutorado) – Universidade Federal do Paraná, Setor de
Tecnologias, Programa de Pós-Graduação em Engenharia de Recursos
Hídricos e Ambiental.

Orientador: Prof. Dr. Fernando Oliveira de Andrade.

Coorientador: Prof. Dr. João Marcelo Vedovotto.

1. Engenharia. 2. Energia eólica. 3. Produção de energia elétrica. 4.
Dinâmica dos fluidos – Simulação por computador. I. Andrade, Fernando
Oliveira de. II. Vedovotto, João Marcelo. III. Universidade Federal do
Paraná. Programa de Pós-Graduação em Engenharia de Recursos Hídricos
e Ambiental. IV. Título.

Bibliotecário: Nilson Carlos Vieira Junior CRB-9/1797

TERMO DE APROVAÇÃO

Os membros da Banca Examinadora designada pelo Colegiado do Programa de Pós-Graduação ENGENHARIA DE RECURSOS HÍDRICOS E AMBIENTAL da Universidade Federal do Paraná foram convocados para realizar a arguição da tese de Doutorado de **LEANDRO JOSÉ LEMES STIVAL** intitulada: **Large eddy simulation of the atmospheric flow around wind turbines with the use of an immersed boundary method**, sob orientação do Prof. Dr. FERNANDO OLIVEIRA ANDRADE, que após terem inquirido o aluno e realizada a avaliação do trabalho, são de parecer pela sua APROVAÇÃO no rito de defesa.

A outorga do título de doutor está sujeita à homologação pelo colegiado, ao atendimento de todas as indicações e correções solicitadas pela banca e ao pleno atendimento das demandas regimentais do Programa de Pós-Graduação.

CURITIBA, 22 de Junho de 2022.

Assinatura Eletrônica

27/06/2022 15:42:17.0

FERNANDO OLIVEIRA ANDRADE
Presidente da Banca Examinadora

Assinatura Eletrônica

27/06/2022 15:32:54.0

ALDEMIR APARECIDO CAVALINI JÚNIOR
Avaliador Externo (32006012)

Assinatura Eletrônica

27/06/2022 15:17:10.0

ANDRE LUIZ TONSO FABIANI
Avaliador Interno (UNIVERSIDADE FEDERAL DO PARANÁ)

Assinatura Eletrônica

28/06/2022 08:49:49.0

MARCELO RODRIGUES BESSA
Avaliador Interno (UNIVERSIDADE FEDERAL DO PARANÁ)

Assinatura Eletrônica

27/06/2022 15:24:39.0

RAFAEL ROMÃO DA SILVA MELO
Avaliador Externo (55001408)

Assinatura Eletrônica

27/06/2022 16:02:27.0

TOBIAS BERNWARD BLENINGER
Avaliador Interno (UNIVERSIDADE FEDERAL DO PARANÁ)

ACKNOWLEDGEMENTS

First, I would like to express my profound gratitude to my partner, Luana Pádua, for being on my side with inexhaustible assistance and continuous encouragement during the years of researching and writing this thesis. To my mother, Luci Lemes, who unfortunately passed away during the course of the thesis but is watching over us. Also, to my father for providing excellent education and support. To my sister, Joseli Stival, and my brother-in-law, Marlon Vaz, for all the motivation and friendship.

I must declare my genuine appreciation to Fernando O. Andrade, my thesis advisor from the Federal University of Technology - Parana (UTFPR), and João Marcelo Vedovotto, my co-advisor from the Federal University of Uberlandia (UFU). They regularly supported and guided me in the right direction whenever they thought I needed it. This accomplishment would not have been possible without them.

I would also like to extend a special thanks to MFLab and UBCO CFD Lab members interested in the development of this research project, especially Prof. Dr. Aristeu Silveira Neto (UFU) and Prof. Dr. Joshua Brinkerhoff (UBC). Beyond that, the board examination deserves a special acknowledgment for helping me in the process, composed by Prof. Dr. André Fabiani (UFPR), Prof. Dr. Aldemir Ap Cavalini Jr (UFU), Prof. Dr. Marcelo Bessa (UFPR), Prof. Dr. Tobias Bleninger (UFPR), and Prof. Dr. Rafael Romão (UFSJ).

Finally, a solemn thanks to the Post-Graduate Water Resources and Environmental Engineering Program at the Federal University of Parana and Coordination for the Improvement of Higher Education Personnel (CAPES) and the Brazilian National Council for Scientific and Technological Development (CNPq) for the scholarship during the whole process. Also Research and Development/ANEEL “SOLUÇÃO INTEGRADA PARA O DIAGNÓSTICO DE DEFEITOS, ANÁLISE DINÂMICA E MONITORAMENTO CONTÍNUO DE UNIDADES GERADORAS FRANCIS”, PD 02949-3007/2020, in cooperation with FOZ DO CHAPECÓ ENERGIA S.A, ENERGÉTICA BARRA GRANDE S.A. (BAESA), CAMPOS NOVOS ENERGIA S.A. (ENERCAN), COMPANHIA ENERGÉTICA RIO DAS ANTAS (CERAN), CSC ENERGIA S.A., and CPFL ENERGIA.

RESUMO

A energia eólica tem ganhado visibilidade em termos de progresso e potencial, principalmente no Brasil. O país atingiu 21,5 GW de capacidade instalada em 2022 e já ocupa a sexta posição no ranking global de produção de energia eólica onshore. Além disso, o país tem um potencial de energia eólica offshore que ultrapassa 700 GWs. Nesse contexto, as pesquisas científicas envolvendo energia eólica têm apresentado avanços significativos, principalmente no desenvolvimento métodos de dinâmica dos fluidos computacional. O presente estudo visa aplicar Simulação de Grandes Escalas em conjunto com o método de Fronteira Imersa para fornecer informações espaciais e temporais detalhadas do escoamento ao redor de turbinas eólicas selecionadas, realizando análises e discutindo sobre: (i) a esteira turbulenta e seus efeitos sobre a turbina eólica, (ii) interações entre o vento e a turbina em termos de geração, e (iii) os efeitos da turbulência na turbina a jusante relacionados à eficiência da produção de energia. A estrutura numérica usada nas simulações executa o LES sob uma malha cartesiana bloco-estruturada que possui um refinamento de malha adaptativo para aumentar a precisão e reduzir os custos computacionais. As análises são desenvolvidas para quatro cenários complementares baseados em uma pá isolada, seguida de uma turbina experimental NREL Phase VI. O terceiro cenário é baseado em uma turbina eólica NREL 5 MW em escala real, em que os resultados são validados com dados fornecidos em cooperação com a Universidade da Colúmbia Britânica e a geração com dados da própria NREL. O quarto cenário compreende dois aerogeradores NREL 5 MW posicionados um a jusante do anterior. Os principais resultados obtidos nas simulações demonstraram que o coeficiente de arrasto da NREL S809 alcança melhor concordância com os dados experimentais do que o coeficiente de sustentação. A simulação da NREL Phase VI mostrou uma maior perda de energia cinética na região da esteira turbulenta mais próxima da turbina. Entretanto, alcança resultados muito semelhantes aos da literatura na região mais a jusante da esteira. Os resultados da NREL 5MW apresentaram menores velocidades de recuperação do MFSim próximos da altura do rotor na esteira turbulenta mais próxima da turbina. Isto pode ser atribuído à simplificação da geometria de resolução da turbina que é aplicada no MARBLLES e SOWFA. Entretanto, a maioria dos resultados apresentou diferenças inferiores a 10% entre os perfis. Além disso, a geração de energia é validada com resultados experimentais NREL atingindo uma diferença de cerca de 3,5%. Enquanto isso, o cenário com duas turbinas demonstrou que a turbina a jusante produz uma recuperação de velocidade mais rápida do que a turbina eólica a montante. No entanto, a turbina a jusante também indica que o desempenho de produção pode diminuir em 30%. Portanto, este estudo é uma abordagem numérica inovadora como ferramenta para aprimorar os projetos e operações de parques eólicos, ainda mais relevante no cenário atual que a energia eólica atingiu no Brasil.

Palavras-chaves: Turbina eólica, dinâmica dos fluidos computacional, simulações de grandes escalas, método da fronteira imersa, esteira turbulenta;

ABSTRACT

The wind energy has gained visibility in terms of progress and potential, especially in Brazil. The country has reached 21.5 GW of installed capacity in 2022 and already occupies the sixth position in the global ranking of onshore wind energy production. Besides that, the country has an impressive potential for offshore wind energy that easily exceeds 700 GWs. In this context, scientific research involving wind energy has shown significant progress, particularly the development of computational fluid dynamics coupled with approaches that fully resolve the wind turbine. The present study aims to apply Large Eddy Simulation (LES) along with the Immersed Boundary Method (IB) to provide crucial spatial and temporal information of the flow around selected wind turbines by performing analyzes and discussing the following: (i) wind turbine generated wakes and their effects, (ii) interactions between the wind and turbine in terms of power generation, and (iii) wake effects for back to back turbines related to energy production efficiency. The numerical framework used in the simulations performs LES under a Cartesian block-structured mesh that is dynamically refined via an adaptive mesh refinement (AMR) to increase accuracy and reduce computational costs. The analysis are performed for four complementary scenarios based on an isolated blade, followed by a Phase VI NREL experimental turbine, compared with bibliography results. The third scenario is based on a stand-alone full-scale NREL 5 MW wind turbine. The results are validated against the data provided in a cooperation with the University of British Columbia, and power generation from the NREL report. The fourth scenario comprehends the back to back NREL 5 MW wind turbines. The main results obtained from simulations demonstrated that the drag coefficient of the NREL S809 airfoil achieves better agreement with the experimental data than the lift coefficient. Validation against experiments from the NREL Phase VI wind turbine scenario showed a higher loss of kinetic energy in the near wake region, mainly in the centerline, compared to benchmark data, but achieves very similar results to literature in the far-wake region. From a 5MW NREL, it is presented lower recovery velocities of MFSim around the hub height centerline in the near wake compared to other profiles, which could be attributed to the simplification blade resolving geometry applied in MARBLLES and SOWFA. Despite that, most results presented differences lower than 10% among the profiles. Also the power generation is validated with NREL experimental results with a difference of around 3.5%. Meanwhile, the back to back scenario demonstrated that the waked turbine produces a quicker recovery than the upstream wind turbine. However, it also indicates that the power performance may decrease by 30% in the downstream turbine. Therefore, this study is an innovative numerical approach as a tool to enhance the design and operation of wind farms, additionally in the current scenario where the wind power has reached in Brazil.

Key words: Wind turbine, computational fluid dynamics, large eddy simulation, immersed boundary method, wake effects;

LIST OF FIGURES

Figure 2.1	Drag and lift Forces	26
Figure 2.2	Lift and drag coefficients for the NACA 0012 symmetric airfoil for different Reynolds number	28
Figure 2.3	LES modelling validation through pressure coefficient on the turbine blades for three different radius rate, (a) 0.3, (b) 0.63, (c) 0.95.	28
Figure 2.4	Schematic drawing presenting the mean and instantaneous velocity profiles	29
Figure 2.5	Two bladed wind turbine from experimental Phase VI of the National Renewable Energy Laboratory (NREL)	31
Figure 2.6	The S809 blade airfoil Phase VI NREL experimental	31
Figure 2.7	Illustration of the (a) Park, (b) Frandsen and (c) Larsen wake models profiles	37
Figure 2.8	Illustration of the velocity recovery along the wake centerline for the wake models compared to LiDAR measurements	38
Figure 2.9	Visualization of large and small structure for free mixing layer flow	44
Figure 2.10	Visualization of large and small structure in terms of the turbulence spectrum	45
Figure 2.11	Representation of the two filters in the dynamic Smagorinsky model	46
Figure 2.12	Immersed geometry on a staggered finite volume computational grid: (a) Interpolation of the Eulerian velocity field to a Lagrangian point, (b) Distribution of the Lagrangian forces to the Eulerian field.	49
Figure 3.1	Example of representation for the Eulerian and Lagrangian mesh in the IB method	61
Figure 3.2	Hat distribution function	62
Figure 4.1	(a) Staggered grid scheme and (b) the colocated grid scheme	66
Figure 4.2	Elementary control volume to discretization	68
Figure 4.3	Interpolation of two nodes in the finite volume to obtain surface information	69
Figure 4.4	Multi-block structured grids for local refinement	71
Figure 4.5	Cartesian mesh refinement around the wind turbine and by vorticity	71
Figure 4.6	Lateral view of the cartesian mesh with vorticity criteria of refinement	72
Figure 4.7	Interpolation schemes to create ghost cells	73
Figure 4.8	Filling the ghost cell with blocks at same level	73
Figure 4.9	Prolongation operation multigrid	74
Figure 4.10	Restriction operation multigrid	75
Figure 4.11	Scheme of virtual and physical levels	75
Figure 5.1.1	NREL S809 (a) frontal, (b) lateral and (c) top view	78
Figure 5.1.2	Mesh area of the NREL S809 blade	78
Figure 5.1.3	Eulerian mesh of the flow	79
Figure 5.1.4	Lift and drag coefficients	80
Figure 5.1.5	Cl/Cd ratio	81
Figure 5.1.6	Probes downstream of the NREL from 1c to 15c	82

Figure 5.1.7	Comparison of time-averaged streamwise velocity \bar{U} (m/s) deficits along the downstream distance for different angles of attack	82
Figure 5.1.8	Comparison of vertical profiles of the time-averaged streamwise velocity \bar{U} (m/s) for different angles of attack, from a) 0, b) 5, c) 10, d) 15, and e) 20°	83
Figure 5.1.9	Vorticity criteria applied to different angles of attack, from (a) 10°, (b) 15° and (c) 20°	85
Figure 5.1.10	Comparison of kinetic turbulent energy k normalized by u_0^2 deficits along the downstream distance for different angles of attack	86
Figure 5.1.11	Reynolds stress tensor components profiles downstream the wind blade turbine for different angles of attack	87
Figure 5.1.12	Comparison of vertical profiles of the turbulence intensity (TI) for different angles of attack, a) 0°, b) 5°, c) 10°, d) 15° and e) 20°	88
Figure 5.1.13	Comparison of Longitudinal profiles of the turbulence intensity (TI) for different angles of attack in z at a) 0.1, b) 1, c) 2.25 and d) 4.5 m height	89
Figure 5.2.1	NREL experimental wind turbine structures: (a) rotor, (b) rotor and tower aligned, and (c) rotor ortogonal to the tower	91
Figure 5.2.2	Lateral view of the eulerian mesh displacement	92
Figure 5.2.3	Front view of the eulerian mesh displacement	92
Figure 5.2.4	Installed probes in the Scenario 2	93
Figure 5.2.5	Annular displacement of the probes for longitudinal analysis	93
Figure 5.2.6	Probes displacement for the cross-section analysis of the wake diameter	94
Figure 5.2.7	Probes displacement for the analysis of vertical profiles	94
Figure 5.2.8	Comparisons of different ratios of r/R for longitudinal velocity recovery profiles	95
Figure 5.2.9	Longitudinal velocity recovery profiles compared to simplified wake models by ratio of r/R	96
Figure 5.2.10	Cross-section wake profiles at the hub height over downstream distances	98
Figure 5.2.11	Cross-section wake profiles compared with simplified wake models for the selected downstream distances	99
Figure 5.2.12	Cross-section wake profiles compared with CFD simulations for the selected downstream distances	101
Figure 5.2.13	Vertical wind velocity profiles over downstream distance normalized by rotor diameters	103
Figure 5.2.14	Vertical wake profiles compared with CFD simulations for the selected downstream distances	104
Figure 5.2.15	Contours of u velocity over flow around the wind turbine on xy -plane at the hub height	106
Figure 5.2.16	Contours of u velocity over flow around the wind turbine on xz -plane at the centerline	107
Figure 5.2.17	Velocity contours for the selected annular sections	108
Figure 5.2.18	Vertical wake comparison between 2D velocity contours and selected vertical profiles	109

Figure 5.2.19	Contours of vorticity over flow around the wind turbine on ZY-plane at the hub height	109
Figure 5.2.20	Vortex visualization using iso-surfaces coloured by velocity	109
Figure 5.2.21	Self-similar cross-section over normalized downstream distances	110
Figure 5.2.22	Self-similar vertical profiles over normalized downstream distances	111
Figure 5.2.23	Comparison of four downstream cross-sections of the time-averaged turbulent kinetic energy k	112
Figure 5.2.24	Comparison of two vertical profiles, (a) and (b), of the time-averaged kinetic turbulent energy k for different downstream distances	113
Figure 5.2.25	Comparison of turbulence intensity TI deficits along the cross-sections downstream distances	114
Figure 5.2.26	Comparison of turbulence intensity TI for vertical profiles along the cross-sections downstream distances	114
Figure 5.3.1	NREL 5MW wind turbine structures: (a) rotor and tower in frontal, (b) top, and (c) lateral view	117
Figure 5.3.2	Lagrangian mesh of the NREL 5MW simulation	117
Figure 5.3.3	Case A	118
Figure 5.3.4	Case B	119
Figure 5.3.5	Case C	119
Figure 5.3.6	Case D	120
Figure 5.3.7	Case E	120
Figure 5.3.8	Lateral view of the 800 m height simulation	121
Figure 5.3.9	Case F - Final Setup	121
Figure 5.3.10	Mesh illustration for (a) vorticity criteria, refinement region with (b) three and (c) four levels of refinement	122
Figure 5.3.11	Installed probes in the Scenario 3	123
Figure 5.3.12	Annular displacement of the probes for longitudinal analysis	124
Figure 5.3.13	Animated longitudinal profiles and countours of streamwise velocity over time	125
Figure 5.3.14	Longitudinal annular velocity recovery profiles by ratio of r/R	125
Figure 5.3.15	Longitudinal streamlines of time-averaged velocity developing over the NREL 5MW wind turbine wake	126
Figure 5.3.16	The flow velocity contours development in top view of the NREL 5MW wind turbine	127
Figure 5.3.17	The flow velocity contours development over the cross-sections around the NREL 5MW wind turbine	127
Figure 5.3.18	Cross-section wake profiles for the 1, 2, 4, and 8 D downstream distances for the refinement region with 5 levels	128
Figure 5.3.19	Cross-section wake profiles comparison with UBC data for the 2, 3, 5 and 7 D downstream distances	130
Figure 5.3.20	The flow velocity contours development in lateral view of the NREL 5MW wind turbine	131
Figure 5.3.21	The flow velocity contours development over the vertical around the NREL 5MW wind turbine	132

Figure 5.3.22	Vertical wind velocity profiles subplots over downstream distance normalized by rotor diameters for the refinement region with 5 levels	133
Figure 5.3.23	Vertical wake profiles for the 3, 5 and 7 D downstream distances	134
Figure 5.3.24	Turbulent kinetic energy (k) cross-section wake profiles for the 2, 4, and 8 D downstream distances	136
Figure 5.3.25	Turbulent kinetic energy (k) vertical wake profiles for the 2, 4, and 8 D downstream distances	137
Figure 5.3.26	Turbulence intensity cross-section wake profiles for the 2, 4 and 8 D downstream distances	139
Figure 5.3.27	Turbulence intensity vertical wake profiles for the 2, 4 and 8 D downstream distances	140
Figure 5.3.28	Streamwise Reynolds Stress ($\sqrt{u'u'}/u_0$) analysis for downstream sections . .	142
Figure 5.3.29	Spectrum of Turbulent Kinetic Energy from upstream 1D to downstream 8D in the longitudinal centerline	144
Figure 5.3.30	Spectrum of Turbulent Kinetic Energy around the induction region and near downstream wake	145
Figure 5.3.31	Spectrum of Turbulent Kinetic Energy around blade's region	146
Figure 5.3.32	Dynamic iso-surfaces colored by velocity over flow around the wind turbine	147
Figure 5.3.33	Iso-surface colored by vorticity over and downstream of the NREL 5MW, where a) captures vorticity above 0.7, b) over 0.5, and c) all the vorticity range	149
Figure 5.3.34	Contours of gradients over flow around the wind turbine, for (a) xy-plane, and (b) xz-plane	150
Figure 5.3.35	Vectors of vorticity magnitude in the downstream position of the wind turbine	151
Figure 5.3.36	Contours vorticity magnitude in the downstream position of the wind turbine	151
Figure 5.3.37	Contours of the gradient components around the swept area	152
Figure 5.3.38	Comparison of the best-fit calculated coefficients and MFSim results	155
Figure 5.3.39	Torque and Power of the NREL 5 MW	158
Figure 5.4.1	Mesh illustration for (a) lateral, at centerline, and (b) superior, at hub height, view of four levels of refinement	161
Figure 5.4.2	Lagrangian mesh detailed for the NREL 5MW simulation	162
Figure 5.4.3	Position of the installed probes in the Scenario 4	162
Figure 5.4.4	Time-average streamwise velocity centerline recovery for the back to back NREL 5MW wind turbines	164
Figure 5.4.5	Time-average streamwise velocity centerline recovery comparison between both turbines	164
Figure 5.4.6	Time-average streamwise velocity recovery comparison between both turbines for cross-sectional and vertical sections	165
Figure 5.4.7	Instantaneous velocity contours with vectors scale by vorticity on xz -plane .	167
Figure 5.4.8	Instantaneous gradient magnitude contours on xy -plane at the hub height .	167
Figure 5.4.9	Animated longitudinal profiles and countours of streamwise velocity over time	168
Figure 5.4.10	Torque of the back to back NREL 5 MW wind turbines	168
Figure 5.4.11	Power generation of the back to back NREL 5 MW wind turbines	169

Figure A.1.1	Comparison of two downstream cross-sections of the time-averaged stream-wise velocity \bar{U} (m/s) for different angles of attack	189
Figure A.2.1	Comparison of two downstream cross-sections, (a) at 3 chord and (b) at 0 chord (9), of the time-averaged kinetic turbulent energy k normalized by u_0^2 for different angles of attack	190
Figure B.1.1	Comparison of normalized turbulent kinetic energy deficits along the down-stream distance for different section of the blade	191
Figure B.1.2	Reynolds stress tensor components profiles downstream the NREL Phase VI for different sections of the blade	192
Figure C.1.1	Longitudinal centerline profiles of time-average streamwise velocity	195
Figure C.1.2	Longitudinal annular velocity recovery profiles by ratio of r/R	196
Figure C.2.1	Cross-section wake profiles for the 1, 2, 4, 6 and 8 D downstream distances for the vorticity criteria	197
Figure C.2.2	Cross-section wake profiles for the 1, 2, 4, 6 and 8 D downstream distances for the refinement region with 3 levels	197
Figure C.2.3	Cross-section wake profiles for the 1, 2, 4, 6 and 8 D downstream distances for the refinement region with 4 levels	198
Figure C.3.1	Vertical wind velocity profiles subplots over downstream distance normalized by rotor diameters for the vorticity criteria	199
Figure C.3.2	Vertical wind velocity profiles subplots over downstream distance normalized by rotor diameters for the refinement region with 3 levels	199
Figure C.3.3	Vertical wind velocity profiles subplots over downstream distance normalized by rotor diameters for the refinement region with 4 levels	200
Figure C.3.4	Vertical wake profiles for the 1, 2, 4 and 8 D downstream distances	201
Figure C.3.5	Vertical wind velocity profiles over downstream distance normalized by rotor diameters for the vorticity criteria	202
Figure C.3.6	Vertical wind velocity profiles over downstream distance normalized by rotor diameters for the refinement region with 3 levels	202
Figure C.3.7	Vertical wind velocity profiles over downstream distance normalized by rotor diameters for the refinement region with 4 levels	202
Figure C.4.1	Longitudinal centerline profiles of time-average streamwise turbulent kinetic energy (k) for the three simulations	203
Figure C.4.2	Comparison of five downstream cross-sections of the time-averaged turbulent kinetic energy (k) for vorticity criteria simulation	204
Figure C.4.3	Comparison of five downstream cross-sections of the time-averaged turbulent kinetic energy (k) for refinement region with 3 levels	204
Figure C.4.4	Comparison of five downstream cross-sections of the time-averaged turbulent kinetic energy (k) for refinement region with 4 levels	205
Figure C.4.5	Turbulence intensity cross-section wake profiles for the 0, 2, 4 and 8 D downstream distances	206
Figure C.4.6	Turbulence intensity vertical wake profiles for the 0, 1, 3, 4, 6 and 8 D downstream distances	208

LIST OF TABLES

Table 1	Complementary reading for more detailed information	51
Table 2	Parameters of the NREL 5MW Wind Turbine	116
Table 3	Control Volume Cases for NREL 5MW Wind Turbine Simulation	118
Table 4	Wake diameter calculated from MFSim simulation	154
Table 5	Best-fit coefficients for the simplified wake models	154

LIST OF ABBREVIATIONS AND ACRONYMS

CFD	Computational Fluid Dynamics
CFL	Courant Friedrich Lewy
DNS	Direct Numerical Simulation
FSI	Fluid-Structure Interaction
FVM	Finite Volume Method
GWEC	Global Wind Energy Council
HAWT	Horizontal Axis Wind Turbine
IB	Immersed Boundary Method
LES	Large Eddy Simulation
LiDAR	Light Detection And Ranging
MARBLLES	Multiscale AtmospheriC Boundary Layer Large Eddy Simulation
MFLab	Fluid Mechanics Laboratory
NACA	National Advisory Committee for Aeronautics
NREL	National Renewable Energy Laboratory
PVM	Physical Virtual Model
RANS	Reynolds-averaged Navier-Stokes
RNG	Renormalization Group
RST	Reynolds Stress Tensor
SA	Spalart-Allmaras
SODAR	Sound Detection And Ranging
SOWFA	Simulator for Offshore Wind Farm Applications
SST	Shear Stress Transport
UBC	University of British Columbia
UFPR	Federal University of Parana
UFU	Federal University of Uberlandia
URANS	Unsteady Reynolds-Averaged Navier-Stokes
VAWT	Vertical Axis Wind Turbine
WTG	Wind Turbine Generator

LIST OF SYMBOLS

α	Shear coefficient
$\bar{f}(\vec{x}, t)$	Filtered part
\bar{U}	Mean wind velocity
β_c	Empirical constant
Δu	Time-averaged streamwise velocity deficit
Δ	Characteristic filter length scale
η_0	Empirical constant
\hat{G}	Second filter process
μ	Dynamic fluid viscosity
ν	Kinematic viscosity
ν_t	Turbulent viscosity
Ω	Rotational speed
$\omega_{i,f}$	Induction factor
ω_x	Angular velocity rotation
\bar{u}_{max}	Maximum time-average streamwise velocity at the section
ρ	Fluid density
σ_k	Prandtl turbulent number
τ_{ij}	Viscous stress tensor
$\tilde{\nu}$	Modified turbulent viscosity
\tilde{G}	Explicit filter
\tilde{x}_{ik}	Center positions of each Lagrangian cell
ε	Dissipation term
\vec{F}	Force acting in each individual lagrangian element
ζ	Vorticity criteria constant
A_s	Swept area
A_w	Cross-sectional wake area associated with the diameter

c	Airfoil chord length
$c(\vec{x}, t)$	Dynamic coefficient function
C_s	Smagorinsky constant
c_1	Prandtl mixing length constant
C_d	Drag coefficient
C_l	Lift coefficient
C_t	Thrust coefficient
D	Rotor diameter
$D_{ij}(\vec{x} - \vec{x}_K)$	Distribution function
D_e	Effective rotor diameter
D_w	Wake development
$E(K)$	Spectrum of the kinetic turbulent energy
$E_{(f)}$	Energy spectrum as function of a wave number
E_c	Kinetic energy
$f(\vec{x}, t)$	Generic signal
f_i	Source term associated with forces of fluid-structure interactions
F_1	Near wall activation function
F_2	Blending function
F_D	Drag force
F_L	Lift force
f_{v1}	Damping function
$f'(\vec{x}, t)$	Fluctuation part
$G(\vec{x} - \vec{x}')$	Filter function
H	Hub height
h^3	Lagrangian volume
I_a	Ambient turbulence intensity
k	Turbulent kinetic energy
K_c	Filter band width
k_{max}	Maximum time-averaged turbulent kinetic energy at the section

L	Length
l	Characteristic length scale
L_{ij}	Leonard tensor
l_{mix}	Mixing length
l_s	Airfoil span
LT_i^t	Right hand side of the momentum equation for the lagrangian element
m	Airflow mass
P	Power
p	Pressure
$P_{\bar{v}}$	Production term
p_{atm}	Atmospheric pressure
P_k	Turbulent kinetic energy production term
R	Radius
$R_{9.5}$	Wake radius at a downstream distance of 9.5 rotor diameters
R_w	Wake radius
Re	Reynolds number
S	Intensity of the mean rate-of-strain tensor
T	Torque
t	Time
$t + \Delta t$	Current time
u	Longitudinal component of the velocity
U^*	Auxiliar parameter in temporal term as a mathematical artifice
u_i	Velocity vector component for the i direction
u_0	Freestream velocity
V	Wind speed
v	Cross-sectional component of the velocity
V^*	Relation of the rate-of-strain tensor and rate-of-rotation tensor
V_r	Wind speed at the reference elevation
w	Vertical component of the velocity

x	Downstream distance
x_{ic}	Rotation reference position of the immersed boundary
z	Vertical height
Z_r	Reference height

CONTENTS

1	INTRODUCTION	21
1.1	General objective	23
1.2	Specific objectives	23
1.3	Project structure	24
2	LITERATURE REVIEW	25
2.1	Wind Power	25
2.1.1	Wind Turbine Design Parameters	26
2.1.2	Wind Turbine Flow Conditions	28
2.2	Experimental Studies	30
2.3	Wind Power Modelling and Simulation	32
2.3.1	Analytical and Empirical Modelling	33
2.3.2	Numerical Modelling	37
2.3.2.1	RANS Models	38
2.3.2.2	LES Modelling	44
2.3.2.3	Immersed Boundary Method	48
2.3.3	CFD Simulations used as Benchmarks	50
2.4	Complementary Reading	51
3	METHODOLOGY	53
3.1	Governing Equations	53
3.2	Large Eddy Simulation	54
3.2.1	Filtering of the Governing Equations	54
3.2.2	Sub-filter Tensor	56
3.2.2.1	Smagorinsky model	56
3.2.2.2	Dynamic model	57
3.2.2.3	Dynamic model with explicit filtering	58
3.3	Immersed Boundary Method	61
4	NUMERICAL METHODS	65
4.1	Finite Volume Method	65
4.1.1	Temporal and Spatial Discretization	66
4.1.2	Pressure-Velocity Coupling	69
4.2	Multiblock Structured Mesh	70
4.3	Multigrid-Multilevel Method	73
5	RESULTS AND DISCUSSION	77
5.1	Scenario 1: NREL Isolated Blade	77
5.1.1	Drag and Lift Coefficients	80

5.1.2	Time-averaged Streamwise Velocity	81
5.1.3	Turbulence Properties and Characteristics	84
5.2	Scenario 2: NREL Experimental Wind Turbine Phase VI	91
5.2.1	Probes Location	92
5.2.2	Longitudinal Profiles of Time-average Streamwise Velocity	94
5.2.3	Cross-sections Profiles of Time-average Streamwise Velocity	97
5.2.4	Vertical Profiles of Time-average Streamwise Velocity	102
5.2.5	Qualitative Analysis of the Flow Visualization	106
5.2.6	Self-similarity of Time-average Streamwise Velocity Profiles	110
5.2.7	Longitudinal, Cross-section and Vertical Profiles of Turbulence Properties	111
5.3	Scenario 3: NREL 5MW Wind Turbine	116
5.3.1	Geometry and Mesh Sensibility Analysis	118
5.3.2	Probes Location	123
5.3.3	Streamwise Velocity Analysis	124
5.3.3.1	Longitudinal Profiles	124
5.3.3.2	Cross-sections Profiles	126
5.3.3.3	Vertical Profiles	131
5.3.4	Profiles of Turbulence Properties and Spectrum	135
5.3.4.1	Turbulent Kinetic Energy	135
5.3.4.2	Turbulence Intensity	138
5.3.4.3	Reynolds Stress Tensor Streamwise Component	140
5.3.4.4	Spectrum of Turbulent Kinetic Energy	141
5.3.5	Qualitative Analysis of the Flow Turbulent Structures	147
5.3.6	Evaluation of the Analytical Wake Models Coefficients	153
5.3.7	Evaluation of Power Generation for Single Turbine	156
5.4	Scenario 4: Back to Back Wind Turbines	160
5.4.1	Geometry, Computational Mesh and Boundary Conditions	160
5.4.2	Probes Location	161
5.4.3	Profiles of Time-average Streamwise Velocity	163
5.4.4	Evaluation of Power Generation for Back to Back Turbines	167
6	CONCLUSIONS	171
7	RECOMMENDATIONS AND FUTURE WORK	173
	References	175
APPENDIX A	SCENARIO 1: ANALYSIS OF CROSS-SECTION VELOCITY AND TURBULENCE PROPERTIES	189
A.1	Cross-section Velocity	189
A.2	Turbulence Properties	190

APPENDIX B	SCENARIO 2: EXTRA ANALYSIS OF TURBULENCE PROPERTIES	191
B.1	Turbulence Properties	191
APPENDIX C	SCENARIO 3: NREL 5MW ANALYSIS FROM PREVIOUS MESHES	195
C.1	Longitudinal Profiles	195
C.2	Cross-sections Profiles	196
C.3	Vertical Profiles	198
C.4	Profiles of Turbulence Properties and Spectrum	203
C.4.1	Turbulent Kinetic Energy	203
C.4.2	Turbulence Intensity	204

1 INTRODUCTION

The demand for energy has been increasing due to the global economic growth. Such development has risen quickly over the past decades, in a way that the consumption of fossil fuels has become a major environmental concern (ZHONG et al., 2017). Increasing energy consumption not only results in depletion of non-renewable energy resources, but also gives rise to problems like global warming and greenhouse effect through emissions generated by the burning of fossil fuels (EDELENBOSCH et al., 2017). As a result of that, some countries were driven to prospect and adjust to renewable resources in order to maintain the expanding energy requirement (LUND, 2007; KILKIS et al., 2018).

The development of several sources of renewable energies, such as solar, hydropower and wind energy is extremely important and timely. Amid these renewable resources, wind energy has offered its advantages, the technology already developed along with a prospection on the market (LEUNG; YANG, 2012).

Wind energy has gained visibility in the last decade in terms of progress and potential, especially in Brazil. The Brazilian wind energy market has already advanced significantly. The country has reached 21.5 GW of installed capacity in 2022, with a total of 795 wind farms, and more than 9,000 wind turbines, and occupies the sixth position in the global ranking of onshore. Besides that, the country has potential for offshore wind energy that easily exceeds 700 GWs (ABEEÓLICA, 2022). The amount of energy generated in a wind farm depends not only on wind availability but also on the characteristics of the wind pattern being supplied. Therefore, it is essential to study the efficiency of wind power generation by assessing the effects of certain wind related parameters and coefficients on the wind turbine. A careful assessment of wind resources is desirable for the development of an effective wind project.

The wind turbine generator (WTG) extracts mechanical energy from the kinetic energy of the wind, converting the kinetic energy of the passing flow through the swept area of the wind turbine, to mechanical torque on the rotor hub (HANSEN, 2008). However, it is important to point out that the efficiency of the wind turbines that have been installed nowadays presents average values around 30% (GWEC, 2014). Therefore, attending to study and design large wind farm layouts, wind turbine modelling is a crucial element of the energy yield. Aiming to diminish the power losses, it is essential to have a valuable understanding of the wind turbine aerodynamics behavior (MO et al., 2013a; VERMEER; SØRENSEN; CRESPO, 2003).

Recently, the wind energy research field has shown progress. The development of wind turbines and their disposal on wind farms have been extensively investigated by the use of experimental and numerical methodologies. The former is usually based on physical models that are constructed in wind tunnels and the properties of interest (such as velocities and forces) are measured by means of experimental techniques. Frequently, this approach requires large wind tunnels and the use of sophisticated and expensive equipment. In many cases, the construction of a physical model is prohibitive for financial and practical reasons. On the other hand, the numerical strategies have expanded, became cheaper, more accessible, and more accurate in the

last three decades. As a consequence, these strategies have become an interesting alternative for wind energy studies.

In this context, the development of Computational Fluid Dynamics (CFD) has been expanded to applications of complex problems involving fluid-structure interaction. Numerical modelling has been employed for wind power projects with the objective of solving the properties of the turbulent flows in details. In particular, the use of Large Eddy Simulation (LES) has increased for wind power simulations, due to the growing of the available computational power (YILDIRIM et al., 2013; RAPAKA; SARKAR, 2016). The use of this method coupled with the Immersed Boundary Method (IB) is the state of the art approach for simulating high Reynolds numbers flows, with fluid-structure interactions involving complex and moving geometries (SOTIROPOULOS; YANG, 2014).

In the present study, LES and IB methods have been used together for modelling turbulent flows around single and coupled wind turbines. The simulations aim describing the dynamics of the turbulent flows in detail and the interactions of the wind with the turbine structures. A complete database (i.e. geometry, velocity and performance data) selected for single turbine, and simulations performed to analyze: (i) the turbine generated wakes and their effects on downstream structures, (ii) the interactions of the wind with the turbines in terms of turbulence properties, and (iii) the effects of turbulence on energy production efficiency. This study is expected to present an innovative numerical approach as a tool for improving the construction and operation of wind farms.

The LES simulations are performed in a dynamically adaptive mesh refinement environment, the present work provides an accurate, yet affordable, methodology for the prediction of wind structures and design of wind turbines. The document is presented in the following structure, the objectives of the study, extended literature review with complementary reading in the end of the section, methodology section presents the applied methodology defining the governing equations and the methods employed, describing the numerical methods in the research, which is divided by finite volume method, multi-block structured grids, and initial and boundary conditions. The results and discussion section are divided in three main scenarios: Scenario 1: NREL Isolated Blade, Scenario 2: NREL Experimental Wind Turbine Phase VI and Scenario 3: NREL 5MW Wind Turbine. By the end, the conclusion and recommendations of future work are presented.

This work contributes to a range of aspects: (i) leading MFSim platform to applications in the wind industry branch, real scale wind turbine, as the measurements by met towers and other equipment provide results only for specific points or at most small regions of the flow; (ii) comprise a full rotor simulation applying LES-IB, not only actuator disk or line modelling, for real scale wind turbine; (iii) simulate in detail the turbulent flow properties around full-scale turbines since turbulence measurements in full-scale turbines is challenging to obtain at scale due to the operational work and phenomenology of turbulence; (iv) evaluate and determine accurate coefficients for the simplified wake models applied in the wind industry branch, then create benchmarking/reference simulations to evaluate the coefficients based on those; v) leading the MFSim code to its high-performance stress by employing a high demand with a couple of millions of cells; vi) verifying and validating the formulation performance of explicit filtering

with the dynamic Smagorinsky model already implemented in the MFSim code for applications in real scales rotational flows; vii) evaluating the dynamic adaptive meshing tool by vorticity criteria already implemented in the MFSim code to capture turbulent structures and vortices in the downstream wake region of the turbine.

1.1 GENERAL OBJECTIVE

The overall objective of this study is to apply Large Eddy Simulation along with the Immersed Boundary Method to provide crucial spatial and temporal information of the flow around selected wind turbines. The results of the developed study aim to help understand and minimizing the wake effects regarding power performance over wind power projects.

1.2 SPECIFIC OBJECTIVES

The specific objectives of this study are:

- a) Literature review and study aiming to establish state of the art on wind power (i) fluid dynamics computational, (ii) turbulence models, including LES and (iii) immersed boundary methodologies;
- b) Modification, update and application of the MFSim code for the wind power branch, with which the Navier-Stokes equations in the transient three-dimensional shape using a multi-block mesh with adaptation and refinement local;
- c) To evaluate the dynamic adaptive mesh tool by vorticity criteria and the explicit filtering tool along the dynamic smagorinsky model for real-scale applications of rotational flow;
- d) To verify and validate the modifications made to adapt the code for full-scale wind turbines and compare to literature results;
- e) To study characteristic details around the downstream near wake of a wind turbine (i.e., mean velocity components distribution, Reynolds stresses distribution, turbulence intensity distribution, etc.);
- f) To evaluate the wake coefficients that are incorporated into simplified wake models, such as Park, Frandsen and Larsen models;
- g) To implement, modify, adapt, and evaluate the calculation of torque and energy production, evaluating a stand alone (i.e., torque, power output, etc.);
- h) To study the wake effects over downstream wind turbines in terms of energy production, evaluating back to back turbines (i.e., mean wind velocity deficits for power output purposes, turbulence effects over the wind turbine performance, etc.);

1.3 PROJECT STRUCTURE

Chapter I presents the introduction of the research. After that, we present the definition of the general and specific objectives of this work, as well as the thesis structure. Chapter II develops the review of principles aspects retreated in the thesis, divided by wind power, wind flow, experimental studies, and wind power modelling and simulation. Chapter III presents the applied methodology defining the governing equations and the methods employed. Chapter IV describes the numerical methods in the research, which are divided into finite volume method, multi-block structured grids, and multigrid-multilevel method. Chapter V presents the thesis results, which includes the NREL S809 blade analysis, the NREL Phase VI experimental wind turbine, and the last scenario composed of the full-scale NREL 5MW wind turbine stand alone and back to back turbines. Chapter VI presents the conclusions of this work. Chapter VII introduces the perspectives for future research on this topic.

2 LITERATURE REVIEW

This chapter presents a literature review that includes the main aspects of the phenomenon involved in wind energy applications and some relevant experimental studies in this research field. The up to date wind power modelling strategies are also reviewed, focusing on computational fluid dynamics methods, including the most popular Reynolds averaged models and a complete description of the Large Eddy Simulation (LES) .

2.1 WIND POWER

The energy quantity available in the wind varies according to the annual season and the time of day, because of the wind speed variation. Topography and ground roughness also influence the wind speed profile and distribution on certain sites. Furthermore, the available wind power depends on performance characteristics, operation time, operation height and positioning layout of the wind turbines.

The wind turbines can be classified in terms of the rotor axis positioning. The denominated horizontal axis wind turbine (HAWT) has blades that spin at the perpendicular plane of the main wind direction. When blades spin at the parallel plane of the main wind direction it is called vertical axis wind turbine (VAWT) . This study focuses on the horizontal axis wind turbine.

Wind turbines convert the kinetic energy of the flow, which causes the rotation of the blades around their axis, to mechanical torque on the rotor hub. The electromagnetic conversion transforms the torque into electrical energy with the assistance of an electric generator. The amount of electricity that can be generated depends on four main factors: the amount of wind over the swept area, the rotor diameter, the blade airfoil design and the system efficiency.

The kinetic energy related to the inflow wind over the wind turbine blades that rotate on a cross section area A_s is given by:

$$E_c = \frac{1}{2}mV^2, \quad (2.1)$$

where E_c is the kinetic energy (J); m is the airflow mass (kg); V is the average wind speed (m/s).

The power produced from the wind speed is associated with the kinetic energy time rate of change, and with the air mass with density ρ flowing at wind speed V trough an area A_s as the following:

$$P = \frac{1}{2}\rho A_s V^3. \quad (2.2)$$

According to Betz's theory, the maximum efficiency that a wind turbine can reach is 59.3%, as the wind speed reduces when approaches the rotor plane (ÇENGEL, 2010). However,

it is important to point out that the efficiency of the wind turbines installed nowadays presents average values around 30% according to (COUNCIL, 2016). Therefore, one of the stages for achieving better wind turbine efficiency is the flow analysis over the blades, where the minimum geometry variation may cause changes in the generated power. The next two sections review the wind turbine parameters design and wind turbine flow conditions.

2.1.1 Wind Turbine Design Parameters

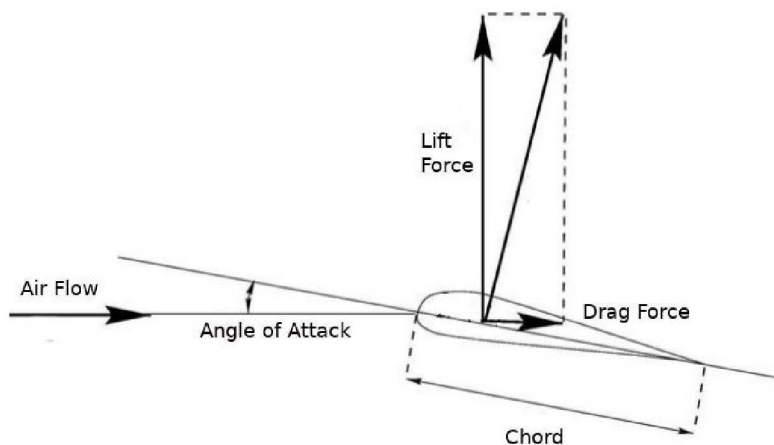
Theoretical, experimental and numerical studies have demonstrated that many flow characteristics can be represented by non-dimensional parameters. An essential non-dimensional parameter for representing the fluid flow conditions is the Reynolds number Re , which is defined as:

$$Re = \frac{VL}{\nu} = \frac{\rho VL}{\mu} = \frac{\text{Inertial force}}{\text{Viscous force}}, \quad (2.3)$$

where ρ is the fluid density, μ is dynamic fluid viscosity, $\nu = \mu/\rho$ is the kinematic viscosity and V and L are velocity and length that characterize the scales of the flow. The last two parameters can be the inflow velocity and the chord length on a blade.

Force and moment coefficients, which are functions of the Reynolds number, can be defined for two or three-dimensional objects. Adopting a two-dimensional object for illustration purposes, the airflow over a blade generates two forces, a lift force (F_L) perpendicular to the airflow direction and a drag force (F_D) in the direction of the air flow, as shown in Figure 2.1.

Figure 2.1 – Drag and lift Forces



SOURCE: Adapted from Manwell, McGowan and Rogers (2010)

The lift force on the blade occurs due to pressure gradient generated by the difference between the pressure on the lower and upper part of the blade. The drag force is created by the pressure distribution around the blade and by the friction between the airflow and the blade

surface. Moreover, the lift/drag ratio is important in designing an efficient turbine blade. Wind turbine blades are twisted, which allow the presence of an angle of attack that establishes the possibility of an ideal ratio of the lift/drag force.

Measurements of the lift and drag forces are performed in wind tunnels under certain conditions in order to understand the behavior of those parameters. Manwell, McGowan and Rogers (2010) developed blades assessments using the same types of airfoil on an HWAT. This study demonstrated that delaying stall may underpredict the power generation, which results in higher loads than expected for high wind speeds, thus reducing the wind turbine lifetime. Such behavior has been associated with the development of a spanwise wind velocity component over the blade that maintains the airflow connected to the blade, delaying stall and intensifying the lift force.

Wind tunnel experiments are also used to determine the two-dimensional lift C_l and drag C_d coefficients for rotor design, employing a large range of Reynolds numbers and angles of attack. Those coefficients are calculated as follows:

$$C_l = \frac{F_L/l_s}{\frac{1}{2}\rho V^2 c} = \frac{\text{Lift forces / unit length}}{\text{Dynamic force / unit length}} \quad (2.4)$$

$$C_d = \frac{F_D/l_s}{\frac{1}{2}\rho V^2 c} = \frac{\text{Drag forces / unit length}}{\text{Dynamic force / unit length}}, \quad (2.5)$$

where c is the airfoil chord length and l is the airfoil span.

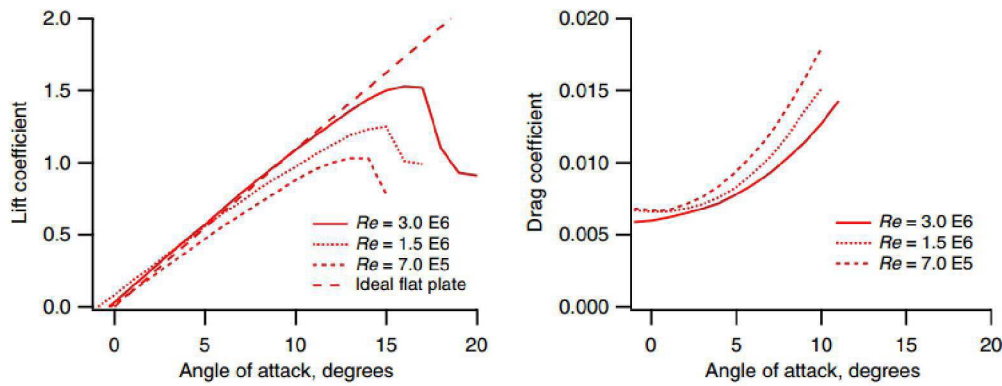
Wind turbine blades of the HAWT are frequently developed to be utilized for small angles of attack, where lift coefficient are rather larger than drag coefficients. The lift coefficient usually is close to zero when the angle of attack is also zero, the coefficient can reach 1.0 for certain angles, then decreases for high angles of attack. On the other hand, the drag coefficient gets bigger for high angles of attack. Figure 2.2 shows the variation of lift and drag coefficients according to Reynolds number and the angle of attack for a NACA 0012 profile from National Advisory Committee for Aeronautics (NACA) with four digits where: (i) the first digit describing maximum camber as percentage of the chord; (ii) the second digit describing the distance of maximum camber from the airfoil leading edge in tens of percents of the chord; (iii) and the last two digits describing maximum thickness of the airfoil as percent of the chord.

Another important parameter which can be used to show the interaction of the blade with the flow is the pressure coefficient that can be expressed as:

$$C_p = \frac{p - p_{atm}}{\frac{1}{2}\rho(V^2 + l^2\Omega^2)} = \frac{\text{Static pressure}}{\text{Dynamic pressure}}, \quad (2.6)$$

where p , p_{atm} and Ω are pressure on the blade surface, atmospheric pressure and the rotational speed, respectively. The pressure coefficient has been used in literature for validation of numerical studies, more specifically for LES modelling of the wind turbine, as presented in Figure 2.3, where pressure coefficients are compared in different locations of the wind turbine blade between the numerical simulations and the experimental results from a wind tunnel experiment. The abscissa axis represents the rate (x) of the profile distance along the chord over the value of the chord

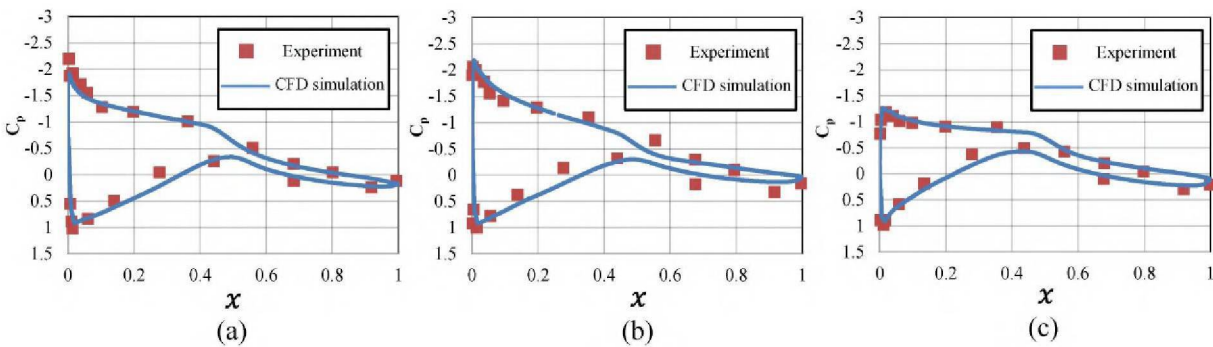
Figure 2.2 – Lift and drag coefficients for the NACA 0012 symmetric airfoil for different Reynolds number



SOURCE: Miley (1982)

itself, while the ordinate axis is the non-dimension pressure coefficient around the superior (suction) and inferior (pressure) surfaces of the blade profile.

Figure 2.3 – LES modelling validation through pressure coefficient on the turbine blades for three different radius rate, (a) 0.3, (b) 0.63, (c) 0.95.



SOURCE: Sedaghatizadeh et al. (2018)

Moreover, an efficient blade shape is based on the aerodynamic calculations of the selected airfoils. Parameters as lift and drag help to find the exact angles of twist and chord lengths for the optimum blade profile. Therefore, a complete assessment of the wind conditions and turbine designs is important to achieve the optimum angular velocity of the axis allowing the wind turbine operation near its maximum efficiency.

2.1.2 Wind Turbine Flow Conditions

Wind turbines operate in the lower part of the atmospheric boundary layer, which complicates the assessment and evaluation of the flow around these turbines. The power output primarily depends on the mean inflow wind velocity. In addition, geometry and surface roughness can also influence the flow distribution around the turbines.

In the boundary layer region, the wind speed distribution usually represents the wind pattern. This region presents high velocity gradients that are responsible for intense vertical transport of horizontal momentum (ROHATGI; BARBEZIER, 1999). Therefore, there is an essential parameter to characterize the wind pattern and its influences, denominated wind shear, which is associated with the difference of wind speed with height above the terrain. The wind shear parameter can influence the wind turbine power generation and affects the wind turbine blades lifetime depending on the hub height (MANWELL; MCGOWAN; ROGERS, 2010; HONRUBIA et al., 2010).

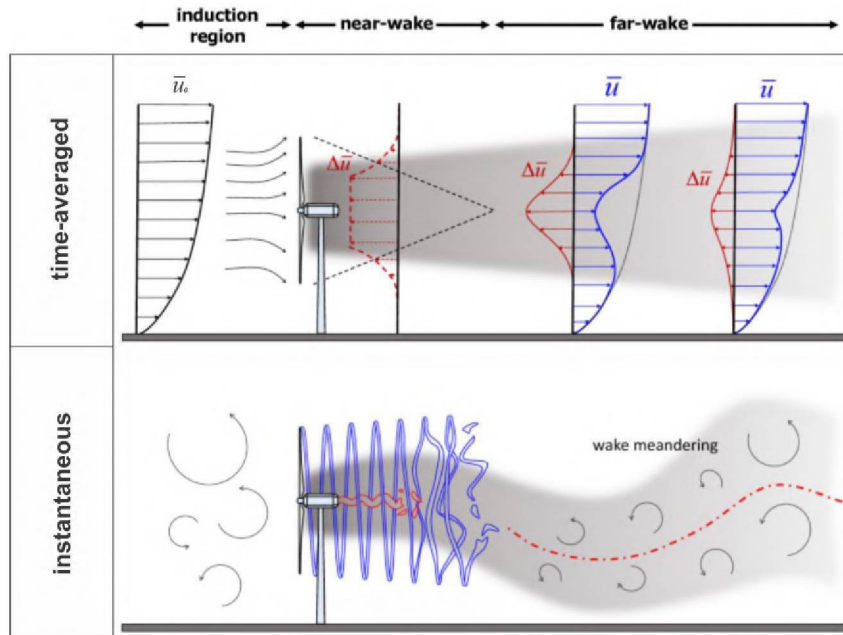
A power law is commonly applied by wind engineering industries and companies to describe the basic equation of wind shear. The equation follows (CHEHOURI et al., 2015):

$$V(z) = V_r \left(\frac{z}{Z_r} \right)^\alpha, \quad (2.7)$$

where Z_r is the reference height, α is the wind shear coefficient and V_r is the wind speed at the reference elevation. The wind shear coefficient usually ranges from 0.1 to 0.4, varying according to the terrain roughness and the turbulence variation (MANWELL; MCGOWAN; ROGERS, 2010; BURTON et al., 2011).

Although, the power law is valid for the mean vertical profile of the streamwise velocity component. The mean of the other components is assumed to be zero. However, instantaneously there are fluctuations different from that mean. A schematic drawing is shown in Figure 2.4 presenting the mean and instantaneous velocity profiles, as this study will work with 3D velocities and turbulence.

Figure 2.4 – Schematic drawing presenting the mean and instantaneous velocity profiles



SOURCE: Adapted from Porté-Agel, Bastankhah and Shamsoddin (2020)

Turbulence is the fluctuations of the airflow that are superimposed to the wind's velocity motion. These fluctuations can impact the power performance, affecting the wind turbine loads, the extension of the wake regions and the noise propagation (GOTTSCHALL; PEINKE,

2008; STIVAL; GUETTER; ANDRADE, 2017). Low turbulence conditions are associated with stable conditions, where low wind speed and its variation prevail. In contrast, high turbulence conditions are linked to unstable conditions, characterized by abrupt and quick vertical changes of the streamwise wind velocity (KAISER et al., 2004; SHEINMAN; ROSEN, 1992). Turbulence that occurs under unstable conditions may influence turbine load and performance due to the development of mixing among air portions at distinct heights (ROY; SHARP, 2013; SATHE et al., 2013). Most of the studies report typical values of atmosphere turbulence intensity in the range from 3% to 20% (WHARTON; LUNDQUIST, 2012).

Wind turbines generate downstream wakes, which are areas of flow with lowered momentum and enlarged turbulence in relation to the freestream region. Such phenomena is induced by the energy extraction from the wind, where each turbine produces a recirculation region downstream, reducing the mean velocity that is transported to the downstream wind turbine. The velocity deficit in the wakes recovers faster for high turbulent incoming wind flows, where most of the turbulent kinetic energy is dissipated in the near wake region (WU; PORTÉ-AGEL, 2012; STIVAL; GUETTER; ANDRADE, 2017). It is important to evaluate this parameter because turbulence from the upwind turbines affects the power performance of the downwind turbines, whenever the wind direction aligns with the wind farm turbines. In addition, fatigue and loads can be enlarged by wake effects (MANWELL; MCGOWAN; ROGERS, 2010).

Improving the knowledge about velocities deficits, turbulence properties, wind shear and wake effects is crucial for achieving the maximum efficiency of energy generation in wind farms. With this in mind, experimental studies are conducted to investigate the role of these variables on the design of turbines and on wind turbines production efficiency.

2.2 EXPERIMENTAL STUDIES

Experiments can simulate wind turbine problems using laboratory physical models or even in real scale. Usually, they are expensive and sometimes they are unable to fully reproduce every characteristic of the real conditions (*i.e.* high altitudes, a wide range of wind speeds, etc). The typical high costs comes from the need of investments in an appropriate laboratory that would be in accordance with the minimum requirements for testing, and also the need to produce a new prototype for each designed model. However, in the absence of established mathematical models, the experimental model is often a suitable alternative available to the developer (MALISKA, 1995).

In the last decades, experimental studies have been elaborated in wind tunnel tests. Ramsay, Hoffman and Gregorek (1995), Somers (1997), Hand et al. (2001), Simms et al. (2001) performed tests that may be considered the most precise and efficient approach to characterize the forces acting over wind turbine blades. These authors developed a structural model and verification procedures for the wind experimental Phase VI of the National Renewable Energy Laboratory (NREL) , which is a two-bladed wind turbine, as depicted in Figures 2.5 and 2.6. Many experimental measurements were described for pressure over the blades, aerodynamic forces, torque and wakes. The wind speeds varied from 5 m/s to 25 m/s at a hub height of 12.2 m and a rotor diameter of 10.058 m. The experiments performed a diverse number of aerodynamic

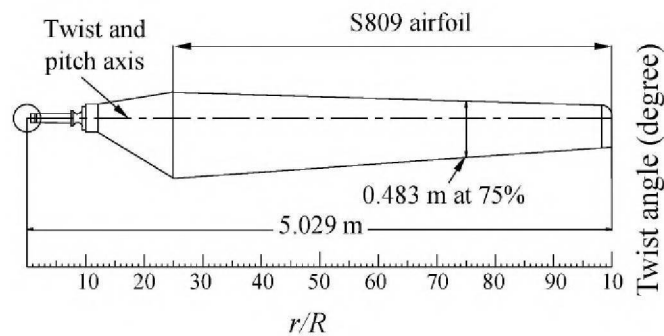
measurements and a great amount of structural information to develop a fluid-structural model.

Figure 2.5 – Two bladed wind turbine from experimental Phase VI of the National Renewable Energy Laboratory (NREL)



SOURCE: Hand et al. (2001)

Figure 2.6 – The S809 blade airfoil Phase VI NREL experimental



SOURCE: Hand et al. (2001)

High-quality field measurements are important to reduce the energy production estimation uncertainty of a project. Clive (2016) and Clive (2012) applied anemometers, LiDAR (Light Detection And Ranging) and SODAR (Sound Detection And Ranging) to identify and measure wind patterns over complex terrain, aiming to achieve the best power curve assessment of a wind turbine. Chaurasiya, Ahmed and Warudkar (2017) used SODAR measurements to characterize the wind shear for different heights and Ahmed and Chaurasiya (2019) presented a turbulence description based on SODAR measurements, aiming to analyze the turbulence intensity.

Other selected studies have measured wind turbine wakes to apply remote sensing (LiDAR and SODAR) in order to estimate wake parameters downstream of the wind turbine

(BINGÖL; MANN; LARSEN, 2010; TRUJILLO et al., 2011). LiDARs have demonstrated the capacity to measure with significant accuracy wake parameters (*i.e.* length, width, and deficit of wakes) in different atmospheric environments (KÄSLER et al., 2010). LiDARs can be positioned in different placements concerning the wind turbine, on the nacelle, or the ground almost a kilometer away from the wind turbine (AITKEN et al., 2014; SMALIKHO et al., 2013). Although, the most significant disadvantage of this type of equipment and measurement is the cost, which is expensive to buy or rent equipment.

Kim et al. (2015) used met mast measurements to report that the flow disturbance caused by wake effects can be estimated through both turbulence intensity and wind shear gradient. The study was based on steady and dynamic power curves. The authors understood that when a site has a low mean wind speed, the energy improvement for low wind speed would compensate for the power losses for higher wind speeds, due to the high turbulence intensity effect. Therefore, the study concluded that high turbulence intensity significantly increases the fatigue load.

Adaramola and Krogstad (2011) showed that the power losses for a turbine operating in the wake of the upstream wind turbine are significant with the maximum loss in the downstream turbine varying from 20 to 45% depending on the distance between the turbines and their operating conditions. Barthelmie et al. (2007) and Barthelmie et al. (2009) also reported that wake losses, for a given wind direction, can be as much as 10–20% of the power when no wakes are present. The comprehension of power losses expected to wind turbine wake on wind plants is vital to improving the wind farm display. The authors detected that power losses by a single wind turbine due to wakes were close to 10% generally. However, for the entire wind farm, the output energy reduction may range from 5% to 8% of the annual energy yield.

2.3 WIND POWER MODELLING AND SIMULATION

Numerical modelling applications have been increasing for wind farm projects, helping to achieve a better knowledge of the flow interaction around wind turbines. This increase was possible due to the development of computational technologies, which allowed the utilization of sophisticated methodologies. Recent developments have offered the possibility to solve in details the properties of interest in atmospheric turbulent flows.

Computational fluid dynamics (CFD) is the branch of fluid mechanics that simulates real flows by means of the numerical solution of governing equations. The objective is to reduce the effects of assumption limitations that are applied in simplified methods. In general, the literature review has shown that numerical solutions for the governing equations of motion permit a plausible description of the flow aerodynamics (VERSTEEG; MALALASEKERA, 1995). The technology has grown up in terms of computing development, which brought CFD as a useful tool in many applications, ranging from flows with simple aerodynamic profiles to atmospheric boundary layers flows.

The complexity of turbulent flows makes the exact solution of the governing equations impossible, particularly for high Reynolds number, three dimensional and transient problems (SUMNER; WATTERS; MASSON, 2010). Solving the governing equations numerically through

Direct Numerical Simulation (DNS) would allow representing all turbulence scales of the flow. The solution idea of this model is the simulation of the entire energy spectrum, from the integral scales to the Kolmogorov scales. This methodology does not need a closure model, as the characteristic size of the mesh tends to the Kolmogorov length scale. It also requires a very refined spatial discretization mesh and tiny time steps.

The determination of the mesh size and the time step is the physical nature of the flow, that is, the value assigned to the Reynolds number (NETO, 2020). However, the need for highly refined meshes makes this approach impracticable for most practical cases because of the required computational resources in terms of memory, storage, and processing. As the refinement of the mesh and the time step depends on the Reynolds number, the higher the value assigned to this parameter, the higher the necessary refinement for the spatial mesh and the time step. Thus, the DNS application for turbulent flow simulation is limited to flows at low Reynolds number values, which is the most significant limitation of this methodology.

To overcome this difficulty, numerical methods have been developed for reducing the degree of freedom in the problems by means of turbulence modelling. The most used approach for turbulence modelling is based on the Boussinesq hypothesis, in which turbulence diffusivity is calculated by a turbulence viscosity (BOUSSINESQ, 1877). This concept is usually implemented in the context of time averaging of the Navier-Stokes equations (REYNOLDS, 1895), resulting in the so-called Reynolds-averaged Navier-Stokes equations (RANS). Most of the numerical simulations in wind energy engineering reported in the literature are based on the RANS approach.

In the last few years, Large Eddy Simulation (LES) has become more viable for practical applications. In this approach, the turbulent kinetic energy spectrum is separated into two pieces by a spatial filtering process. The large scales (those greater than the filter width) are calculated explicitly on the mesh. The residual or small scales are determined by turbulence modelling. This approach has become more popular for wind turbine applications in recent years, with the development of more precise turbulence models and also methods for solving complex fluid-structure problems (YILDIRIM et al., 2013).

For situations involving complex moving geometries, an alternative is to use LES with Fluid-Structure Interactions (FSI) methods, also known as Immersed Boundary methods (IB). Presently, this approach is considered the most advanced strategy for wind turbine numerical simulations (RAPAKA; SARKAR, 2016).

2.3.1 Analytical and Empirical Modelling

Despite the recent developments of numerical and experimental methodologies, elementary analytical and empirical models with low computational costs are still convenient tools for forecasting flows over wind power plants.

One type of empirical models is based on the description of the wind speed in the atmospheric boundary layer. Tieleman (2008) analyzed the comparison of different wind profile models against wind speed observations in order to evaluate the prediction efficiency presented from theoretical and empirical models. For an open source terrain with no obstacle, particular

variations of wind profiles were observed in terms of the surface roughness. The study concluded that surface layer height influences can reach 150 m depending on the roughness and wind speed conditions.

Stival, Guetter and Andrade (2017) performed a study investigating the influence of the wind shear coefficient on the power performance of the wind turbines. The results permitted to conclude that events with large wind shear coefficients can lead to power losses around 20% for low wind speeds.

Another class of the analytical and empirical models estimates downstream wake developments and effects. These models can be classified into two groups: (i) kinematic models and (ii) roughness distribution models. The first category considers a single wind turbine wake and employs the superposition property to engage the adjacent wind turbine wakes (KATIC; HØJSTRUP; JENSEN, 1987). In the second category, the wind turbines represent distributed roughness elements that modify the atmospheric flow (FRANDBSEN, 1992). Examples of these types of models are Park (JENSEN, 1983), Frandsen (FRANDBSEN et al., 2006) and Larsen (LARSEN, 1988) models.

Park Model

The Park model, also called Jensen model, assumes a gradually developing wake with a velocity deficit that is only relative to the distance behind the rotor, expanding radially at linear rate. This model is not indicated for the far wake prediction, but it is a fairly good representation for the near wake (JENSEN, 1983).

For the longitudinal centerline, the model considers a gradually developing wake that is a linear function of the turbine downstream distance x . The wake development can be computed as, D_w , is given by:

$$D_w = D + 2Kx, \quad (2.8)$$

where D is the rotor diameter and K is an empirical decay constant, that represents the dissipation process as the wake width increases. A common value of K used for onshore wind farms simulations is 0.075 (PENA; RETHORE; LAAN, 2016).

In the Park model the longitudinal velocity downstream from a turbine is calculated according to:

$$\frac{u}{u_0} = 1 - 2\omega_{if} \left(1 + \frac{2Kx}{D}\right)^{-2}, \quad (2.9)$$

where u is the longitudinal component of the velocity downstream from the turbine, u_0 is the freestream velocity and ω is a induction factor given by:

$$\omega_{if} = \frac{1 - \sqrt{1 - C_t}}{2}, \quad (2.10)$$

where C_t is a thrust coefficient lower than 1,0, which is associated with the maximum thrust force resulting from the energy conversion in the equipment (JENSEN, 1983).

Frandsen Model

Frandsen et al. (2006) had developed a wake model that was firstly applied for offshore wind turbines, but could be extended for onshore conditions in the case of low roughness. The wind speed deficit calculation considers a circular wake area, which develops until hitting the terrain or sideways wakes. The model assumes three distinct wake zones: (i) in the first zone a single wake is produced with no synergy among adjacent wakes; (ii) the second zone begins when two adjacent wake flows merge; (iii) the third zone occurs when the wake flow is in equilibrium with the atmospheric boundary layer, which occurs when the wind farm is sufficiently large.

This model also assumes a top-hat shape for the velocity distribution in the wake cross sections. The wake diameter of a single wake is given by:

$$D_w = D \left(\beta^{\frac{3}{2}} + \gamma x \right)^{\frac{1}{3}}, \quad (2.11)$$

where D_w is the wake diameter, D is the rotor diameter, x is the downstream distance in rotor diameter (D), γ and β are non dimensional parameters written as functions of the thrust coefficient according to:

$$\gamma = 1 - \sqrt{1 - C_t}, \quad (2.12)$$

$$\beta = \frac{1 + \sqrt{1 - C_t}}{2\sqrt{1 - C_t}}. \quad (2.13)$$

In the Frandsen model the longitudinal velocity downstream from a turbine is given by:

$$u = \frac{u_0}{2} \left(1 \pm \sqrt{1 - 2 \frac{A}{A_w} C_t} \right), \quad (2.14)$$

where u is the longitudinal component of the velocity downstream from the turbine, u_0 is the freestream velocity, A_w is the cross-sectional wake area associated with the diameter D_w , A is the cross-sectional region in the beginning of the wake expansion.

Larsen Model

The model developed by Larsen (1988) simulates wakes through two main parameters, (i) the wake width and (ii) the velocity variation behind the wind turbine. The Larsen model is based on Prandtl's turbulent boundary layer equations, where the wind speed deficit depends on both perpendicular and longitudinal distance from the wind turbine. The model takes into

account just the dominant terms of the boundary layer equations, assuming incompressible fluid and steady flow.

The model is able to calculate velocity distribution for cross sections and longitudinal distances downstream from the turbine. Besides that, the wake radius, (R_w), of a single wind turbine is given by:

$$R_w = \left(\frac{35}{2\pi}\right)^{3/10} (3c_1^2)^{1/5} (C_t A (x + x_0))^{1/3}, \quad (2.15)$$

where A is the rotor area, C_t is the thrust coefficient and x_0 is the normalized position of the wind turbine. The constant namely c_1 is associated to the Prandtl mixing length, dependent of x_0 , is calculated according to:

$$c_1 = \left(\frac{D_e}{2}\right)^{5/2} \left(\frac{105}{2\pi}\right)^{-1/2} (C_t A x_0)^{-5/6}, \quad (2.16)$$

and the normalized position of the WTG is given by:

$$x_0 = \frac{9.5D}{\left(\frac{2R_{9.5}}{D_e}\right)^3 - 1}. \quad (2.17)$$

The x_0 parameter is a function of the effective rotor diameter (D_e) and the wake radius at a downstream distance of 9.5 rotor diameters ($R_{9.5}$) from the hub, calculated as follows:

$$R_{9.5} = 0.5 [R_{nb} + \min(H, R_{nb})], \quad (2.18)$$

in which R_{nb} is defined by,

$$R_{nb} = \max(1.08D, 1.08D + 21.7D(I_a - 0.05)), \quad (2.19)$$

where I_a represents the ambient turbulence intensity and H the hub height.

The parameter D_e , in equation (2.16), is only function of the thrust coefficient (C_t), according to:

$$D_e = D \sqrt{\frac{1 + \sqrt{1 - C_t}}{2\sqrt{1 - C_t}}}. \quad (2.20)$$

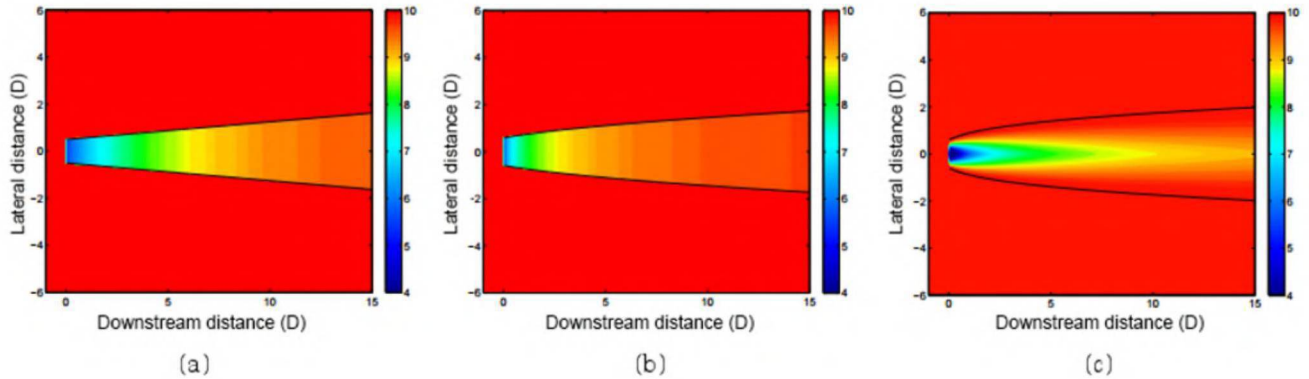
Therefore, the subsequent expression represent the main parameter of the Larsen model, which is the wind speed deficit inside the wake, ($u_0 - u$), as follows:

$$u_0 - u = \frac{-u_0}{9} (C_t A (x + x_0)^{-2})^{1/3} \left\{ r^{\frac{3}{2}} (3c_1^2 C_t A (x + x_0))^{-1/2} - \left(\frac{35}{2\pi}\right)^{3/10} (3c_1^2)^{-1/5} \right\}^2, \quad (2.21)$$

where u_0 is the freestream wind speed at rotor u is the wind speed in the wake.

Figure 2.7 illustrates the calculation of the wake development for the three wake models cited above, where the x -axis stands for the downstream distance from the wind turbine in rotor diameters and the y -axis is the lateral cross-section of the wake expansion in rotor diameters. The contours represent the wind speeds varying from 4 to 10 m/s.

Figure 2.7 – Illustration of the (a) Park, (b) Frandsen and (c) Larsen wake models profiles



SOURCE: Adapted from Hu (2016)

A recent study developed by Stival (2017) aimed to simulate the turbine induced wind speed deficits and the ratio of restoration for three free stream wind speed. The work compared Park, Frandsen, Larsen and Eddy Viscosity (Ainslie) models with LiDAR wake measurements for a single turbine on flat terrain. The study simulated wind speeds from 5 to 12 m/s and presented results for distinct cross sections located downstream from the wind turbine. The author concluded that, in terms of centerline wake analysis, the Larsen model presented the best results for 5 m/s wind speeds, and the Park wake model yielded the best velocity simulations for wind speeds from 6 to 8 m/s. Meanwhile, Ainslie wake model yielded the best performance for wind speeds from 9 to 12 m/s.

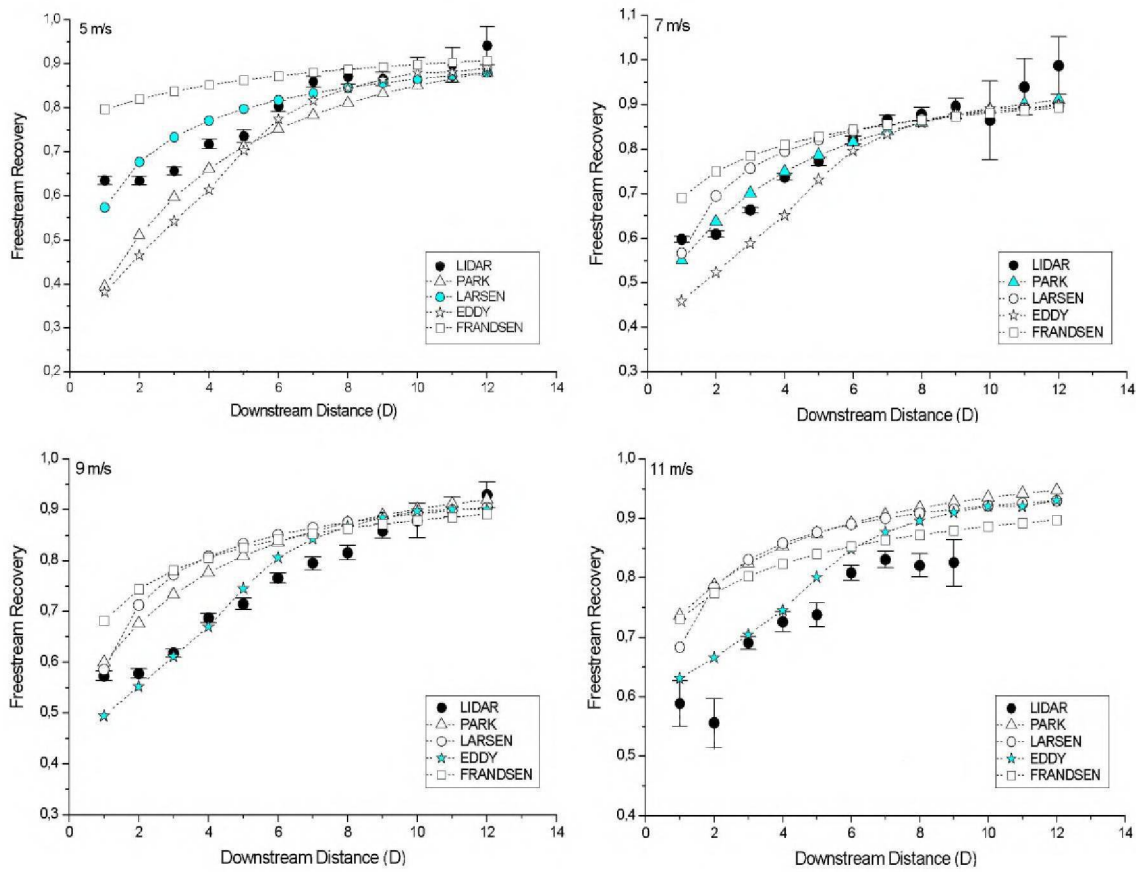
Figure 2.8 illustrates the centerline velocity recovery performance in the wake region for each model, over 5, 7, 9 and 11 m/s wind speeds. The perpendicular cross section wake analysis presented domination of the Park model for the 5D downstream distance. Meanwhile, along the 7D downstream distance cross section, the Larsen wake model produced the best results.

Vermeer, Sørensen and Crespo (2003) reviewed several analytical models that estimate wake development, interaction and superposition. The authors concluded that an advantage of the empirical models is the lower cost compared to the more computationally expensive models. However, the authors emphasized that the simplified empirical models sometimes fail in representing the wake development with accuracy.

2.3.2 Numerical Modelling

In the present study, the evolution of the flow aerodynamics is described by the mass and momentum conservation equations. In cartesian coordinates and using index notation, for

Figure 2.8 – Illustration of the velocity recovery along the wake centerline for the wake models compared to LiDAR measurements



SOURCE: Stival (2017)

$i, j = 1, 2, 3$, these equations are given by:

$$\frac{\partial \rho}{\partial t} + \frac{\partial \rho u_i}{\partial x_i} = 0, \quad (2.22)$$

$$\frac{\partial \rho u_i}{\partial t} + \frac{\partial \rho u_i u_j}{\partial x_j} = -\frac{\partial p}{\partial x_i} + \frac{\partial \tau_{ij}}{\partial x_j}, \quad (2.23)$$

where p is the pressure, ρ is the fluid density, u_i is the velocity vector component for the i direction, τ_{ij} is the viscous stress tensor.

2.3.2.1 RANS Models

Many of the CFD studies related to wind turbine aerodynamics have been proposed since the original approach elaborated by Sørensen and Hansen (1998). In this context, RANS models have been the most applied methodology for simulating horizontal axis wind turbine aerodynamics (BAI; WANG, 2016). This section reviews this type of models and their applications for wind turbines.

RANS method solves the temporal averaged Navier-Stokes equations numerically, providing more consistent and physically realistic results when compared to empirical models for wind turbine flows. The average flow is calculated in the mesh, whereas the effects of the residual fluctuations are determined by means of turbulence models. The most popular turbulence models employ the Boussinesq hypothesis that is based on the concept of turbulent viscosity.

There are different approaches for the turbulent viscosity calculation, including the so-called zero-equation, one-equation and two-equation approaches. The zero equation approach has been proposed by Prandtl (1925) and denominated mixing length model, where the turbulent viscosity, ν_t , is calculated based on characteristic velocity and length scales, as represented in equation 2.24:

$$\nu_t = l_{mix}^2 \left| \frac{\partial \bar{u}}{\partial x} \right|, \quad (2.24)$$

where l_{mix} is the mixing length and $\left| \frac{\partial \bar{u}}{\partial x} \right|$ is the velocity length scale.

Cebeci and Smith (1974) proposed an algebraic model to calculate the turbulent viscosity for the turbulent boundary layer. In this model, the boundary layer is divided into two layers, the internal layer close to the wall and the external layer, where one equation for each layer is solved. It was found that the model required detailed knowledge of the conditions at the boundary layer borders. To overcome this difficulty, Baldwin and Lomax (1978) improved the model by removing excessive border dependence.

The first one-equation model was proposed by Prandtl (1945), in which the velocity scale was determined by a transport equation for the turbulent kinetic energy, k . The model limitation was related to the prescription of the characteristic length scale, which is usually difficult for complex flows. Equations 2.25 and 2.26 represent the turbulence kinetic energy transport equation and the turbulent viscosity expression proposed by Prandtl (1945):

$$\frac{\partial k}{\partial t} + \bar{u}_j \frac{\partial k}{\partial x_j} = -P_k - \varepsilon + \frac{\partial}{\partial x_j} \left[\left(\nu + \frac{\nu_t}{\sigma_k} \right) \frac{\partial k}{\partial x_j} \right], \quad (2.25)$$

$$\nu_t = l\sqrt{k}, \quad (2.26)$$

where P_k is the turbulent kinetic energy production term, ε is the rate of dissipation of turbulent kinetic energy, k is the mean kinetic energy, σ_k is the Prandtl turbulent number and l is the characteristic length scale.

Baldwin and Barth (1990) proposed a new one-equation model, where the transported variable was the turbulent Reynolds Number, allowing then to calculate the turbulent viscosity. This model showed an improvement in relation to the Prandtl one-equation model, even though it still presented problems for prescribing the length scale in the boundary layer.

A particular type of one-equation approach solves directly a transport equation for a modified turbulent viscosity, and uses damping functions close to the solid walls to calculate the turbulent viscosity. A very popular model of this type was proposed by Spalart and Allmaras (1992) and is described in the following paragraphs.

Spalart-Allmaras Model

The one-equation Spalart-Allmaras (SA) model was projected for aerodynamics applications, particularly for airfoil predictions by Boeing Company (THÉ; YU, 2017), and applied to problems that involved external flow over solid boundaries. There was no need to calculate the length scale related to the shear layer thickness, which brought robustness for the model. This was verified by the great results obtained for adverse pressure gradients flows (SPALART; ALLMARAS, 1992). In this model, RANS equations are calculated in combination with a transport equation for the modified turbulent viscosity, $\tilde{\nu}$, which is used to determine the turbulent viscosity, ν_t , according to:

$$\frac{\partial \tilde{\nu}}{\partial t} + \bar{u}_j \frac{\partial \tilde{\nu}}{\partial x_j} = -P_{\tilde{\nu}} - \varepsilon + \frac{\partial}{\partial x_j} \left[\left(\nu + \frac{\tilde{\nu}}{\sigma_{\tilde{\nu}}} \right) \frac{\partial \tilde{\nu}}{\partial x_j} \right], \quad (2.27)$$

$$\nu_t = \tilde{\nu} f_{v1}, \quad (2.28)$$

where f_{v1} is a damping function, which is equal to zero at the wall and starts increasing to one far away from the wall, $P_{\tilde{\nu}}$ is the production term and ε is the dissipation of $\tilde{\nu}$.

In wind engineering applications, You, Yu and Kwon (2013) and Song and Perot (2014) applied the SA model for the well-known NREL Phase VI wind turbine. With a fully turbulent approach, the SA model achieved great performance over the blade span in low wind speeds inflow. This occurred due to the irrelevant boundary layer separation. However, the SA model could not replicate the flow separation precisely and diverged in the distribution of the surface pressure.

The SA model presented a good performance for moderate inflow wind speeds, showing the ability for capturing laminar separation over the surface of the blades (ARANAKE; LAKSHMINARAYAN; DURAISAMY, 2015). In the case of wake effect studies, Nini et al. (2014) performed tri-dimensional simulations of the flow around a three-blade VAWT. Results indicated that divergence occurred between model and experiments in the near wake region for wind speed profiles. Therefore, the cited studies results indicated the inconsistency of applying the SA model alone for a wind turbine simulation.

An evolution of the one-equation approach is the so-called two-equation approach, where one transport equation is solved for the characteristic length scale, in addition to the previously developed turbulent kinetic energy equation. This approach has been established as base to most numerical studies in wind engineering in the last three decades (SILVEIRA et al., 2001; THÉ; YU, 2017). The next sections discuss the two-equation models.

$k - \varepsilon$ Model

In the two-equations approach, the velocity and length scales for the turbulent viscosity calculation are determined by means of transport equations. The first two-equation model

proposed by Kolmogorov (1942) solved a transport equation for the turbulent kinetic energy, k , similar to equation 2.25, and one equation for turbulent kinetic energy dissipation, ε . The turbulent viscosity was then calculated based on the ratio of these variables, as the following:

$$\frac{\partial \varepsilon}{\partial t} + \bar{u}_j \frac{\partial \varepsilon}{\partial x_j} = \frac{\varepsilon}{k} (C_{1\varepsilon} P_k - C_{2\varepsilon} \varepsilon) + \frac{\partial}{\partial x_j} \left[\left(\nu + \frac{\nu_t}{\sigma_\varepsilon} \right) \frac{\partial \varepsilon}{\partial x_j} \right], \quad (2.29)$$

$$\nu_t = C_\mu \frac{k^2}{\varepsilon}, \quad (2.30)$$

where $C_{1\varepsilon}$, $C_{2\varepsilon}$, C_μ , σ_ε and σ_k are constants that can be determined empirically.

This is the classical formulation of the so-called $k-\varepsilon$ model. This model has demonstrated the ability to simulate free shear layer flows with relatively small pressure gradients. In an analogue way, for internal or external flows, the model has produced great results in cases where the average pressure gradients were small (MELO, 2017). The model has been commonly applied to simulate mean flow properties, often adopting its coefficients based on the work of Launder and Sharma (1974). Nevertheless, the model was not recommended for large adverse pressure gradients flows.

There are many $k-\varepsilon$ derivation from the original, such as the Renormalization Group (RNG) $k-\varepsilon$ model (YAKHOT et al., 1992) and the realizable $k-\varepsilon$ model (SHIH et al., 1995). YAKHOT et al. (1992) proposed the RNG model that considered different scales of motion through changes of the production term, thus the original constant $C_{2\varepsilon}$ was replaced by a ratio of the turbulent to mean strain time scale, as follows:

$$C_{2\varepsilon}^* = C_{2\varepsilon} + \frac{C_\mu \eta^3 (1 - \eta/\eta_0)}{1 + \beta_c \eta^3}, \quad (2.31)$$

where $\eta = Sk/\varepsilon$, S is the intensity of the mean rate-of-strain tensor, and η_0 and β_c are two empirical constants. Results demonstrated that this model was more responsive to the effects of rapid strain than the original $k-\varepsilon$.

Shih et al. (1995) proposed a new formulation for the turbulent viscosity and a new transport equation for the turbulent dissipation rate. This model improved the performance for rotational flows, strong adverse pressure gradients and plane and rounded jet flows, showing a superior ability to capture the mean fluxes of the complex structures. The new formulation for the turbulent viscosity consisted of an evaluation of C_μ as follows:

$$C_\mu = \frac{1}{A_0 + A_s \frac{kV^*}{\varepsilon}}, \quad (2.32)$$

where V^* is a relation of the rate-of-strain tensor and rate-of-rotation tensor, and A and A_0 are defined constants that are described with detail in Shih et al. (1995).

The new transport equation for the turbulent dissipation rate was given by:

$$\frac{\partial \varepsilon}{\partial t} + \bar{u}_j \frac{\partial \varepsilon}{\partial x_j} = \left(C_1 S \varepsilon - C_2 \frac{\varepsilon^2}{k + \sqrt{\nu \varepsilon}} \right) + \frac{\partial}{\partial x_j} \left[\left(\nu + \frac{\nu_t}{\sigma_\varepsilon} \right) \frac{\partial \varepsilon}{\partial x_j} \right], \quad (2.33)$$

where $C_1 = \max[0.43, \eta/(\eta + 5)]$ and C_2 is an empirical constant, usually defined as 1.9.

AbdelSalam and Ramalingam (2014) applied the $k-\varepsilon$ model to simulate the wake effects over a field test horizontal wind turbine. The authors considered the atmospheric boundary layer effect and concluded that the total rotor simulation presented advantages when compared to actuator disk (AD) methodology in terms of velocity recovery. Another study by the same group of researchers (ABDELSALAM et al., 2014) applied the same method with modified coefficients for a real scale 2 MW wind turbine. The results showed good agreement in terms of flow velocity compared to field measurements. However, turbulence intensity comparisons presented notable deviation, which was attributed to the lack of accuracy of the LiDAR measurements.

Alaimo et al. (2015) used the $k-\varepsilon$ model within ANSYS-Fluent CFD package to evaluate the performance of four Darrieus turbine designs. A comparison between 2D and 3D wind turbine simulations was performed, where the 2D simulations over-predicted the aerodynamics performance in comparison to 3D simulations. This behavior was associated with the difficulty of the 2D approximation in representing tip vortices.

Zhang et al. (2013) applied the RNG $k-\varepsilon$ model to analyze aerodynamic loads over a straight-bladed VAWT. The authors simulated the tangential forces, which presented good agreement in the upstream region, but largely underestimated the values downstream of the turbine when compared to experimental data. This downstream disagreement could be caused by the dynamic stall and blade turbulence. In addition, the high values of turbulent viscosity of the model might have been another possible source of errors. In spite of that, the authors stated that the RNG $k-\varepsilon$ model could precisely predict the power generation for high tips speed ratios and could indicate a discrepancy for low tip speed ratio, which could be the reason for dynamic stall.

A recent study elaborated by Stergiannis, Beeck and Runacres (2017) compared the results of realizable $k-\varepsilon$ simulations against experimental data from a HAWT. The turbulence modelling presented great agreement at the mid and far wake regions. The authors concluded that the $k-\varepsilon$ models are generally precise in shear flows, presenting satisfactory behavior in regions far from walls.

$k-\omega$ Model

Another popular two-equation approach for the turbulent viscosity calculation is the $k-\omega$ model, which solves transport equations for turbulence kinetic energy, k , and specific dissipation rate, ω , as the following:

$$\nu_t = \frac{k}{\omega}, \quad (2.34)$$

$$\frac{\partial k}{\partial t} + \bar{u}_j \frac{\partial k}{\partial x_j} = -P_k - \beta^* k \omega + \frac{\partial}{\partial x_j} \left[(\nu + \sigma^* \nu_t) \frac{\partial k}{\partial x_j} \right], \quad (2.35)$$

$$\frac{\partial \omega}{\partial t} + \bar{u}_j \frac{\partial \omega}{\partial x_j} = -P_k \alpha^* \frac{\omega}{k} - \beta^* \omega^2 + \frac{\partial}{\partial x_j} \left[(\nu + \sigma^* \nu_t) \frac{\partial \omega}{\partial x_j} \right], \quad (2.36)$$

where β^* , α^* and σ^* are empirical constants.

These equations represent the first approach of the $k - \omega$ model developed by Wilcox (1988), which presented a great performance for boundary layer flows with adverse or favorable pressure gradients, and worked very well in areas close to solid surfaces. The model has been improved over the last two decades with different adaptations and adjustments, as proposed by Wilcox (2008), where the constants of the original model were replaced by proportionality functions that were determined from the flow over time, improving its robustness.

The $k - \omega$ model tends to be more accurate and numerically stable in regions close to the walls. Recognizing the differences and exploring the similarity of the $k - \varepsilon$ and $k - \omega$ equations, Menter (1994) proposed a combined model denominated SST $k - \omega$, where the SST stands for the shear stress transport. The model combined the essence of the $k - \omega$ model near the wall regions, and applied a transition to a standard $k - \varepsilon$ model in the free stream, through the use of weighting functions, as follows:

$$\nu_t = \frac{a_1 k}{\max(a_1 \omega, SF_2)}, \quad (2.37)$$

$$\frac{\partial k}{\partial t} + \bar{u}_j \frac{\partial k}{\partial x_j} = P_k - \beta^* k \omega + \frac{\partial}{\partial x_j} \left[(\nu + \sigma_k \nu_t) \frac{\partial k}{\partial x_j} \right], \quad (2.38)$$

$$\frac{\partial \omega}{\partial t} + \bar{u}_j \frac{\partial \omega}{\partial x_j} = -P_k \alpha^* S^2 - \beta^* \omega^2 + \frac{\partial}{\partial x_j} \left[(\nu + \sigma^\omega \nu_t) \frac{\partial \omega}{\partial x_j} \right] + 2(1 - F_1) \sigma_{\omega 2} \frac{1}{\omega} \frac{\partial k}{\partial x_i} \frac{\partial \omega}{\partial x_i}, \quad (2.39)$$

where a_1 , α^* , σ_ω , $\sigma_{\omega 2}$ are constants, F_1 is a near wall activation function and F_2 is blending function, both are better described in Menter (1994).

According to Thé and Yu (2017), this model is the most popular RANS methodology. These authors used SST $k - \omega$ to simulate aerodynamic flows with adverse pressure gradient and boundary layer separation. Subsequently, Menter, Kuntz and Langtry (2003) presented improvements by exploring the advantages of each model, in order to achieve an optimization that improved the model convergence and has decreased the grid resolution requirements close to the wall, then improving substantially the industrial applicability.

In wind engineering applications, the SST $k - \omega$ was the first RANS model to totally simulate a three-dimensional wind turbine (HANSEN; SØRENSEN; MICHELSEN, 1997; SØRENSEN; HANSEN, 1998). Sørensen and Shen (2002) have developed one of the earlier studies to perform a simulation in the NREL Phase VI rotor by applying this model. The 3D simulations were carried out in the EllipSys3D, their own research code. The results presented an agreement with experimental data in most part of the conditions excepted for 10 to 15 m/s wind speeds.

Tachos, Filios and Margaris (2010) emphasized that the SST $k - \omega$ model had greater performance over the SA and RNG $k - \varepsilon$ models at all spanwise points of the blade in the NREL Phase VI rotor. In spite of that, every model presented difficulties in characterizing pressure distribution on the inboard region, where flow separation developed even for low wind speeds. Nobari, Mirzaee and Nosratollahi (2016) showed numerical improvement in the NREL Phase VI

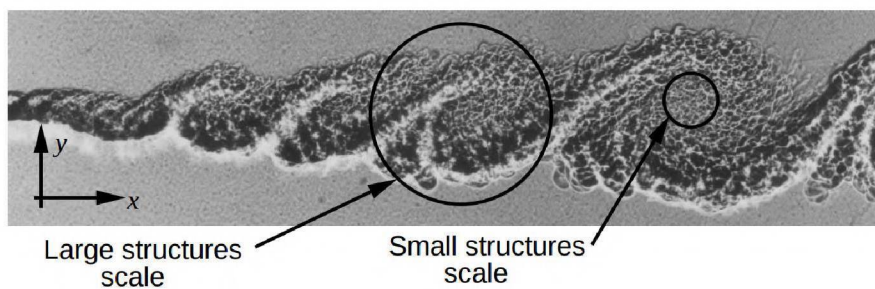
performance, adding a tip plate structure to overcome the tip vortices that induced the drag. Results presented 16% of improvement in terms of power generation for the NREL.

The applications of SST $k-\omega$ model in OpenFOAM have been increasing after the study presented by [Rahimi et al. \(2016\)](#), which investigated the flow over the NREL phase VI rotor with 3D simulations. The results demonstrated that simulations consistently agreed with experimental data. Furthermore, the SST $k-\omega$ model has been applied in several different horizontal types of wind turbines, producing satisfactory outcomes, such as those in the MEXICO rotor ([PLAZA; BARDERA; VISIEDO, 2015](#)) and the NREL 5MW Reference Rotor ([WILSON et al., 2015; ROCHA et al., 2014; LANZAFAME; MAURO; MESSINA, 2016](#)).

2.3.2.2 LES Modelling

Large eddy simulations of wind power plants have the ability to provide detailed information about wind turbine aerodynamics, power production and turbine loading. Because of that, the application of LES by wind energy research groups is increasing and stimulating the evolution of the methodology. LES is based on a spatial filtering process of the governing equations, which allows an explicitly solution to the largest turbulent structures on computational meshes and to model only the smallest scales. The difference between large and small scales is illustrated qualitatively in Figure 2.9 for a free mixing layer flow. The large turbulent structures, that contain most part of the kinetic energy, show temporal and spatial heterogeneous distribution, whereas the small structures are more isotropic and homogeneous. For this reason, the small turbulent movements are easier to model.

Figure 2.9 – Visualization of large and small structure for free mixing layer flow



SOURCE: Adapted from [Brown and Roshko \(1974\)](#)

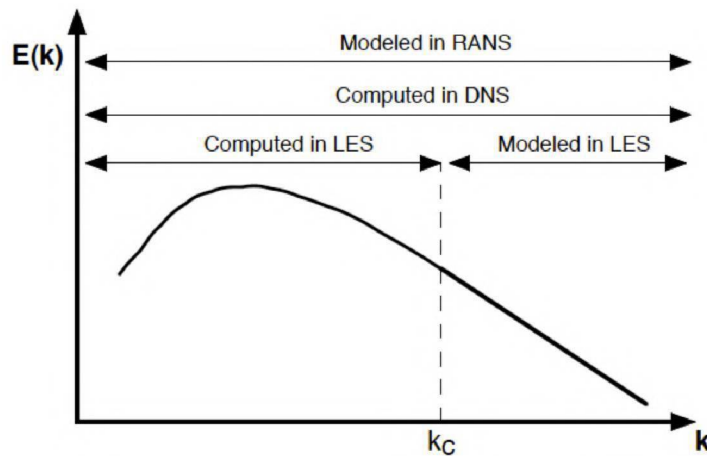
Searching a better way to model turbulence in order to obtain realistic solutions in space and time, [Smagorinsky \(1963\)](#) proposed an original approach for calculating the turbulent viscosity in LES. The model is based on the equilibrium hypothesis, which states that the injected turbulent kinetic energy in the large scales is balanced by the transferred energy to the smallest scales. In other words, the energy is transferred from the large to the small scales in a constant rate (inertial band of the energy spectrum). This process is considered in the Smagorinsky model by calculating a turbulent viscosity that depends on the characteristic length and velocity scales, as the following:

$$\nu_t = 2(C_s \Delta)^2 \left| \overline{S_{ij}} \right|, \quad (2.40)$$

where C_s is the Smagorinsky constant, Δ is the characteristic filter length scale, usually associated with the local mesh dimensions, and $|\overline{S_{ij}}|$ is the characteristic velocity scale, represented by the filtered rate of strain tensor.

The first applications showed that the model overestimated the turbulent viscosity in regions near solid walls. In order to minimize this problem, damping functions started to be applied, as the ones proposed by Van-Driest (1956) that were firstly developed for RANS models. Another particular characteristic of this model is associated with the filter length: when the filter band length tends to zero, the model tends to a DNS. In contrast, when the filter band length tends to a high value, the model tends to RANS. Consequently, the ideal condition for LES is when the filter scale tends to an intermediate value, balancing the band width for turbulent modelling with the optimal use of computational resources. Figure 2.10 helps to visualize a characteristic filter width in LES. This figure represents the spectrum of the kinetic turbulent energy, $E(K)$, as a function of wavelength, K , where K_c is the filter band width for LES (POINSOT et al., 2015). It can be seen that DNS solves directly the whole spectrum, whereas RANS models the entire spectrum of the turbulent kinetic energy. LES offers an intermediate choice between DNS and RANS.

Figure 2.10 – Visualization of large and small structure in terms of the turbulence spectrum



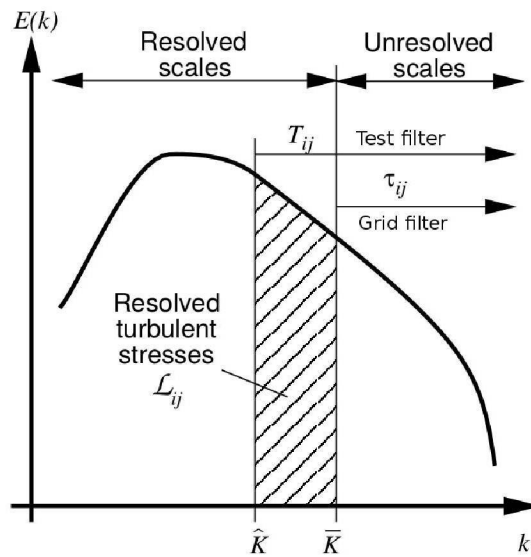
SOURCE: Poinso et al. (2015)

Recent developments for calculating the turbulent viscosity in LES have been proposed based on the classical Smagorinsky model. The sub-filter dynamic model (or simply Smagorinsky dynamic model), established by Germano et al. (1991) and improved by Lilly (1992), presented a substantial advantage, replacing the ad-hoc Smagorinsky constant by a proportionality function that is variable in space and time.

The dynamic model is based on the application of two filters with different sizes. The first one employs the grid dimension to calculate a first characteristic length, whereas the second filter uses a multiple of the grid dimension to calculate a second characteristic length, denominated test filter. Figure 2.11, adapted from Piomelli (2001), illustrates that the first filter is associated with the wavelength \overline{K} , and the test filter is related to the wavelength \widehat{K} . Utilizing the information in the region between the two filters, and calculating the resolved turbulent stresses, given by the Leonard tensor, L_{ij} it is possible to develop a proportionality function that is calculated

over time and space. As a result, the model constant is replaced by a dynamic function, which implies greater robustness to model complex flows.

Figure 2.11 – Representation of the two filters in the dynamic Smagorinsky model



SOURCE: Adapted from Piomelli (2001)

These methods have been applied in numerical studies in order to simulate wind turbine aerodynamics, wake effects and their interactions with the atmospheric boundary layers, as well as wind turbine loading and fatigue (JIMENEZ et al., 2007; CALAF; MENEVEAU; MEYERS, 2010; STOREY; CATER; NORRIS, 2016; SØRENSEN, 2011; VERMEER; SØRENSEN; CRESPO, 2003).

Jimenez et al. (2007) created an algorithm based on the dynamic Smagorinsky model to simulate a wind turbine into an atmospheric boundary layer. The authors applied the actuator disk concept, which is based on the pressure drop over the disc (*i.e.*, better described in Mikkelsen (2003)), to represent the wind turbine through the utilization of a forcing constant and compared the results with wind turbine field data, called Sexbierim. The comparison presented a good correlation between the simulation and measurements, showing the capability of the LES in representing the wake flows.

Ivanell et al. (2009) also utilized the actuator disk model to simulate Horns Rev wind power plant considering a neutral atmospheric boundary layer that was prior defined. The authors applied the rotating actuator disk model developed by Mikkelsen (2003) and aimed to evaluate the influence of yaw angle on the velocity deficits in the wake flow. They concluded that the simulations presented a lower level of agreement when the yaw angle was zero degrees, then was not totally aligned. In this case, there was an over-prediction of the wake effect and in consequence of that an under-prediction of the wind turbine power generation.

Troldborg, Sørensen and Mikkelsen (2007) performed a detailed research applying the actuator line (ALM) concepts and uniform freestream flow. The model was based on the blade loading implementation over the lines to represent the rotor blades, then applied in the Navier-Stokes equations as body forces. The study documented the inflow turbulence effects on the

wake profiles.

Two different CFD codes were compared using two distinct sub-filter scale models by Calaf, Meneveau and Meyers (2010). The first code utilized the standard Smagorinsky model, whereas the second applied the scale-dependent Lagrangian dynamic Smagorinsky model, developed by Bou-Zeid, Meneveau and Parlange (2005). The authors aimed to simulate a completely developed infinite wind power plant to evaluate the behavior of the wind turbine into a neutrally stratified atmospheric boundary layer. Besides that, they proposed a model to characterize the roughness height that could represent the turbine effects.

Most part of the atmospheric boundary layer simulations for wind turbine applications have been established with neutral stratification. Recently, Porté-Agel et al. (2011) presented a LES study applying both actuator disk and line models to investigate the wind turbine wake effects. The calculations were performed for strongly stratified flows applying a variation of the dynamic Lagrangian sub-grid model. Based on the dynamics of the resolved scales, the model tried to optimize the local value of its coefficients. The simulations were compared with wind tunnel measurements and concluded that the rotational effects are essential to predict the wake with accuracy for near and middle wake areas.

Another type of LES application is related to studies of the flow over airfoils. These applications are scarce in the literature, probably due to the difficulties associated with the existence of solid walls and significantly complex geometries that require extensively computational technology. In spite of that, studies in the past decade have shown the ability of LES in terms of airfoil performance.

Davidson et al. (2003) performed a research to evaluate the LES potential in terms of predicting the characteristics of the airfoil at high Reynolds numbers. The study evaluated many features of the simulations, mesh resolution effects, computational domain size, sub-grid scale models and near wall damping functions. The authors concluded that the mesh resolution and span length have considerable influence on the model's accuracy to predict the flow.

The study of Storey, Cater and Norris (2016) coupled LES with an aeroelastic method in order to investigate the wake effects for different wind speeds, wind power performance and loading effects. Results presented a peak of power losses that exceed 40% for a totally waked downstream wind turbine. Therefore, the authors concluded that aeroelastic algorithms could bring good information for calculating wind turbine performance in determined conditions.

Mehta et al. (2014a) and Breton et al. (2017) have summarized some aspects and conclusions about the application of LES methods involving wind turbine aerodynamics and wind energy. These works reviewed aspects that considered sub-grid scale modelling, representation of the rotor, the atmospheric boundary layer, complex terrains effects, LES data utilization and fluid-structure interaction. The author also mentioned that modelling properly the atmospheric boundary layer in the LES context is crucial to investigate the wind power plant performance for stable and unstable conditions, and in the case of extreme wind events.

LES simulations of atmospheric flows over wind power plants have been frequently executed using the strategies based on the turbulent viscosity concept. Furthermore, studies have shown that the application of the Smagorinsky model is enough for qualitative assessment of

wind turbine aerodynamics. However, when focus and extreme precision is required, the applications must rely on more sophisticated sub-grid scale models. In addition, for complex problems involving moving structures, the use of LES along with moving bodies approaches might be necessary. The next section discusses the immersed boundary approach that is possible to couple with LES in order to simulate complex flow aerodynamics around wind turbines.

2.3.2.3 Immersed Boundary Method

The approach is known as immersed type methods, in which the immersed boundary method (IB) is a classical example (PESKIN, 2002). The IB method arose as a strong and effective simulation tool for dealing with complex flows, because of its capacity to take care of complex structures without the need for expensive and complicated dynamic meshing techniques (SOTIROPOULOS; YANG, 2014). Due to the meshing flexibility, the IB approach has acquired significant popularity over the past two decades for several problems, especially for heavy movements in solids or large deformation in the fluid (MITTAL; IACCARINO, 2005).

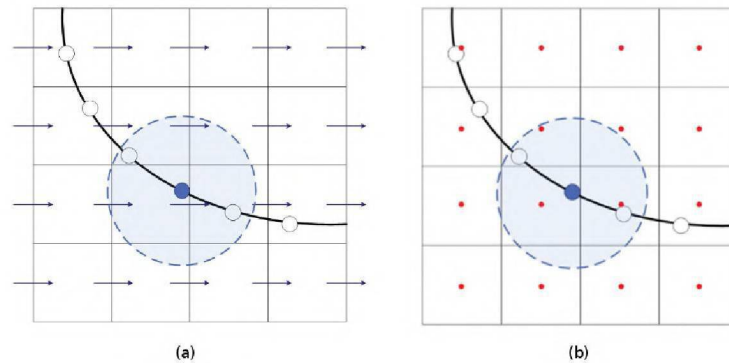
Peskin (1972) and Peskin (1977) introduced the formulation of the IB method, which was first developed to simulate blood flow in heart valves. The IB formulation combines Eulerian and Lagrangian coordinates for solving fluid flow and structure movement, respectively. The fluid-solid interface is depicted by imposing a momentum forcing in the Eulerian framework (KIM; CHOI, 2019).

The IB method combines mathematical formulations written in the eulerian and lagrangian frameworks, for the fluid and solid domains, respectively (WANG; ZHANG, 2009). The main idea of the method focus on utilizing an eulerian computational mesh to simulate the flow field coupled to lagrangian representation of the immersed boundary, which applies a singular force field over the fluid. This immersed boundary simulates the structure effects inside the flow that is represented by a finite number of distributed points over fluid-structure interface (MELO, 2017). Thus, one of the main advantages is that both meshes coexist independently of the immersed body geometry, turning it possible to simulate the flow over any geometry. Another advantage of the IB method concerns the capacity that the fluid-structure interface has to be automatically tracked, thus avoiding high computational costs over the adaptative or re-meshing algorithms (WANG; ZHANG, 2009; HAN; LIU; ABDALLAH, 2019).

Figure 2.12 illustrates the interaction process between the lagrangian nodes, that represent the solid structure, and the fluid flow in the eulerian mesh (VEDOVOTO; SERFATY; NETO, 2015). In Figure 2.12(a) the velocity field is interpolated to the lagrangian nodes. The forces are then calculated and redistributed to the mesh as shown in Figure 2.12(b).

In general, there are two main methods to calculate the forces that represent the immersed boundary. The first method considers that forces are calculated through the momentum equation and distributed over the cartesian mesh, employing a distribution function known as the distributive method of the immersed boundary. The second one is a non-distributive method, where the eulerian forces are calculated directly from the momentum equation or employing an adequate boundary condition over the immersed boundary (GILMANOV; ACHARYA, 2008; PESKIN, 2002; MITTAL; IACCARINO, 2005; IACCARINO; VERZICCO, 2003).

Figure 2.12 – Immersed geometry on a staggered finite volume computational grid: (a) Interpolation of the Eulerian velocity field to a Lagrangian point, (b) Distribution of the Lagrangian forces to the Eulerian field.



SOURCE: Adapted from Vedovoto, Serfaty and Neto (2015)

In order to solve efficiently the immersed boundary region localized into the boundary layer in high Reynolds flows, the integration of IB methods with a local refinement of the eulerian mesh, either manual or adaptative, provides a powerful approach to come up with a solution to its difficulty. This procedure is based on algorithms that are capable of solving precisely the flow in locally refined meshes (SILVA; SILVEIRA-NETO; DAMASCENO, 2003; ANGELIDIS; CHAWDHARY; SOTIROPOULOS, 2016). Besides that, as a sake of information more studies about IB methods involving the mesh type structures were developed for curvilinear meshes by (GE; SOTIROPOULOS, 2007), unstructured meshes by (WANG; LIU, 2004; ZHANG et al., 2004) and locally refined meshes by (IACCARINO; VERZICCO, 2003).

The first study involving the immersed boundary formulation was developed by Peskin (1972), with the objective to solve the Navier-Stokes equations for fluid-structure flows. The motivation of this work was based on the blood flow in heart valves intending to develop artificial hearts and valves. From this original work, many alterations and refinements have been suggested, resulting in a number of variants of this method.

Mohd-Yusof (1997) proposed a model to determine the force at each point in the boundary. Following by the calculation of the lagrangian force based on the momentum equation on the fluid interface, such method, called direct forcing, did not employ any constants that needed adjustment. However, it had high computational cost due to the requirement of complex algorithms to track down the boundary.

Silva, Silveira-Neto and Damasceno (2003) proposed a methodology to calculate the force term, denominated Physical Virtual Model (PVM), which is based on the momentum balance over the fluid close to the boundary, allowing the virtual form to model the no-slip condition over the boundary. The method applied the momentum conservation equations in the centered volumes of the lagrangian points. The velocity in the boundary was imposed indirectly (virtual) from the flow data. Campregher (2005), presented a extension of this method for three-dimensional applications. The final dynamic system aimed to represent the complex mutual relation between the formation and emission process of the swirl structures in the flow and the force balance.

Wang, Fan and Luo (2008) presented an extension of the direct forcing, but proposing a iterative form denominated as multi-direct forcing. This methodology interpolates the fluid properties in the lagrangian points, by means of calculating the force at those points, and then distributing over the eulerian volumes. Results showed that the geometry was well characterized in all time steps, ensuring the physical characteristics of the numerical model.

There are several studies available in the literature applying the IB method for complex geometries with stationary boundaries (*i.e.*, (CAMPREGHER, 2005; OLIVEIRA et al., 2005; MARK; WACHEM, 2008)). A considerable part of these studies mention the difficulty of correctly simulating the flow in the boundary layer regions, as exposed by (DELORME; FRANKEL, 2017). When the simulation of moving boundaries immersed in high Reynolds number flows is concerned, a very limited number of work is available.

Some of the studies available were conducted by Troldborg et al. (2014) and Keck et al. (2013). The authors presented an application of LES coupled with an IB method with the objective of evaluating the turbulent fluctuations in a plane near the wind turbine. The comparisons of the simulations with measurements appointed that the IB concept applied had a good response for the turbulent characteristics in the wake flow of the wind turbine.

2.3.3 CFD Simulations used as Benchmarks

The paper of Mo et al. (2013b) applies LES through commercial CFD ANSYS FLUENT, applying the turbulence dynamic Smagorinsky–Lilly model. The upstream distance from the wind turbine to the inlet is two rotor diameters and a downstream domain of 20 D in length. This study applies a uniform flow at the upstream boundary. The domain consists of two parts, the rotational components (cylinder and rectangle element) and the stationary component (wind tunnel element). The sliding mesh method is applied to the moving components with two mesh interface zones (interface zone 1: cylindrical and rectangular element, interface zone 2: cylindrical component and wind tunnel element) in the shared faces, where the meshes overlay. LES simulations were performed for approximately 30 revolutions of the turbine blades.

Sedaghatizadeh et al. (2018) applied a numerical model employing LES with the dynamic Smagorinsky-Lilly model, as well. The domain consists of two zones: 1. cylindrical zone around the blades, 2. base of the domain. A sliding mesh method is employed in the cylindrical zone allowing the relative mobility of the zones on the interface. Once again, the authors applied the ANSYS FLUENT, a commercial CFD code utilized to perform the calculations. The software employs a finite-volume technique to discretize the partial differential equations. The simulations were carried out at close to 30 revolutions, as well.

The work of Syed Ahmed Kabir and Ng (2019) employed Unsteady Reynolds-Averaged Navier-Stokes (URANS) using $k-\epsilon$ turbulence closure models and also performed in the ANSYS FLUENT. The CFD simulations for the full rotor on a flat surface with different roughness lengths were applied. The article also brings the homogenous ABL profile applied as one of the boundary conditions. URANS simulation was based on the sliding mesh technique, as well. The number of time steps was 720, which means two revolutions.

Laan et al. (2014) study using the EllipSys3D code is based on LES applying a Smagorin-

sky model with symmetry boundaries conditions. The authors also simulated a NREL 5MW for a turbulent uniform flow. The authors set a uniform mean velocity of 8 m/s at the inlet, and the wind turbine is modeled as an actuator disk, representing the geometry of the rotor as a disk of 126 m. The authors also presented results, with same configuration, for SnS code, which is a Cartesian, fractional step, non-staggered, finite volume, possible configuration of RANS or LES in the code. The wind turbine is modeled as an actuator disk.

The data provided from UBC Okanagan CFD Lab, supervised by Prof. Dr. Joshua Brinkerhoff, are based on LES simulations with Smagorinsky turbulence modelling, from their own in-house code, MARBLLES (Multiscale AtmospheriC Boundary Layer Large Eddy Simulation) which is based on actuator disk model, also from SOWFA (Simulator for Offshore Wind Farm Applications) developed by National Renewable Energy Laboratory.

2.4 COMPLEMENTARY READING

This final section presents a complementary literature review, which includes the papers that have been read, but were not incorporated into the text. Table 1 presents the references and the corresponding sections.

Table 1 – Complementary reading for more detailed information

Section	References
2.2 Experimental Studies	Vogt and Thomas (1995), Barthelmie et al. (2006)
2.3.1 Analytical and Empirical Modelling	Lissaman (1978), Calaf, Meneveau and Meyers (2010) Abkar and Porté-Agel (2013), Crespo, Hernández and Frandsen (1999) Gualtieri (2019), Deaves and Harris (1978), Deaves (1981)
2.3.2.1 RANS Modelling	Souza et al. (2011), Thé and Yu (2017)
2.3.2.1 $k - \varepsilon$ Model	Yakhot and Orszag (1986), McTavish, Feszty and Sankar (2012)
2.3.2.1 $k - \omega$ Model	Moshfeghi, Song and Xie (2012), Tsalicoglou et al. (2013) Troldborg et al. (2015)
2.3.2.2 LES Modelling	Mellen, Fröhlich and Rodi (2003), Eisenbach and Friedrich (2008) Métais and Lesieur (1992), Kim and Menon (1997) Uranga et al. (2009)
2.3.2.3 Immersed Boundary Method	Borazjani, Ge and Sotiropoulos (2008), Roma, Peskin and Berger (1999) Kajishima and Taira (2016)

3 METHODOLOGY

This chapter presents the theoretical concepts and mathematical formulations of the LES and IB methods. Initially, it is shown the description of the governing equations and their simplifications until they reach the appropriate formulation for the LES used in this study. Subsequently, it presents the filtering process for the governing equations and the modelling of the sub-filter stress tensor. The description of the Immersed Boundary Method is shown, and in the last sub-section, the coupling of the hybrid LES-IB model is presented.

3.1 GOVERNING EQUATIONS

In the present study, the evolution of the flow aerodynamics is described by the mass and momentum conservation equations. In cartesian coordinates and using index notation, for $i, j = 1, 2, 3$, these equations are given by:

$$\frac{\partial \rho}{\partial t} + \frac{\partial \rho u_i}{\partial x_i} = 0, \quad (3.1)$$

$$\frac{\partial \rho u_i}{\partial t} + \frac{\partial \rho u_i u_j}{\partial x_j} = -\frac{\partial p}{\partial x_i} + \frac{\partial \tau_{ij}}{\partial x_j} + f_i, \quad (3.2)$$

where p is the pressure, ρ is the fluid density, u_i is the velocity vector component for the i direction, τ_{ij} is the viscous stress tensor and f_i is the component i of a source term associated with forces of fluid-structure interactions.

Then assuming an incompressible flow due to any heat transference consideration in the air flow, considering Mach number lower than 0.3. Snel (2003) and Sanderse (2009) confirm the incompressibility assumption for wind power application, mainly based on the lower velocities in the wake region to justify.

The viscous stress tensor, τ_{ij} , is modelled using the Boussinesq hypothesis, which is justified by the small density changes occurring over the flow, as follows:

$$\tau_{ij} = \mu \left(\frac{\partial u_i}{\partial x_j} + \frac{\partial u_j}{\partial x_i} \right), \quad (3.3)$$

where μ is the dynamic viscosity and the right hand side term is the rate of strain tensor.

Combining this relation with equations 3.1 and 3.2 and dividing by the fluid density, the resulting mass and momentum conservation equations are the following:

$$\frac{\partial u_i}{\partial x_i} = 0, \quad (3.4)$$

$$\frac{\partial u_i}{\partial t} + \frac{\partial u_i u_j}{\partial x_j} = -\frac{1}{\rho} \frac{\partial p}{\partial x_i} + \frac{\partial}{\partial x_j} \left[\nu \left(\frac{\partial u_i}{\partial x_j} + \frac{\partial u_j}{\partial x_i} \right) \right] + f_i, \quad (3.5)$$

where ν is the kinematic viscosity.

These equations are the so-called Navier-Stokes equations. They are a set of four partial differential equations that can be solved for a description of the velocity and pressure fields. In the present study, these equations are solved using a method called Large Eddy Simulation (LES).

3.2 LARGE EDDY SIMULATION

A complete solution for the system that includes equations 3.4 and 3.5 by direct numerical simulation is quite complex, considering the computational effort required to represent all temporal-spatial scales in a high Reynolds Number flow. In particular, the flow over a wind power plant contains small eddies from the boundary layer of the blades to large ones that comprise many wind turbines (MEHTA et al., 2014b). As a choice to address this problem, LES allows the modelling of particular eddies to reduce the degrees of freedom, which means removing certain information and then solving explicitly the remaining structures of the flow.

The LES method consists of applying a spatial filter in the transport equations, which enables the selection of the large eddies of the flow to be calculated explicitly, whereas appropriate models calculate the tiny structures. It is important to note that the most critical eddies to be explicitly solved at a wind power plant are the ones that will help to know about wind farm aerodynamics. These eddies, or turbulent structures, correspond to those of the size of the wind turbine blade, which are responsible for most of the momentum transportation.

According to the energy cascade theory, the larger turbulent structures contain most of the turbulent kinetic energy. This energy is transferred to the smaller structures at a constant rate and dissipated by viscous effects toward the minor scales. There is a range of scales where the energy transfer is in equilibrium (i.e., the energy provided by the larger scales are dissipated toward the smaller ones at a similar rate) and where the turbulent structures are approximately homogeneous isotropic. In LES, these scales are taken as the small scales, which are the ones calculated by turbulence models.

These turbulence models can be classified as explicit and implicit. In the first type, the filtering process should be independent of spatial numerical discretization. In general, the pass frequency is lower than the local grid. Examples of explicit filters are the top hat and Gaussian filters. In the second case, the filtering process is implicit, based on the fact that the discretization process of the numerical method is by itself a spatial and temporal filtering process (POPE, 2000; ANDRADE, 2019).

The next session demonstrates the filtering process of the governing equations and the modelling strategies for turbulence used in this study.

3.2.1 Filtering of the Governing Equations

In the filtered Navier-Stokes equations, there is a dissociation of the generic signal $f(\vec{x}, t)$ into two parts, one that characterizes the filtered part $\bar{f}(\vec{x}, t)$, and $f'(\vec{x}, t)$ that represents the fluctuation part, as follows:

$$f(\vec{x}, t) = \bar{f}(\vec{x}, t) + f'(\vec{x}, t). \quad (3.6)$$

Note that the filtered property is designated with the top bar and the fluctuating part is represented with a single quotation mark.

The filtered part can be expressed as:

$$\bar{f}(\vec{x}, t) = \int_D f(\vec{x}', t) G(\vec{x} - \vec{x}') d\vec{x}', \quad (3.7)$$

where $G(\vec{x} - \vec{x}')$ is the filter function. There are many ways to define the filter function. The most common approach is to express as a function of the local control volume:

$$G(\vec{x} - \vec{x}') = \begin{cases} 1/\Delta & |\vec{x}| \geq \Delta/2, \\ 0 & |\vec{x}| < \Delta/2, \end{cases} \quad (3.8)$$

where Δ is the characteristic length of the control volume, symbolizing the filtering frequency band.

Considering the mass balance exposed in the continuity equation 3.4 and applying the filtering process on this equation, assuming the cumulative property over both operators, it is possible to obtain the filtered equation for conservation of mass:

$$\frac{\partial \bar{u}_i}{\partial x_i} = 0, \quad (3.9)$$

where \bar{u}_i is the filtered velocity vector.

In an analog way of the above process, it is possible to filter the momentum equation. Applying the filter over equation 3.5, the momentum equation writes:

$$\frac{\partial \bar{u}_i}{\partial t} + \frac{\partial \overline{u_i u_j}}{\partial x_j} = -\frac{1}{\rho} \frac{\partial \bar{p}}{\partial x_i} + \frac{\partial}{\partial x_j} \left[\nu \left(\frac{\partial \bar{u}_i}{\partial x_j} + \frac{\partial \bar{u}_j}{\partial x_i} \right) \right]. \quad (3.10)$$

Defining the global sub-filter tensor τ_{ij} as:

$$\tau_{ij} = \overline{u_i u_j} - \bar{u}_i \bar{u}_j, \quad (3.11)$$

and mathematically manipulating the equation 3.10 using equation 3.11, it is possible to obtain the filtered momentum equation:

$$\frac{\partial \bar{u}_i}{\partial t} + \frac{\partial \bar{u}_i \bar{u}_j}{\partial x_j} = -\frac{1}{\rho} \frac{\partial \bar{p}}{\partial x_i} + \frac{\partial}{\partial x_j} \left[\nu \left(\frac{\partial \bar{u}_i}{\partial x_j} + \frac{\partial \bar{u}_j}{\partial x_i} \right) - \tau_{ij} \right], \quad (3.12)$$

or even rewrite as equation 3.13, after transposing the tensor to the second member of the equation and grouping with the viscous tensor,

$$\frac{\partial \bar{u}_i}{\partial t} + \frac{\partial \bar{u}_i \bar{u}_j}{\partial x_j} = -\frac{1}{\rho} \frac{\partial \bar{p}}{\partial x_i} + \frac{\partial}{\partial x_j} \left[\nu \left(\frac{\partial \bar{u}_i}{\partial x_j} + \frac{\partial \bar{u}_j}{\partial x_i} \right) - \overline{u_i' u_j'} \right] \quad (3.13)$$

Note that the filtering process introduces a new variable in the last term of the right-hand side of the momentum equation, 3.13. This term is a sub-filter tensor known as Reynolds Stress Tensor (RST) and represents the contribution of the dynamics of the sub-filter turbulent fluctuations on the resolved scales of LES. It can be seen that the system of equations is now opened since there are four equations available to use and seven variables to be solved. To overcome this problem, the sub-filter tensor needs to be modeled.

3.2.2 Sub-filter Tensor

For most cases involving wind power applications, the Direct Numerical Simulation (DNS) is not adequate due to the need to solve the large energy spectrum associated with high Reynolds number flows. For this reason, LES becomes an intermediate and exciting choice once the flow is divided into filtered and sub-filter scales. In LES, the contributions of the sub-filter scales fluctuations are calculated by turbulence models.

A usual strategy for the sub-filter tensor modelling is to adopt an analogy with the Boussinesq hypothesis for the viscous stress, which represents a diffusive gradient type of transport. A coefficient called turbulent viscosity is then introduced to balance the rate of turbulent kinetic energy transfer from the large to the small scales. The turbulent viscosity coefficient, different from the molecular viscosity, is a scalar quantity characteristic of individual flows (not individual fluids).

The Reynolds Stress Tensor is modelled according to:

$$-\overline{u_i' u_j'} = \nu_t \left(\frac{\partial \bar{u}_i}{\partial x_j} + \frac{\partial \bar{u}_j}{\partial x_i} \right), \quad (3.14)$$

where ν_t is the turbulent viscosity.

The final filtered momentum equation can be written as the following:

$$\frac{\partial \bar{u}_i}{\partial t} + \frac{\partial \bar{u}_i \bar{u}_j}{\partial x_j} = -\frac{1}{\rho} \frac{\partial \bar{p}}{\partial x_i} + \frac{\partial}{\partial x_j} \left[(\nu + \nu_t) \left(\frac{\partial \bar{u}_i}{\partial x_j} + \frac{\partial \bar{u}_j}{\partial x_i} \right) \right], \quad (3.15)$$

The problem now concerns to find an expression for the turbulent viscosity. Three different models are discussed, two of them are implicit based models and are the most used in practical applications. The third one is an explicit type of model.

3.2.2.1 Smagorinsky model

The Smagorinsky model assumes the existence of a balance among production, transferring and dissipation of turbulent kinetic energy. The turbulent viscosity is a scalar that represents the intensity of the energy transfer between the filtered and sub-filter scales, and its value is calculated based on time and velocity scales that are obtained from the resolved flow in the large scales. Accordingly, the turbulent viscosity is given by:

$$\nu_t = 2 (C_s \Delta)^2 |\overline{S}_{ij}|, \quad (3.16)$$

where C_s is the Smagorinsky constant and $|\overline{S}_{ij}|$ is the filtered rate of strain tensor.

The filtered rate of strain tensor is adopted as the characteristic velocity scale, and it is given by:

$$|\overline{S}_{ij}| = \frac{1}{2} \left(\frac{\partial \overline{u}_i}{\partial x_j} + \frac{\partial \overline{u}_j}{\partial x_i} \right), \quad (3.17)$$

whereas the length scale Δ is a function of the grid discretization:

$$\Delta = \sqrt[3]{\Delta x \Delta y \Delta z}, \quad (3.18)$$

where Δx , Δy and Δz are the length of the computational grid in cartesian coordinates.

For homogeneous and isotropic turbulence, Lilly (1992) found out that the Smagorinsky constant has a value of $C_s = 0,18$. However, close to edges or solid walls the viscosity effects are more pronounced. Then turbulence becomes less homogeneous and isotropic, which can represent a lower Smagorinsky constant. An alternative approach to solve this problem is the application of functions that damp the viscosity at certain areas close to the walls (MELO, 2017).

One of the main limitations of this model is associated with the determination of the constant C_s , since it is assumed to be constant in space and time. With this in mind, dynamic models have been proposed for calculating automatically the Smagorinsky constant, depending on the position and characteristics of the flow.

3.2.2.2 Dynamic model

Germano et al. (1991) proposed a dynamic sub-filter model, in which the momentum equation is filtered twice. The proportionality coefficient is a function that adjusts itself according to the flow in time and space. The first filtering process works similarly to the Smagorinsky model, using the grid dimension to prescribe the characteristic length, whereas the second filter employs multiples of grid dimensions to determine the characteristic length scale. The objective of the dynamic model is to account for the spatial and temporal variability of the Smagorinsky constant.

The first filtering process is represented by equation 3.12. Applying the second filter process \hat{G} with the characteristics lengths $\hat{\Delta} > \Delta$ into equation 3.10, it gives:

$$\frac{\partial \hat{u}_i}{\partial t} + \frac{\partial \widehat{\overline{u}_i \overline{u}_j}}{\partial x_j} = -\frac{1}{\rho} \frac{\partial \hat{p}}{\partial x_i} + \frac{\partial}{\partial x_j} \left[\nu \left(\frac{\partial \hat{u}_i}{\partial x_j} + \frac{\partial \hat{u}_j}{\partial x_i} \right) \right], \quad (3.19)$$

where the operation $\hat{\cdot}$ defines the double filtering, and the new length is multiple of Δ , in general twice of its value. Defining the sub-test tensor, T_{ij} , as the following:

$$T_{ij} = \widehat{\overline{u}_i \overline{u}_j} - \hat{u}_i \hat{u}_j, \quad (3.20)$$

it is possible to rewrite equation 3.19 as:

$$\frac{\partial \hat{u}_i}{\partial t} + \frac{\partial \hat{u}_i \hat{u}_j}{\partial x_j} = -\frac{1}{\rho} \frac{\partial \hat{p}}{\partial x_i} + \frac{\partial}{\partial x_j} \left[\nu \left(\frac{\partial \hat{u}_i}{\partial x_j} + \frac{\partial \hat{u}_j}{\partial x_i} \right) - T_{ij} \right]. \quad (3.21)$$

Then, also applying the second filter in equation 3.12, it is possible to obtain:

$$\frac{\partial \hat{u}_i}{\partial t} + \frac{\partial \widehat{\hat{u}_i \hat{u}_j}}{\partial x_j} = -\frac{1}{\rho} \frac{\partial \hat{p}}{\partial x_i} + \frac{\partial}{\partial x_j} \left[\nu \left(\frac{\partial \hat{u}_i}{\partial x_j} + \frac{\partial \hat{u}_j}{\partial x_i} \right) - \hat{\tau}_{ij} \right]. \quad (3.22)$$

After that, subtracting equation 3.21 from equation 3.22 it is possible to obtain the global Leonard stress tensor in the following form:

$$L_{ij} = \widehat{\hat{u}_i \hat{u}_j} - \hat{u}_i \hat{u}_j = T_{ij} - \hat{\tau}_{ij}. \quad (3.23)$$

This expression was graphically represented in Figure 2.11 of chapter 2, and also this equality is known as Germano identity, which can be utilized to determine the dynamic coefficient function $c(\vec{x}, t)$, written as:

$$c(\vec{x}, t) = \frac{1}{2} \frac{L_{ij} M_{ij}}{M_{ij} M_{ij}}. \quad (3.24)$$

In this equation M_{ij} can be defined as:

$$M_{ij} = \widehat{\Delta^2 |\hat{S}| \hat{S}_{ij}} - \overline{\Delta^2 |\bar{S}| \bar{S}_{ij}}. \quad (3.25)$$

In this model, the dynamic coefficient also depends on variables already calculated in the large scales of LES, and the calculated values of turbulent viscosity tend to represent more accurately the distribution of non-homogeneous turbulence (MELO, 2017).

3.2.2.3 Dynamic model with explicit filtering

The turbulence models previously presented depends on the characteristics length of the local mesh. However, the mesh formulation in the MFSim code is multiblock, and depending on the flow configuration this method lead to a large increase in turbulent viscosity, when passing abruptly from fine mesh to coarse mesh. Therefore, seeking a mesh independence in the calculation of this characteristic length scale, the technique of explicit filtering presented in Bose, Moin and You (2010) was applied.

Bose, Moin and You (2010) proposed that the explicit filter must be an order lower than the advective scheme used in the numerical solution. The MFSim code uses second-order schemes, therefore the hat filter was implemented because it is a first-order scheme. The authors also claim that the filter should be applied on non-linear terms only, due to the possibility of numerical oscillations occur from those terms. They also sustain the idea that flow resolution loss is lower than the loss by filtering the entire equation.

Explicit filtering consists of applying a filter to the Navier-Stokes equations that has been filtered by the mesh. The first filtering done by the mesh was presented by equation 3.12, then there is an application of the second filter, \tilde{G} , which is the explicit filtering process that is applied in non-linear terms ($\bar{u}_i \bar{u}_j$) and stress tensor τ_{ij} :

$$\frac{\partial \bar{u}_i}{\partial t} + \frac{\partial \widetilde{\bar{u}_i \bar{u}_j}}{\partial x_j} = -\frac{1}{\rho} \frac{\partial \bar{p}}{\partial x_i} + \frac{\partial}{\partial x_j} \left[\nu \left(\frac{\partial \bar{u}_i}{\partial x_j} + \frac{\partial \bar{u}_j}{\partial x_i} \right) - \tilde{\tau}_{ij} \right], \quad (3.26)$$

$$\tilde{\tau}_{ij} = \widetilde{\bar{u}_i \bar{u}_j} - \bar{u}_i \bar{u}_j. \quad (3.27)$$

After applying the explicit filter in the filtered Navier-Stokes equations and the tensor, there is the application of the third filter, the test filter \hat{G} , over equations 3.26 and 3.27:

$$\frac{\partial \hat{u}_i}{\partial t} + \frac{\partial \widehat{\widetilde{\bar{u}_i \bar{u}_j}}}{\partial x_j} = -\frac{1}{\rho} \frac{\partial \hat{p}}{\partial x_i} + \frac{\partial}{\partial x_j} \left[\nu \left(\frac{\partial \hat{u}_i}{\partial x_j} + \frac{\partial \hat{u}_j}{\partial x_i} \right) - \hat{\tau}_{ij} \right]. \quad (3.28)$$

$$\hat{\tau}_{ij} = \widehat{\widetilde{\bar{u}_i \bar{u}_j}} - \widehat{\bar{u}_i \bar{u}_j}. \quad (3.29)$$

Up to the present point, the Navier-Stokes equations had been filtered by the mesh, then filtered explicitly, \tilde{G} , and by the end filtered by the test filter, \hat{G} . The RST generated by the mesh filtration process had also been filtered explicitly, \tilde{G} , and then filtered by the test filter, \hat{G} .

In the meantime, there is also the application of the test filter, \hat{G} , over the implicit tensor and equations 3.11 and 3.12 respectively, that had been filtered by the mesh only, resulting in:

$$\hat{\tau}_{ij} = \widehat{\bar{u}_i \bar{u}_j} - \widehat{\bar{u}_i \bar{u}_j}. \quad (3.30)$$

$$\frac{\partial \hat{u}_i}{\partial t} + \frac{\partial \widehat{\bar{u}_i \bar{u}_j}}{\partial x_j} = -\frac{1}{\rho} \frac{\partial \hat{p}}{\partial x_i} + \frac{\partial}{\partial x_j} \left[\nu \left(\frac{\partial \hat{u}_i}{\partial x_j} + \frac{\partial \hat{u}_j}{\partial x_i} \right) - \hat{\tau}_{ij} \right]. \quad (3.31)$$

The stress tensor relative to the explicit filtering process, \hat{T}_{ij} , as being:

$$\hat{T}_{ij} = \widehat{\bar{u}_i \bar{u}_j} - \widehat{\hat{u}_i \hat{u}_j}. \quad (3.32)$$

Isolating the $\widehat{\bar{u}_i \bar{u}_j}$ and replacing in the equation 3.30, results in:

$$\hat{\tau}_{ij} = \hat{T}_{ij} + \widehat{\hat{u}_i \hat{u}_j} - \widehat{\bar{u}_i \bar{u}_j}, \quad (3.33)$$

After that, replacing the tensor ($\hat{\tau}_{ij}$) of the equation 3.33 in the equation 3.31 results in:

$$\frac{\partial \hat{u}_i}{\partial t} + \frac{\partial \widehat{\hat{u}_i \hat{u}_j}}{\partial x_j} = -\frac{1}{\rho} \frac{\partial \hat{p}}{\partial x_i} + \frac{\partial}{\partial x_j} \left[\nu \left(\frac{\partial \hat{u}_i}{\partial x_j} + \frac{\partial \hat{u}_j}{\partial x_i} \right) - \hat{T}_{ij} \right]. \quad (3.34)$$

Finally, the Leonard tensor explicitly filtered, \widetilde{L}_{ij} can be obtained subtracting equation 3.34 from equation 3.28

$$\widehat{\widehat{u_i u_j}} - \widehat{u_i u_j} = \widehat{\widehat{T}_{ij}} - \widehat{\tau_{ij}} = \widetilde{L}_{ij}. \quad (3.35)$$

The anisotropic part of the global sub-filter Reynolds stress tensor can be modeled with the Boussinesq hypothesis:

$$\tau_{ij} - \frac{\delta_{ij}}{3} \tau_{kk} = -2c(x, t) \bar{\Delta}^2 |\bar{S}| \bar{S}_{ij}. \quad (3.36)$$

Then applying the explicit filter, \widetilde{G} , and the test filter, \widehat{G} , over this tensor, it is possible to obtain:

$$\widehat{\widehat{\tau_{ij}}} - \frac{\delta_{ij}}{3} \widehat{\widehat{\tau_{kk}}} = -2c(x, t) \widehat{\Delta}^2 |\widehat{S}| \widehat{S}_{ij}. \quad (3.37)$$

In a similar way, the same process occurs with the tensor, T_{ij} , obtaining:

$$\widehat{\widehat{T_{ij}}} - \frac{\delta_{ij}}{3} \widehat{\widehat{T_{kk}}} = -2c(x, t) \widehat{\Delta}^2 |\widehat{S}| \widehat{S}_{ij}. \quad (3.38)$$

Replacing the equations 3.37 and 3.38 from 3.35, and rearranging, results in:

$$\widetilde{L}_{ij} - \frac{\delta_{ij}}{3} \widetilde{L}_{kk} = -2c(x, t) \widetilde{M}_{ij}, \quad (3.39)$$

where:

$$\widetilde{M}_{ij} = \widehat{\Delta}^2 |\widehat{S}| \widehat{S}_{ij} - \bar{\Delta}^2 |\bar{S}| \bar{S}_{ij}. \quad (3.40)$$

However, defining an equation for the error square ES , from equation 3.39:

$$ES = \left(\widetilde{L}_{ij} - \frac{\delta_{ij}}{3} \widetilde{L}_{kk} - 2c(x, t) \widetilde{M}_{ij} \right)^2 \quad (3.41)$$

Deriving this error equation as function of the $c(\vec{x}, t)$, and equating to zero. It is possible to find the minimum point of this dynamic coefficient function $c(\vec{x}, t)$:

$$c(\vec{x}, t) = \frac{1}{2} \frac{\widetilde{L}_{ij} \widetilde{M}_{ij}}{\widetilde{M}_{ij} \widetilde{M}_{ij}}. \quad (3.42)$$

Therefore, the turbulent viscosity from now, is given by:

$$\nu_t = \left(c(\vec{x}, t) \widetilde{\Delta} \right)^2 |\widetilde{S}_{ij}|, \quad (3.43)$$

where the turbulent viscosity, ν_t , depends on the length of the explicit filter, $\widetilde{\Delta}$, and of the coefficient function $c(\vec{x}, t)$, which calculation occurs dynamically according to the flow and varies over time and space. In summary, the dynamic model with explicit filtering is a triple filtering process.

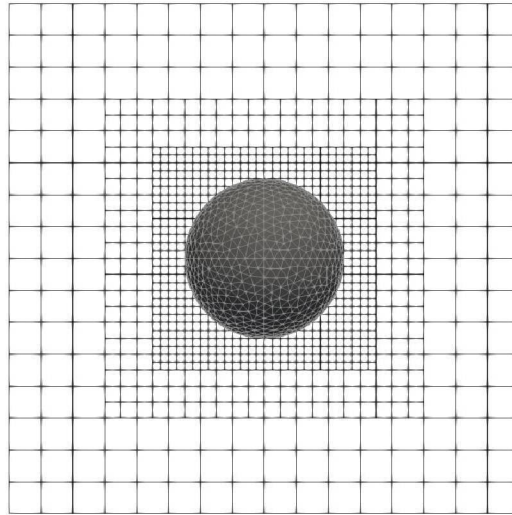
The filter length applied in the MFSim code is based on the mesh size of the finest level. Thus, the filtering process is based on the length of the higher turbulence intensity region, since the main refinement criteria for turbulent flows is vorticity. This procedure minimizes the amount of the modelled eddies, allowing a larger range of the turbulence spectrum to be solved explicitly (VEDOVOTO, 2011; MELO, 2017). Besides that, the code executes a smooth transition between the previous and refined meshes for the turbulent viscosity calculation, in which the viscosity fields present coherence and restrain possible numerical oscillation that could be associated with larger changes of turbulent viscosity.

The next sections describe the immersed boundary method framework and the formulation to couple with LES.

3.3 IMMERSSED BOUNDARY METHOD

The immersed boundary method uses an independent grid to define a solid body inside the fluid flow. The flow is solved on Eulerian cartesian grids whereas the solid structures are represented by Lagrangian elements. In the MFSim code, the immersed boundary is discretized by a superficial mesh of triangular elements, as shown in Figure 3.1.

Figure 3.1 – Example of representation for the Eulerian and Lagrangian mesh in the IB method



SOURCE: The Author (2019)

The main advantage of this approach is the ability to simulate the flows over complex geometries with the possibilities of moving structures. The formulation proposed by Vedovoto, Serfaty and Neto (2015), which uses the multi-direct forcing method based on an iterative process, is applied in this work.

The force term, f_i , in the momentum equation controls the definition of the immersed boundaries. To calculate this force a distribution function is used:

$$f_i(\vec{x}) = \sum_K \vec{F}(\vec{x}_K) D_{ij}(\vec{x} - \vec{x}_K) \Delta V(\vec{x}_K). \quad (3.44)$$

where \vec{x} is the coordinate of the eulerian volume, \vec{x}_K is the coordinate of the langrangian element, $\Delta V(\vec{x}_K)$ is the volume of the lagrangian element, $D_{ij}(\vec{x} - \vec{x}_K)$ represents the distribution function and \vec{F} is the force acting in each individual lagrangian element.

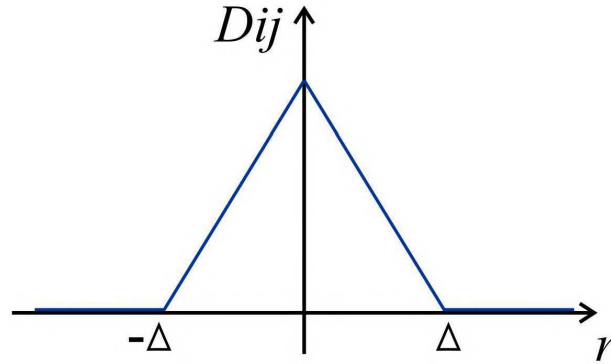
The hat distribution function, which is used in this work, can be written as the following:

$$D_{ij}(\vec{x}) = g(\vec{x}_K - \vec{x}) g(\vec{y}_K - \vec{y}) g(\vec{z}_K - \vec{z}). \quad (3.45)$$

$$g(r) = \begin{cases} \frac{1-\|r\|/\Delta}{\Delta} & , \|r\| \leq \Delta \\ 0 & , \|r\| > \Delta. \end{cases} \quad (3.46)$$

where Δ is the characteristic length of the eulerian grid. This function express the form presented in Figure 3.2.

Figure 3.2 – Hat distribution function



SOURCE: Adapted from Melo (2017)

An important characteristic of this function is that the force distribution is proportional to the distance from the face of the eulerian control volumes. Besides, the integration of the function over the entire domain is equal to unity. The force of the lagrangian element, $\vec{F}(\vec{x}_K)$, is distributed over the eulerian domain to define the boundary of the solid structure. Moreover, the momentum equation is still solved when the overlapping of lagrangian element with an eulerian control volume exists, and the conservation of mass is also retained (MELO, 2012).

It is possible to rewrite the momentum equation for each lagrangian element. For incompressible flow and taking uppercase variables for the lagrangian domain, the total lagrangian force is:

$$F_i(\vec{X}, t) = \rho \frac{\partial U_i}{\partial t} + \rho U_j \frac{\partial U_i}{\partial X_j} + \frac{\partial P}{\partial X_i} - \frac{\partial}{\partial X_j} \left[\mu \left(\frac{\partial U_i}{\partial X_j} + \frac{\partial U_j}{\partial X_i} \right) \right], \quad (3.47)$$

where U_i and U_j are the components of the velocity vector, P is pressure and $F_i(\vec{X}, t)$ is the acumulate lagrangian force.

The temporal discretization of equation 3.47 using a second order scheme, can be written as the following:

$$F_i(\vec{X}, t) = \frac{\alpha_2 U_i^{t+\Delta t} - \alpha_1 U_i^t + \alpha_0 U_i^{t-\Delta t}}{\Delta t} + LT_i^t, \quad (3.48)$$

where $LT_i^t = \rho U_j \frac{\partial(U_i)}{\partial X_j} + \frac{\partial P}{\partial X_i} - \frac{\partial}{\partial X_j} \left[\mu \left(\frac{\partial U_i}{\partial X_j} + \frac{\partial U_j}{\partial X_i} \right) \right]$ is the right hand side of the momentum equation for the lagrangian element, α_0 , α_1 and α_2 are temporal discretization coefficients.

The next step consists in using an auxiliar parameter U^* into the temporal term as a mathematical artifice, that allows the superposition principle and resolution of equation 3.49 in two parts:

$$F_i(\vec{X}, t) = \frac{\alpha_2 U_i^{t+\Delta t} - \alpha_1 U_i^t + \alpha_0 \alpha_2 U_i^{t-\Delta t} + \alpha_2 U_i^* - \alpha_2 U_i^*}{\Delta t} + LT_i^t, \quad (3.49)$$

resolving for:

$$\frac{\alpha_2 U_i^* - \alpha_1 U_i^t + \alpha_0 U_i^{t-\Delta t}}{\Delta t} + LT_i^t = 0, \quad (3.50)$$

and

$$F_i(\vec{X}, t) = \frac{\alpha_2 U_i^{t+\Delta t} - \alpha_2 U_i^*}{\Delta t}. \quad (3.51)$$

The equation 3.52 calculates the value of U_i^* evaluated in the lagrangian points, where there is an interpolation of the components u^* evaluated in the eulerian cells that are closest to each lagrangian element:

$$U_i^* = \sum_{\Omega} u_i^* D_h(x_i - x_K) h^3, \quad (3.52)$$

where D_h is a distribution function as previously mentioned, u^* is the velocity at the eulerian volumes that is calculated based on the solution of linear systems through multigrid-multilevel methodology, and h^3 is the lagrangian volume, considering that the eulerian volume remains uniform.

To obtain the desired velocity in the boundary of lagrangian element, $U_i^{t+\Delta t}$, it is important to note that for a stationary boundary the velocity will be a null value. If the lagrangian element is moving, the velocity value will be equal to the boundary velocity. Based on the equation 3.51 but evaluated in eulerian volumes, the velocity components for each eulerian volume that is close to the immersed boundary could be determined as:

$$f_i(\vec{X}, t) = \frac{\alpha_2 u_i^{t+\Delta t} - \alpha_2 u_i^*}{\Delta t} \rightarrow u_i^{t+\Delta t} = u_i^* + \frac{f_i \Delta t}{\alpha_2}. \quad (3.53)$$

In summary, the multi-direct forcing scheme calculates the velocity in the lagrangian element followed by the force. In the next step that force is distributed over the eulerian domain. This procedure is realized iteratively until reaches the convergence criteria, which is based on the convergence of the new velocity to a minimum required residue every time step.

In order to contemplate the established objectives involving a blade, experimental and real scale wind turbine, the Navier-Stokes equations had been discretized and implemented in

the multidisciplinary in-house platform that will be detailed in the next chapter. This study will apply, modify, and update this platform to validate the in-house code to real scale scenarios that will simulate a wind tunnel domain and a stand-alone wind turbine.

4 NUMERICAL METHODS

The partial differential equations presented in Chapter 3 require solution by means of numerical methods developed in computer programs. The computational code applied in this work was written in FORTRAN, C and C++. The MFSim is code developed at Fluid Mechanics Laboratory (MFLab), located in Federal University of Uberlandia (UFU), which is based on the finite volume method and solves three-dimensional flow using conservative forms of mass and momentum equations. The code applies a block-structured regular and cartesian adaptive mesh refinement that reduces the computational cost. The MFSim is code developed at Fluid Mechanics Laboratory (MFLab), located in Federal University of Uberlandia (UFU), which is based on the finite volume method and solves three-dimensional flow using conservative forms of mass and momentum equations. The code applies a block-structured regular and cartesian adaptive mesh refinement that reduces the computational cost. Moreover, the final linear systems related to the transport equations were solved based on the multigrid-multilevel method (VILLAR, 2007). Besides that, the portable message-passing standard designed of parallel computing architectures in the MFSim code is done by the MPI (Message Passing Interface). At this pattern, the simulation is composed by one or more processes that communicates through functions, which are activated in terms of message-passing along the processes.

The code have been started according to Villar (2007), and nowadays the platform application allows to simulate 3D problems involving turbulent flows (DAMASCENO; VEDOVOTO; SILVEIRA-NETO, 2015), fluid-structure interaction (NETO et al., 2019), multi-phase (BARBI et al., 2018), particles collision (SANTOS, 2019), reactive (DAMASCENO; SANTOS; VEDOVOTO, 2018) and even with LES approach considering 3D domains and parallel processing. The platform present the possibilities of temporal and advective discretization schemes, besides the ability to apply SIMPLE, SIMPLEC or fractional-step method for the pressure-velocity coupling (MAGALHÃES et al., 2019).

The first section of this chapter describes the finite volume method and its application for the simulations. Followed by the the discretization of the equations, spatial and temporal, then the pressure-velocity coupling and finishing with the adaptive mesh refinement enrolled at MFSim.

4.1 FINITE VOLUME METHOD

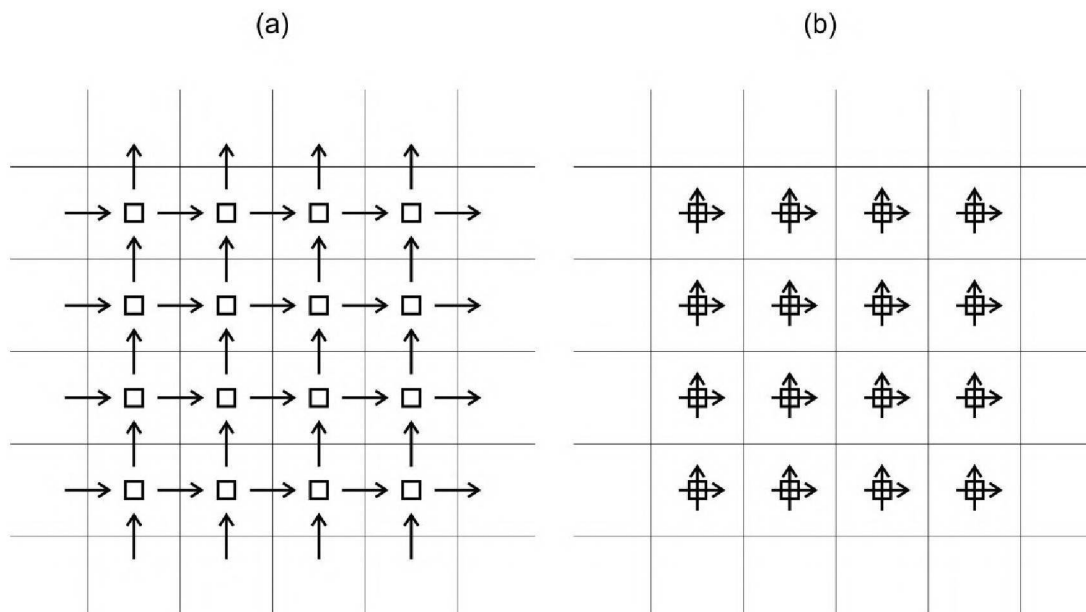
The finite volume method (FVM) is employed in this study to numerically simulate the mass and momentum conservation equations (PATANKAR, 1980). In the FVM the solution domain is divided into a finite number of elementary control volumes, considering that each centroid of the control volumes is the computational node. The computational domain is then composed by a collection of these nodes, which are the frame for the domain discretization and are independent of the reference coordinate system.

Integrating the mass and momentum equations over each control volume and assuming

a piecewise linear profile for the variable changes across the volume faces, it is possible to obtain the discretized equations. These equations express the conservation of the flow properties, which are calculated for each control volume. Therefore, the final solution assures a global conservation for the entire domain.

There are two main arrangements for storing properties information of flow in the control volumes. In the first one, called staggered arrangement, the components of the velocity vector are stored at the control volume faces, while pressure is stored in the control volume centroid. This option shows great advantage associated with the strong coupling between pressure and velocity, mainly due to the agreement of the pressure gradients with the velocity positioning. In the second one, called colocated arrangement, all variables are stored in the centroid of the control volumes. This is a less complex method to develop the algorithm when compared with the staggered arrangement (CAMPREGHER, 2005). Figure 4.1 shows a graphical representation of both arrangements.

Figure 4.1 – (a) Staggered grid scheme and (b) the colocated grid scheme



SOURCE: Campregher (2005)

In this study, the equations are discretized using the staggered arrangements. The discretized equations are linear equations with coefficients that are calculated based on the finite volume method. Next, the temporal and spatial discretization schemes for the transport equations are presented.

4.1.1 Temporal and Spatial Discretization

The spatial discretization of the transport equations relative to the eulerian domain is elaborated based on the finite volume method alongside with staggered grid to the velocities components, due that the block-structured grid is applied. The temporal discretization occurs with second-order semi-implicit methods, allowing the variation of the time-step along the simulations to reach the restrictions of these formulations (SANTOS, 2019). The momentum

equations can be discretized by the divergent and non-divergent forms, and also by conservative or non-conservative form, being both optional by the user.

According to Vedovoto (2011), in LES the time steps need to be small enough to capture the smallest resolved scales, then temporal integration should be treated correctly. For explicit schemes, the Courant Friedrich Lewy (CFL) number greater than unity can cause numerical instability. Therefore, the criteria can be used to define the time step size to retain the numerical stability of the method. The time step is given by:

$$\Delta t = CFL \left(\frac{1}{\Delta t_{adv}} + \frac{1}{\Delta t_{dif}} \right)^{-1}, \quad (4.1)$$

where the coefficient CFL ranges from 0 to 1, Δt_{adv} and Δt_{dif} stand for the maximum allowed size of advective and diffusive time step, which are defined as:

$$\Delta t_{adv} = \left(\frac{\Delta x}{|u|_{max}} + \frac{\Delta y}{|v|_{max}} + \frac{\Delta z}{|w|_{max}} \right), \quad (4.2)$$

$$\Delta t_{dif} = \left(\frac{\Delta x^2}{\nu} + \frac{\Delta y^2}{\nu} + \frac{\Delta z^2}{\nu} \right), \quad (4.3)$$

where, Δx , Δy , Δz stand for the discretization mesh length in the x , y and z directions in cartesian coordinates, $\nu = \mu/\rho$ is the kinematic viscosity. $|u|_{max}$, $|v|_{max}$ and $|w|_{max}$ are the maximum absolute value of the norm of velocity vector components in the cartesian directions.

For explicit schemes the advective and diffusive terms result into the following order of time step size $O(\Delta x^2)$, mainly based on the diffusive term (FERZIGER; PERIC, 2002; VEDOVOTO, 2011; MELO, 2017). Such numerical limitation does not occur with the implicit or semi-implicit schemes, because they present higher numerical stability. In those scheme treatment of diffusive terms, the temporal constraint of order $O(\Delta x^2)$ turns into $O(\Delta x)$ (VILLAR, 2007; VEDOVOTO, 2011; MELO, 2017).

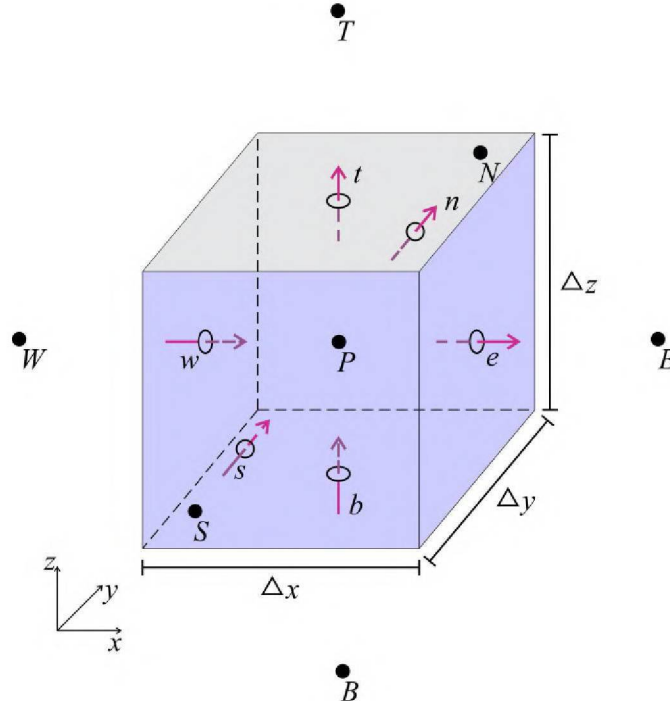
In order to illustrate the spatial and temporal discretization of the transport equations, consider the tridimensional control volume presented in Figure 4.2, with lengths of Δx , Δy , Δz for each direction in cartesian coordinates. The capital letters (E, W, N, S, T and B) represent the centroid of the neighbor control volumes, letters (e, w, n, s, t and b) stand for the faces east, west, north, south, top and bottom, and P is the centroid or node of reference (MELO, 2017).

Based on this representation of control volume, considering the x direction only to $i, j = 1$ and the current time $t + \Delta t$, the exemplification of discretization of the advective term in the momentum equation for finite volume follows:

$$\frac{\partial \rho u^{t+\Delta t} u^{t+\Delta t}}{\partial x} = [(\rho u u)_e - (\rho u u)_w] \Delta y \Delta z, \quad (4.4)$$

where the right hand side is the net advective flux of the control volume in the x direction. As a example of the same conditions, considering the x direction only to $i, j = 1$ and the current time $t + \Delta t$, the diffusive term can be written as:

Figure 4.2 – Elementary control volume to discretization



SOURCE: Adapted from Vedovoto (2011)

$$\begin{aligned}
 \frac{\partial}{\partial x} \left[\mu \left(\frac{\partial u}{\partial x} + \frac{\partial u}{\partial x} \right) \right] &= \left[\left(\mu \left(\frac{\partial u}{\partial x} + \frac{\partial u}{\partial x} \right) \right)_e - \left(\mu \left(\frac{\partial u}{\partial x} + \frac{\partial u}{\partial x} \right) \right)_w \right] \Delta y \Delta z = \\
 \left[\mu_e \left(\frac{u_E - u_P}{\Delta x} + \frac{u_E - u_P}{\Delta x} \right) - \mu_w \left(\frac{u_P - u_W}{\Delta x} + \frac{u_P - u_W}{\Delta x} \right) \right] \Delta y \Delta z &= \\
 2 \left[\mu_e \left(\frac{u_E - u_P}{\Delta x} \right) - \mu_w \left(\frac{u_P - u_W}{\Delta x} \right) \right] \Delta y \Delta z. &
 \end{aligned} \tag{4.5}$$

The transient term is discretized using an implicit scheme according to:

$$\frac{\partial \rho u}{\partial t} = \frac{\alpha_2 (\rho u)^{t+\Delta t} + \alpha_1 (\rho u)^t + \alpha_0 (\rho u)^{t-\Delta t}}{\Delta t}, \tag{4.6}$$

where α_0, α_1 and α_2 are coefficients associated with the CFL criteria, which is better described in Vedovoto (2011).

The pressure gradient is discretized as:

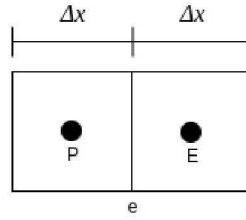
$$\frac{\partial p}{\partial x} = \frac{p_P - p_W}{\Delta x}. \tag{4.7}$$

Besides that, both advective and diffusive terms require information at the face of the control volume. As the code structure uses a multi-block structured grid that will be described in the section 4.2. The information can be obtained applying the average of the two neighbors nodes, which can be represented as a central difference scheme:

$$\theta_e = \frac{\theta_E + \theta_P}{2}, \tag{4.8}$$

and better demonstrated in Figure 4.3, where Δx stands for the mesh length in the x direction.

Figure 4.3 – Interpolation of two nodes in the finite volume to obtain surface information



SOURCE: The Author (2019)

4.1.2 Pressure-Velocity Coupling

This study used the fractional step method proposed by Chorin (1968), which is based on two steps in order to its application: the first one, called predictor step, estimates the velocity, and the second part, called corrector step, corrects the velocity from the pressure fluctuations. The implicit formulation solves a Poisson equation to correct pressure, which is applied to correct the velocity and pressure fields. Therefore, the predictor step estimates the velocity in the implicit way, where a linear system has to be solved for each component of the velocity vector.

From the momentum equation and the discretized temporal term, using a second order approximation, it is possible to obtain the following equation:

$$\begin{aligned} & \frac{\alpha_2 \rho u_i^{t+\Delta t} + \alpha_1 \rho u_i^t + \alpha_0 \rho u_i^{t-\Delta t}}{\Delta t} + \frac{\partial (\rho u_i^{t+\Delta t} u_j^{t+\Delta t})}{\partial x_j} = \\ & - \frac{\partial p^{t+\Delta t}}{\partial x_i} + \frac{\partial}{\partial x_j} \left[\mu \left(\frac{\partial u_i^{t+\Delta t}}{\partial x_j} + \frac{\partial u_j^{t+\Delta t}}{\partial x_i} \right) \right]. \end{aligned} \quad (4.9)$$

The estimation of the velocity is obtained from:

$$\begin{aligned} & \frac{\alpha_2 \rho \tilde{u}_i^{t+\Delta t} + \alpha_1 \rho u_i^t + \alpha_0 \rho u_i^{t-\Delta t}}{\Delta t} + \frac{\partial (\rho \tilde{u}_i^{t+\Delta t} \tilde{u}_j^{t+\Delta t})}{\partial x_j} = \\ & - \frac{\partial p^t}{\partial x_i} + \frac{\partial}{\partial x_j} \left[\mu \left(\frac{\partial \tilde{u}_i^{t+\Delta t}}{\partial x_j} + \frac{\partial \tilde{u}_j^{t+\Delta t}}{\partial x_i} \right) \right]. \end{aligned} \quad (4.10)$$

It is important to point out that advective and diffusive velocity terms are in the current time step, $(t + \Delta t)$, whereas the pressure term represents the previous time step. Therefore, the linear system calculates the estimating velocity implicitly. Then it is necessary to subtract the equation 4.10 from equation 4.9, which results in:

$$\frac{\alpha_2 \rho u_i^{t+\Delta t} - \alpha_2 \rho \tilde{u}_i^{t+\Delta t}}{\Delta t} = - \frac{\partial p^{t+\Delta t}}{\partial x_i} + \frac{\partial p^t}{\partial x_i}. \quad (4.11)$$

After that, the following quantity is defined:

$$p' = p^{t+\Delta t} - p^t, \quad (4.12)$$

where p' stands for the pressure fluctuation at the current time step. Applying the equation 4.12 into equation 4.11 and utilizing the divergent on both sides:

$$\frac{\alpha_2}{\Delta t} \left(\frac{\partial u_i^{t+\Delta t}}{\partial x_i} - \frac{\partial \tilde{u}_i^{t+\Delta t}}{\partial x_i} \right) = - \frac{\partial}{\partial x_i} \left(\frac{1}{\rho} \frac{\partial p'}{\partial x_i} \right). \quad (4.13)$$

Thus, from the estimated velocity is possible to calculate the pressure correction by solving the linear system of the equation 4.13. The next step of the method consists in the pressure correction, called the corrector step, which presents:

$$p^{t+\Delta t} = p^t + p'. \quad (4.14)$$

Then rewriting the equation 4.11, it brings the velocity correction:

$$u_i^{t+\Delta t} = \tilde{u}_i^{t+\Delta t} - \frac{\Delta t}{\alpha_2 \rho} \frac{\partial p'}{\partial x_i}. \quad (4.15)$$

After discretizing the momentum equation and also coupling the pressure-velocity, the initial and boundary conditions need to be prescribed in order to solve the equations, in which it will be described at the beginning of each results section. Finally, the next sections treat the adaptive mesh refinement inside the MFSim code.

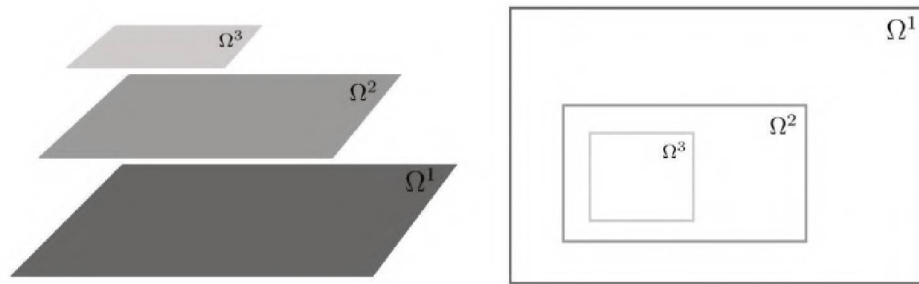
4.2 MULTIBLOCK STRUCTURED MESH

Even considering a very effective methodology for turbulence modelling, the mesh refinement is still very important to improve the quality of the solution. Applying an extremely refined mesh in the whole domain is possible, although the solution becomes computationally impracticable depending on the size of the domain.

In order to diminish this cost associated with the use of excessive refinement, the MFSim code is based on multiblock structured grids for local refinement. The solution of the discretized Navier Stokes equation occurs through a sequence of properly refined cartesian meshes. The levels of refinement are given by the connection of oriented meshes with sequentially smaller sizes (VILLAR, 2007).

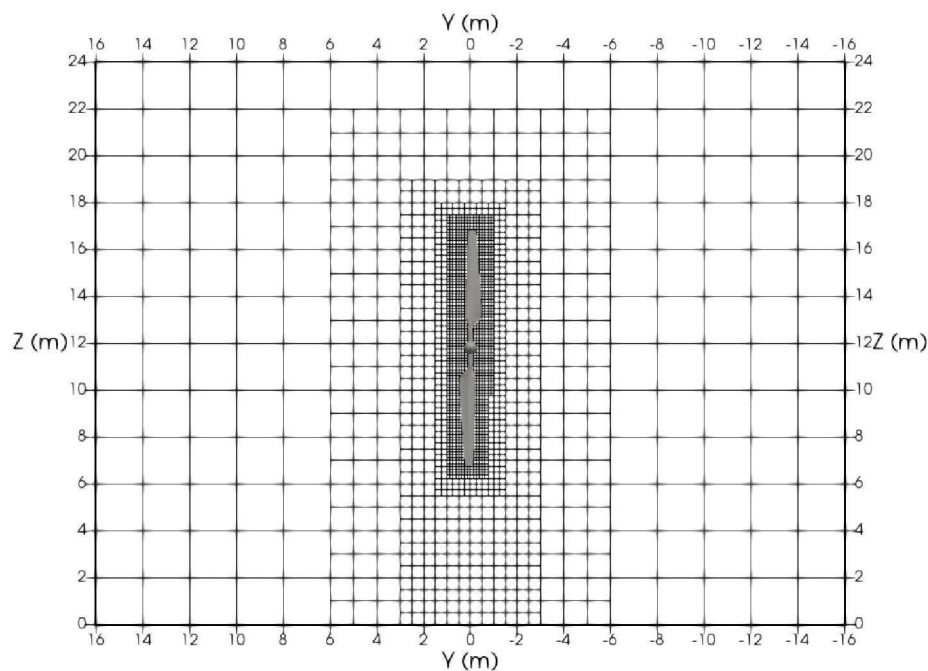
Figure 4.4 shows the refinement procedure for the multiblock mesh arrangements, the finest level of the mesh aligns, overlapping the superior coarse mesh, in predetermined areas or where it is necessary high numerical accuracy. There are areas where refinement is crucial, such as those in which occurs flow instabilities, the high intensity turbulence regions, and near wall areas or regions with a fluid-structure interface (SANTOS, 2019). Figure 4.5 represents an example of the local adaptive mesh refinement application around a fluid-structure interaction, where the mesh presents a refinement ratio equals two. In this case, the cell of the coarser level will be divided into 4 cells of the immediately fine level.

Figure 4.4 – Multi-block structured grids for local refinement



SOURCE: Santos (2019)

Figure 4.5 – Cartesian mesh refinement around the wind turbine and by vorticity



SOURCE: The Author (2019)

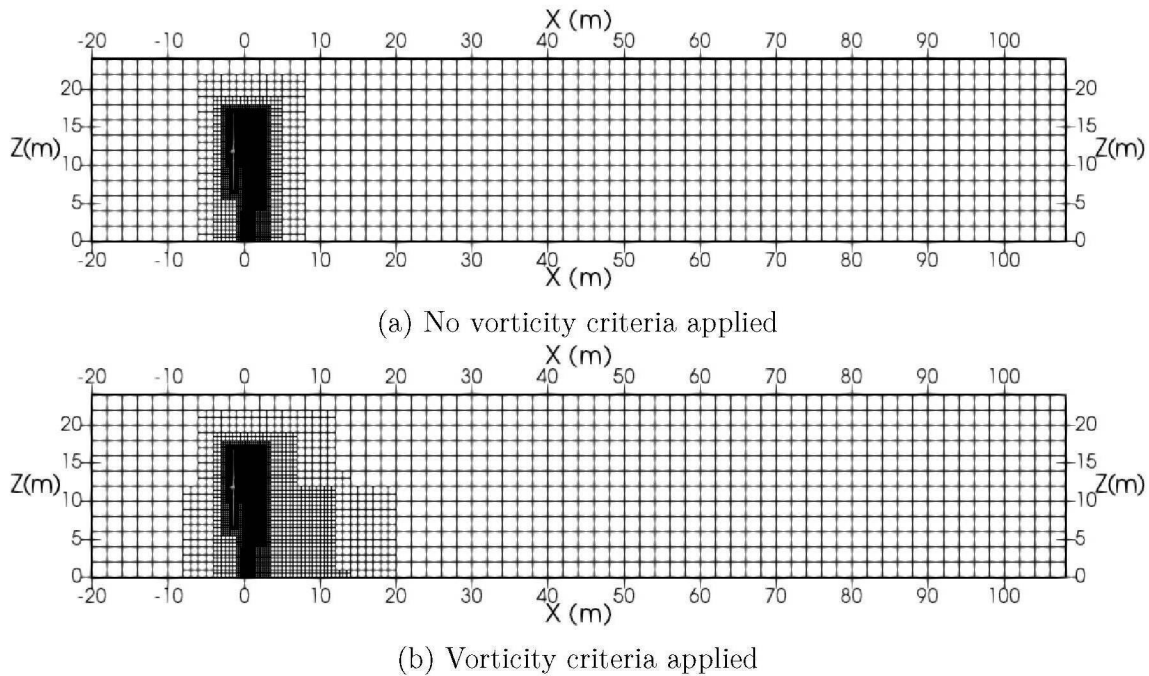
Applying refined meshes throughout the calculation domain would lead to a prohibitive increase in the computational cost involved in the solution of differential equations. Then, the need to use a localized refinement to obtain a refined mesh only in the region of interest. One of the advantages of the MFSim code is related to the fact that it solves the equations using block-structured adaptive mesh, allowing local fixed refinement or criteria based on flow properties to define the positioning of the refinement levels.

At first, two types of adaptive approximation are distinguished: static refinement, in which the regions of refinement in the computational domain are determined before the execution of the numerical method start, and dynamic refinement, in which the refinement regions are determined during the execution of the numerical method, controlled by appropriate adaptive criteria. There is also a possibility to combine both of them.

Firstly, the specific fixed refinement region can be applied with the chosen level of re-

finement covering the informed region. Then can inform the coordinates of the refinement block to be positioned. Secondly, the refinement module in MFSim code can be based on a vorticity criteria. It means that the mesh is refined only in specific regions according to predefined thresholds determined in terms of local vorticity. Figure 4.6 can illustrate such criteria, where Figure 4.6(a) presents the mesh around the langrangian points, which are the wind turbine structure with no refinement applied. Figure 4.6(b) shows the refinement regions applied by the use of a vorticity criteria downstream of the wind turbine. With this procedure, it is possible to reduce the computational cost and ensure greater numerical accuracy.

Figure 4.6 – Lateral view of the cartesian mesh with vorticity criteria of refinement



SOURCE: The Author (2020)

The vorticity criteria is based on evaluating equation 4.16 for each computation cell through a non-dimensional number given by (Barbi, 2016):

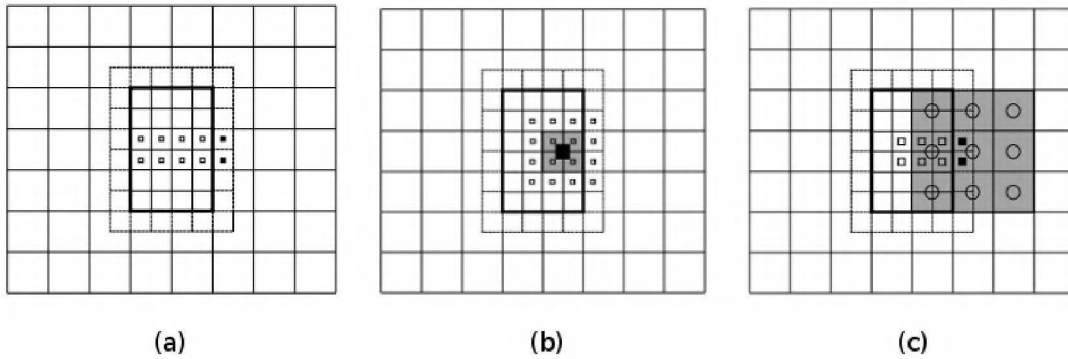
$$\frac{\|\omega\| \Delta}{\|u_{max}\|} \geq \zeta, \quad (4.16)$$

where $\|\omega\|$ is the norm of the vorticity, Δ is the local grid length, u_{max} is the maximum norm of the velocity field and ζ is a constant, which is arbitrary set to $\zeta = 0.08$. Therefore, the local refinement occurs on computational cells that respect the logical expression above.

In addition to the vorticity criteria, the calculation of the flow properties in a determined cell, in certain cases, requires values of the neighbor's cells properties. When a cell of the thinner level connects a cell of the level below (coarser level), there is a creation of ghosts cells and properties are calculated following a procedure of three steps: (i) cubic extrapolation utilizing the cell properties of the thinner level for its own layer (Figure 4.7 (a)); (ii) cubic extrapolation utilizing the cell properties of the thinner level to cells of the level below that are in the border of thinner level (Figure 4.7 (b)); (iii) quadratic interpolation between the cells of the thinner level and the level below (coarser level) (Figure 4.7 (c)). There is also a creation of ghost cells if

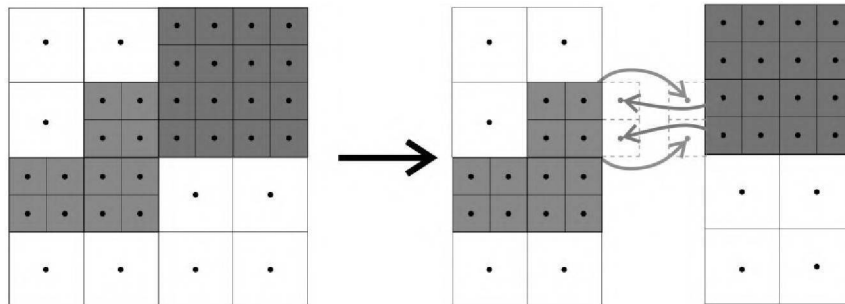
two cells of the same level, but different layers connect between them. The difference in this case is that the properties do not need be extrapolated or interpolated, although they are transferred from the real cell to the ghost cell (Figure 4.8), procedure called injection (LIMA, 2012; MELO, 2017).

Figure 4.7 – Interpolation schemes to create ghost cells



SOURCE: Adapted from Lima (2012)

Figure 4.8 – Filling the ghost cell with blocks at same level



SOURCE: Adapted from Melo (2017)

In terms of applying boundary condition, ghost cells created at the physical borders of the domain are filled in for each property respecting the chosen condition. The user of the MFSim code can choose the type boundary conditions, among Dirichlet, Neumann, advective (only for velocity) and periodic.

4.3 MULTIGRID-MULTILEVEL METHOD

To solve the linear systems from the discretization, the method implemented in the MFSim code is Multigrid, both for velocity and the pressure correction solution. The Multigrid method is an iterative algorithm for solving linear systems using mesh hierarchy (TROTTEMBERG; SCHULLER, 2000).

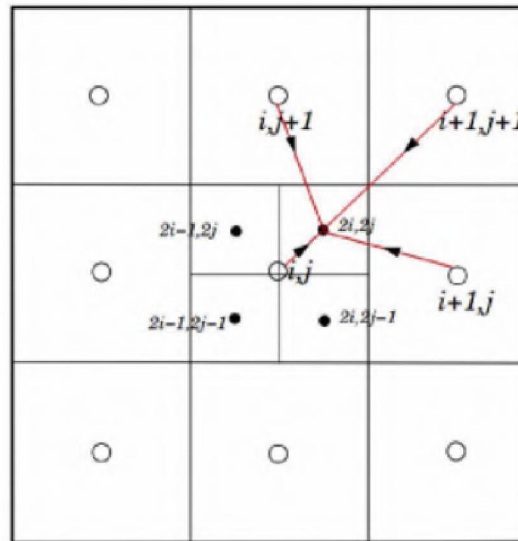
There are two main distinct ideas of the Multigrid method. The first is based on the error smoothing of iterative methods applied in the solution of linear systems. The second states that the error smoothed on a mesh at a certain level can be approximated on a coarser mesh. It is preferable to use multigrid with a sequence of meshes instead of an only coarse mesh, because

the long wavelengths in a fine mesh are decreased in coarser meshes, which allows the error components to be efficiently smoothed, speeding up the convergence (VILLAR, 2007; LIMA, 2012).

The linear systems solution to solve every component of the velocities and the pressure correction, for the multigrid method, occurs through the implementation of Correction Storage formulation, which states a transference of the residue from a mesh to another (RABI; LEMOS, 2001; RABI; LEMOS, 2003).

Throughout the method, there are transference of error and residue values from a mesh to another. When information passes from a coarser mesh to a thinner mesh the process is called prolongation, representing in Figure 4.9. On the other hand, when the variable transfer information occurs from a thinner mesh to a coarser mesh the process is called restriction, shown in Figure 4.10.

Figure 4.9 – Prolongation operation multigrid

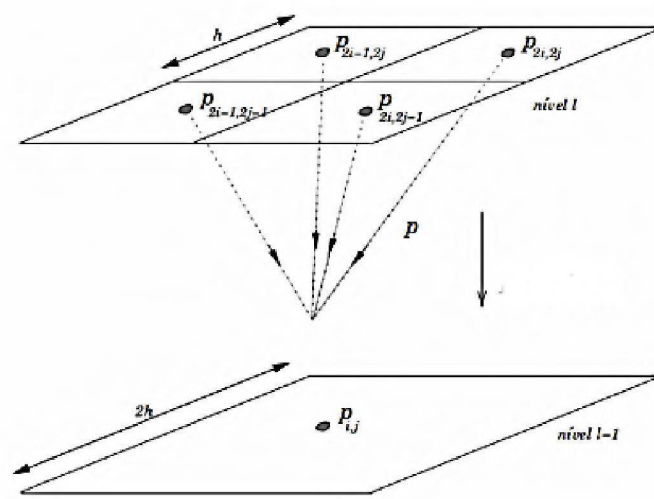


SOURCE: Villar (2007)

The MFSim code uses a local refinement, then the Multigrid method turns into a Multigrid-Multilevel method, where there are two groups of meshes, which can be called virtual levels and physical levels. The virtual levels generate the base mesh to apply the multigrid method cycle. Physical levels are responsible for generating blocks of local refinement, and the multigrid method travels through physical levels as well. Figure 4.11 schematically illustrates the physical and virtual levels. For more detailed information see Villar (2007) and Melo (2017).

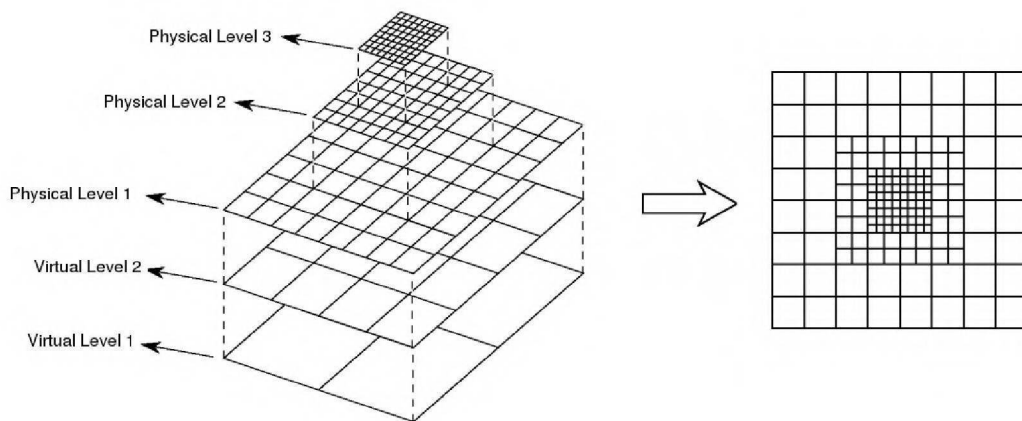
In the next chapter, the results will seek verification and validation of the methods that have been modified and updated in the MFSim code to be adequate for wind power applications. In order to evaluate the maximum capability of the code when simulating real scale domains, leading the code to its highest stress level. Moreover, capture crucial spatial and temporal information of the velocity field and the forces acting on selected wind turbines.

Figure 4.10 – Restriction operation multigrid



SOURCE: Villar (2007)

Figure 4.11 – Scheme of virtual and physical levels



SOURCE: Adapted from Melo (2017)

5 RESULTS AND DISCUSSION

This chapter presents the results from simulations involving the coupling of LES and IB methods applied to model turbulent flows around wind turbines.

Before applying the methodology directly to a real scale turbine, it was decided to simulate a less complex system in order to better understand the problem proposed in this work. In this way, a first simulation scenario has been dedicated to the simulation of an isolated turbine blade in a stationary flow regime with varying angles of attack. This allowed the analysis of aerodynamic parameters involved in the flow around an airfoil. Besides, this simplified case allowed a better understanding of the most important tools of the methodology, the adaptive mesh refinement, with the objective of further applications in most complex simulations.

A subsequent topic presents the results of a second simulation scenario, which consists of an experimental turbine well-known as NREL Phase VI. The simulations were based on experimental studies that had been elaborated in wind tunnel tests, which were described by (HAND et al., 2001; SIMMS et al., 2001). These authors developed a structural model and verification procedures for the wind experimental Phase VI of the National Renewable Energy Laboratory (NREL). The section illustrates the probes locations and the chosen selection. Results were obtained and discussed in terms of longitudinal comparisons for four different annular profiles as well as comparisons of downstream wake cross-sections plotted against simplified wake models, besides the evaluation of vertical velocity profiles in the downstream wake of the wind turbine.

The third scenario, which consists of simulations of a real scale operating turbine. The simulations comprehended a stand alone real scale turbine, 5 MW NREL (JONKMAN et al., 2009), where the properties of mean and turbulent flows will be analyzed and discussed. The international cooperation between the Federal University of Parana (UFPR) and the University of British Columbia (UBC), the data provided from UBC Okanagan CFD Lab, supervised by Prof. Dr. Joshua Brinkerhoff, are based on LES simulations with Smagorinsky turbulence modelling, from their own in-house code, MARBLLES (Multiscale AtmospheriC Boundary Layer Large Eddy Simulation) which is based on actuator disk model, also from SOWFA (Simulator for Offshore Wind Farm Applications) developed by National Renewable Energy Laboratory. The last section of this chapter will present and discuss back to back NREL 5 MW wind turbines in a real scale case in order to represent what occurs in a wind farm power plant, in addition the power generation is validated with NREL experimental results.

5.1 SCENARIO 1: NREL ISOLATED BLADE

The first simulation scenario developed in this work presents the analysis based on the flow around an isolated wind blade. For these simulations, it was chosen a well-known blade named NREL S809, developed in the context of the National Renewable Energy Laboratory (HAND et al., 2001; SIMMS et al., 2001). This blade has been studied in wind tunnels and experimental data in terms of aerodynamics coefficients and parameters are available.

For the simulations, the NREL S809 blade had been constructed in the CATIA[®] software and meshed in the ICEM[®] CFD software. The blade mesh was represented by a lagrangian domain containing 80,730 triangular cells. The eulerian computational domain had 30 *m* in the *x*-direction, 10 *m* in the *y*-direction and 10 *m* in the *z*-direction. Figure 5.1.1 presents the experimental NREL S809 blade, following the airfoil characteristics and patterns. Figure 5.1.1(a) depicts the frontal view of the blade, characterizing the height of the blade, Figure 5.1.1(b) shows the perspectives of the variation in terms of the chord length of the blade, and Figure 5.1.1(c) presents the airfoil characteristics and the twisted angles applied. Figure 5.1.2 shows the color map of the blade in terms of the area distribution for each mesh cell, presenting the variation of the area at each cell.

Figure 5.1.1 – NREL S809 (a) frontal, (b) lateral and (c) top view

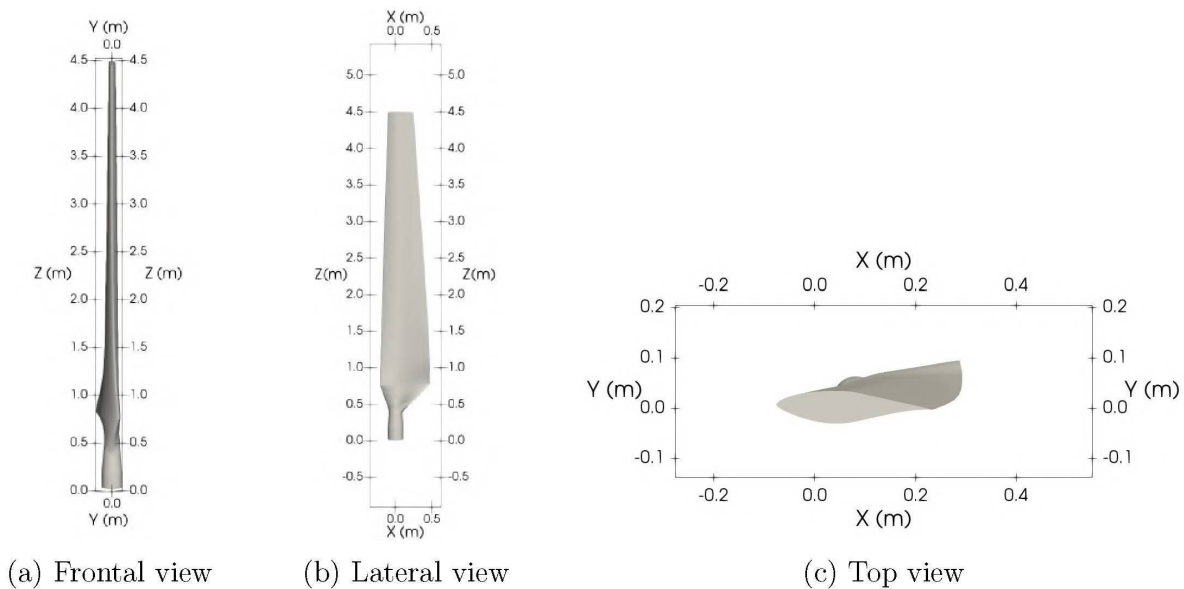
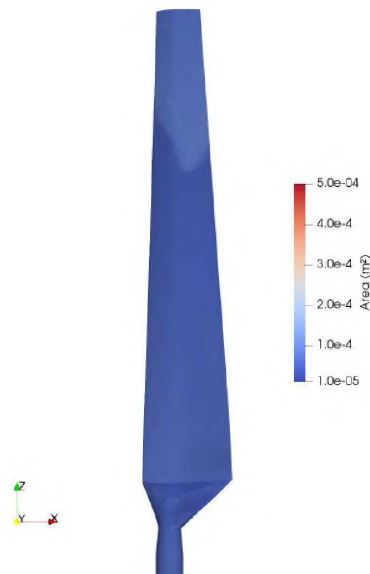
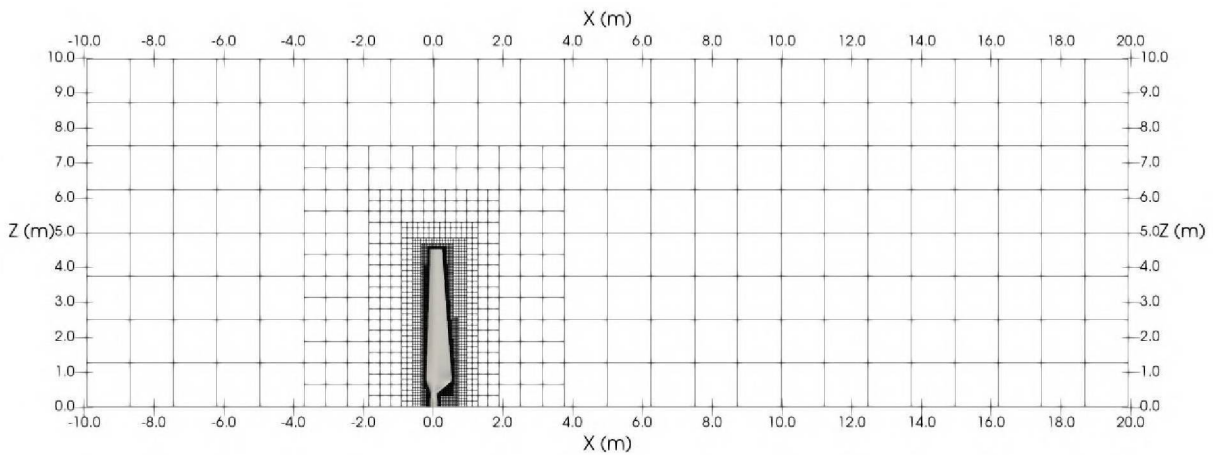


Figure 5.1.2 – Mesh area of the NREL S809 blade



These simulations were performed with an adaptive mesh composed of seven levels. The initial mesh arrangement was set up with $24 \times 8 \times 8$ volumes for the coarser grid (base level) in the xyz directions, obtaining an initial computation domain with approximately 540 thousand volumes. The finest grid level was always around the blade shape. Figure 5.1.3 represents a lateral computational grid view of the eulerian domain. The x -axis assigns the longitudinal direction, whereas the z -axis stands for the vertical direction.

Figure 5.1.3 – Eulerian mesh of the flow



For the boundary conditions, a uniform wind velocity distribution has been employed in the inflow ($u = 10$ m/s, $v = 0$ m/s, $w = 0$ m/s), characterizing a Dirichlet type of boundary condition that consists of an imposed distribution of velocity. The lateral planes (xz -planes) and top plane (xy -plane) were characterized as symmetry conditions. The bottom plane (xy -plane) was set as a free-slip condition in order to represent the blade attachment of the blade with the rotor. A Neumann boundary condition was applied for pressure and an advective condition for the outflow.

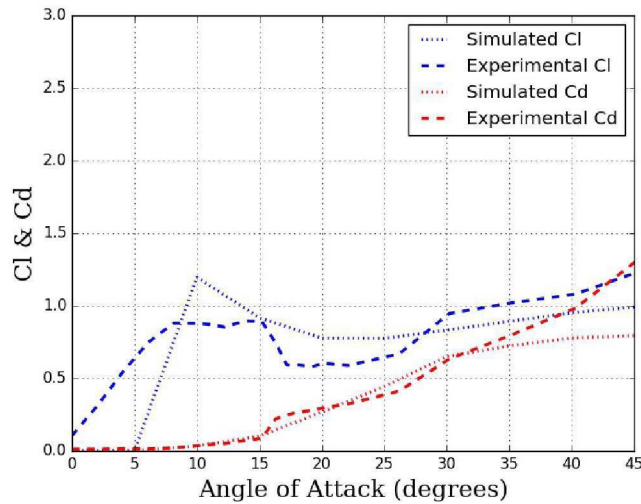
The initial conditions for velocities were $u=10$, $v=0$ and $w=0$ m/s, while pressure was set to atmospheric. In these simulations, the fluid properties were $\rho=1.225$ kg/m³, $\mu=0.0000182$ kg/(m·s) and setting a Reynolds number ($Re \approx 300,000$) based on the characteristics scales of the blade and the inflow velocity. The final simulation time was 60 seconds, period along which the flow presented approximately steady state conditions. Utilizing a Intel i7-7700T 2.9GHz quad-core machine utilizing approximately 5.6 GB RAM, the simulations required approximately 112 hours.

The following results are obtained in terms of drag and lift coefficients, being compared to experimental measurements of Hand et al. (2001). Later, it will be presented the longitudinal and transversal distributions of the streamwise component of velocity, and by the end, the main turbulence properties downstream from the blade are shown.

5.1.1 Drag and Lift Coefficients

The averaged integral lift and drag coefficients were calculated for different angles of attack, varying from 10 to 45°, by 5° increments. Figure 5.1.4 presents the lift and drag coefficients obtained as a function of the angles of attack for the chosen blade in comparison to the experimental data provided by NREL.

Figure 5.1.4 – Lift and drag coefficients

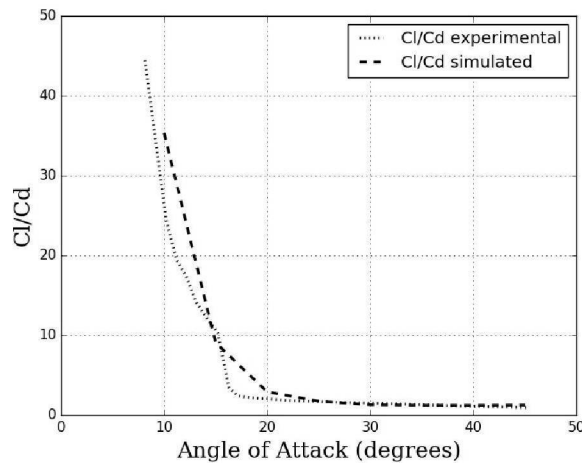


It was observed that the drag coefficient obtained a better agreement with the experimental data than the lift coefficient. For the angles of attack from 0° to 35°, the simulated drag coefficients followed the experimental data behavior very closely, presenting a maximum absolute discrepancy of 17% at the angle of attack of 15°. Except that, the remaining profiles over this range had captured drag coefficients differences lower than 10%, where the 30° profile presented the lowest discrepancy value slightly over 2.5%. On the other hand, for higher angles of attack, 40° and 45°, it was noticed bigger differences between the experimental and simulated data, the highest discrepancy occurred for the angle of attack of 45° reaching almost 34%. Therefore, the drag coefficient is practically constant for lower angles of attack but quickly after 15°.

In terms of lift coefficient, it was observed that the simulations followed the general distribution of the experimental data, except for the angles of attack from 0° to 10°. In this interval, there was a rapid lift coefficient increasing up to 10°, where the highest difference between the data reached a value of around to 35%. It has been expected a linearly increasing profile but not a very steep slope. This behavior might have been produced by the 5° increments in the simulations. For the 0° to 10° range, it should be simulated cases with a 2° increments up to 10°. After this range, there was a decreasing rate up to 20°, where the minimum discrepancy value around 3% occurs at the 15°, close to the stall angle of 16°.

Figure 5.1.5 shows the relation between lift and drag coefficients (C_l/C_d) as a function of different angles of attack. This relation is important to determine the performance and efficiency of an airfoil at a particular angle of attack. It is known that C_l/C_d will be affected by the shape of the airfoil and the changes in the angle of attack. The C_l/C_d , illustrated in Figure 5.1.5, presents high values of lift coefficient compared to the drag coefficient as the angle of attack

develops up to the stall. A particular blade has its best lifting ability before reaching the stalling angle of attack. However, near to the stalling angle, the values of the drag coefficient begin to increase while the lift is stagnated. Because of that, it is important to select an airfoil regarding the stall parameters and roughness sensitivity, which are correlated to the lift and drag ratio. Hansen (2008) expressed that a laminar aerofoil is identified by a large Cl/Cd ratio for angles of attack that are lower than the designed stall. Thus, if an airfoil is roughness sensitive, the power generation of the wind turbine will be conditional to the wind direction.

Figure 5.1.5 – Cl/Cd ratio

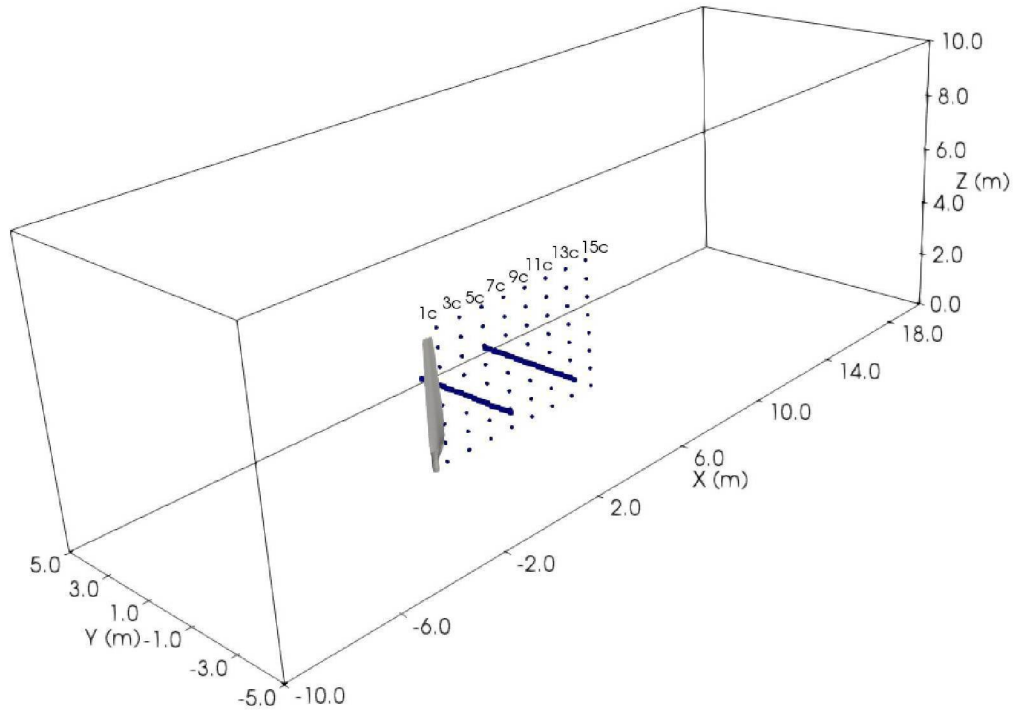
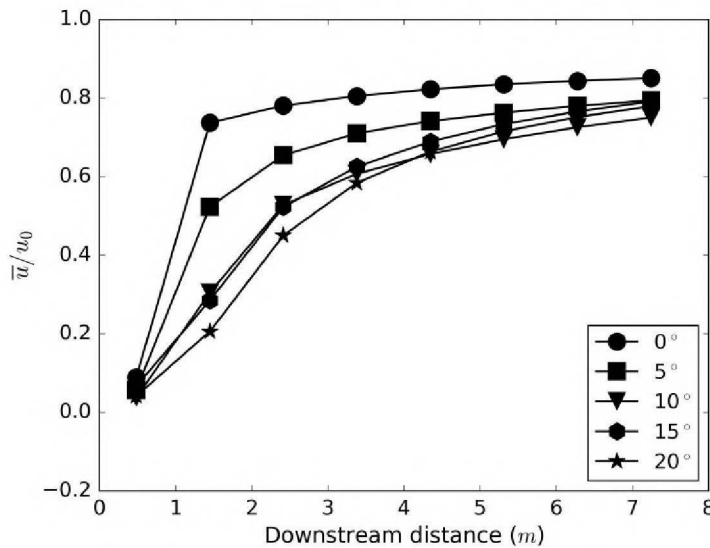
5.1.2 Time-averaged Streamwise Velocity

Streamwise components of time-average velocity were analyzed in a region downstream from the blade, for angles of attack from 0° to 20° , and increments of 5° . Figure 5.1.6 shows the probes that were installed to capture the flow results in order to calculate the velocity statistics. Such probes had been distributed $1c$ to $15c$ downstream from the NREL in the longitudinal direction, where c stands for the blade chord. It was also implemented 20 probes located at $3c$ and $9c$ downstream from the blade, in cross-sections varying from $-2m$ to $2m$ in the y direction, to capture the transversal time-average streamwise velocity distribution.

Figure 5.1.7 presents the time-averaged streamwise velocity recovery (also named as velocity deficit) as a function of the distance downstream of the wind turbine blade, in a longitudinal centerline at $z = 2m$, which is half of the blade height.

Figure 5.1.7 displays the high extraction of kinetic energy in the near wake region downstream from the blade, where the velocity recovery reaches a minimum value before the $1c$ distance, immediately downstream from the blade. After this region, there is a large velocity recovery for all angles of attack. Even more distinguished for lower angles as 0° and 5° , where the velocity recovery increases to around 80% and 60%, respectively. As expected in the near wake, the highest angles of attack extracted the largest amount of energy from the wind flow. Thus, presenting the lowest velocity recovery profile up to $4m$ downstream of the wake region. The maximum velocity recovery was obtained for a downstream distance of $7m$. Therefore, for

Figure 5.1.6 – Probes downstream of the NREL from 1c to 15c

Figure 5.1.7 – Comparison of time-averaged streamwise velocity \bar{U} (m/s) deficits along the downstream distance for different angles of attack

the angle of attack of 0° , 80% of the velocity was recovered, whereas for the angles of attack from 5° to 20° approximately 70% of the velocity was recovered.

An analysis of the longitudinal development of velocity can be demonstrated based on Figure 5.1.8, which presents vertical profiles of time-averaged streamwise velocity downstream from the blade for angles of attack varying from 0° to 20° . It can be seen that the profiles at 1 *c* are very similar for all angles of attack, this similarity of profiles also occurs approximately to

the blade tip, above 4 m, where all profiles show a high velocity recovery. Besides that, from 3c to 9c for all angles of attack, there is a decreasing pattern occurring at the height of z in terms of the maximum velocity recovery.

Figure 5.1.8 – Comparison of vertical profiles of the time-averaged streamwise velocity \bar{U} (m/s) for different angles of attack, from a) 0, b) 5, c) 10, d) 15, and e) 20°

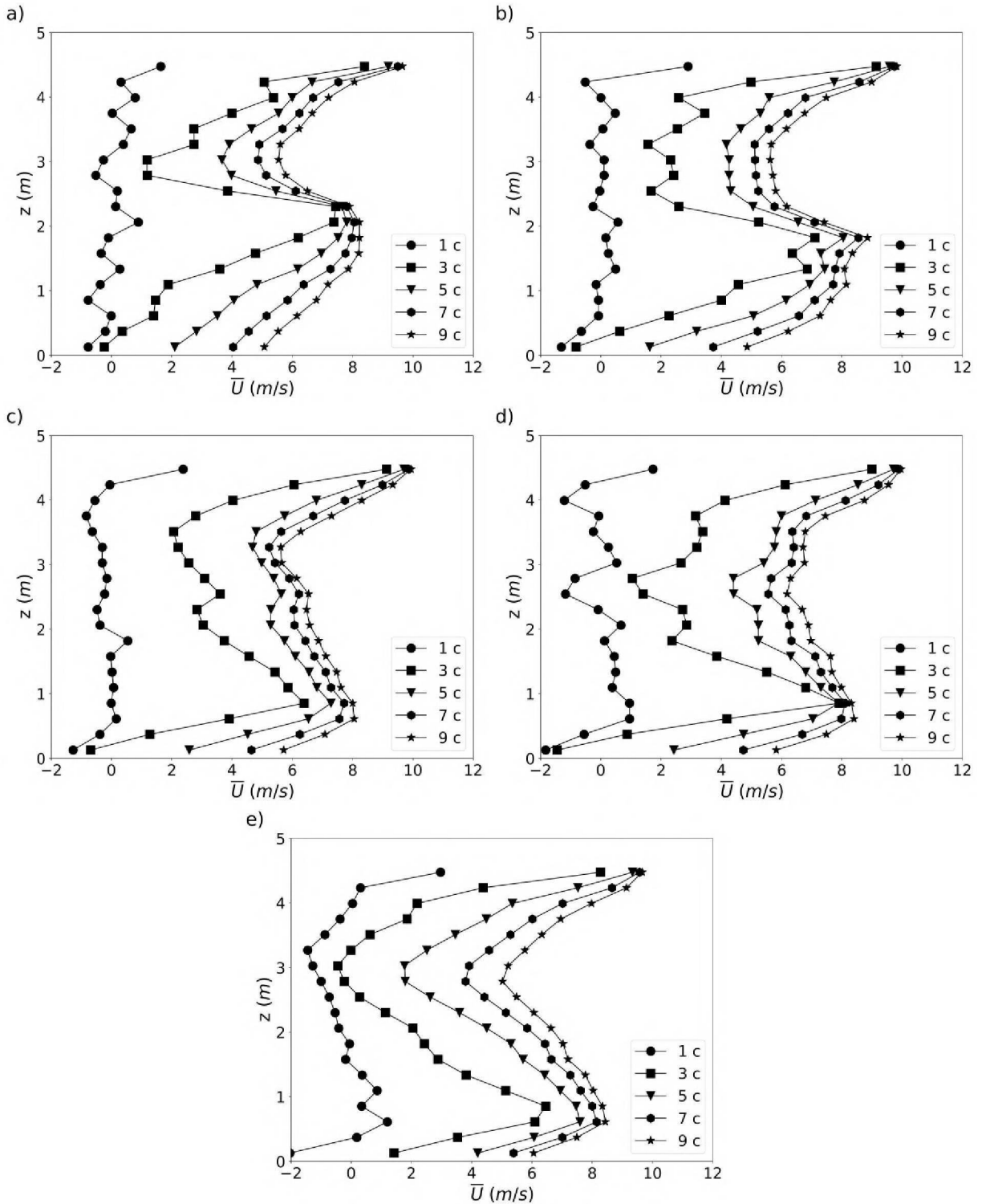


Figure 5.1.8(a) shows a velocity recovery peak at z approximately higher than 2 m, while Figure 5.1.8(b) demonstrates the same block but in z approximately less than 2 m. In Figures

5.1.8(c) and 5.1.8(d), the maximum velocity recovery decreased to z approximately equals to $1 m$. Meanwhile, Figure 5.1.8(e) also presented a decrease in z for the peak of the velocity recovery, reaching almost $0.5 m$. Those velocity recovery peaks approaching the blade base may have been caused by the development of the angles of attack because it has been considered an analysis where the flow centerline is displayed. Therefore, it can be inferred that as lower as the angle of attack, the larger are centerline velocity recovery close to the base of the base, where the blade airfoil design has a lower velocity deficit influence for higher angles in the blade root.

Figure 5.1.9 presents the instantaneous vorticity distribution for a horizontal plane located at $z = 2m$, for angles of attack of 10° , 15° and 20° . As expected, the greater is the angle of attack, the bigger are the eddy structures developed in the downstream wake of the blade. The vorticity parameter is the criteria applied in this work for the adaptive refinement of the mesh, and it can be observed in Figure 5.1.9 how the parameter behaviors in the downstream flow from the blade. This vorticity analysis is important to understand that a great refinement criteria chosen by the user can lead to a lower computational cost along with better accuracy and physical representation. Figure 5.1.9 also inferred that when the blade is nearly aligned with the flow, the boundary layer holds attached, whereas the adverse pressure gradient caused by bigger angles can lead to separation.

5.1.3 Turbulence Properties and Characteristics

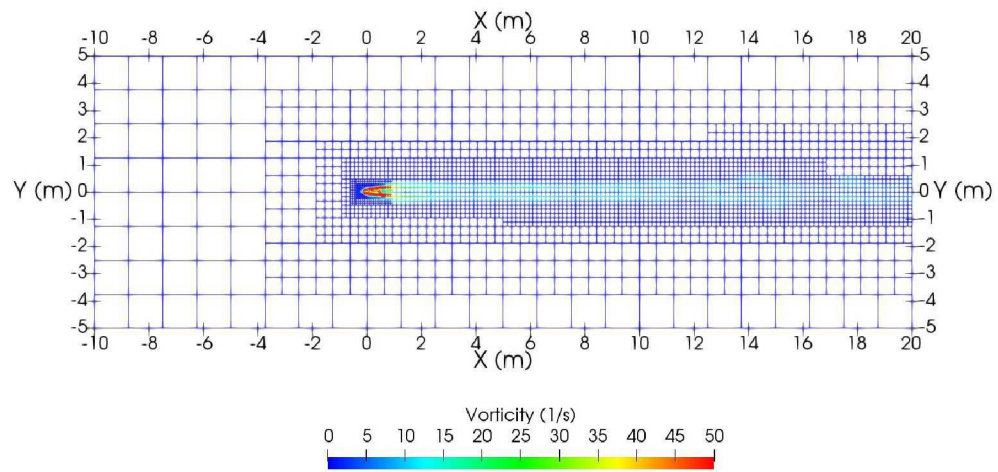
The ability of the LES-IB methodology to simulate the interaction between wind blade structure and turbulence is first highlighted through an analysis of the turbulent kinetic energy extracted over the flow field. Figure 5.1.10 illustrates the turbulent kinetic energy k distribution along the downstream distance for angles of attack ranging from 0° to 20° that are arbitrary calculated at $2 m$ height of the wind turbine blade. The calculated turbulent kinetic energy k , for $i = 1, 2, 3$, is expressed by:

$$k = \frac{1}{2} \overline{u'_i u'_i} = \frac{1}{2} \left(\overline{u'^2} + \overline{v'^2} + \overline{w'^2} \right). \quad (5.1)$$

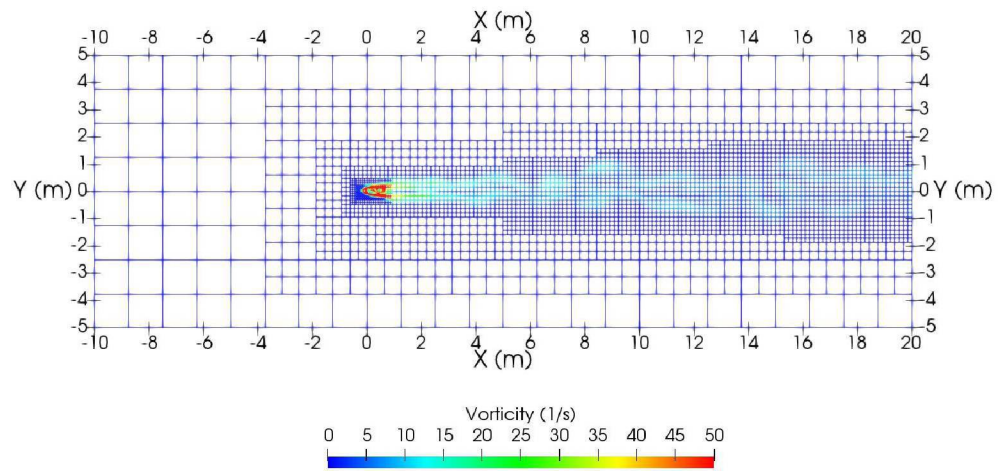
As expected, the higher values of turbulent kinetic energy occur in the near wake due to the high density of eddies structures occurring in this region. Besides that, profiles 0° and 5° presented an almost flat distribution over the entire wake downstream distance due to the low angles of attack. For angles of attack greater than 5° , turbulent kinetic energy levels decrease over the downstream distance, demonstrating the energy dissipation along the way. The majority of the dissipation tends to occur between 1 to $2 m$ for angles of attack of 0° and 5° , whereas for the 20° profile tends to exponential decay. This behavior is due to the high angle of attack and bigger eddies structures developed in this case.

Figure 5.1.11 shows the distribution of the Reynolds stress components downstream from the blade for angles of attack ranging from 0° to 20° in intervals of 5° . Figure 5.1.11(a) illustrates the normal component $\overline{u'^2}$, which restates the turbulent kinetic energy behavior. It can be seen a strong production of this component, especially for the angle of attack 20° . Figure 5.1.11(b) and Figure 5.1.11(c) present the results for the normal components $\overline{v'^2}$ and $\overline{w'^2}$, respectively. It was observed a strong production of these components over a $1c$ distance and a rapid dissipation

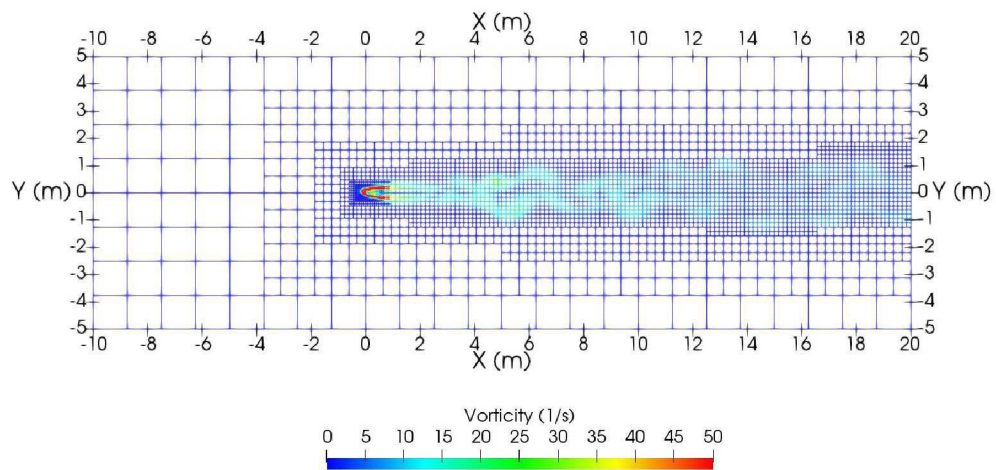
Figure 5.1.9 – Vorticity criteria applied to different angles of attack, from (a) 10° , (b) 15° and (c) 20°



(a) 10°



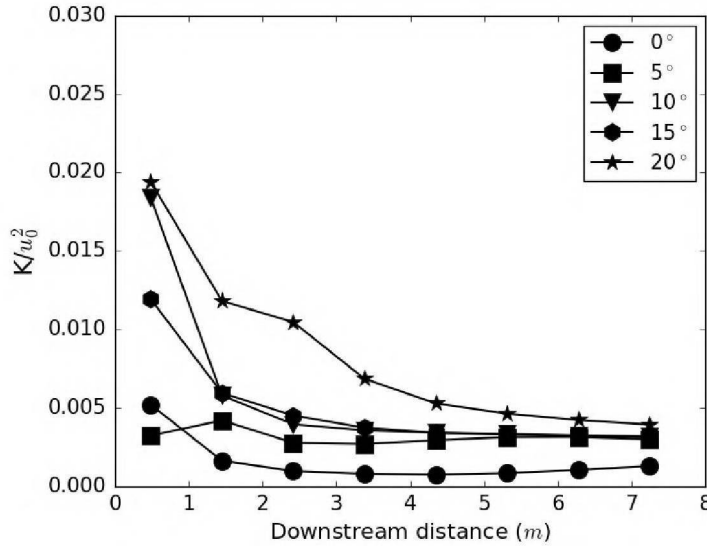
(b) 15°



(c) 20°

that occurs immediately downstream from this region. This pattern probably happens due to the blade profile design, which leads to increasing velocity fluctuations in the cross-flow direction

Figure 5.1.10 – Comparison of kinetic turbulent energy k normalized by u_0^2 deficits along the downstream distance for different angles of attack



immediately downstream from the blade.

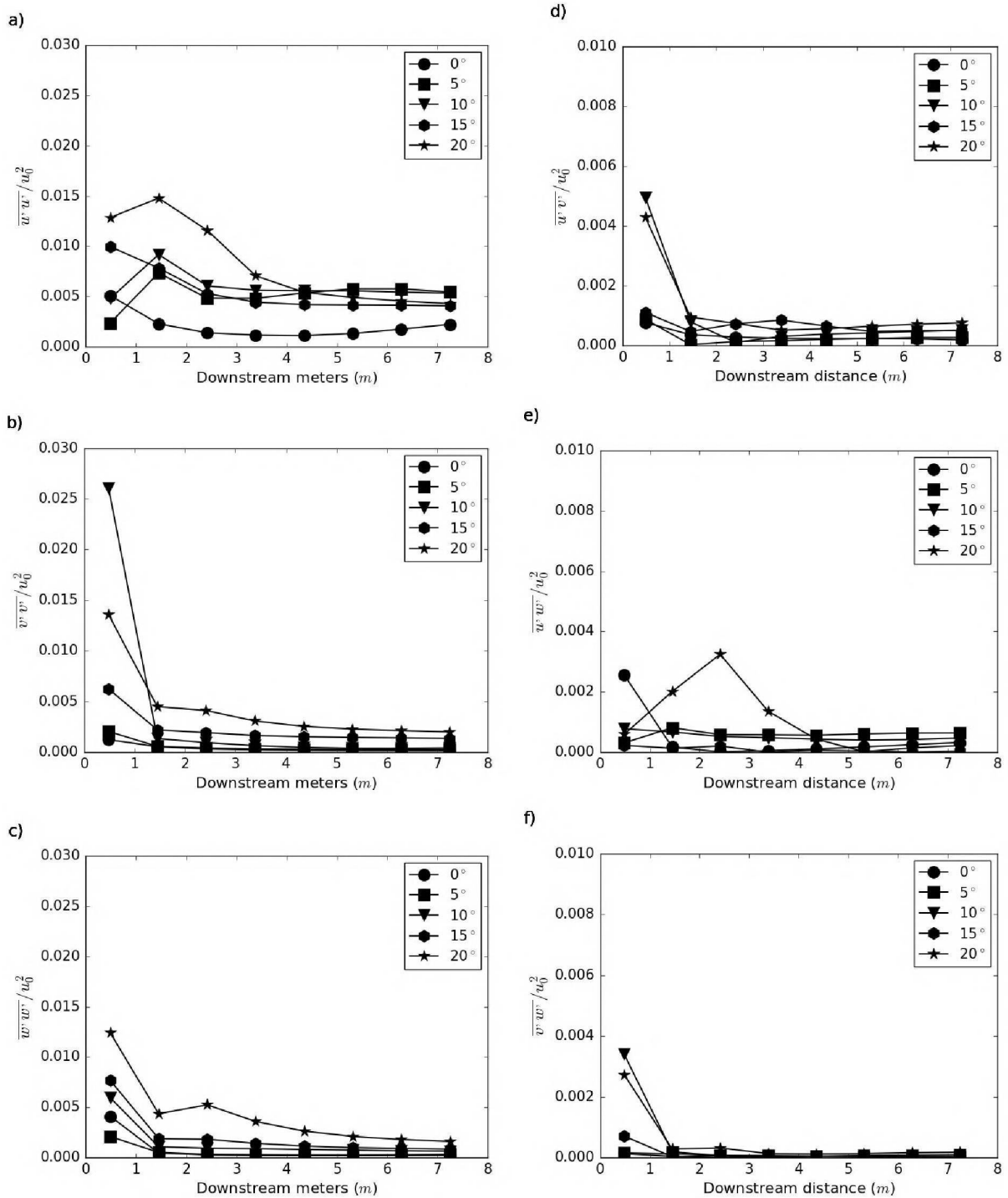
Figures 5.1.11(d), 5.1.11(e) and 5.1.11(f) illustrate the shear components of the Reynolds stress tensor. The components $\overline{u'v'}$ and $\overline{u'w'}$ present similar patterns presenting moderate values at $1c$ downstream distance. The $\overline{v'w'}$ component presents an interesting behavior for the 20° profile, demonstrating its higher value at $5c$ downstream. This could be a prolongation of bigger eddies, but further analysis are needed.

Previous studies, Stival, Guetter and Andrade (2017), Kim et al. (2015), Roy and Sharp (2013), Sathe et al. (2013), have shown that turbulence intensity is an important parameter that influences energy production. Usually, the velocity deficit related to power losses in wind farms recovers faster when the turbulence intensity level of the incoming flow is higher, mainly in the near wake. This affects the power performance of the downstream turbines in wind farms with a high degree of turbine density. Figure 5.1.12 presents the vertical profiles of the turbulence intensity over the wind turbine blade for angles of attack that varies from 0° to 20° . Turbulence intensity is estimated by the ratio of the root-mean-square of the component $\overline{u'^2}$, and the corresponding mean wind velocity, \bar{U} , as follows:

$$TI = \frac{\sqrt{\overline{u'^2}}}{\bar{U}} \quad (5.2)$$

Figure 5.1.12(a) presented a negative gradient of TI in z ranging from 2 to 2.5 m . Below this height, the TI tends to increase as the downstream distance from the blade develops. Figures 5.1.12(b) and 5.1.12(c) showed their maximum TI value, slightly below 0.20, around the blade root at the downstream distance of $3c$. Figure 5.1.12(d) demonstrates a negative gradient of TI in z around 1 m height with a more considerable difference occurring at $1c$, the gradient tends to flatten as the downstream distance increases. Figure 5.1.12(e) presents two considerable peaks of TI at $1c$ downstream distance, one close to the blade root that is slightly lower than 1 m height,

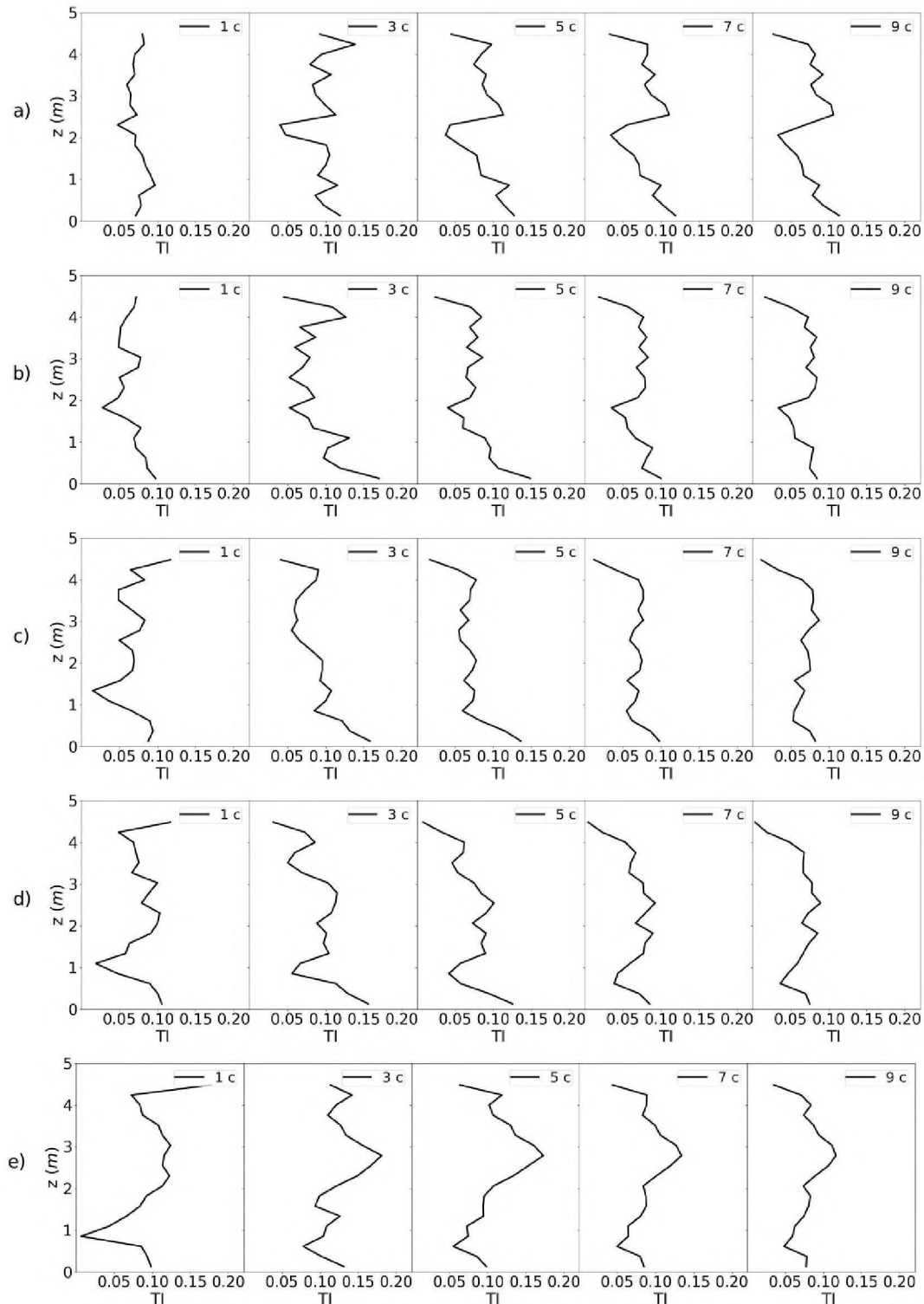
Figure 5.1.11 – Reynolds stress tensor components profiles downstream the wind blade turbine for different angles of attack



which presents the minimum value of TI close to 0. On the other hand, the second displays the maximum TI value close o 0.20 around the blade TI over 4 m.

It is essential to point out that the authors tried to plot the Figure 5.1.12(a) in a way to show all downstream distance chords in one for each angle of attack, similar pattern presented in Figure 5.1.8, but unfortunately, the display obtained was not clean and would show a confusing presentation. Because of that, the author decided to maintain the configuration presented above.

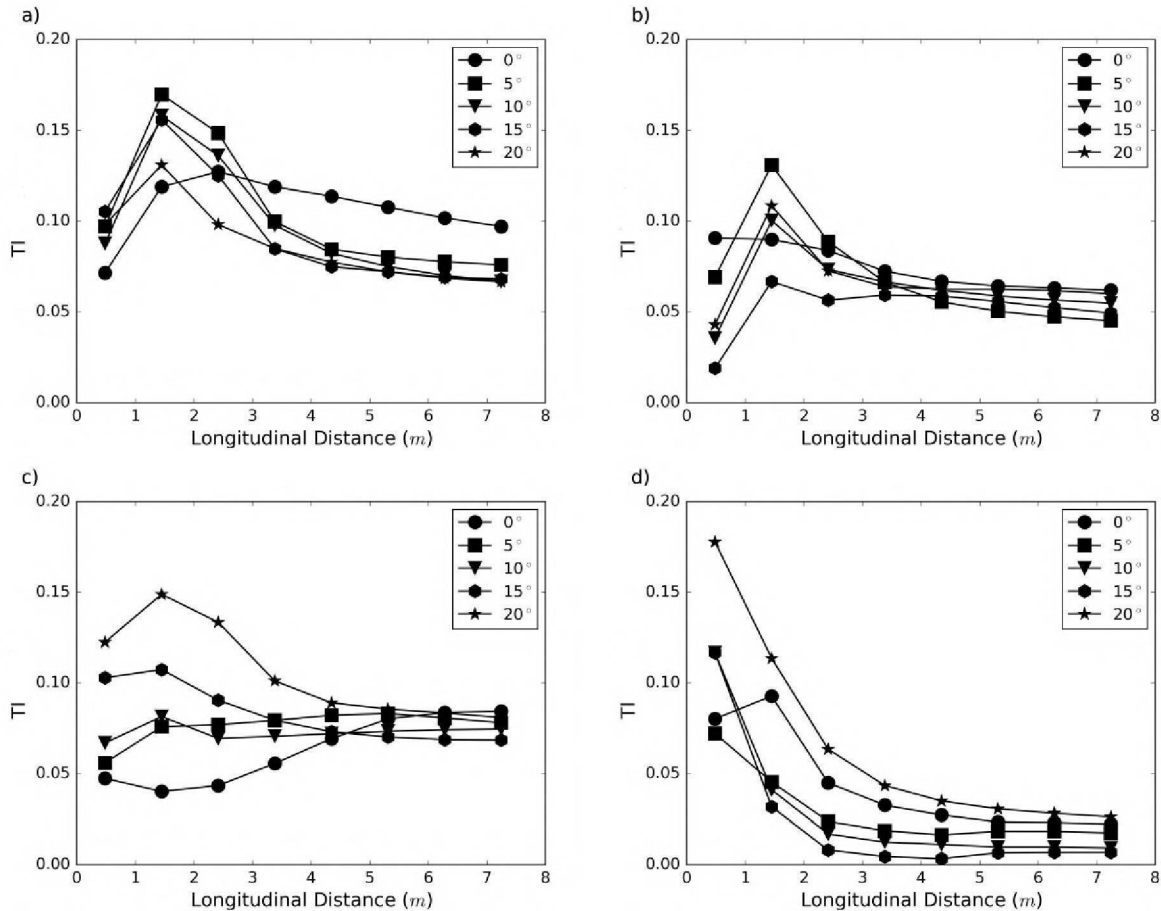
Figure 5.1.12 – Comparison of vertical profiles of the turbulence intensity (TI) for different angles of attack, a) 0° , b) 5° , c) 10° , d) 15° and e) 20°



From Figure 5.1.12, it is possible to observe that the minimum values of TI, at the downstream distance of $1c$, tend to decrease in terms of height location as the angle of attack increases. Therefore, peaks of TI that occurred close to the blade root may be caused by the transition from the root to the wind blade itself. Otherwise, peaks of TI around the half of the blade height may be an effect of the blade design when the angles of attack increase. Due to

that, it was decided to plot longitudinal analysis in z at 0.1, 1, 2.25, and 4.5 m for angles of attack ranging from 0° to 20° , by increments of 5° , presented in Figure 5.1.13.

Figure 5.1.13 – Comparison of Longitudinal profiles of the turbulence intensity (TI) for different angles of attack in z at a) 0.1, b) 1, c) 2.25 and d) 4.5 m height



For z close to 0 m height, Figure 5.1.13(a) restated the maximum value of TI above 0.15 found for 5° , 10° and 15° , which had been observed in Figures 5.1.12(b), 5.1.12(c) and 5.1.12(d), in the root of the blade at a downstream distance of $3c$. Figure 5.1.13(b) confirmed the presence of peaks that occurs in the transition from the blade root until the blade design, through the gradients observed from $1c$ to $3c$ downstream distance, also confirming the low values of TI, below 0.05, at $1c$ for angles from 10° to 20° . Meanwhile, close to half of the blade height, it can be observed in Figure 5.1.13(c) the low values of TI, around 0.05, for the 0° profile, which stated the negative gradient of TI as demonstrated before in Figure 5.1.12(a). Besides that, Figure 5.1.13(c) also presents high values of TI for 20° at the beginning of the profile, reaching 0.15 at the downstream distance of $3c$. Then, after the downstream distance of $5c$, all profiles tend to be flat. Therefore, Figure 5.1.13(c) confirms what had been inferred before about how the TI values increase as the angle of attack develops. In the blade tip, Figure 5.1.13(d) restates that the maximum value of TI reached close to 0.2 for the 20° at the downstream distance $1c$, which had been inferred in the Figure 5.1.13(e). Moreover, Figure 5.1.13(d) also showed a high decay that occurs before the profiles approach the downstream distance of $5c$. After that, the profiles tend to be flat for the rest of the downstream distances. This behavior might be due to low recirculations occurring at this height because of the laminar profile design of the blade at the tip.

Therefore, values of turbulence intensities greater than 0.15 or close to 0 are a concern in wind engineering because the power output is likely to drop as the turbulence intensity intensifies or even underestimate the power for low values of turbulence intensity.

Scenario 1 Remarks

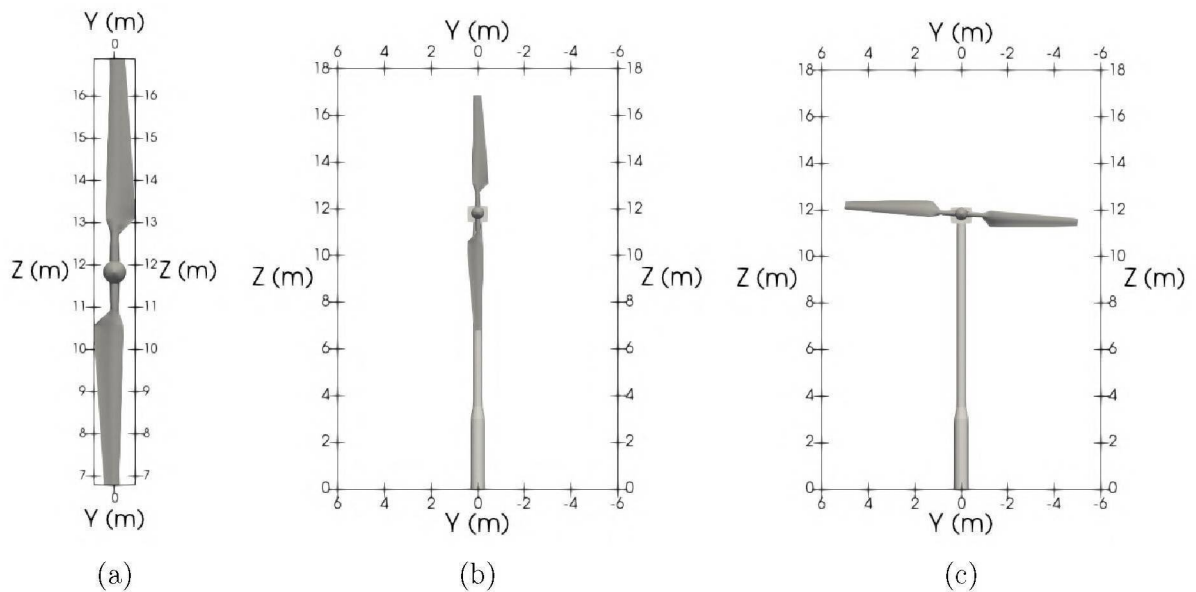
In conclusion for scenario 1, the downstream wake centerline velocity analysis for different angles showed high energy extraction nearest the blade wake. Besides that, there is a fast recovery for small angles of attack, while in higher angles, the recovery was a piece slower. Therefore, all the angles of attack finished up the recovery close to 70%, excepted for the 0° case that achieved 80% recovery. The drag and lift coefficient results showed satisfactory agreement compared to the experimental data from NREL. The drag coefficient presented an excellent agreement for all the angles ranges up to 35° . The relation C_l/C_d showed high ratios for small angles of attack, closer to the stalling angle. For the turbulence characteristics, the higher values of kinetic turbulence energy occur in the near wake, as expected, due to the high density of eddies occurring in this area. The energy dissipation mainly occurs between 1 to 2 m downstream of the wind turbine blade. From vertical (i.e. spanwise) profiles, the tip-vortex and other 3D phenomena become stronger with increasing angle of attack, resulting in a spanwise shift in the velocity deficit towards the hub as the angle of attack increases. From the vorticity analysis, it is concluded that when the blade is nearly aligned with the flow, the boundary layer holds attached, whereas the adverse pressure gradient caused by higher angles can lead to separation. The vorticity parameter is the criteria applied in this work for the adaptive mesh refinement, allowing the vortical structures to be accurately resolved with reasonable computational cost.

5.2 SCENARIO 2: NREL EXPERIMENTAL WIND TURBINE PHASE VI

This simulation scenario was based on an experimental study named NREL Phase VI presented in the work of Hand et al. (2001), Simms et al. (2001), which analyzed flow characteristics around a model-scale wind turbine. These authors developed a structural model and verification procedures for the wind experimental Phase VI of the National Renewable Energy Laboratory (NREL), based on a two-bladed wind turbine. In addition, the numerical studies of Mo et al. (2013b), Sedaghatizadeh et al. (2018) and Syed Ahmed Kabir and Ng (2019) were used for comparison with the obtained results, see chapter 2, section 2.3.3.

For the MFSim simulations, the geometry of the experimental wind turbine NREL Phase VI was designed in the CATIA[®] software and meshed in the ICEM[®] CFD framework. Figure 5.2.1 represents the main components of the developed wind turbine used in the experimental NREL Phase VI. Figure 5.2.1(a) shows the rotor containing the 2 blade design, Figure 5.2.1(b) depicts the unification of tower and rotor aligned, and Figure 5.2.1(c) illustrates an ortogonal representation of the rotor in relation to the tower.

Figure 5.2.1 – NREL experimental wind turbine structures: (a) rotor, (b) rotor and tower aligned, and (c) rotor ortogonal to the tower



The wind turbine mesh respect the same patterns applied to the blade in the previous section, although the number of cells of the lagrangian domain have increased to 451,900 triangular cells. Besides that, the eulerian computational domain corresponds to 128 *m* in the *x*-direction, 32 *m* in the *y*-direction and 24 *m* in the *z*-direction.

The simulations were performed with an adaptive mesh composed by 7 levels. The initial mesh arrangement is set up with 64 x 16 x 12 volumes for the coarser grid (base level) in the *xyz* directions using hexahedral uniform grid, obtaining an initial computation with approximately 900 thousand control volumes. From this initial configuration, a mesh refinement was implemented around the blades and tower. Figure 5.2.2 and 5.2.3 represent the computational grid of the eulerian mesh for the *xz*-plane and *yz*-plane, respectively.

Figure 5.2.2 – Lateral view of the eulerian mesh displacement

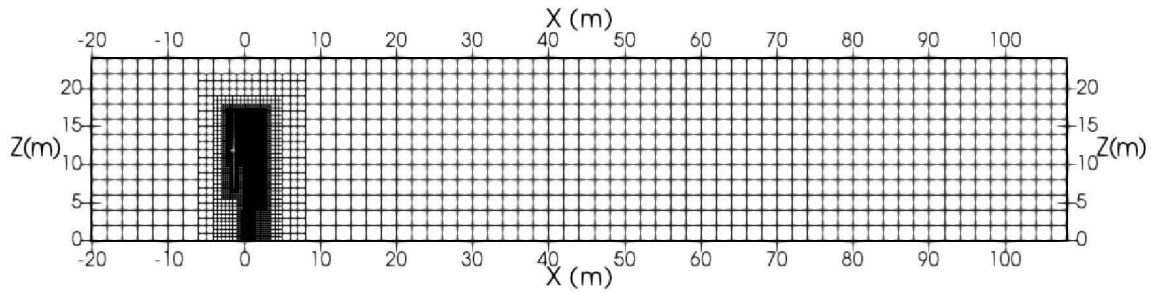
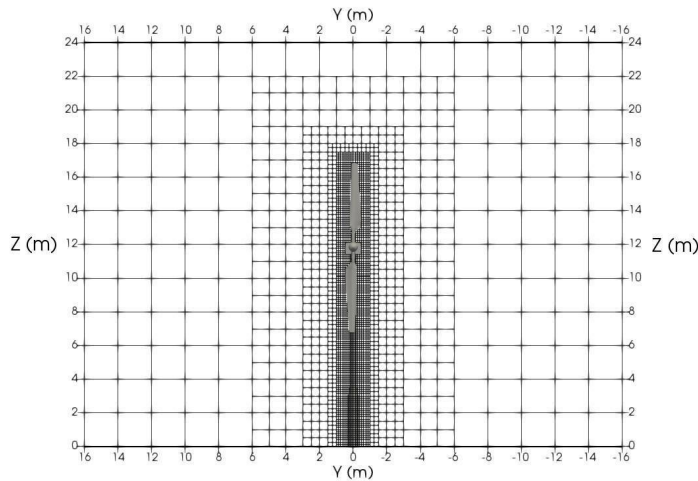


Figure 5.2.3 – Front view of the eulerian mesh displacement



The inflow wind velocity condition was $u=10$, $v=0$ and $w=0$ m/s, in the MFSim code, then characterizing a Dirichlet type of boundary condition. The boundary conditions for the lateral planes (xz -planes) were characterized as symmetry, this condition was also applied in the top plane (xy -plane). The bottom plane (xy -plane) sets a no-slip condition in order to represent the ground where the turbine was placed in the wind tunnel. A Neumann boundary condition was used for pressure matters, meanwhile an advective condition was employed at the outflow condition, which is time varying to allow for vortical structures to cleanly exit the computational domain without reflecting back into the domain or disturbing the solution in the inner domain. In these simulations, the fluid properties were $\rho=1.225$ kg/m³, $\mu=0.0000182$ kg/(m s) . It was adopted variable numerical time steps in the range of 10^{-4} to 10^{-5} s, maintained a CFL criteria of 0.25. The final simulation time was 20 s, period along which the flow presented steady state conditions. With an Intel Xeon E5650 2.67GHz 24-core machine utilizing approximately 11 GB RAM, the simulations required approximately 144 hours. All statistics were calculated based on the last 10s of simulation, period along which the flow presented approximately steady state conditions.

5.2.1 Probes Location

Figure 5.2.4 represents the probes installed in the numerical domain to captured the results in order to calculate the statistics of the variables of interest. Such probes were positioned from $1D$ to $10D$ downstream distance from the NREL Phase VI wind turbine in the longitudinal

direction. The discrete annular points used to extract an average of the velocity and pressure components across the rotor plane are illustrated in Figure 5.2.5, where R is the radius of the NREL blade which is equal to 5.028 m . The innermost probe is related to the blade root, while the outermost point corresponds to the tip of the blade.

Figure 5.2.4 – Installed probes in the Scenario 2

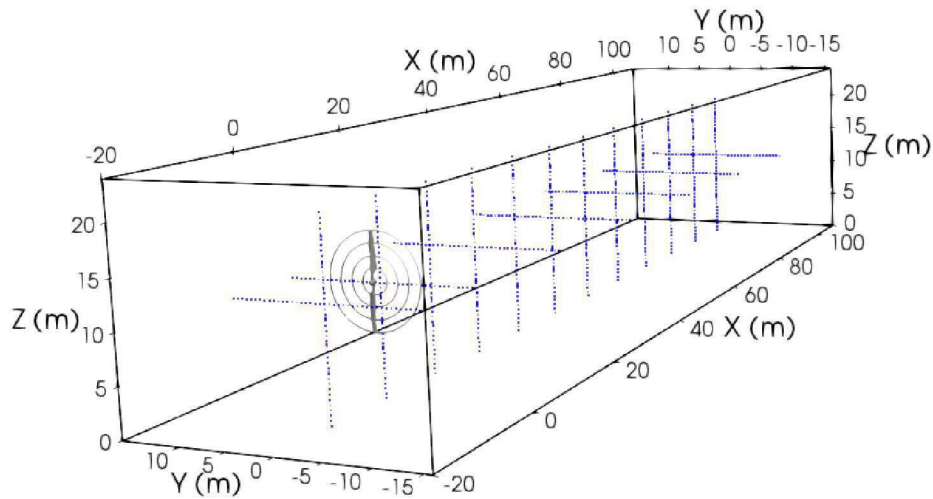


Figure 5.2.5 – Annular displacement of the probes for longitudinal analysis

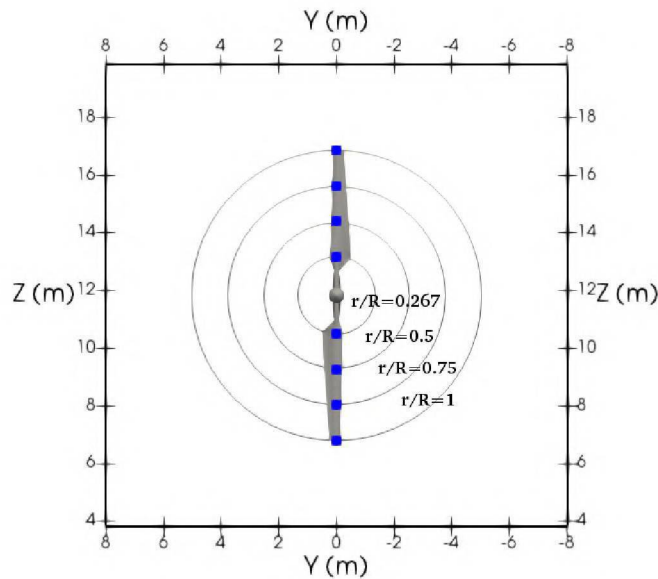


Figure 5.2.6 represents the cross-sectional profiles to capture the wake diameter. There was an implementation of 41 probes for each chosen section varying from -10 m to 10 m in the y -direction. The chosen sections are $1D$ upstream, and $2D$, $4D$, $6D$, $8D$ and $10D$ downstream from the wind turbine.

Additionally, seeking to visualize the wake behavior downstream from the turbine, vertical profiles were established before and after the wind turbine represented by 40 probes, from 0 to 20 m , for each section, where the sections begin at 1 D upstream and end at 10 D downstream of the wind turbine as represented in Figure 5.2.7.

Figure 5.2.6 – Probes displacement for the cross-section analysis of the wake diameter

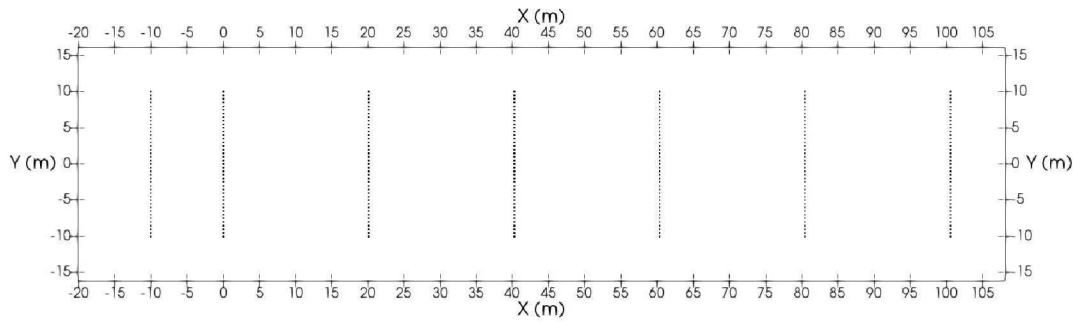
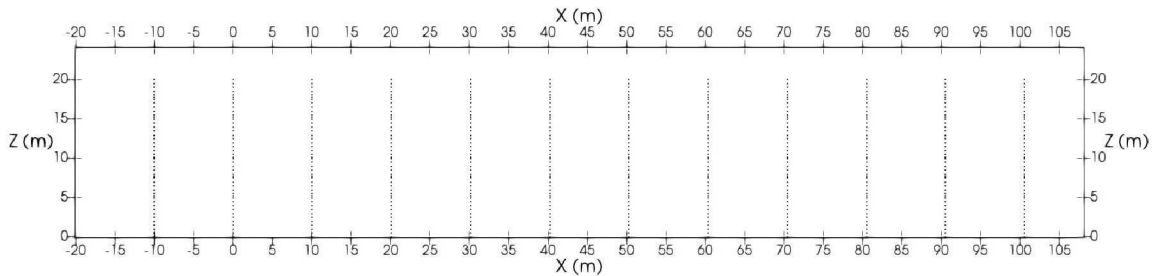


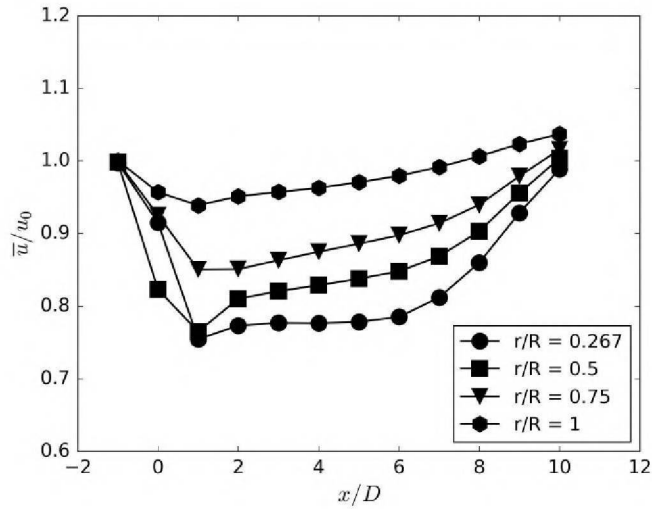
Figure 5.2.7 – Probes displacement for the analysis of vertical profiles



5.2.2 Longitudinal Profiles of Time-average Streamwise Velocity

The streamwise component of time-average velocity was analyzed in a region downstream from the wind turbine, focusing on the longitudinal wind velocity recovery for selected locations behind the chosen annular segments. Figure 5.2.8 shows comparisons of velocity recovery for ratios r/R in the range of 0.267 (close to the center) to 1 (in the blade tip). It is possible to observe high velocity deficits in the region immediately downstream from the wind turbine. These high extractions of energy in the near wake of the wind turbine indicates that the flow passing through the rotor area loses a fraction of its mean kinetic energy. Looking at the positions further away from the root and, consequently, closer to the tip, the velocity recovery increases immediately downstream of the wind turbine. This pattern is followed for the entire downstream distances.

It can be seen that the largest difference of velocity occurs for $r/R = 0.267$ and $r/R = 0.5$, where the velocity recovery reaches a minimum value range around 0.75, which is 75% of the inflow wind velocity. This occurred right after the turbine close to a longitudinal distance

Figure 5.2.8 – Comparisons of different ratios of r/R for longitudinal velocity recovery profiles

of 10 m . The longitudinal profile for $r/R = 0.75$ reached lowest velocities right above 0.85 in the same location as the previous ones, meanwhile, $r/R = 1$ profile showed velocity recovery a little bit lower than 95% of its inflow condition in the near wake.

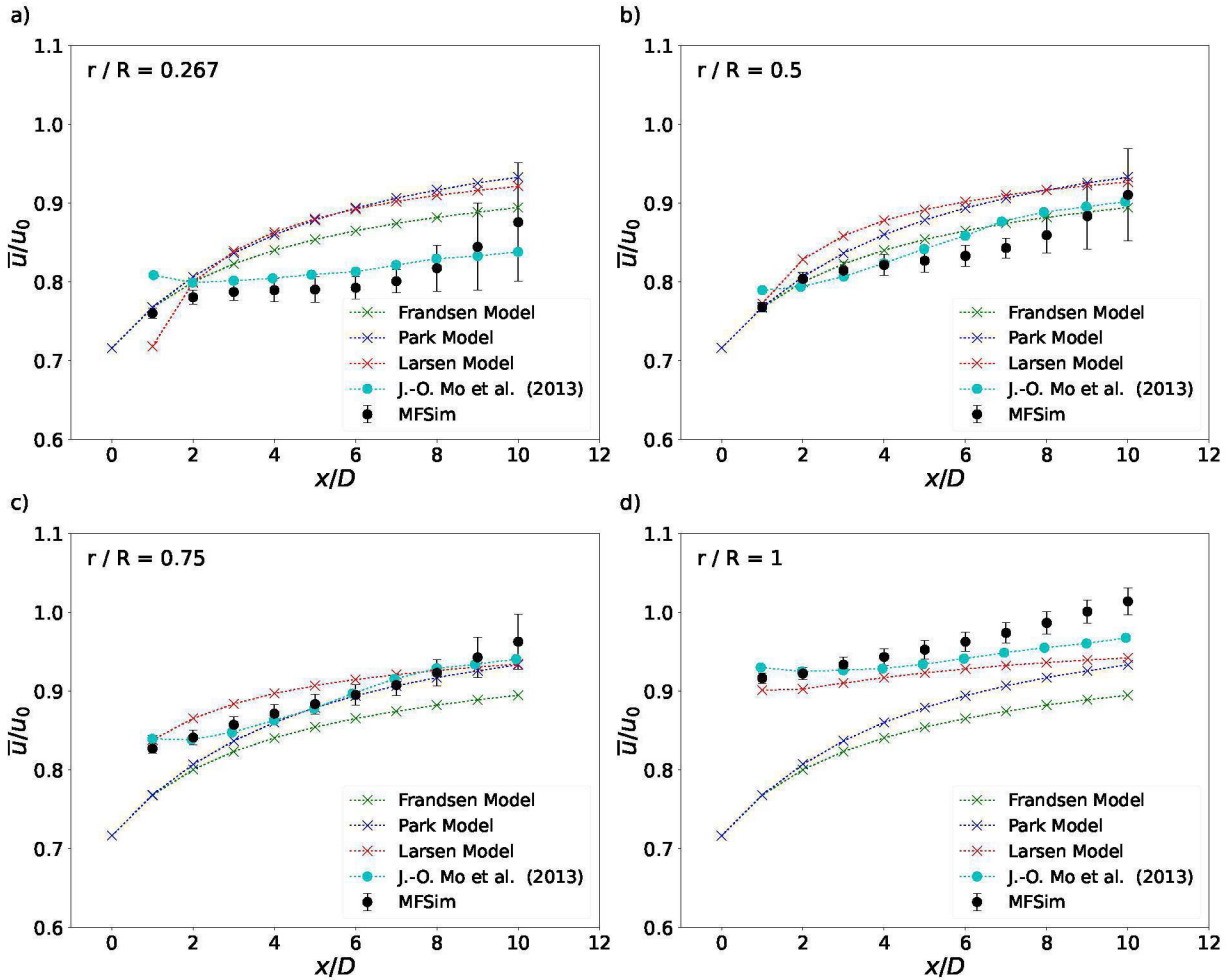
It is interesting to notice that the profile of $r/R = 0.267$ presented an apparent velocity recovery stagnation in 5 downstream distances, from 20 to 60 m , which could be attributed to its proximity to the blade root. After that, there is a steep increase in the velocity recovery reaching over 90% of the inflow wind velocity by the end of the downstream distance simulation. Besides that, the other three profiles appear to have the same increasing pattern for the velocity recovery, where $r/R = 0.5$ and $r/R = 0.75$ had achieved a velocity recovery of around 95% of the inflow wind velocity. Meanwhile, the 100% velocity recovery for the $r/R = 1$ occurred at 80 m downstream distance of the wind turbine.

The streamwise component of time-average velocity was analyzed downstream from the wind turbine, focusing on the longitudinal wind velocity recovery for selected locations behind the chosen annular segments.

The longitudinal velocity recovery for selected annular sections obtained in the present work was compared to the predictions of largely used simplified wake models Park, Frandsen, and Larsen, and also compared with the results from the work of (MO et al., 2013b), the results are shown in Fig. 5.2.9. Four different annular sections of the blade are presented for ratios r/R in the range of 0.267 (close to the center) to 1 (in the blade tip). The normalized time-average velocities (\bar{u}/u_0) with standard deviation are plotted against the normalized longitudinal distance (x/D). Fig. 5.2.9 is subdivided into four sub-figures that present the comparisons between the present work and the references for each section relative to each sub-figure. Due to the simplifications of the wake models, Park and Frandsen models present downstream distance results from the blade while the Larsen model starts from a downstream distance of $1D$.

It is observed that the present work presents excellent agreement concerning the results from (MO et al., 2013b) for all four sections of the wind turbine blade. The best agreement is

Figure 5.2.9 – Longitudinal velocity recovery profiles compared to simplified wake models by ratio of r/R



presented at the section in $3/4$ of the blade, Fig. 5.2.9(c), represented by the profile of $r/R=0.75$, where the lowest value around 0.85, occurred at the wind turbine section ($x/D=0$), and the highest value of \bar{u}/\bar{u}_0 close to 0.9 occurred in the far wake, at $x/D=9$. On the other hand, the lowest agreement came from the far wake of the tip blade profile, $r/R=1$ as shown in Fig. 5.2.9(d), where the present work results showed a higher recovery velocity than (MO et al., 2013b) results, this can be seen from 7 to 10 x/D , where the last section showed the MFSim results close to 1 of recovery velocity while (MO et al., 2013b) results reached slightly over 0.9 at the same downstream distance. Moreover, in the mid-section of the wake, around x/D from 4 to 6, the MFSim profiles of $r/R=0.5$, Fig. 5.2.9(b), and $r/R=0.267$, Fig. 5.2.9(a), presented slightly lower recovery velocities than (MO et al., 2013b) at those sections.

In terms of the comparison to the simplified wake models, Fig. 5.2.9(a) illustrating the $r/R = 0.267$ section, a similar correlation of Park, Frandsen and MFSim results can be observed at the downstream distance of $1D$ and $2D$, where wake models have reached differences from the the present work lower than 0.5% and 4%, respectively. Larsen model also presented great correlation at $2D$ with a 2% difference. Meanwhile, for for an annular section of $r/R = 0.5$, Fig. 5.2.9(b) shows that the best correlation occurred for the Frandsen profile, highlighted by sections $1D$ to $4D$, $9D$, and $10D$ downstream distances. Differences lower than 1% between

MFSim and analytical models were found over 1, 2, 3, 9 and 10D Frandsen model, 1 and 2D for Park model, and also at 1D for Larsen model. In addition, the present work results from downstream distances of 9D and 10D presented to have both Park and Larsen models inside the error bar range of the simulation.

Fig. 5.2.9(c) depicts the downstream velocity recovery in the 3/4 of the blade radius, at $r/R = 0.75$ annular section. It was best represented by the Larsen model among the simplified models, presenting values no higher than a 5% difference from the present work results. Park model also displayed great results in the transition from near wake to far wake, from downstream distances of 4D to 7D, where the Park model differences to MFSim reached lower than 1%. However, in the far wake, the MFSim results increased up the error bar velocity recovery quickly, and both Park and Larsen models well correlate with the present work results from 8D to 10D. In this section the Frandsen model underestimates all the sections from MFSim results. At the tip of the blade section, at $r/R = 1$, presented by Fig. 5.2.9(d) it can be observed that Park and Frandsen models highly underestimated the results from the present work simulation for the entire longitudinal profile. On the other hand, Larsen model showed the best agreement among simplified wake models compared to the MFSim results, presenting excellent correlation values that are lower than 5% from downstream distances of 1D to 6D.

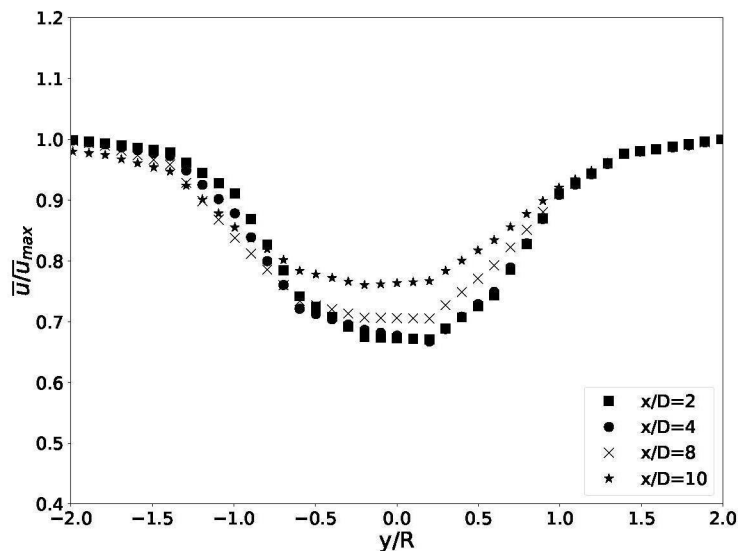
5.2.3 Cross-sections Profiles of Time-average Streamwise Velocity

Comparisons of the velocity recovery over the wake cross-section have been analyzed for four cross-section locations, corresponding to downstream distances of 2D, 4D, 8D, and 10D, which are represented by Figure 5.2.10. For all cross-sections, 41 points have been chosen and separated in 20 points on each side of the centerline. The cross-section points were equally spaced, with 0.5 m between adjacent points. The total represented cross-section width corresponds to 20 m. Besides that, the analysis considers the xy plane, where the height is at the hub of the wind turbine. The wake diameter calculation is based on the velocity gradient between the low-velocity area in the centerline of the wake and the freestream wind velocity, which is a good representation for the wake boundary. The wake diameter can be detected from positions where the velocity profile reaches a determined threshold, as applied in this work based on Barthelmie, Frandsen and Réthoré (2006), or as an outcome of the fitting method, where some helpful profile shape has to be known. Based on an average velocity profile, the wake diameter would be great for similar studies to decide which variant of any arrangement generates a smaller wake.

Figure 5.2.10 demonstrates that the velocity recovery is lower in the near wake when compared to the far wake for the wind turbine downstream distances. The velocities represented for the $x/D = 2$ and $x/D = 4$ profiles reached around 70% of the inflow velocity in a region around the wake centerline, whereas the $x/D = 8$ profile showed a velocity recovery close to 78% of the inflow velocity, and the $x/D = 10$ profile presented a recovery slightly over the 85% of the initial velocity.

Further away from the root and closer to the tip, it can be seen that velocity recovery increases a lot close to the rotor diameter around -5 m and 5 m of the cross-section distance, where the velocities presented values in a range of 0.95 to 1. Therefore, the variation from the

Figure 5.2.10 – Cross-section wake profiles at the hub height over downstream distances



velocity recoveries from the centerline to the blade tip was 25%, 24%, 22%, and 17.5% for cross-section profiles of $x/D = 2$, $x/D = 4$, $x/D = 8$ and $x/D = 10$, respectively. In terms of wake width, the profiles in Figure 5.2.10 tend to slow the differences around the neighbors points at -7 m and 7 m , which produces a wake width of 14 m for all profiles in the downstream wake of the wind turbine, where the velocity recovery reaches values around 1.05.

Cross-sections of simplified wake models

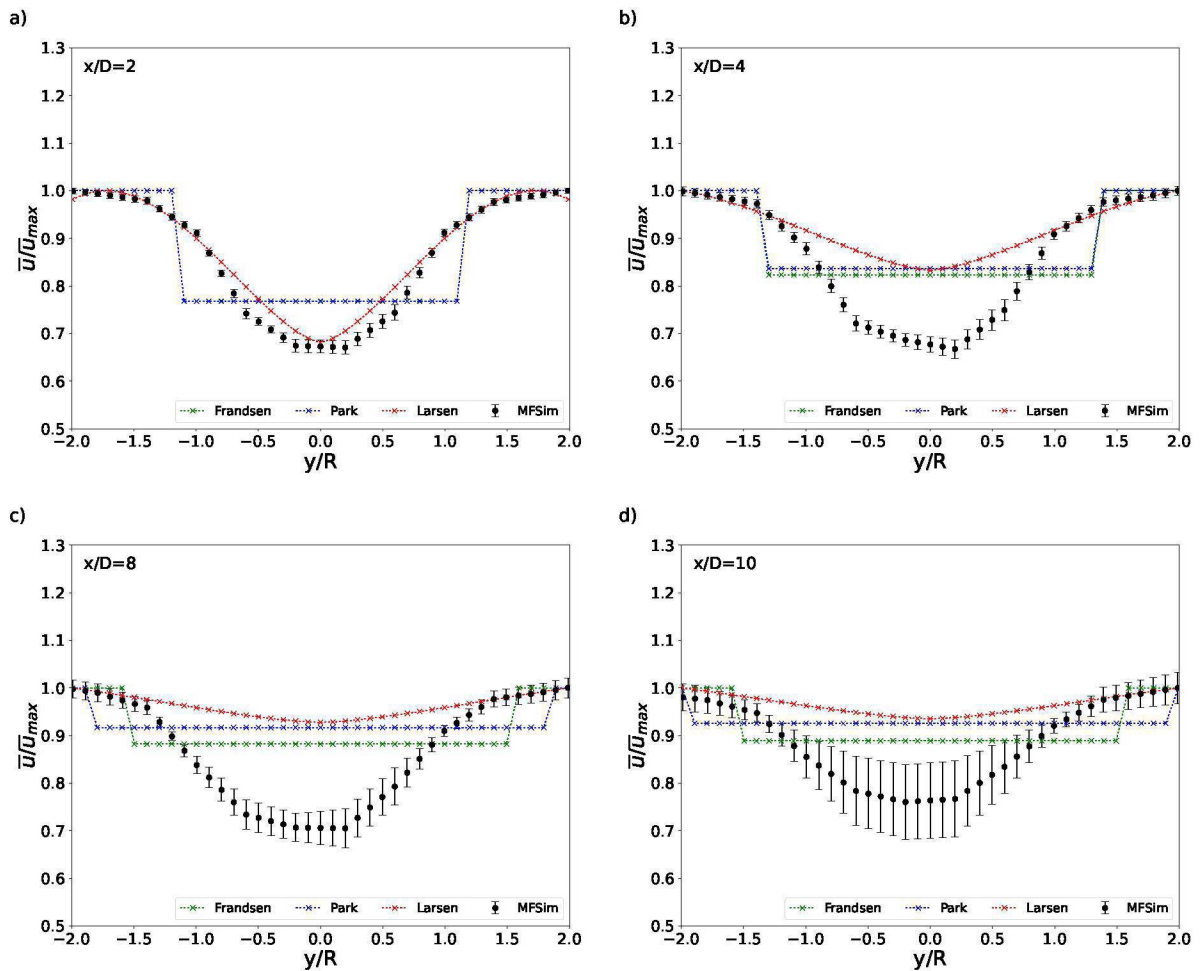
To compare the results obtained from MFSim to the simplified wake models results, the wake expansion is presented in Figure 5.2.11 for four different cross-sections located at $x/D = 2$, $x/D = 4$, $x/D = 8$, and $x/D = 10$.

Figure 5.2.11(a) shows the near wake cross-section profile at $x/D = 2$ for results from MFSim code and the simplified wake models. Despite the simplicity of Frandsen and Park models when compared to Larsen model, all three models reached their lowest velocity recovery close to 0.8 in the centerline of the wake expansion downstream of the wind turbine. The lowest velocity recovery for the MFSim code also occurred at the wake centerline with a value of around 70% of the inflow velocity. Therefore, the difference between simplified models compared to the MFSim is around 13% at the cross-section distance close to 0 m . Larsen model demonstrated a higher estimation of the wake diameter reaching close to 16 m , whereas MFSim code presented to have 14 m , a difference of 14% between the results. Meanwhile, the wake diameter for Frandsen and Park models occurred to be 12 m , which also brings a difference around 14% in relation to the MFSim results.

The downstream $x/D = 4$ cross-section profile presenting the simplified wake models compared to the MFSim results is represented by Figure 5.2.11(b). Park model demonstrated a slightly larger wake diameter, 14 m , than the 13 m presented by Frandsen model. Larsen model showed the highest wake diameter, reaching almost 18 m . As seen before, the wake diameter of the MFSim code is about to 14 m . These values represent a difference close to 0%, 7%,

and 28.5% in terms of the wake diameter for the Park, Frandsen, and Larsen models compared to MFSim results, respectively. Although presenting the lower wake diameter among the wake models, Frandsen model has shown the lowest velocity recovery among them, reaching 84% of the inflow velocity at the wake centerline. Meanwhile, Park and Larsen models demonstrated to have velocity recovery around 86% of the inflow velocity. For the MFSim results, the lowest velocity recovery occurred to be close to 7.2 m/s, which represents a difference of 18%, 20.5%, and 22.5% from Frandsen, Park, and Larsen models, respectively.

Figure 5.2.11 – Cross-section wake profiles compared with simplified wake models for the selected downstream distances



Representing the first cross-section profile in the far wake, Figure 5.2.11(c) illustrates the downstream distance of $x/D = 8$ containing the velocity recovery profiles for the kinetic wake models and MFSim. It can be seen that the velocity recovery for the MFSim profile reached its lowest value around 0.78 at the centerline wake region, which is close to a 10% difference from the value that has been previously found in the near wake region. The velocity recovery for the Frandsen model reached close to 88% of the inflow velocity, while both Park and Larsen models presented similar value again, around 91% of the inflow velocity. It should be noted that the lowest wake diameter among the results occurred to be 14 m for the MFSim profile, followed by Frandsen model with a wake diameter of 15 m. The wake diameter produced by Park model profile has increased from near to far wake, reaching a value of 18 m. Once again, Larsen model

showed the highest wake diameter value of around 20 m at the downstream cross-section of $x/D = 8$. However, there are velocity recovery values in a range from the 3/4 of the blade to the blade tip, where the differences between the MFSim and simplified wake models are low, reaching values around 1% to 2% deviation.

Figure 5.2.11(d) shows the far wake cross-section profiles at $x/D = 10$ for the simplified wake models and the MFSim results. In terms of velocity recovery, from the MFSim results is possible to observe that the lowest velocity was close to 0.85 that occurred at the wake centerline. Frandsen model presented its lowest velocity recovery around 0.89, while Larsen and Park models reached a value close to 0.93. It should be noted that Park model has presented a straight line with a unique value for velocity recovery, which is due to its simplification and the linear wake expansion rate that the model produces. Therefore, its wake diameter turned larger than 20 m that has been specified as the range of the wake analysis. Besides that, Larsen model seems to present a wake diameter that almost exceeded the range of analysis, displaying a wake diameter close to 20 m . On the other hand, Frandsen model demonstrated a wake diameter of 16 m , while the MFSim presented a wake diameter of around 14 m , as seen before. However, all three models showed velocity recovery results where the variation, when compared to MFSim, occurred to be lower than 1%, occurring in a range of ± 2 to ± 3 m of the cross-section distance.

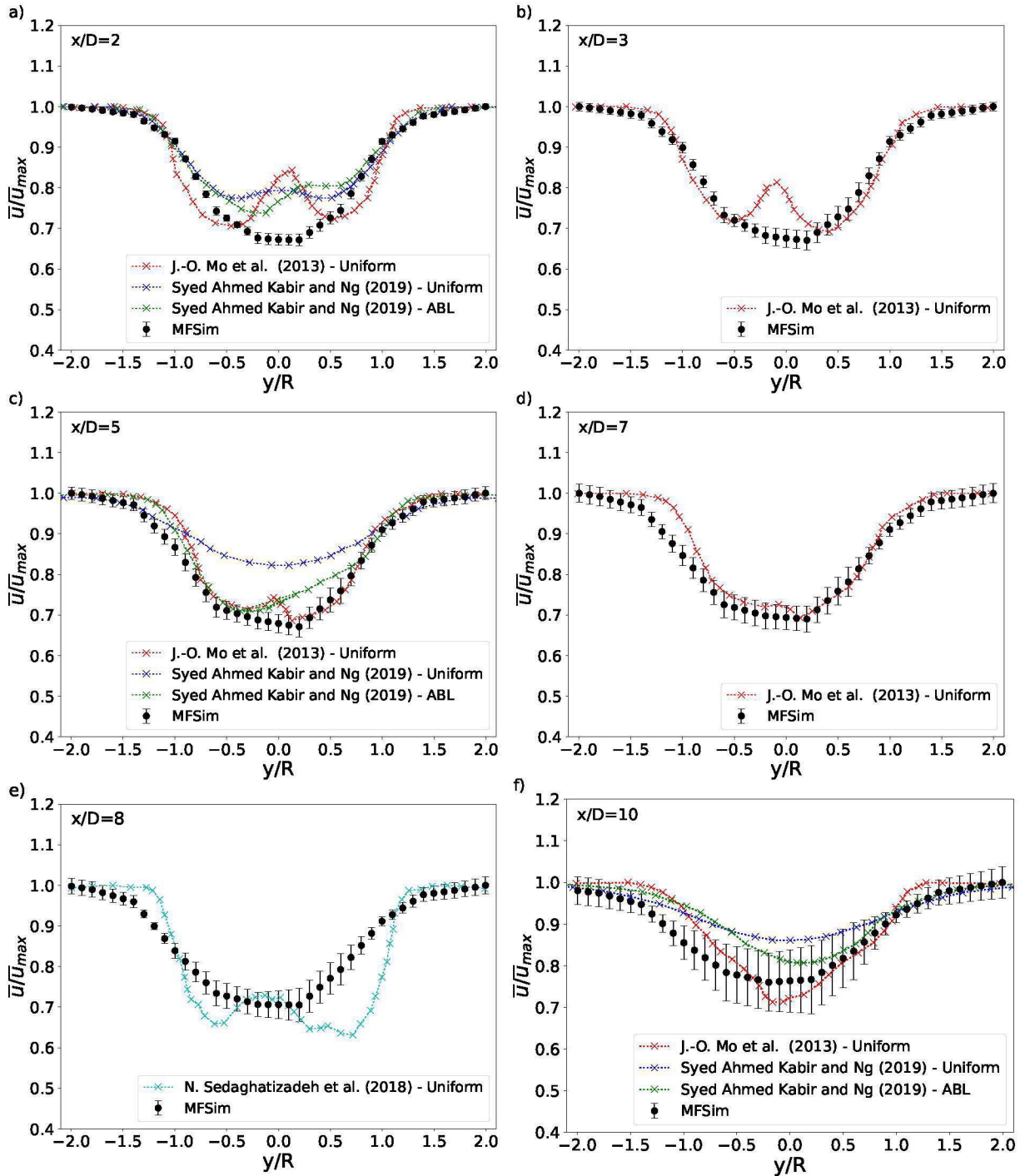
Cross-sections of benchmark CFD simulations

Fig. 5.2.12 presents the comparison between the MFSim results and three article results, extracted from (MO et al., 2013b), (SEDAGHATIZADEH et al., 2018) and (Syed Ahmed Kabir; NG, 2019). Those comparisons are performed for the time-averaged streamwise velocity recovery considering six different downstream cross-sections, located at x/D equals 2, 3, 5, 7, 8, and 10. On the abscissa axis, it is placed normalized velocity \bar{u}/\bar{u}_{max} with standard deviation plotted against the transversal value y normalized by the radius of the blade R . It is important to point out that not every cross-section has all results from all the references that have been analyzed.

Fig. 5.2.12 (a) shows the velocity recovery for the cross-section of $x/D=2$. All the results demonstrate the same recovery pattern up to approximately the centerline or close to the rotor. The (Syed Ahmed Kabir; NG, 2019) results show similar profile behavior as the MFSim except by the region between $-0.5 < y/R < 0.5$, where the present work presents a higher deficit in velocity recovery that goes below 0.7 at $y/R = 0$ while (Syed Ahmed Kabir; NG, 2019) results show values around 0.8 at the same point. Besides that, (MO et al., 2013b) presents a velocity recovery peak in the centerline in relation to the other profiles, reaching a normalized velocity close to 0.85 at $y/R=0$. Behavior that can also be seen in Fig. 5.2.12 (b), which shows velocity recovery normalized for the $x/D=3$ cross-section. Both simulations showed excellent agreement up the centerline of the wake, where the results by (MO et al., 2013b) had a peak of velocity recovery of \bar{u}/\bar{u}_{max} around 0.85.

The next downstream section to be evaluated is $x/D=5$, depicted in Fig. 5.2.12 (c). In this section, MFSim results are similar to (MO et al., 2013b), and (Syed Ahmed Kabir; NG, 2019) ABL profile results, where most of the results are inside MFSim error bars. Differences among those three profiles occur between $-1.3 < y/R < -1$, also around the centerline ($y/R=0$)

Figure 5.2.12 – Cross-section wake profiles compared with CFD simulations for the selected downstream distances



only for (MO et al., 2013b), and between $-0.4 < y/R < 0$ in case of (Syed Ahmed Kabir; NG, 2019) ABL profile. As can be seen, most of the profiles presented the lowest velocity recovery approaching \bar{u}/\bar{u}_{max} of 0.7 at the centerline, excepted by the uniform result of the (Syed Ahmed Kabir; NG, 2019), which showed higher recovery velocity, close to $0.85 \bar{u}/\bar{u}_{max}$, around the rotor area than the others.

Further downstream, Fig. 5.2.12 (d) shows comparison of the present work profile and (MO et al., 2013b) for $x/D=7$. Both profiles are very similar, including most of the swept area,

where both results presented a \bar{u}/\bar{u}_{max} close to 0.7 in the centerline region. The only exception occurred between $-0.9 < y/R < -1.3$ region, where (MO et al., 2013b) results overestimated the MFSim results. One diameter further downstream, at $x/D=8$, Fig. 5.2.12 (e) presents the results of (SEDAGHATIZADEH et al., 2018) for a uniform inflow condition, demonstrating results inside MFSim error bars in the wake centerline region close to the rotor, around $-0.3 < y/R < 0.3$. However, in the region closer to the blade's tip, it shows two velocity deficit gaps compared to the present work. This can result from prolonged turbulent structures until the far wake, and slower dissipation occurs.

The last cross-section presented in this analysis corresponds to the far wake, equivalent to $x/D=10$ represented by Fig. 5.2.12 (f), shows the results of the present work compared with the results of the works of (MO et al., 2013b) and (Syed Ahmed Kabir; NG, 2019). As can be seen, the MFSim results show high error bar values around the swept area, which contributes to (MO et al., 2013b) and (Syed Ahmed Kabir; NG, 2019) ABL profiles to be represented by the present work results in most of the profile. Although, the (MO et al., 2013b) results still produce a better correlation over the MFSim profile. Besides that, the highest velocity recovery on the centerline is \bar{u}/\bar{u}_{max} slightly below 0.9, representing the uniform profile of (Syed Ahmed Kabir; NG, 2019), while (MO et al., 2013b) profile had the lowest velocity recovery slightly above 0.7.

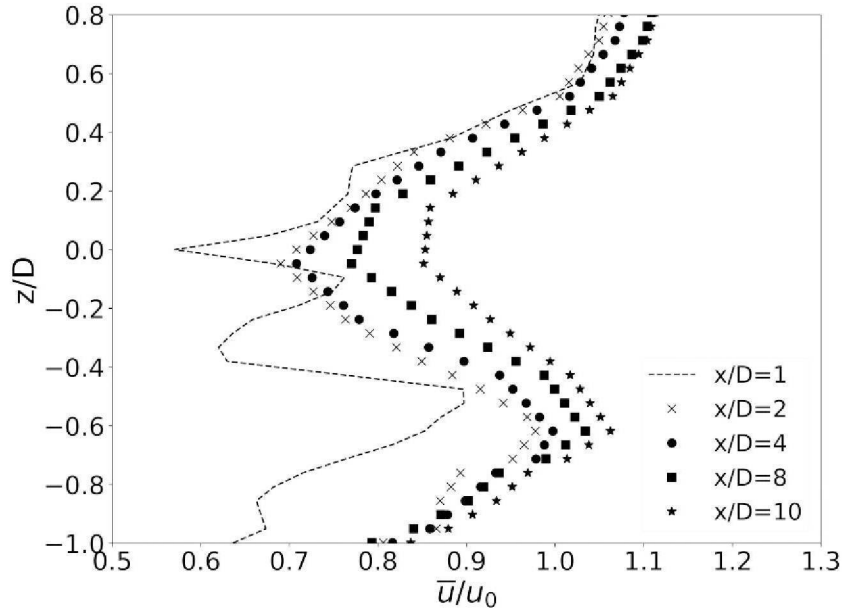
5.2.4 Vertical Profiles of Time-average Streamwise Velocity

The behavior of the streamwise mean velocity recovery is considered for vertical profiles along the wake downstream distance. Figure 5.2.13 shows five different vertical profiles from $x/D = 1$ to $x/D = 10$ downstream distance, representing the wind velocity profile before and after the wind turbine. The analysis considers the xz plane, where the centerline is taken in place, which is the line of the tower ($y = 0$). On the abscissa axis, it is placed the height z normalized by the rotor diameter D plotted against the normalized velocity \bar{u}/u_0 , where $z/D=0$ is the hub height.

In Figure 5.2.13, It can be seen that downstream distance of $1D$, which represents the near wake behind the wind turbine, is a region with large momentum extraction from the wind turbine, where a high level of turbulence production can be expected at the three peaks with a high-velocity gradient. One of those peaks depicts the lowest velocity recovery that found to be just lower than $0.6 \bar{u}/u_0$ close to the hub height ($z/D=0$). On the other hand, the highest velocity recovery occurred at the top plane of the simulation with wind velocities over $1 \bar{u}/u_0$, representing the no wake effect of the wind turbine at this region, which from a vertical height of $0.6 z/D$, the profile tended to be linear once again. Besides that, there is one more section, where the velocity recovery showed an increased development reaching close to 90% of the inflow velocity, this region is close to the height of the blade tip around $-0.5 z/D$. Below that, the tower shadow affects the velocity recovery allied with the wall effect of the ground.

For vertical mean velocity profile located at $x/D = 2$, it should be noted that the profile does not have a W shape anymore in comparison with the previous section. Instead of that, there is a V shape that represents the area covered by the rotor, where the lowest velocity recovery value is slightly lower than $0.7 \bar{u}/u_0$ at z/D around -0.05 that is close to the hub height. Once

Figure 5.2.13 – Vertical wind velocity profiles over downstream distance normalized by rotor diameters



again, there is a high-velocity deficit around the ground level due to the boundary layer effect, where the velocity reached almost $0.8 \bar{u}/u_0$. On the other hand, the highest velocity value close to $1.05 \bar{u}/u_0$ occurred around the top plane again, where the freestream wind velocity profile takes place. The vertical velocity recovery profile at a downstream distance of $4D$ is pretty similar to the previous one. Although, it is possible to observe a little bit less influence of the tower shadow at this downstream distance, where the velocity recovery increases almost linearly from ground height to the area close to the blade tip.

In the far wake for the downstream distances of $8D$ and $10D$, respectively, it is possible to observe that both figures have similar S shape profiles, and more exclusively in the rotor area, both of them demonstrated a U shape instead of V shape as the previous Figures. For $8D$ profile, the lowest velocity recovery value was slightly lower than 80% of the inflow velocity, occurring close to the hub height and ground level. Meanwhile, the highest velocity deficit for $10D$ profile occurred at the ground level due to the boundary layer effect, reaching a value close to $0.85 \bar{u}/u_0$, whereas, the velocity recovery around the hub height reached values of 85% of the inflow velocity. Besides that, both downstream distance profiles have presented the highest values of velocity, just over $1.1 \bar{u}/u_0$, close to the top plane at $z/D=0.8$. There is also a peak of velocity recovery in both profiles that also occurred at a vertical height of $-0.6 z/D$., where the velocity reached values around \bar{u}/u_0 of 1.05 to 1.075 for the $8D$ and $10D$ profiles, respectively.

In order to compare the vertical profile from MFSim, Fig. 5.2.14 shows six different vertical profiles with standard deviation from $x/D = 1$ to $x/D = 10$ downstream distance, representing the wind velocity comparisons with results from the work of Mo et al. (2013b), Sedaghatizadeh et al. (2018), and Syed Ahmed Kabir and Ng (2019). The analysis considers the xz plane, where the centerline is taken in place, which is the line of the tower ($y = 0$). The produced results depict the velocity deficit due to the kinetic energy extraction of the wind turbine, followed by the subsequent recovery in the downstream wake region.

Figure 5.2.14 – Vertical wake profiles compared with CFD simulations for the selected downstream distances

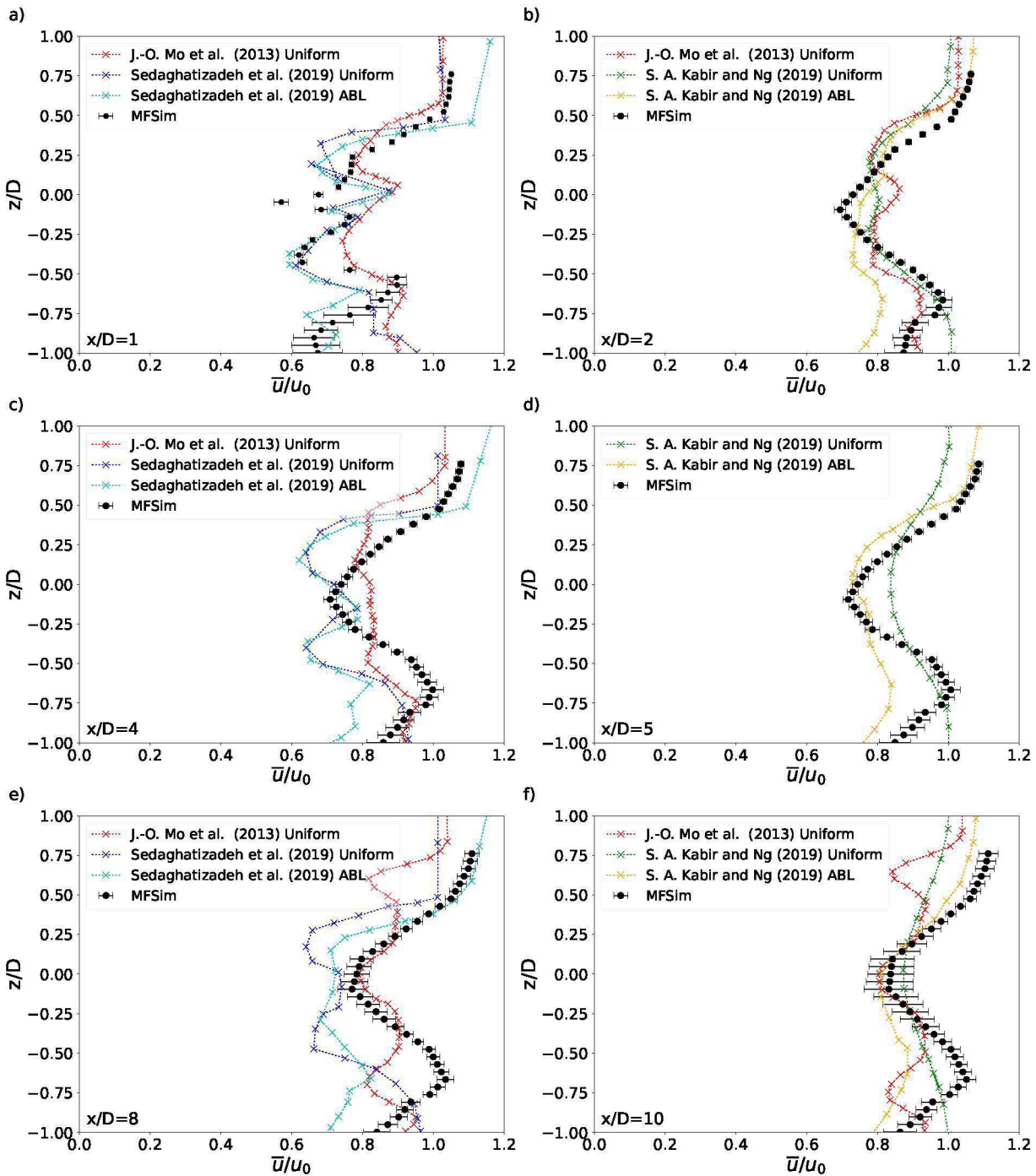


Fig. 5.2.14(a) shows the vertical velocity profile for the downstream distance of $1D$, which represents the near wake right behind the wind turbine. Although the simulations were carried out with a uniform boundary condition in the inlet, the wall condition and tower effect caused the results close to the ground to have similar values with the work of (Syed Ahmed Kabir; NG, 2019) using ABL condition. Meanwhile, both uniform profiles from (Syed Ahmed Kabir; NG, 2019) and (MO et al., 2013b) did not show much roughness or tower shadow in the region of z/D between -1 and -0.75 . In the z/D region from -0.5 to -0.1 near the hub height, the present work values corresponded very well with ABL and uniform profiles of (Syed Ahmed

Kabir; NG, 2019).

Moreover, similar results were also obtained by MFSim, from section z/D close to 0.2 to 0.75, compared to the work of (MO et al., 2013b) in this region. The most significant difference occurred at the height of the hub height, where the values of MFSim presented a slower velocity recovery than the other works, which can be explained by the influence of the nacelle design, which is more extended in the present work than others, thus causing a more significant deficit in velocity in the first section downstream of the turbine.

Fig. 5.2.14(b) shows the vertical mean velocity profile for the next downstream distance section, located at $x/D = 2$. In general, all the four profiles present similar values except for the region close to the ground, where (Syed Ahmed Kabir; NG, 2019) ABL profile showed lower velocity recovery (z/D from -1 to approximately -0.6) with most of the \bar{u}/u_0 values close to 0.8. On the other hand, the higher similarity between the present work and (MO et al., 2013b) results occurred at this region, where both profiles presented values of \bar{u}/u_0 in the range of 0.85 to 0.9. From z/D of -0.75 to -0.20, the uniform profile (Syed Ahmed Kabir; NG, 2019) demonstrated excellent results compared to MFSim values.

Once again, the present work results presented lower velocity recovery close to the hub height with a value close to 0.7, which may still be an effect of the nacelle geometry that still influences the recovery at this point. However, right above the hub height, around z/D of 0.15, all four profiles return to tend similar results as approaching the velocity recovery of \bar{u}/u_0 equals 1 around 0.75 z/D .

The results presented in Fig. 5.2.14(c) show a very similar behavior between the present work results and the uniform profiles of (SEDAGHATIZADEH et al., 2018) and (MO et al., 2013b), in the section close to the ground, z/D lower than -0.75, with values around 0.85 to 0.95 of \bar{u}/u_0 . The most significant differences between the results were exposed in the regions close to z/D between -0.3 to -0.4, and 0.25 to 0.3, concerning the (SEDAGHATIZADEH et al., 2018) profiles that presented two velocity deficit peaks close to 0.6 \bar{u}/u_0 in these regions.

Next section, $x/D = 5$, shown in Fig. 5.2.14(d) demonstrated very similar profiles between MFSim and (Syed Ahmed Kabir; NG, 2019) ABL in the region above $z/D=-0.25$, with its lowest velocity recovery occurring at hub height, in $z/D=0$, with a value close to 0.8 for \bar{u}/u_0 . Meanwhile, in the region located between the turbine bottom tip and close to the ground, $-0.75 < z/D < -0.25$, the present work results showed a better correlation with the uniform profile of (Syed Ahmed Kabir; NG, 2019) concerning the ABL, reaching a value of \bar{u}/u_0 close to 1 in $z/D=-0.6$. Although closer to the ground, $z/D < -0.75$, the MFSim profile displayed values that were between the uniform and ABL profiles of (Syed Ahmed Kabir; NG, 2019). Therefore, presenting a similar behavior with the ABL profile but with a higher velocity recovery.

In the far wake presented by Fig. 5.2.14(e) with the cross-section of $x/D=8$. The results of the (MO et al., 2013b) uniform profile matched the MFSim error bars in the hub height region up to close to 3/4 of the blade, $-0.35 < z/D < 0.35$. Then, both profiles present similar behavior and reach values close to 0.8 \bar{u}/u_0 at the height of the hub height. However, the correlation did not continue in regions close to $z/D=\pm 0.6$, where the uniform profile of (MO et al., 2013b) presented two expressive peaks of velocity deficit, also with values around 0.8 \bar{u}/u_0 .

Moreover, the two most significant differences occurred between the present work and (SEDAGHATIZADEH et al., 2018) profiles, both uniform and ABL, around $z/D=0.25$ and $z/D=-0.5$, where (SEDAGHATIZADEH et al., 2018) profiles presented two peaks of velocity deficits. In the section near the ground, the behavior of the present work was similar to the ABL profile of (SEDAGHATIZADEH et al., 2018) in terms of the slope of the curve in this region, but with a higher offset of 0.1 to 0.2 velocity recovery.

The section farthest from the turbine, at $x/D=10$, is shown in Fig. 5.2.14(f). Once again, the regions close to the height of the hub height, $z/D=0$, stand out for the higher correlation among the profiles, with velocity values \bar{u}/u_0 between 0.85 to 0.9, and also characterized by the higher values of the error bars in the MFSim profile. Another section that is important to point out is $0 < z/D < 0.75$, where a very similar behavior occurred between the present work results and (Syed Ahmed Kabir; NG, 2019) - ABL profile.

On the other hand, (MO et al., 2013b) profile once again presented two very distinct peaks of velocity deficits compared to the present work around $z/D=0.75$ and $z/D=-0.75$. But both profiles showed 3 points very close to each other in the lower region that is close to the ground, with \bar{u}/u_0 around 0.9.

5.2.5 Qualitative Analysis of the Flow Visualization

This section presents analyses to demonstrate that the LES-IB methodology is capable of simulating the interaction within the NREL Phase VI wind turbine and flow turbulence. To closure the section, instantaneous illustrations of time-averaged velocity contours represented by Figures 5.2.15 and 5.2.16 display the upstream to downstream flow structures around the wind turbine. Figure 5.2.15 shows instantaneous velocity contours on xy plane at the hub height, while Figure 5.2.16 displays the wind velocity on xz plane at the centerline. It is possible to observe different flow structures in the wake, depending on the distance and height development. Furthermore, the wind velocity decrease in the tower near wake region detected the effects of tower shading. Moreover, the far wake tends have the predominancy of larger turbulent structures as can be seen after $5D$ (70m) downstream of the turbine. This qualitative analysis shows that the wind velocity recovery and the flow structures in the wake are hardly connected.

Figure 5.2.15 – Contours of u velocity over flow around the wind turbine on xy -plane at the hub height

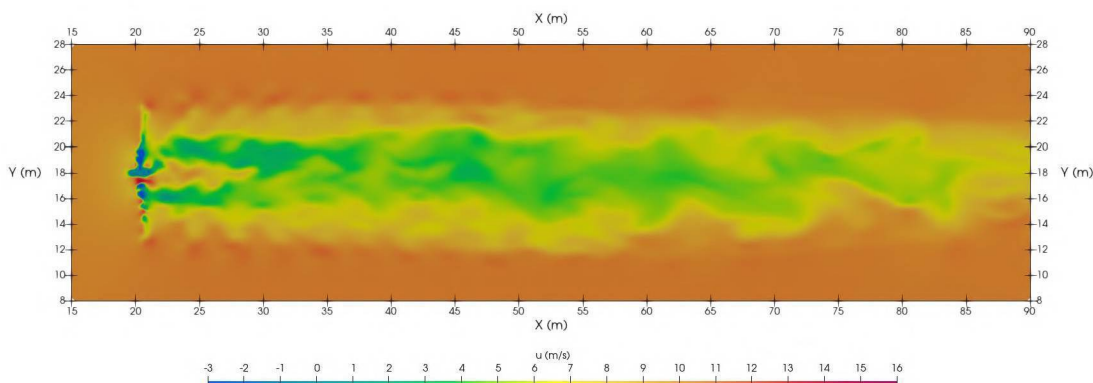
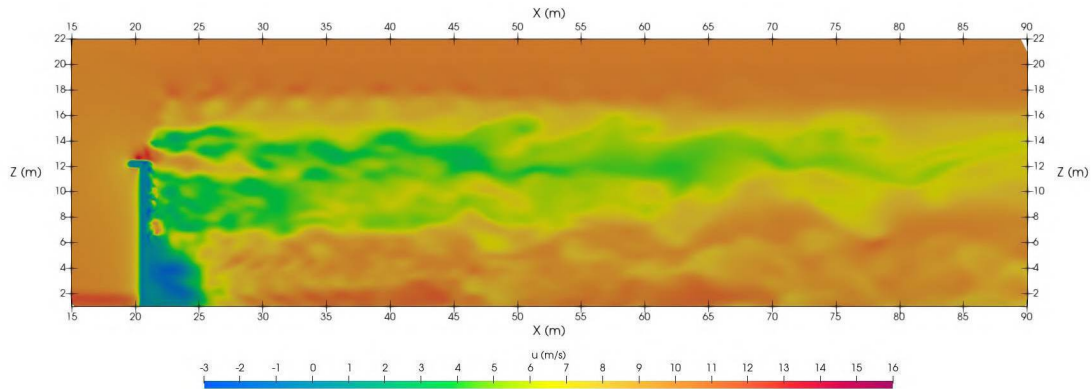


Figure 5.2.16 – Contours of u velocity over flow around the wind turbine on xz -plane at the centerline



The distribution of velocities contours in 2D vertical planes for the selected annular sections are presented in Figure 5.2.17. It is possible to observe that Figure 5.2.17(a), representing the $r/R = 0.267$, shows the highest velocity deficit profile in the downstream wake of the wind turbine. Moreover, this section demonstrates a substantial influence of the boundary layer effect in the velocity deficit close to the ground. Figure 5.2.17(b) shows a smaller wake diameter difference produced for the $r/R = 0.5$ section when compared to the $r/R = 0.267$ section. Although the velocities in the near wake suffer high deficits, there is an increase in the velocity recovery for the far wake compared to the previous section. Figure 5.2.17(c) illustrates a lower wake diameter displacing, and the velocity recovery profile has presented a large growth as demonstrated in Figure 5.2.8 for the $r/R = 0.75$ section. Finally, the section $r/R = 1$ displayed in Figure 5.2.17(d), represents flow field region close to the blade tip. It should be noted the low momentum extraction in this section, which had also been presented before in Figure 5.2.8. It is possible to see that the lowest velocity recovery values occurred at the ground level due to the boundary layer effect instead of the rotor height.

An illustration of the mean streamwise velocity profiles is plotted together with the instantaneous streamwise velocity contours, and shown in Figure 5.2.18. It should be noted that in general, the vertical velocity profiles represent well the flow behavior demonstrated by the velocities contours. It is easy to observe the high-velocity deficit that occurs over the rotor area for the downstream near wake at $x/D = 1$ section. As the downstream distance develops, the wake diameter tends to decrease. Therefore, the velocity recovery increases in the downstream far wake region. Besides that, it can be seen the great representation of the boundary layer effect regarding the vertical profiles. The vertical profiles also represented well the velocity recovery information in the transition from the boundary layer effect passing through the tower shadow, mainly in the near wake, until reaching the height close to the blade tip.

Moreover, in order to restate the qualitative analysis, Figure 5.2.19 displays an illustration of instantaneous vorticity magnitude with a visualization on the xy -plane, showing the vortices carried over the flow. It also allows visualization of small turbulent structures in the near wake, and when occurs the transition to far wake, the larger eddies are as prevalent. Figure 5.2.20 shows a representation of the iso-surfaces of velocity values that provide important 3D dynamically visualization of the eddies occurring over the turbulent flow, where the vortices mainly happen due to the blade tip motion. More specifically, the blade's top tip vortices are

Figure 5.2.17 – Velocity contours for the selected annular sections

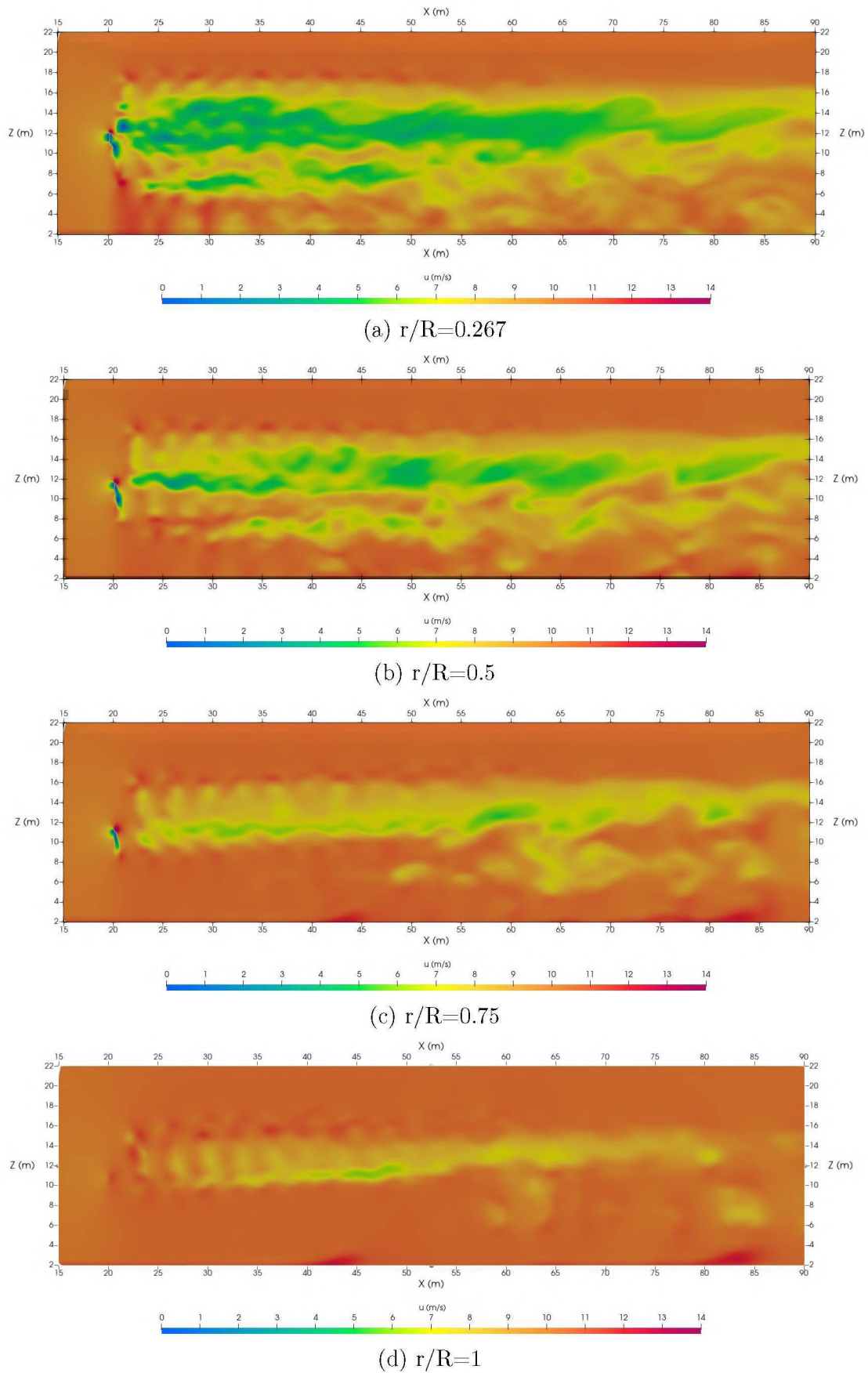
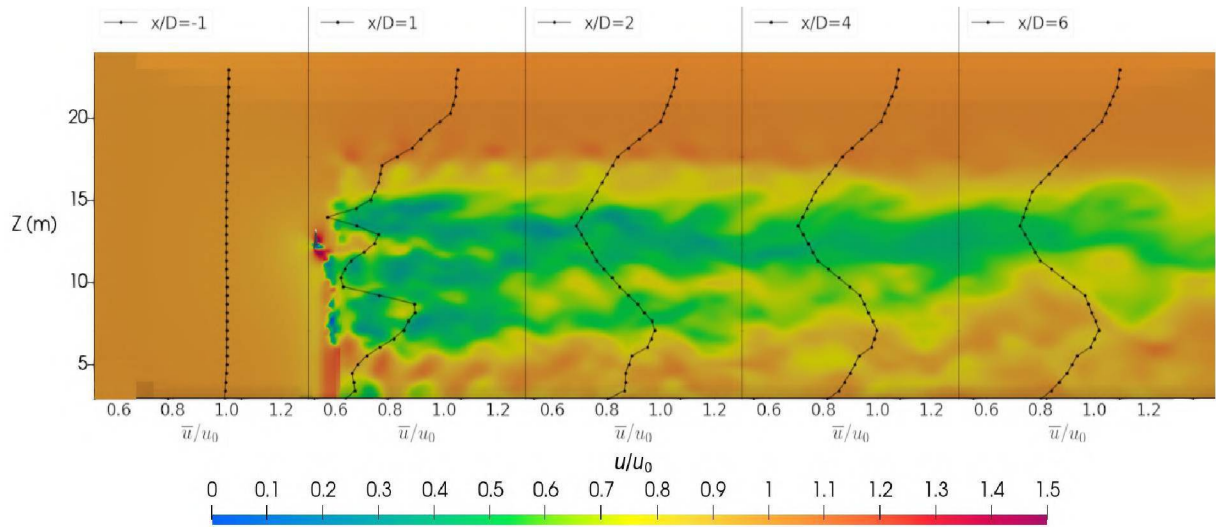


Figure 5.2.18 – Vertical wake comparison between 2D velocity contours and selected vertical profiles



more pronounced over the downstream, whereas the structures from the bottom tip interact with the eddies from the tower, mixing their shape.

Figure 5.2.19 – Contours of vorticity over flow around the wind turbine on ZY-plane at the hub height

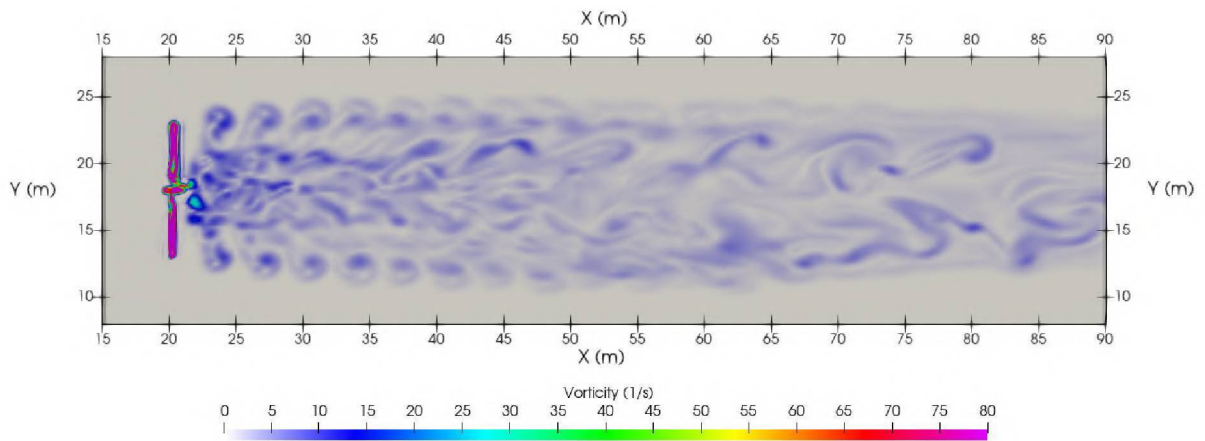
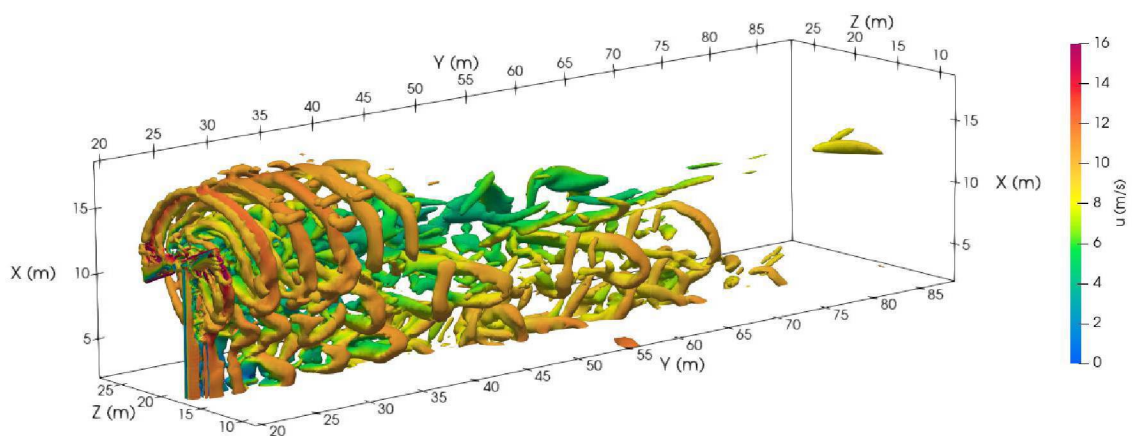


Figure 5.2.20 – Vortex visualization using iso-surfaces coloured by velocity



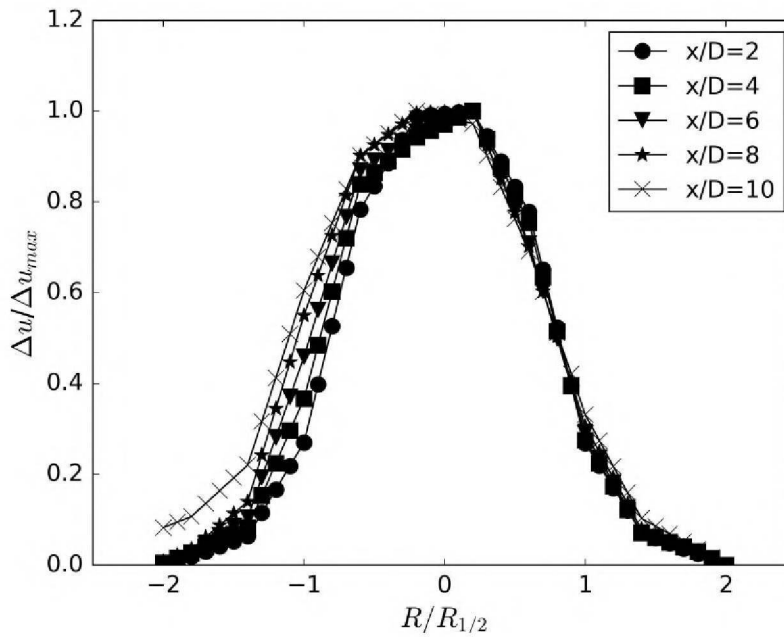
5.2.6 Self-similarity of Time-average Streamwise Velocity Profiles

The traditional theories of shear flow provide that in the wake areas of bluff bodies in freestream flows, the deficit of velocity tends to a self-similar profile (POPE, 2000). Some studies showed that wakes downstream of wind turbines may present self-similar patterns for flat and most recently complex terrain conditions. Some of those had observed that wakes for complex terrain also keep self-similarity, however, for shorter downstream distances when compared to flat terrain conditions (XIE; ARCHER, 2014; ABKAR; PORTÉ-AGEL, 2015; DAR et al., 2019)

The hypothesis of time-average velocity self-similarity is vital in many analytical, semi-empirical and empirical wind turbine wake models. However, this hypothesis is still questionable considering that a rotating wind turbine is much more complicated than a bluff body (XIE; ARCHER, 2014; FRANDBSEN et al., 2006; BARTHELMIE et al., 2003). In a fully developed wake, the time-averaged streamwise velocity deficit Δu is normalized by its maximum Δu_{max} and plotted against the ratio of $R/R_{1/2}$, where R is the distance from the centerline of the wake and $R_{1/2}$ is the half-width of the wake.

As depicted in Figure 5.2.21, in the bulk region of the wake, the self-similarity assumption works reasonably well for the cross-sections at the hub height of the wind turbine. The deviation from the pattern increases with the radius toward the edge of the wake where the shear is strong, mainly distinct at the $x/D=10$, which is considered as the last section and occurring in the far wake region.

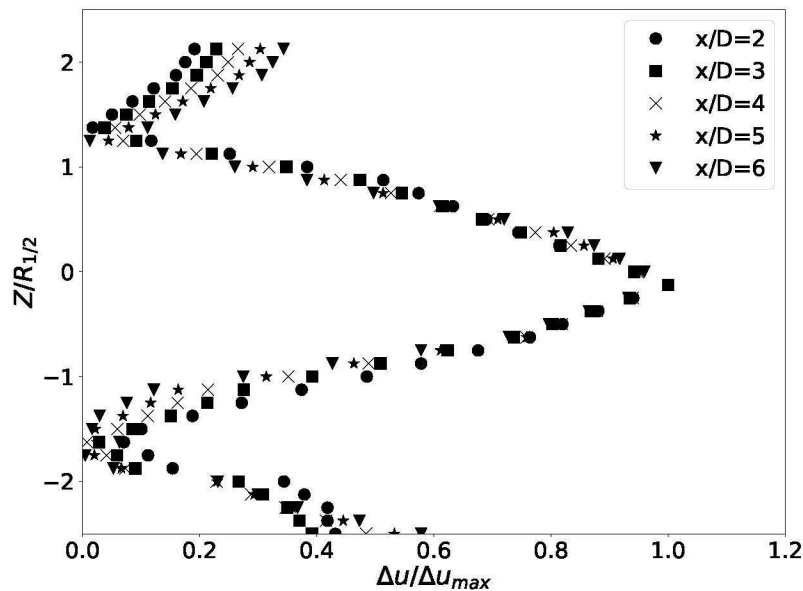
Figure 5.2.21 – Self-similar cross-section over normalized downstream distances



Self-similar profiles of time-averaged streamwise velocity deficit in the vertical central plane are shown in Figure 5.2.22, where 0 is the hub height position and downstream distance x/D varies from 2 to 6. It was observed that self-similarity is lost for downstream distances greater than $x/D=6$. The velocity deficits are normalized by its value at the centerline while the y -axis is the height z normalized by the half-width at that section. The self-similarity concept

works considerably well in the vertical plane for the rotor area, the region defined from -1 to 1 of $z/R_{1/2}$. There is a deviation in the similarity in the low edge, close to $z/R_{1/2}=-1$ (bottom tip), that could be attributed to the region of interference of the tower shading and flow acceleration. Moreover, close to the ground it is invalidated by the strong shear near the ground, while the upper section outside the swept area, $z/R_{1/2}>1.2$, there is an influence of the velocity profile due to faster velocity recovery and flow acceleration.

Figure 5.2.22 – Self-similar vertical profiles over normalized downstream distances



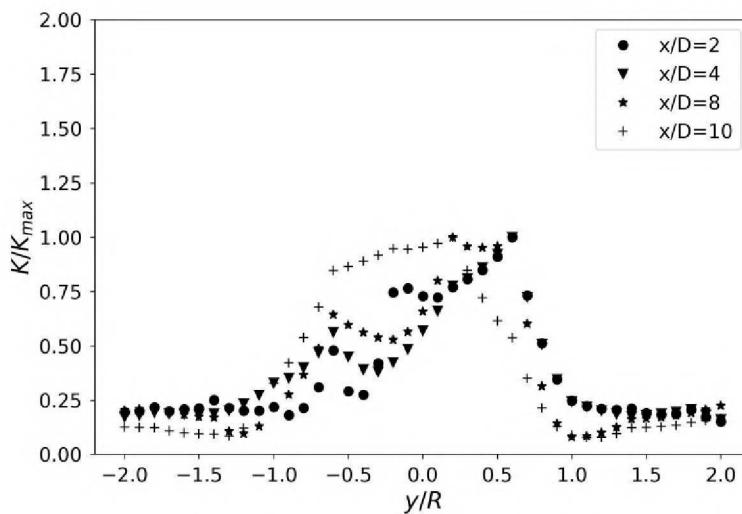
It is possible to conclude that self-similarity is validated for cross-sectional and vertical profiles in most parts of the wake area. It is in the rotor area behind the wind turbine, where the wake velocity deficit has self-similar properties, except near the edges of the turbine due to strong wind shear and flow acceleration. Also, the self-similarity assumption is less verified near the ground, where wind shear is strong once again. Those self-similar behaviors are in coherence with the conclusion and findings from [Xie and Archer \(2014\)](#) and [Abkar and Dabiri \(2017\)](#). Most of the simplified analytical wake models available in the literature are based on the assumption of self-similarity of time-average velocity profiles downstream from the wind turbine.

5.2.7 Longitudinal, Cross-section and Vertical Profiles of Turbulence Properties

The capability of the LES-IB methodology to simulate the interaction between the experimental wind turbine and turbulence of the flow is firstly presented through an analysis of the turbulent kinetic energy retained over the flow field. Figure 5.2.23 depicts the turbulent kinetic energy k normalized by its maximum value in the profile for four different cross-sections located downstream of the wind turbine, sections x/D equals 2, 4, 8, and 10.

From Figure 5.2.23 it is possible to verify that most of the high values in the ratio k/k_{max} occur between the region from -0.5 to 0.5 y/R , that is, closer to the root of the paddle or the center of the wake region. The profiles have a similar behavior between them, except for the profile $x/D = 10$ in a given region, -0.5 to 0 y/R , in which the profile has higher values than the others with a more symmetrical behavior. This may be related to the location of this profile, being more in the far wake, and therefore further away from the turbine, where velocity fluctuations would be smaller due to the flow velocity recovery. It can be seen the highest values of the ratio k/k_{max} in the right side of the profile, close to 0.5 y/R , reaching the ratio values around 1, except for the $x/D = 10$ profile. This may be attributed to the direction of rotation of the wind turbine generator.

Figure 5.2.23 – Comparison of four downstream cross-sections of the time-averaged turbulent kinetic energy k



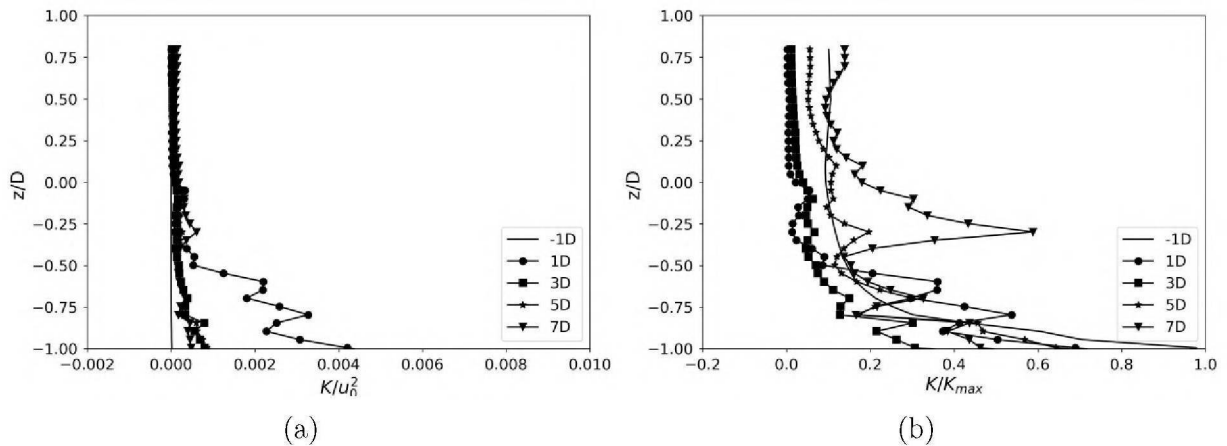
The analysis of the streamwise vertical profiles of the calculated turbulent kinetic energy k is considered along with the wake downstream distance and plotted all together in the same graph. Figure 5.2.24 shows five different vertical profiles from $x/D = -1$ upstream to $x/D = 7$ downstream distance, representing profiles upstream and downstream from the wind turbine. The analysis considers the xz plane, where the centerline is taken in place, which is aligned with the tower ($y = 0$). Figure 5.2.24(a) illustrates the turbulent kinetic energy k normalized by the square of the freestream velocity u_0^2 while Figure 5.2.24(b) shows the vertical profiles of k normalized by its maximum value.

Figure 5.2.24(a), shows a region with high values of turbulent kinetic energy in the profile of $x/D = 1$, with the highest value close to the ground and reducing until it gets close to the bottom tip of the blade, up to z/D close to -0.5 . The other profiles present a small slope in this same region right behind the tower, but with a lower intensity of k . This behavior may be due to the tower shading effect occurring at the first profile after the wind turbine.

Figure 5.2.24(b) presents the ratio k/k_{max} with profiles tending to decay, where the highest values are in the region outside the area of rotation of the blades, located further down with some peaks close to the ground, and other two peaks between the z/D region between

-0.75 to -0.5. In addition, it is worth noting the peak of the highest value of the vertical profile of the section $x/D = 7$ occurring close to z/D of -0.25 with a value of k/k_{max} close to 0.6, or that is, this implies that the farther the profile is from the turbine, the more the far wake, the smaller the influence of tower shading on turbulent kinetic energy. Therefore, the highest values of k/k_{max} in the profile $x/D = 7$ will occur in the rotation region behind the turbine, close to the height of the hub height.

Figure 5.2.24 – Comparison of two vertical profiles, (a) and (b), of the time-averaged kinetic turbulent energy k for different downstream distances



Turbulence intensity (TI) is one of the parameters that influence wind power production. Seeking to show its behavior in the wake downstream, Figure 5.2.25 presents the cross-sections profiles of the turbulence intensity defined in equation 5.2, from $2D$ to $8D$ of x/D and for y/R from -2 to 2. Figure 5.2.25 demonstrates that the highest TI values occur in the section where the probes were installed close to the turbine, as expected since the velocity fluctuations are greater in this section, while the average velocity in this region is reduced. The cross-sections downstream of the turbine presented TI values lower than 0.05, which are considered low values of turbulence intensity. On the other hand, the section in the turbine area, $x/D=0$, presents high TI indices, with the highest TI value occurring at the central point of the transverse section, slightly above 0.30. Meanwhile, the lowest values occur in the part of the cross-section that is beyond the radius of the blades, that is, beyond y/R of -1 or 1. Therefore, the highest rates of TI occurring in the swept area as expected in this analysis of cross-sections where height meets hub height.

With similar behavior in terms of higher TI indices occurring in the profile $x/D=0$, Figure 5.2.26 shows a vertical analysis of the TI profile, where the height is normalized by the diameter D of the turbine. Again, the profiles further away from the turbine show less expressive TI values, while the $x/D=0$ profile reaches a maximum TI value close to 0.5. The value of TI at the height of the hub height, $z/D=0$, is consistent with Figure 5.2.25, being slightly higher than 0.3. Another interesting point to be noted is that the highest TI values that occur in the $x/D=1$ profile are located below the swept area, that is, they occur due to velocity fluctuations imposed by the turbine tower, occurrences of the effect of tower shading, with TI values close to 0.1. The same effect was not presented in section $x/D=0$ due to the location of the probes being in overlap with the tower points in this profile.

Figure 5.2.25 – Comparison of turbulence intensity TI deficits along the cross-sections downstream distances

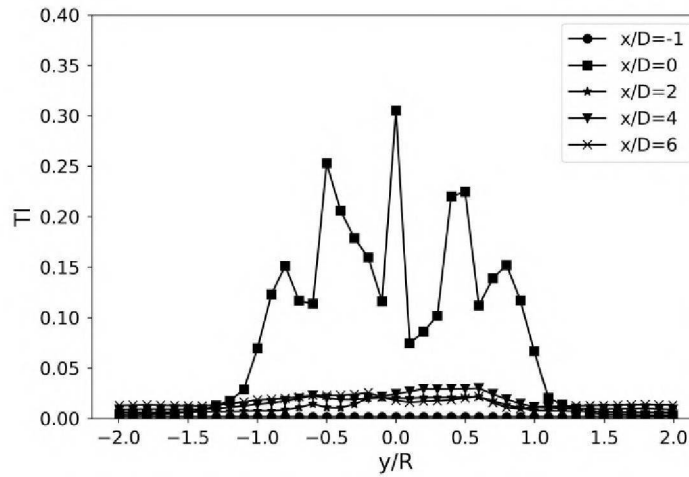
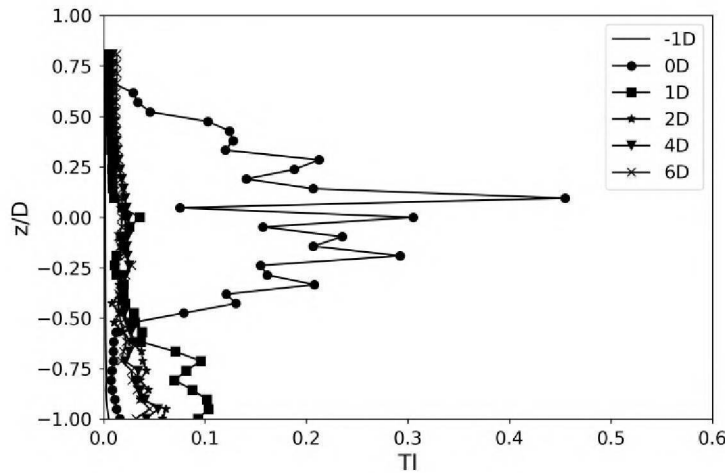


Figure 5.2.26 – Comparison of turbulence intensity TI for vertical profiles along the cross-sections downstream distances



Scenario 2 Remarks

In the aerodynamic analysis of the experimental wind turbine Phase VI, scenario 2, significant results were obtained from the time-averaged streamwise velocity profiles. In conclusion of the development of the wind turbine wake analysis, the LES simulations showed a higher loss of kinetic energy in the near wake region when compared to the wake references presented. In terms of longitudinal profiles, the simplified wake models tend to overestimate the wake downstream velocity recovery compared to the present work for the annular sections close to the blade root. Meanwhile, Park model tends to underestimate the results close to the blade tip. But in general, the results of (MO et al., 2013b) present similar behavior and significant agreement for the near and far wake compared to the present results. The present study achieves generally better agreement in the middle to far wake region, which could be attributed to the stronger

influence of the rotor design and nacelle in the near wake region.

In terms of flow visualization, the wind velocity decrease in the near-wake region captures the effects of tower shading. Also, the qualitative analysis highlights vortical flow structures in the wake, with smaller turbulent structures occur primarily in the near wake, while larger eddies are dominant in the far wake. The interaction between the experimental wind turbine and the flow turbulence is presented by analyzing the turbulent kinetic energy and turbulence intensity. The results suggest that most of the turbulent kinetic energy dissipation occurs in the near sections, corresponding to the near wake. Regarding, self-similarity of the wakes downstream of wind turbine, it is possible to conclude that self-similarity is validated for cross-sectional and vertical profiles in most parts of the wake area. The wake velocity deficit has mostly self-similar properties in the rotor area behind the wind turbine, reducing the similarity near the edges of the turbine due to strong wind shear and flow acceleration.

5.3 SCENARIO 3: NREL 5MW WIND TURBINE

The third simulation scenario developed in this thesis was based in a real scale case of an offshore wind turbine that was designed by NREL, called NREL 5 MW, it is one of the most reported turbine containing geometry information (JONKMAN et al., 2009). The reference case presents data in terms of aerodynamics coefficients and parameters, but not contain measurements of the downstream wake. Because of that, the international cooperation and partnership between UFPR and UBC, represented by UBC Okanagan computational fluid dynamics laboratory was crucial. UBCO CFD Lab provided data and results from their own-house code simulations of the NREL 5 MW to verify and validate our work, since due to the lack of publicly available large scale measurements, a validation against experimental data is currently not possible. It was provided data from SOWFA, which applies an actuator line model (ALM), and also from MARBLLES, with detailed actuator disk model (AD) and their universal AD model that will be called MARBLLES UADM from now on. The simulations will comprehend a complete real scale turbine where the properties of mean and turbulent flows will be analyzed and discussed, Table 2 gives an overview about the dimensions and operating conditions of the NREL 5MW.

Table 2 – Parameters of the NREL 5MW Wind Turbine

Parameter	Value
Number of rotor blades	3
Rotor Diameter	126 m
Rated Power	5.3 MW
Rated Wind Speed	11.4 m/s
Rated Rotational Speed	12.1 rpm
Blade Length	61.5 m

For the MFSim simulations, the geometry of the NREL 5MW wind turbine was designed in the CATIA[®] software and meshed in the ICEM[®] CFD framework. Figure 5.3.1 illustrates the main components of the real scaled 5MW NREL wind turbine. Figure 5.3.1(a) shows the rotor containing the 3 blades design, where the rotor diameter is equal to 126 m, Figure 5.3.1(b) presents the unification of tower and nacelle aligned, characterizing the hub height at 90 m and Figure 5.3.1(c) depicts an ortogonal representation of the rotor in relation to the tower. The wind turbine mesh, which represents the lagrangian domain, contains a total of 67288 triangular cells. Where, 39465 cells represents the rotor geometry meanwhile 27823 cells characterizes the tower and nacelle as shown in Figure 5.3.2.

The inflow wind velocity profile was implemented at the inlet with a hub height velocity of $u=8$, $v=0$ and $w=0$ m/s, in the MFSim code, then characterizing a Dirichlet type of boundary condition. The boundary conditions for the lateral planes (xz -planes) were characterized as symmetry, this condition was also applied in the top plane (xy -plane). The bottom plane (xy -plane) sets a no-slip condition in order to represent the ground where the turbine was placed in the wind tunnel. A Neumann boundary condition was used for pressure matters, meanwhile an advective condition was employed at the outflow condition, which is time varying to allow for vortical structures to cleanly exit the computational domain without reflecting back into the

Figure 5.3.1 – NREL 5MW wind turbine structures: (a) rotor and tower in frontal, (b) top , and (c) lateral view

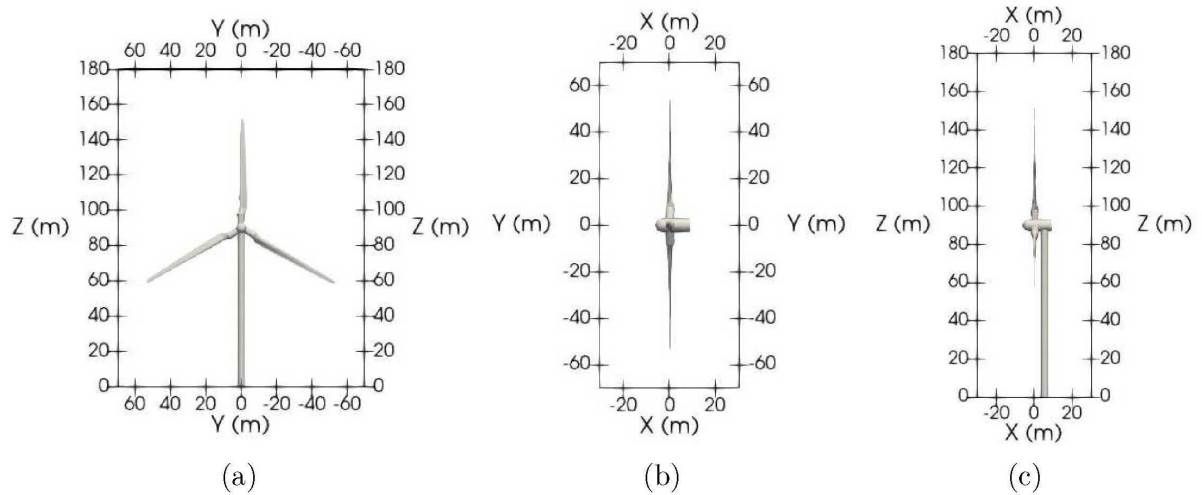
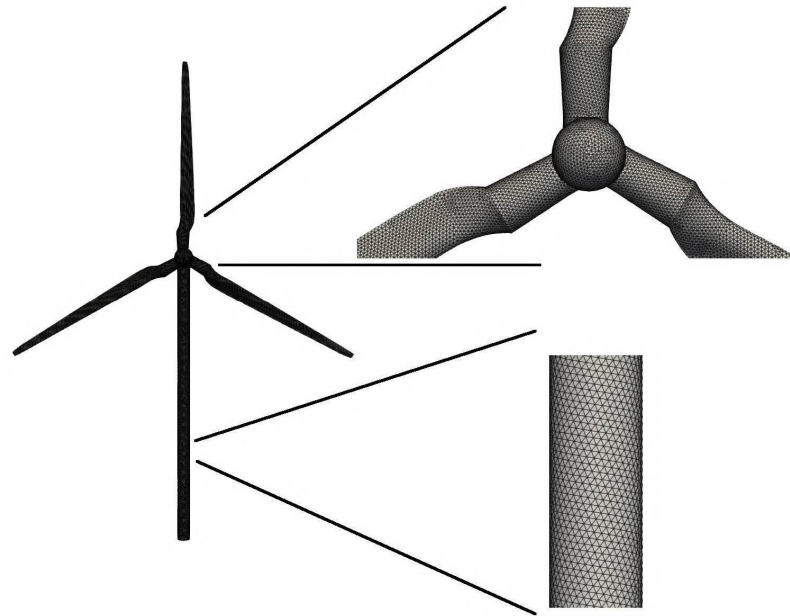


Figure 5.3.2 – Lagrangian mesh of the NREL 5MW simulation



domain or disturbing the solution in the inner domain. The initial conditions of the simulations for velocities profiles at the hub height, $u=8$, $v=0$ and $w=0$ m/s. In these simulations, the fluid properties were $\rho=1.225$ kg/m³, $\mu=0.0000182$ kg/(m s) and setting a Reynolds number ($Re \approx 2.46 \times 10^6$) around the blade. It was adopted variable numerical time steps in the range of 10^{-4} to 10^{-5} s, maintained a CFL criteria of 0.5. The final simulation time was 1200 s. All statistics were calculated based on the last 500s of simulation, period along which the flow presented approximately steady state conditions.

5.3.1 Geometry and Mesh Sensibility Analysis

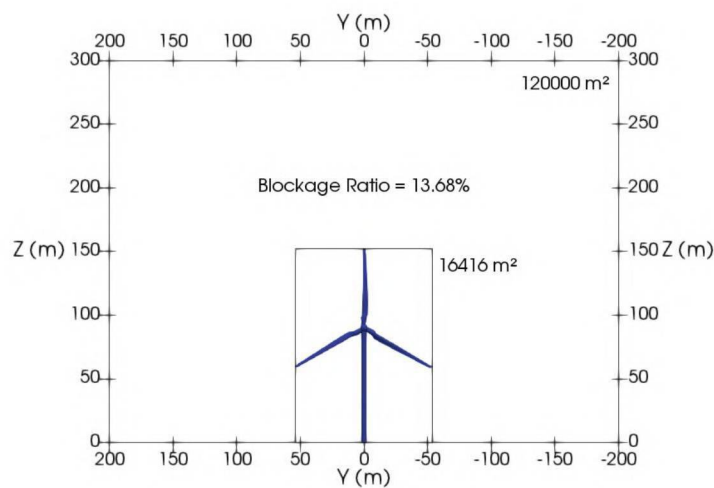
This section presents quick analysis of how it was applied a sensibility analysis order to find the best geometry and mesh option to simulate the NREL5MW, done through sensitivity analysis with several simulations done until we got the best-fit option. Table 3 presents the simulations elaborated with the respective dimensions of the control volume in the directions x , y and z , with the levels of refinement applied as well as subdivisions for the cells of the coarsest level.

Table 3 – Control Volume Cases for NREL 5MW Wind Turbine Simulation

	Control Volume Cases					
	A	B	C	D	E	F
X	1600 m	1600 m	1600 m	1600 m	1600 m	1600 m
Y	400 m	800 m	1000 m	1200 m	800 m	800 m
Z	300 m	500 m	500 m	500 m	800 m	600 m
Refinement Level	6	6	6	6	6	6
Subdivision	64 16 12	64 32 20	64 40 20	64 48 20	64 32 32	64 32 24

In terms of the control volume, the first attempt to simulate the NREL 5 MW considered the application of 300 m height with a 200 m width on each side (400 m) and a longitudinal distance of 1600 m. At the end of the simulation, a significant blockage influence occurred mainly in the z component related to the height of the domain. This simulation presented a blockage ratio value of 13.68%, as can be seen in Figure 5.3.3, which is a high value for simulation of this nature.

Figure 5.3.3 – Case A



From the previous simulation result, an increase in the width and height of the simulation domain occurred. Therefore, for simulations B, C, and D, a height of 500 m in z was chosen, which would lead to less influence of the upper boundary condition of the domain on the flow while keeping the same longitudinal distance of 1600 m for direction x . Besides that, the widths in y were increased as well to values for (i) simulation B: 400 m on each side (800 m), (ii)

simulation C: 500 m on each side (1000 m), and (iii) simulation D: with 600 m on each side (1200 m).

Simulation B, Figure 5.3.4, has a blockage ratio of 4.1%, while simulation C, Figure 5.3.5, shows a blockage ratio of 3.28%, while simulation D, Figure 5.3.6 reached a blockage ratio of 2.73%. All the simulations demonstrated a blockage ratio lesser than 5%, which is an acceptable value to simulate a case of this nature. The lateral influence of the walls was tiny and practically equal regardless of the simulation width, from 800 to 1200 m of the total width.

The height continued to have a small influence on the flow even with 500 m height. Such influence of the upper boundary condition had no effect in reflecting the flow back to the wake region. However, it might miss capturing some wake vortices that exceed 500 m height. For this reason, it was decided to create the simulation E, where the height in z increased to 800 m while the width value of 800 m in y was kept, since the width values presented similar results from 800 to 1200 m (simulation B to D), thus providing a lower computational cost for testing the flow at the chosen height.

Figure 5.3.4 – Case B

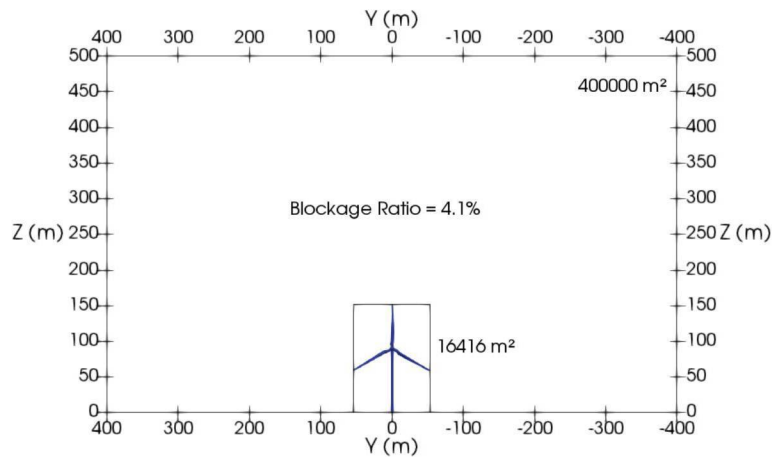
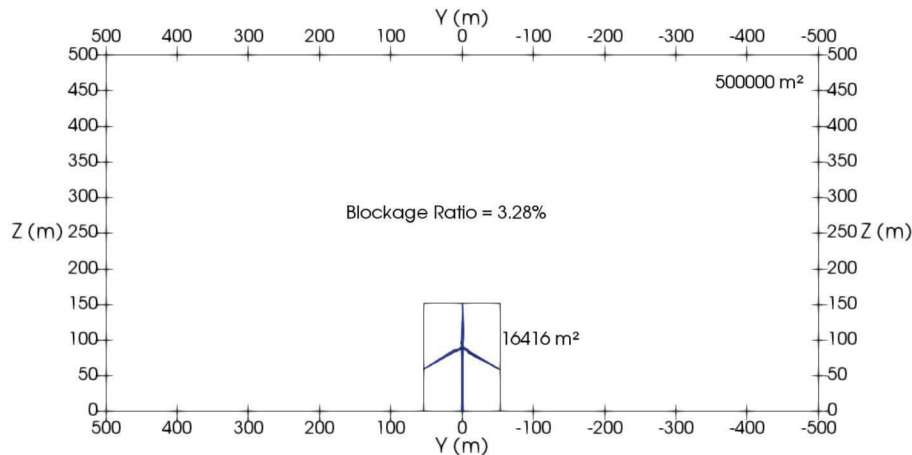
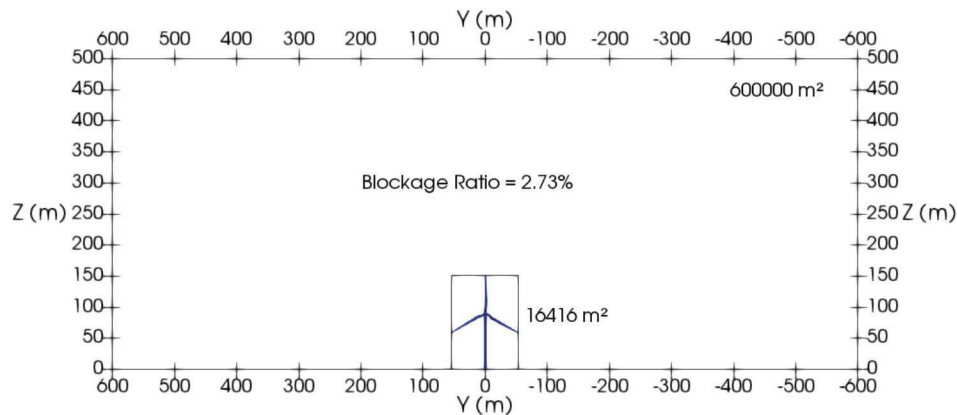


Figure 5.3.5 – Case C



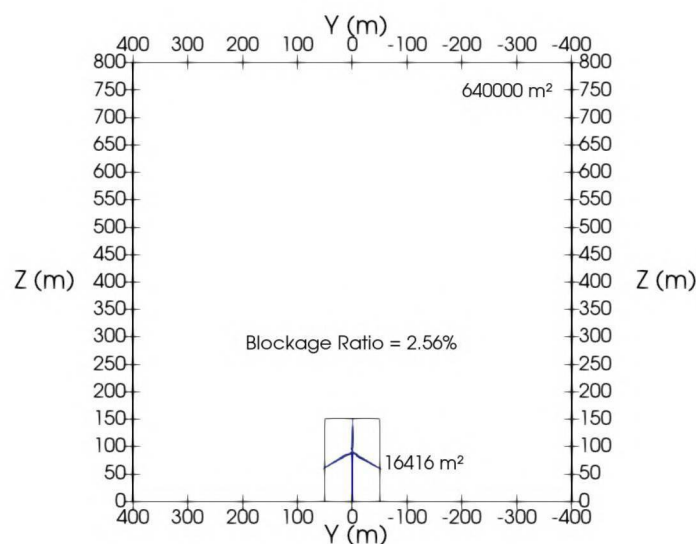
Simulation E, with values of x , y , and z of 1600, 800, and 800 m respectively, present a blockage ratio value of 2.65% considered very suitable for this type of simulation, as shown

Figure 5.3.6 – Case D



in Figure 5.3.7. Meanwhile, Figure 5.3.8 illustrates the flow from a lateral view downstream of the turbine, making it possible to visualize the entire development of the vortices downstream of the turbine. Through this figure, it is possible to identify the influence of the turbine on the downstream flow that occurs up to a height slightly above 500 m in z , indicating that a simulation with a height of 600 m in the direction z would be enough to capture all the influences of the wind turbine wake with a lower computational cost than when using 800 m of height.

Figure 5.3.7 – Case E



Because of the eddies that still appear around 500 m height and the higher computational cost that lower blockage ratios would bring, a simulation with 800 m width and 600 m height was chosen for the final results. This setup presents a blockage ratio of 3.42% that is within the standard applied to wind tunnel tests of less than $5\text{-}10\%$ (CHOI; KWON, 1998). From this point on, all analyzes will consider 800 and 600 ratios for width and height.

Finally, four cases were performed to simulate the flow around the wind turbine, il-

Figure 5.3.8 – Lateral view of the 800 m height simulation

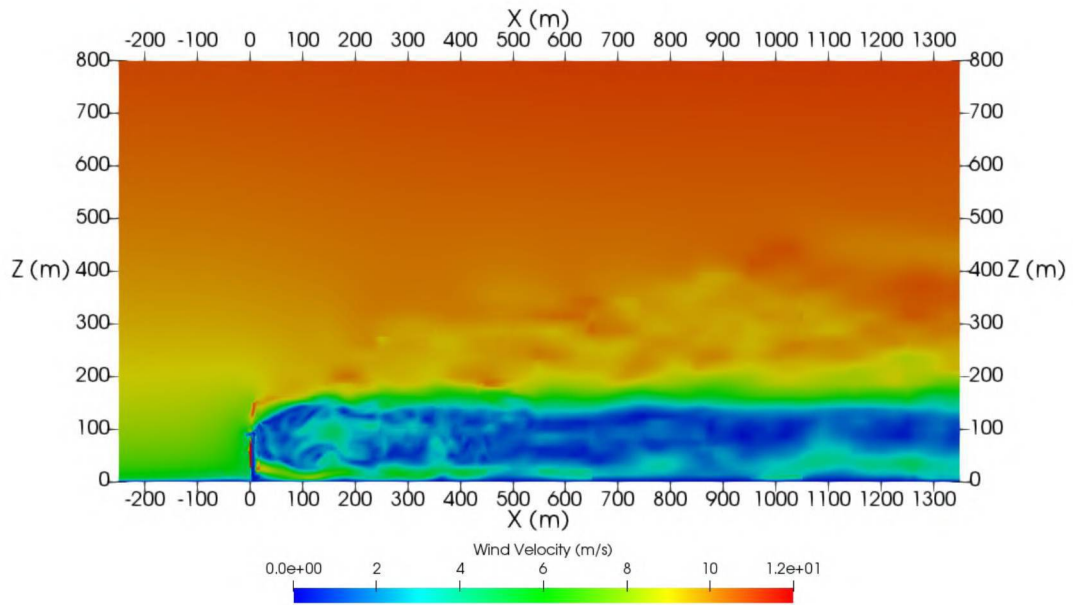
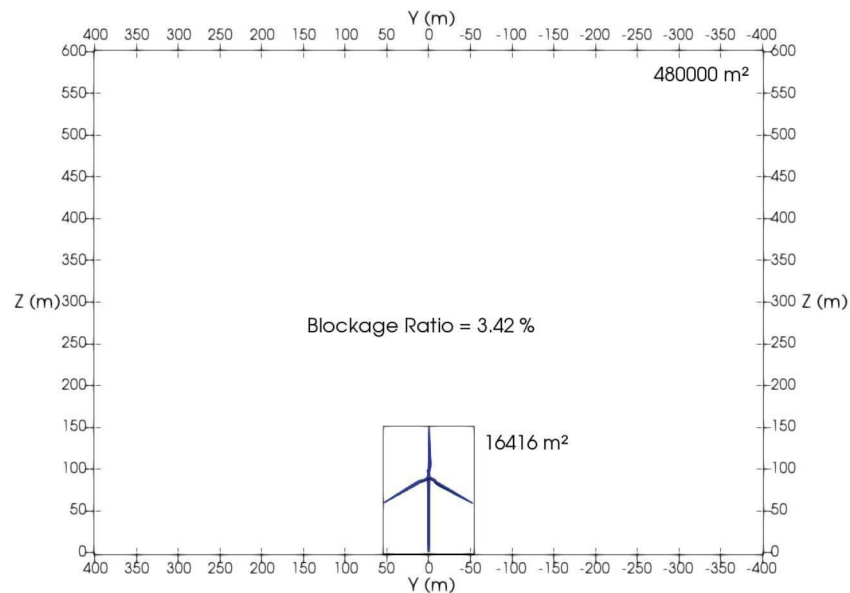


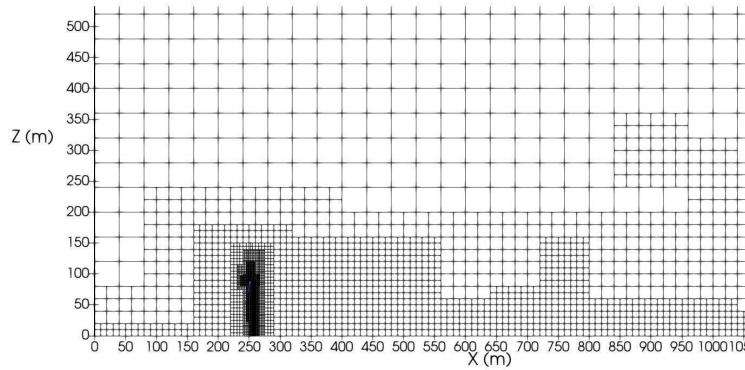
Figure 5.3.9 – Case F - Final Setup



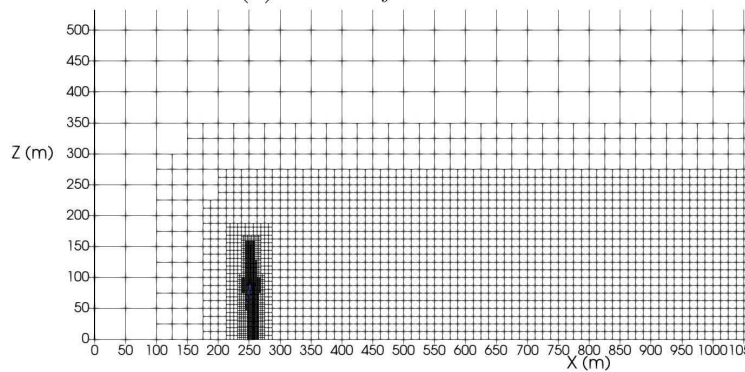
illustrated as example in Figure 5.4.1, (i) applying the vorticity criteria and also by fixing a refinement region around the wind turbine and wake downstream with (ii) three, (iii) four, (iv) five levels of refinement, in order to understand how the behavior of the results would be with different approaches that are allowed in the MFSim code. Then, it was decided to use the most refinement case (five levels of refinement) to present the following results in this scenario. The final simulation time was 1200 s, where the statistics were calculated based on the last 500s of simulation. The computational resource was based on two nodes of Intel Xeon E5650 2.67GHz 24-core machine utilizing approximately 26 GB RAM, the simulations required approximately

340 hours due its mesh with more than 3.5 millions of volumes.

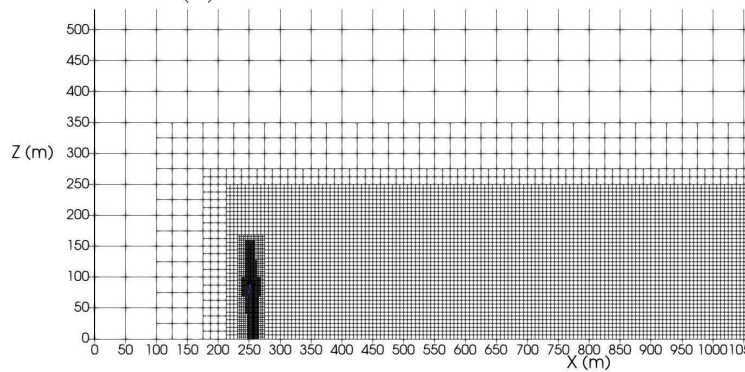
Figure 5.3.10 – Mesh illustration for (a) vorticity criteria, refinement region with (b) three and (c) four levels of refinement



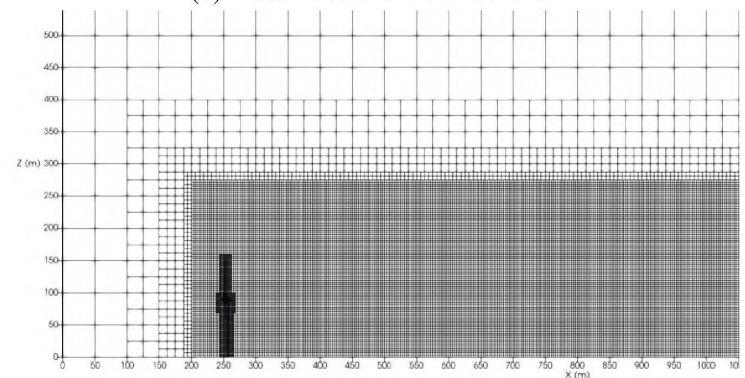
(a) Vorticity criteria



(b) Three levels of refinement



(c) Four levels of refinement

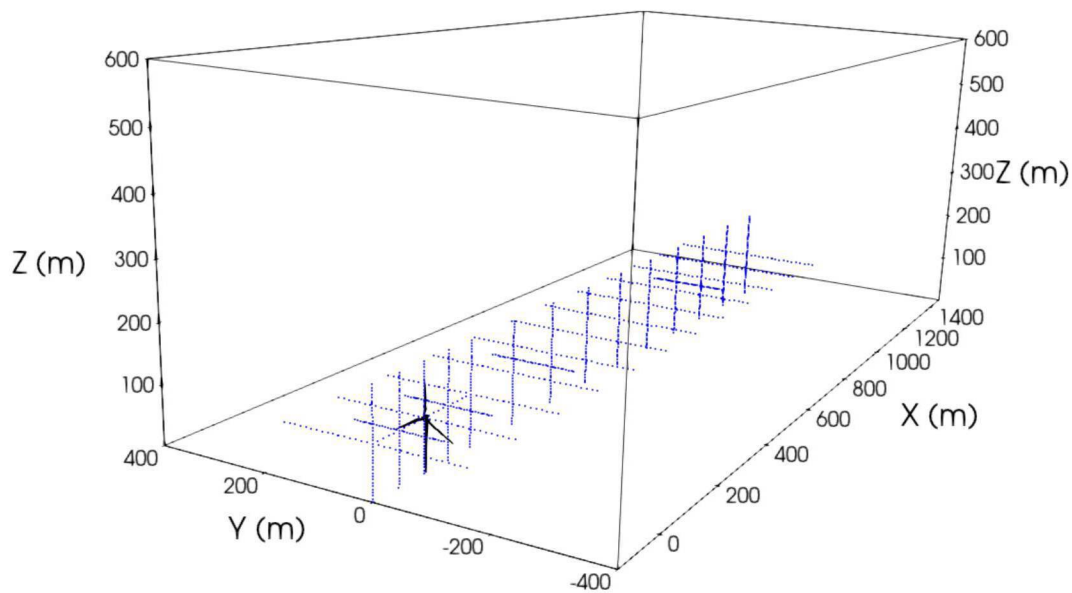


(d) Five levels of refinement

5.3.2 Probes Location

Figure 5.3.11 illustrates the probes installed in the numerical domain to retain the results in order to capture the statistics of the variables of interest. Those probes were positioned from $1D$ upstream to $10D$ downstream distance from the NREL 5 MW wind turbine in the longitudinal direction, which is the x -direction. The discrete annular points used to extract an average of the velocity components across the rotor plane are illustrated in Figure 5.3.12, where R is the radius of the NREL 5 MW blade which is equal to 63 m . The innermost probe is related to the blade root, while the outermost point corresponds to the tip of the blade.

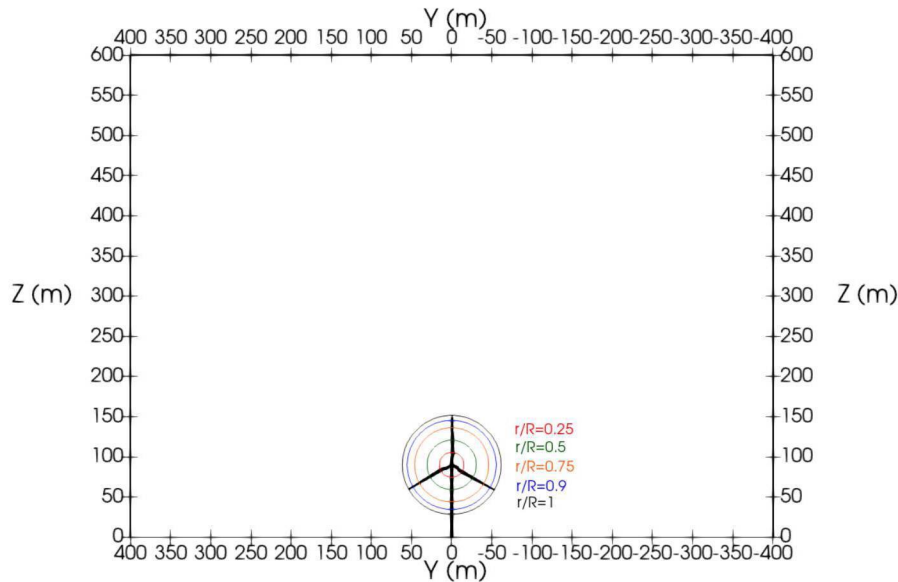
Figure 5.3.11 – Installed probes in the Scenario 3



The cross-sectional probes to capture the wake diameter had an implementation of 33 probes for each chosen section varying from -160 m to 160 m in the y -direction, spaced by 10 m . The chosen sections are $1D$ upstream, and end at $10D$ downstream from the wind turbine. Adding, two more sections at 2.5 and $7.5 D$

Additionally, seeking to visualize the wake behavior downstream of the turbine, vertical profiles were established before and after the wind turbine represented by 37 probes, from 0 to 180 m , for each section, where the sections begin at $1 D$ upstream and end at $10D$ downstream of the wind turbine.

Figure 5.3.12 – Annular displacement of the probes for longitudinal analysis



5.3.3 Streamwise Velocity Analysis

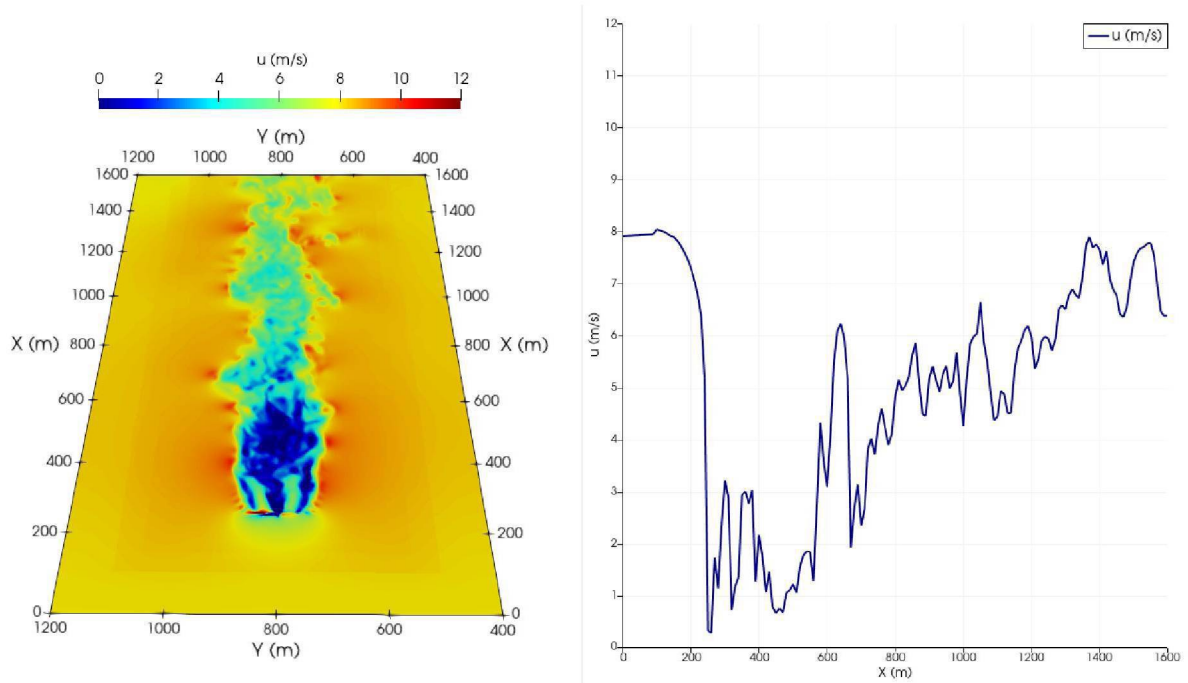
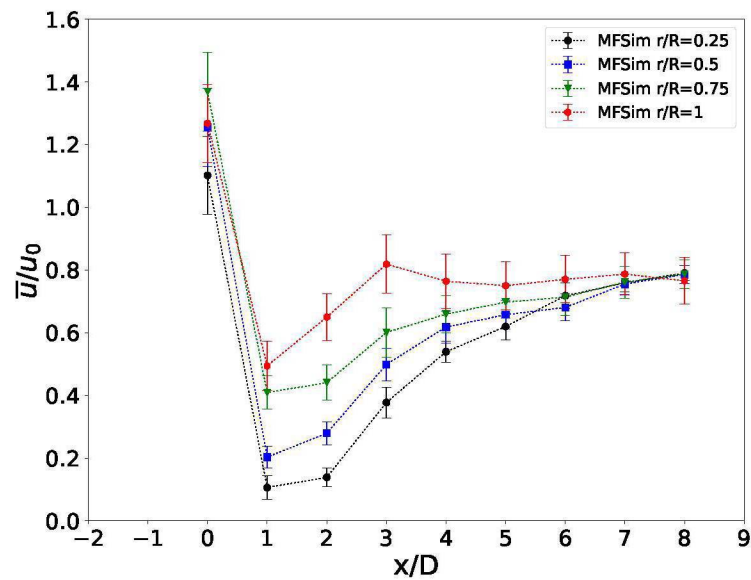
5.3.3.1 Longitudinal Profiles

The streamwise component of the velocity was analyzed downstream from the wind turbine, focusing on the longitudinal wind velocity recovery for chosen sections behind the centerline and annular segments. Figure 5.3.13 shows the instantaneous centerline velocity recovery behind the turbine for the 5 levels of refinement simulation applied in the MFSim, with the mesh adaptivity occurring around the wind turbine itself. Figure 5.3.13 also presents a dynamic instantaneous velocity contours visualization in an $x - y$ plane at the hub height. It is possible to discern high-velocity deficits in the near wake area immediately downstream from the wind turbine. These large extractions of energy in the near wake of the wind turbine indicate that the flow crossing into the rotor region loses a substantial portion of its mean kinetic energy.

Four different annular sections of the blade are presented for ratios r/R in the range of 0.25 (close to the center) to 1 (at the blade tip). The normalized time-average velocities (\bar{u}/u_0) with standard deviation are plotted against the normalized longitudinal distance (x/D), as shown in Figure 5.3.14.

Figure 5.3.14 presents velocity recoveries in four annular blade sections, sections at r/R of 0.25, 0.5, 0.75, and 1. From the results, it is possible to observe similar behavior for the simulations with the refinement region, where the highest velocity values occur for the $r/R=1$ section at the blade tip, reaching out \bar{u}/u_0 values over to 0.8 from $x/D = 3$. Meanwhile, the r/R profiles of 0.25, 0.5 and 0.75 reached \bar{u}/u_0 values close to 0.8 at far wake only. As expected in the simulations, the lowest values \bar{u}/u_0 were obtained close to the turbine, in the near wake region, in the downstream sections of $x/D = 1$ and $x/D = 2$ with values of \bar{u}/u_0 between 0.1 to 0.25 for r/R profiles of 0.25 and 0.5, while for 0.75 r/R profile the lowest value was close to 0.4,

Figure 5.3.13 – Animated longitudinal profiles and countours of streamwise velocity over time

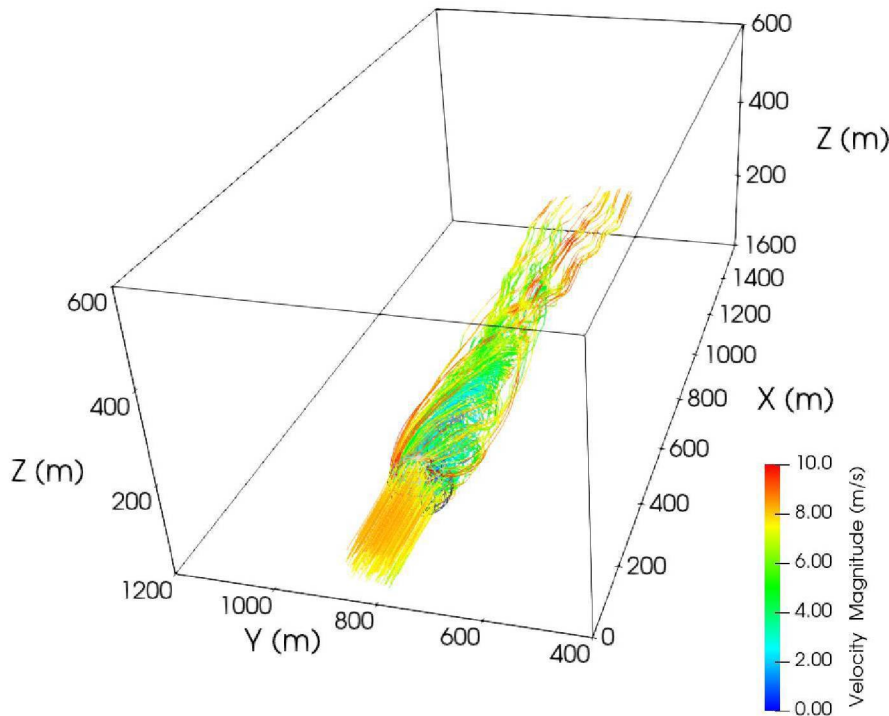
Figure 5.3.14 – Longitudinal annular velocity recovery profiles by ratio of r/R 

and around 0.5 for $r/R=1$. Moreover, high velocities were also found at $x/D = 0$, between 1.1 to 1.4 \bar{u}/u_0 , due to the rotation of the blades since this section is characterized by the presence of the wind turbine.

Lastly, as seek of exemplification, Figure 5.3.15 displays a dynamic illustration of time-averaged streamwise velocity magnitude streamlines that were selected upstream of the rotor, with 63 m radius, and carried to downstream flow showing the streamline behavior over the

wind turbine wake region.

Figure 5.3.15 – Longitudinal streamlines of time-averaged velocity developing over the NREL 5MW wind turbine wake



It is possible to observe the development of different flow streamlines in the wake, depending on the distance, height and r/R analyzed. This qualitative analysis shows that the wind velocity recovery and the streamline flow development in the wake are highly related, as it is important to point out high velocities occurring around the blade tip (represented by the streamlines in outer inner of the diameter) in the near wake. On the other hand, lower velocities are colored visible in the near wake centerline region, and as the flow develops to far wake the velocity recovery increases for all swept area streamlines.

5.3.3.2 Cross-sections Profiles

The streamwise component of velocity was analyzed downstream from the wind turbine, focusing this section on the cross-sectional wind velocity recovery for chosen sections. Moreover, as an attempt of embodiment, Figure 5.3.16 showcases an instantaneous screenshot with mesh visualization to highlight the flow structures around the wind turbine. It also allows visualization of small turbulent structures in the near wake and when the transition to far wake behavior occurs, where larger eddies prevail. Meanwhile, Figure 5.3.17 displays a dynamic representation of the instantaneous streamwise velocity u from a top point of view $x - y$ plane at the hub height, demonstrating the visualization and characteristics of turbulent flow over the cross-sections. Also providing a qualitative comparison among the four different downstream section of the simulation. The chosen section 1, 2, 4 and $8D$ downstream for the graphs were based on the distinction of near and far wake.

Figure 5.3.16 – The flow velocity contours development in top view of the NREL 5MW wind turbine

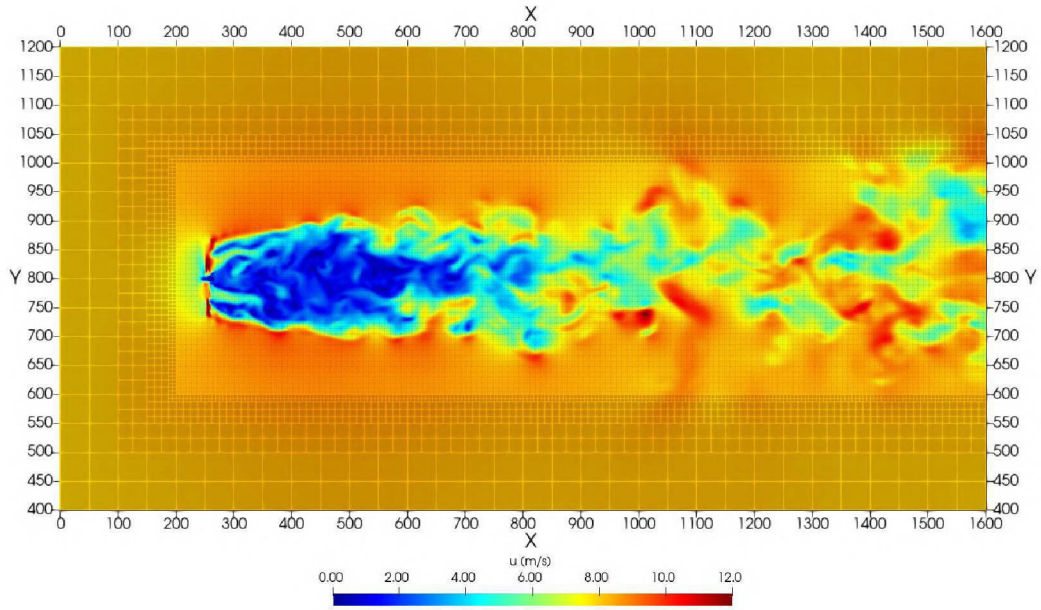


Figure 5.3.17 – The flow velocity contours development over the cross-sections around the NREL 5MW wind turbine

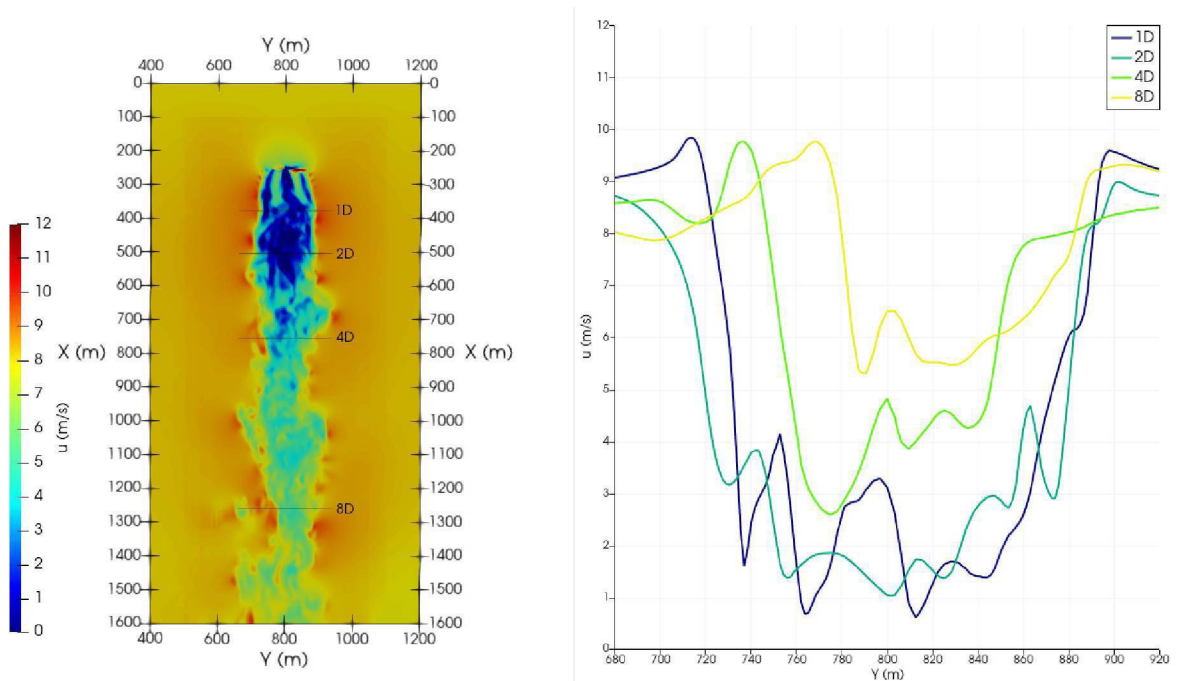
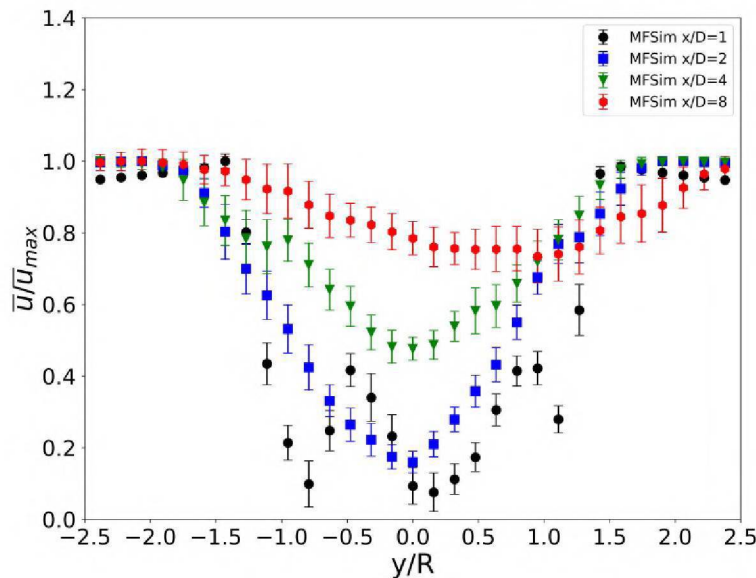


Figure 5.3.17 demonstrates that the velocity recovery is lower in the near wake when compared to the far wake for the wind turbine downstream. The velocities represented for the $x/D = 1$ and $x/D = 2$, reached velocity deficit around to 1 to 3 m/s in the swept area. Meanwhile, the $x/D = 4$ profile showed a velocity recovery between 3 to 5 m/s , and the far wake $x/D = 8$ profile presented a recovery around 6 m/s at the centerline. The wake diameter calculation is based on the velocity gradient between the low-velocity area in the centerline of the wake and the freestream wind velocity, which is a good representation of the wake boundaries. In terms of wake width the profiles presented to have close to 170 m for section 1D, 180 m for 2D, 140 m for 4D, 110 m for 8D.

Comparisons of the time-average streamwise velocity recovery over the wake cross-section have been analyzed for four cross-section locations, corresponding to downstream distances of 1D, 2D, 4D, and 8D, presenting the simulation for five levels of refinement, which are represented by Figure 5.3.18. For all cross-sections, 33 points have been chosen and separated into 16 points on each side of the centerline ($y/R=0$). The cross-section points were equally spaced, with 5 m between adjacent points. The total sampled cross-section width corresponds to 160 m . Besides that, the analysis considers the $x - y$ plane, where the height is at the wind turbine's hub. On the abscissa axis, the scaled velocity normalized by the maximum velocity \bar{u}/\bar{u}_{max} in the section with standard deviation is plotted against the transversal value y normalized by the radius of the blade R .

Figure 5.3.18 – Cross-section wake profiles for the 1, 2, 4, and 8 D downstream distances for the refinement region with 5 levels



The time-average streamwise velocity recoveries, displayed in Figure 5.3.18, for the five levels of refinement presented similar behavior, compared to the instantaneous field showed in the previous figure. The velocities expressed by the $x/D = 1$ and $x/D = 2$ profiles have reached a velocity deficit of around 10 to 20% of the maximum velocity at the centerline. At $x/D = 4$, there is a velocity recovery around 50% its maximum, at the centerline, while the $x/D = 8$ profile presented a velocity slightly above 80% of its maximum.

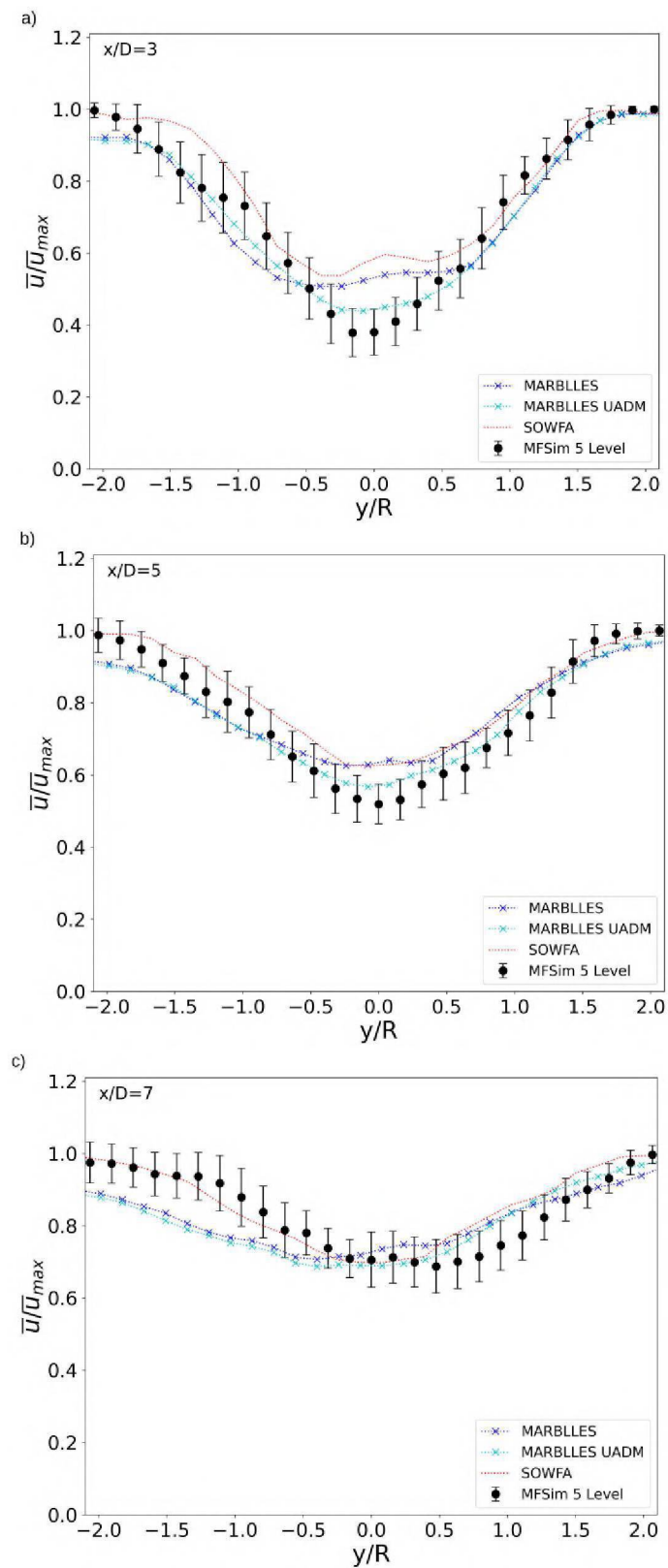
In order to validate the produced results from MFSim, the selected cross-sections are compared with the MARBLLES and SOWFA results, acquired due to the international exchange that had been occurred at the UBCO CFD Lab, from UBC. Since, there is no experimental data available regarding downstream wake modelling. Figure 5.3.19 depicts the time-average stream-wise velocity recoveries (\bar{u}/\bar{u}_{max}) with standard deviation over the wake width for downstream sections (x/D) of 3, 5, and 7 available from the comparison code's results.

As expected, the velocity profiles for $x/D = 3$, Figure 5.3.19(a), had low velocity recoveries around the centerline ($-0.5 < y/R < 0.5$), due to the closeness distance from the turbine, where the values of \bar{u}/\bar{u}_{max} ranged between 0.35 to 0.45 for the MFSim results. besides both MARBLLES numbers the figure also includes the results from SOWFA, which is also based on actuator line methodology. It is possible to observe that the MFSim profile had an increase in the velocity recovery compared to the previous downstream section, although the lower recoveries still occurring over the centerline with values slightly lower than $0.4 \bar{u}/\bar{u}_{max}$. Meanwhile, SOWFA reached values close to 0.6, MARBLLES around 0.53, and MARBLLES UADM produced the closest result to MFSim, close to 0.45, which leads to a difference of 34%, 27%, and 13%, respectively. This could be explained due the fact that both SOWFA and MARBLLES code apply actuator line and disk model, respectively, instead of fully resolving the wind turbine geometry, and they also did not account for tower and nacelle shading effects. Despite of that, outside region from the half of the blade, $y/R = \pm 0.5$, the MFSim deviations were able to capture most part of the velocity recoveries from the other codes, excepted by the range $-1.2 < y/R < -1.6$ for SOWFA resulting in a 14% difference, and from -1.05 to 0.85 y/R for MARBLLES leading a distinction of 17%. On the other hand, the most of points outside $y/R = \pm 0.5$ presented variations lower than 10%, where the highest accuracy occurred around to the blade's tip area ($y/R \approx \pm 1$) for SOWFA with lowest difference of 4%. However, compared to both MARBLLES results the MFSim profile obtained higher agreements close to half of the blade ($y/R \approx \pm 0.5$), and also in the regions just outside the blade's tip from $y/R \approx \pm 1.2$, where the highest accuracy reached differences lower than 1%.

The following section $x/D = 5$, illustrated by Figure 5.3.19(b), which corresponds to the transition region between near wake to far wake. Besides displaying greater velocity recovery compared to the previous ones, the profiles are characterized by their similar pattern. Despite of that, MFSim results still producing lower velocity recoveries in the centerline, where its lowest \bar{u}/\bar{u}_{max} is close to 0.52. Once again, the closest results was produced by MARBLLES UADM in this area, reaching $0.57 \bar{u}/\bar{u}_{max}$, difference of 9%, but this value is inside the MFSim upper deviation at the centerline. Meanwhile, SOWFA and MARBLLES results are pretty close to each other, they overestimate the MFSim results over the centerline, their recoveries are slightly over $0.6 \bar{u}/\bar{u}_{max}$, leading a difference just lower than 20%, which is the highest difference among the profiles. Out of the centerline region, from ± 0.3 in direction of the blade's tip, all the points produced deviation lower than 10% among the profiles compared to MFSim. Moreover, it can be seen that all MFSim results over the swept area ($-1 < y/R < 1$), their deviations incorporates at least one result from the other codes, even in the centerline where the difference is greater.

Entering in the far wake region, Figure 5.3.19(c) shows the results for the $x/D = 7$ section where there has been a more significant increase in the recovery velocity, which the

Figure 5.3.19 – Cross-section wake profiles comparison with UBC data for the 2, 3, 5 and 7 D downstream distances



lowest recovery was slightly lower than $0.7 u/\bar{u}_{max}$. On contrast with the previous downstream distances, the centerline region produced similar results among all the profiles, where from -

$0.4 < y/R < 0.4$, all u/\bar{u}_{max} values are inside the MFSim deviations, with differences lower than 7% in this region. It is possible to observe that both MARBLLES results underestimate MFSim results from $-2.0 < y/R < -0.7$, where differences are higher than 10% in most of the points, reaching the highest difference close to 17% at $y/R \approx -1.1$. However, MFSim results better correlated with SOWFA profile, where all differences were lower than 5%, excepted for 5 points around $0.7 < y/R < 1$, when the highest variation is 11.5%, which might be attributed to the direction of the blade rotation that offset MFSim result slightly to the right.

5.3.3.3 Vertical Profiles

The time-averaged streamwise velocity recovery behavior is considered for vertical profiles along the centerline. The analysis considers the $x - z$ plane, where the centerline is taken in place, which is the line of the tower ($y = 0$). Figure 5.3.20 showcases an instantaneous screenshot with mesh visualization to highlight the flow structures downstream of the turbine in vertical distribution. It also allows visualization of small turbulent structures in the near wake, and when the transition to far wake behaviour occurs around to $4D$ to $5D$, where larger eddies prevail. Moreover, in order to exemplify the velocity behavior, Figure 5.3.21 displays a dynamic representation of the instantaneous streamwise velocity u from a top point of view $x - z$ plane at the centerline ($y = 0$), demonstrating the visualization and characteristics of turbulent flow over the vertical distribution downstream of the wind turbine. Also providing a qualitative comparison among the four different downstream section of the simulation. The chosen sections $1, 3, 5$ and $8D$ downstream depicted on the graphs were based on the representation near and far wake, and also its transition region, without compromising the visual interpretation of the profiles.

Figure 5.3.20 – The flow velocity contours development in lateral view of the NREL 5MW wind turbine

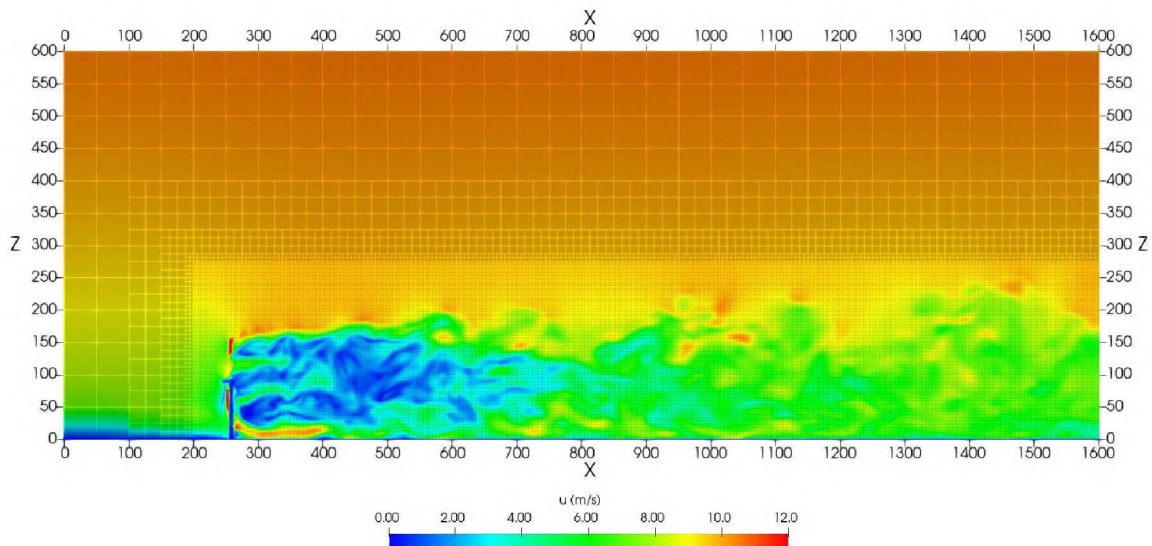
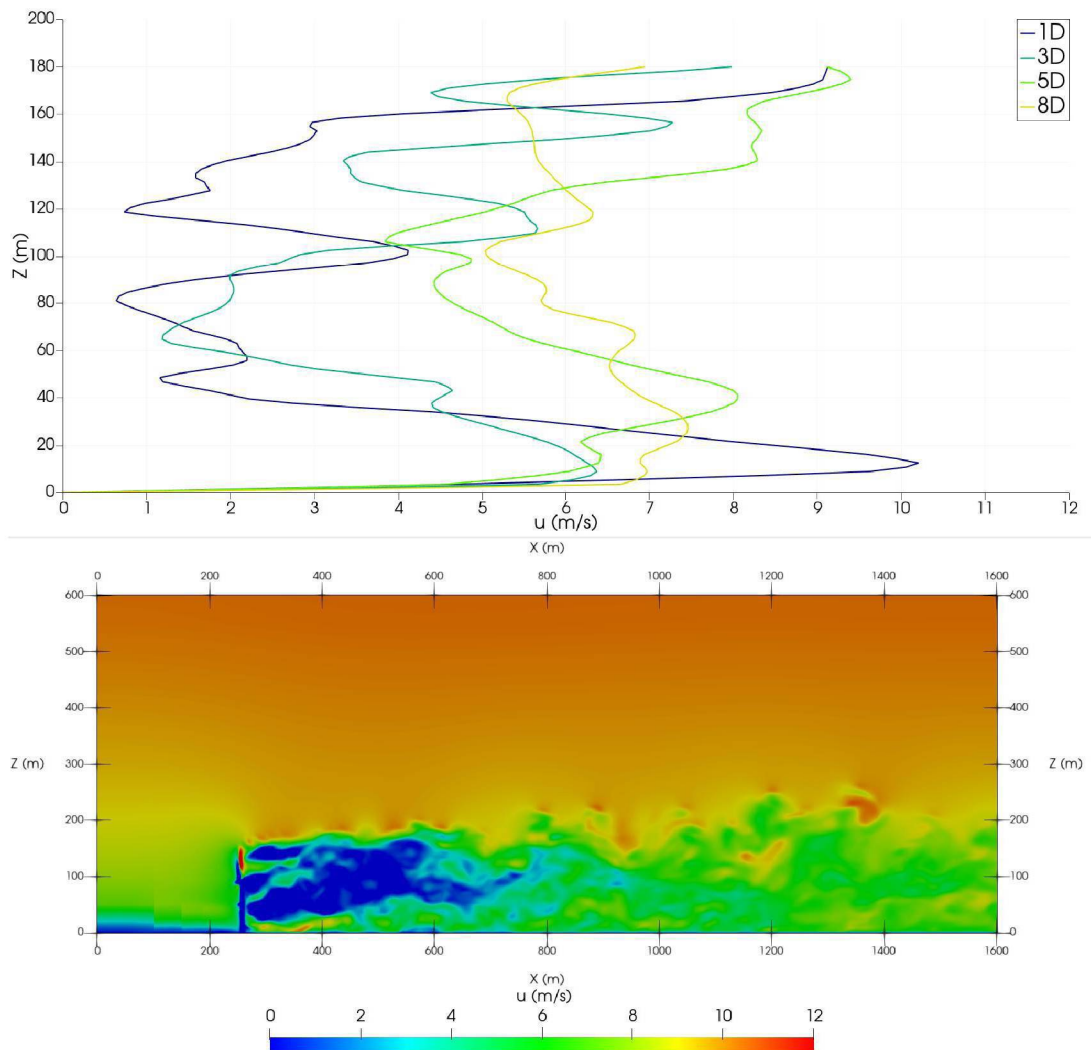


Figure 5.3.21 demonstrates that the velocity recovery is lower in the near wake when compared to the far wake for the wind turbine downstream, as expected. The velocities repre-

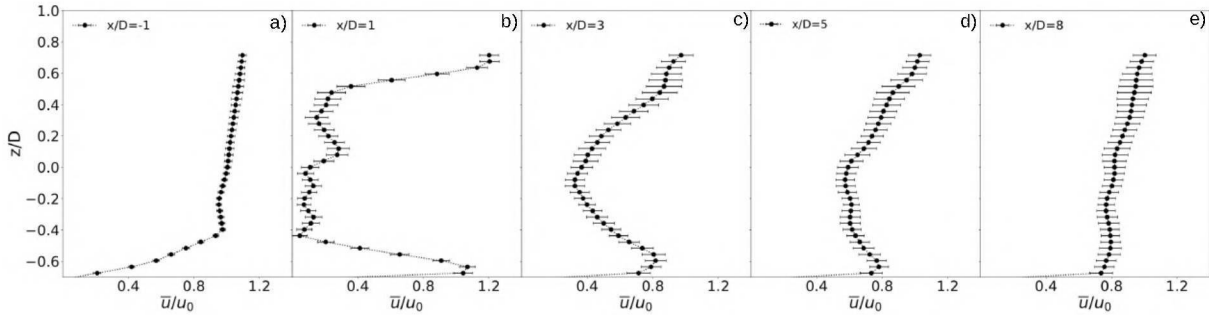
Figure 5.3.21 – The flow velocity contours development over the vertical around the NREL 5MW wind turbine



sented for the $x/D = 1$, reached instantaneous velocity recoveries close to 1 m/s just outside the hub height, and values around 3 to 4 on the blade's tip area. Meanwhile, the $x/D = 3$ profile showed a velocity recovery between 1.5 to 4 m/s , in the lower part of the swept area, from hub height to bottom tip of the blade, then increasing as the heights develops. Over the transition from near to far wake, represented by $x/D = 5$ profile, it is possible to observe that the lowest velocity recovery around the swept area occurs in the hub height region ($z=90\text{m}$) with values around 4 m/s . Lastly, the far wake $x/D = 8$ profile presented a recovery between 5 to 7 m/s for most part of the profile due the far wake velocity recovery.

Figure 5.3.22 illustrates the wind velocity profiles for five sections in the wake downstream, corresponding to downstream distances of $-1D$, $1D$, $3D$, $5D$, and $8D$, in order to integrate the instantaneous velocity presented in the previous figure over time. On the abscissa axis, we have the scaled component z/D , where $z/D=0$ corresponds to the hub height, plotted against the time-averaged streamwise velocity normalized by the inflow velocity \bar{u}/u_0 with standard deviations. In addition, for all vertical profiles, 37 points have been chosen and equally spaced with 5 m between adjacent points, reaching a maximum height of 180 m .

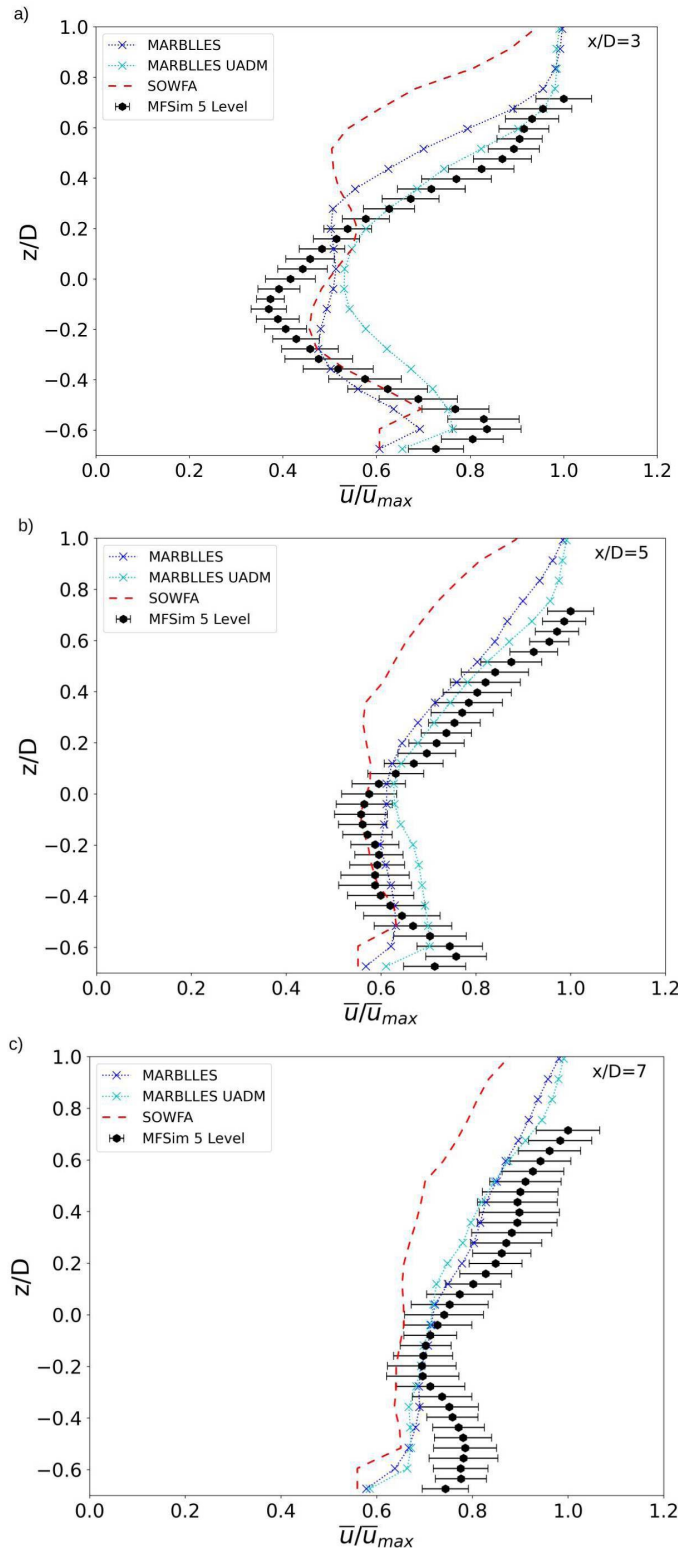
Figure 5.3.22 – Vertical wind velocity profiles subplots over downstream distance normalized by rotor diameters for the refinement region with 5 levels



The first section analyzed corresponds to the upstream distance of $x/D = -1$, illustrated in the first subplot of Figure 5.3.22 (a) which is the inflow velocity profile chosen in the simulation. From bottom to $-0.4 z/D$, there is quickly velocity increase from 0.2 to close to 1, due the ABL distribution in the inlet boundary condition. The first downstream section $x/D = 1$ is shown in Figure 5.3.22 (b), demonstrating high velocity deficits in the swept area, mainly between $-0.4 < y/R < 0.4$, where the results are lower than $0.3 \bar{u}/u_0$, then the waked region covers around $1.1 D$ total. The velocity recovery over the wake region begins to increase around the section $x/D = 3$ of 5.3.22 where the the lowest recovery occurred at the hub height with values of \bar{u}/u_0 around 0.4, or 40% of the inflow velocity. In the transitional region between near to far wake, representing $x/D = 5$, depicted in 5.3.22 (d) presents great increase in the velocity recovery, which the lowest recovery value jumped from 0.4 to near 0.6, or 60% of the inflow. While, in the last section that comprehends the far wake region, at $x/D = 8$, shown in Figure 5.3.22 (e), the velocity profile shows less wake effect since the profile tends to linear and uniform development of the velocity over height. Therefore, all the points present \bar{u}/u_0 higher than 0.7.

Aiming to validate the vertical results produced by MFSim, three selected downstream sections were chosen to compare with the results provided by the international exchange at UBC. The profile's results are presented in Figure 5.3.23 where the time-averaged streamwise velocity recoveries (\bar{u}/\bar{u}_{max}) with standard deviation are plotted against the z/D for the 3, 5, and 7 x/D downstream sections. Since there is no experimental data available regarding downstream wake effects from NREL, the comparison with MARBBLES and SOWFA results are crucial to validate the results from MFSim.

The first section analyzed corresponds to the upstream distance of $x/D = 3$, illustrated in the first subplot of Figure 5.3.23 (a). The highest differences among the profiles occurred slightly lower than the hub height ($z/D \approx 0$), where the values of \bar{u}/\bar{u}_{max} ranged around 0.4 for the MFSim results, while MARBBLES can reach values close to 0.5 and MARBBLES UADM showed numbers slightly lower than 0.55 in the this area. Which leads to a maximum difference from 25% to 32%, respectively. Meanwhile, SOWFA produced results around 0.47 at the same region and the difference between MFSim results is 19%. On the other hand, when the results develop in direction of the blade's top tip, from $z/D \approx 0.3$ and up, there is less influence from the tower and nacelle over the results. Thus, both MARBBLES UADM and MFSim results performed

Figure 5.3.23 – Vertical wake profiles for the 3, 5 and 7 D downstream distances

well between them, where at least eight points of the MFSim deviations include MARBLLES UADM results inside. The differences over this top region between both profiles did not exceed 8%, reaching its lowest lower than 1% at $z/D \approx 0.7$. However, the same performance did not happen with SOWFA results that produced the highest difference in this region, where values could reach just over than 40% variation compared to MFSim results, which might be attributed

do the actuator line approach at SOWFA. Despite of that, SOWFA and MARBLLES produced similar results compared with MFSim in the lower part of the swept area ($-0.45 < z/D < -0.2$), where the results are inside the MFSim deviations and demonstrating differences lower than 10%, even lower than 3% near $-0.3 z/D$.

Figure 5.3.23(b) depicts the section $x/D = 5$, localized in the transition region between near to far wake. It can be seen the evolution of the velocity recoveries compared to the previous section in the near wake. But, it is also noticeable the higher difference between SOWFA results compared to the other profiles above the hub height area, from $z/D \approx 0.1$ and up, where the highest variation is near 30% close to $0.65 z/D$. In contrast, both MARBLLES profiles produced similar behavior compared to MFSim results, where MFSim deviations included at least one of those codes from the hub height ($z/D=0$) to top tip of the blade ($z/D=0.5$). Over this section, MARBLLES UADM presented difference lower than 5% while MARBLLES showed values lower than 9% in comparison to MFSim profile in this area. However, in the lower part of the sweep area, between ($-0.4 < z/D < -0.1$), MARBLLES UADM displayed its highest difference compared to MFSim profile with velocity recovery \bar{u}/\bar{u}_{max} ranging from 0.65 to 0.7, where the variation could reach 16% difference between profiles. Meanwhile, MARBLLES results were in agreement with MFSim deviations between hub height to blade's bottom tip ($z/D=-0.5$), producing differences lower than 8% over this region, with velocity recovery a little bit over 0.6 \bar{u}/\bar{u}_{max} . Besides that, SOWFA and MFSim results over such area presented extremely similar results, which could be characterized by differences lower than 3% between the profiles in the range of $-0.5 < z/D < 0$, where the values of \bar{u}/\bar{u}_{max} vary from 0.56 to 0.63.

The furthest downstream section, $x/D = 7$, is shown in Figure 5.3.23(c). This section represents the far wake region results in the simulations, and also shows a greater increase in the recovery velocity for MFSim among the profiles, which the lowest recovery was near $0.7 u/\bar{u}_{max}$. It is possible to observe that SOWFA profile produced the lowest u/\bar{u}_{max} values for the whole vertical profile, with minimum value close to 0.56 in the bottom section of the profile, similar values occurred for both MARBLLES around $0.58 u/\bar{u}_{max}$, thus all profiles underestimate MFSim results in this region. Moreover, there are five points only where the SOWFA results are comprehended into the MFSim deviations, from -0.25 to $0 z/D$, where the variation are lower than 10% difference between profiles. Despite of that, from $z/D \approx 0.2$ and up, the results from SOWFA presented higher than 20% differences once again similar to the previous figure. On contrast, both MARBLLES and MFSim profiles demonstrated similar behavior from $z/D \approx 0.2$ to outside of the blade's top tip, where most of the both MARBLLES are inside the MFSim deviations, leading in variations lower than 11% among the profiles. Lastly, the best correlation came from the region around the hub height, with both MARBLLES presenting values close to $0.7 u/\bar{u}_{max}$, which leads to a lower than 1% difference between $-0.2 < z/D < 0$.

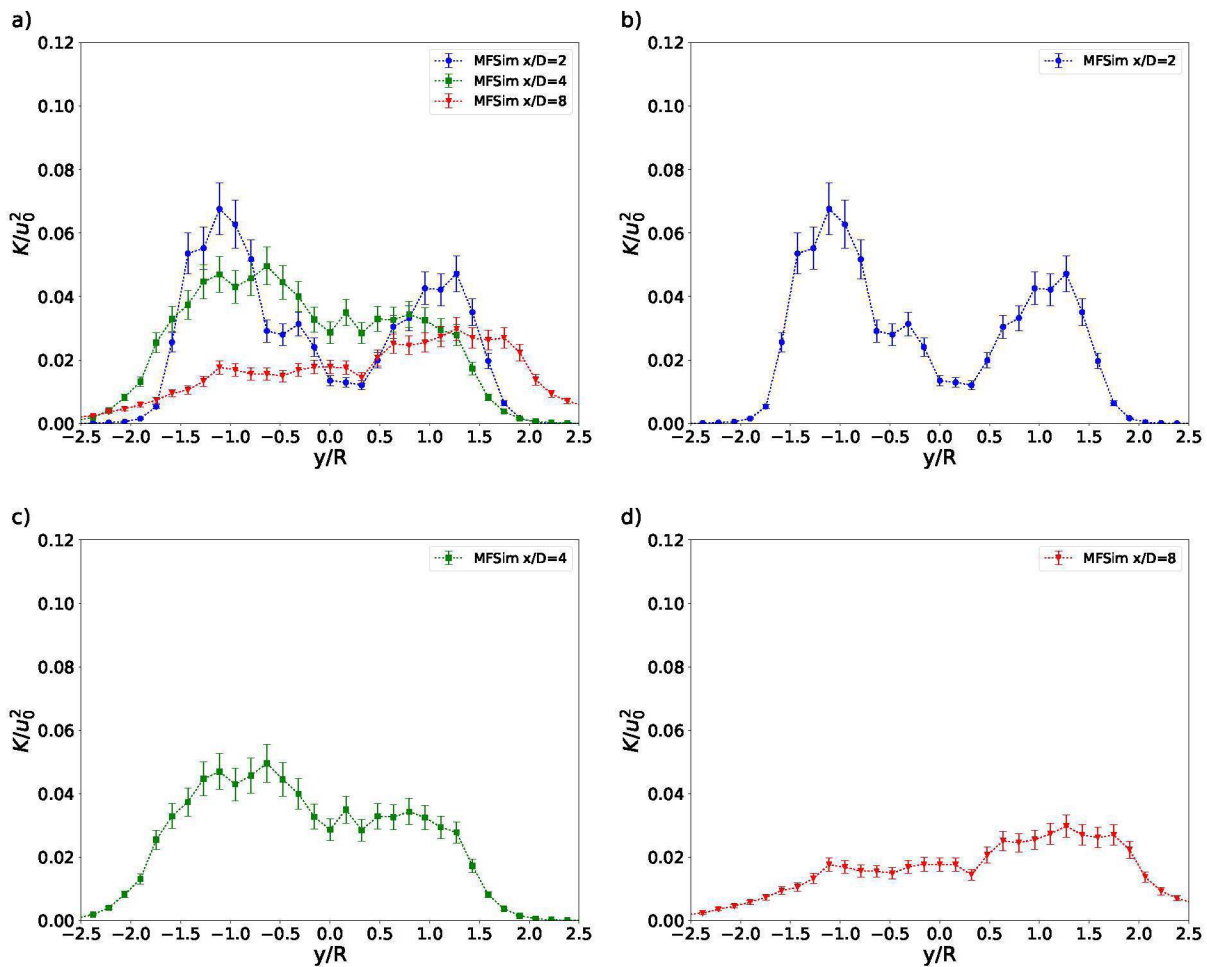
5.3.4 Profiles of Turbulence Properties and Spectrum

5.3.4.1 Turbulent Kinetic Energy

The first evaluation is through an analysis of the turbulent kinetic energy retained over the flow field. In order to have at least a qualitative idea of the level of resolution obtained

with the grid employed in the simulations, we computed the amount of resolved kinetic energy (CHEN; LIANG; LI, 2022). Figure 5.3.24 and 5.3.25 show the turbulent kinetic energy distribution normalized by the square of the inflow velocity k/u_0^2 with standard deviation along with the downstream distance evaluation. Figure 5.3.24 presents the analysis for cross-sections $2D$, $4D$, and $8D$ at the hub height, plotted against the transversal value y normalized by the radius of the blade R , while Figure 5.3.25 depicts the vertical profiles for the same sections at the centerline ($y=0$), where the height (z) is normalized by the rotor diameter (D).

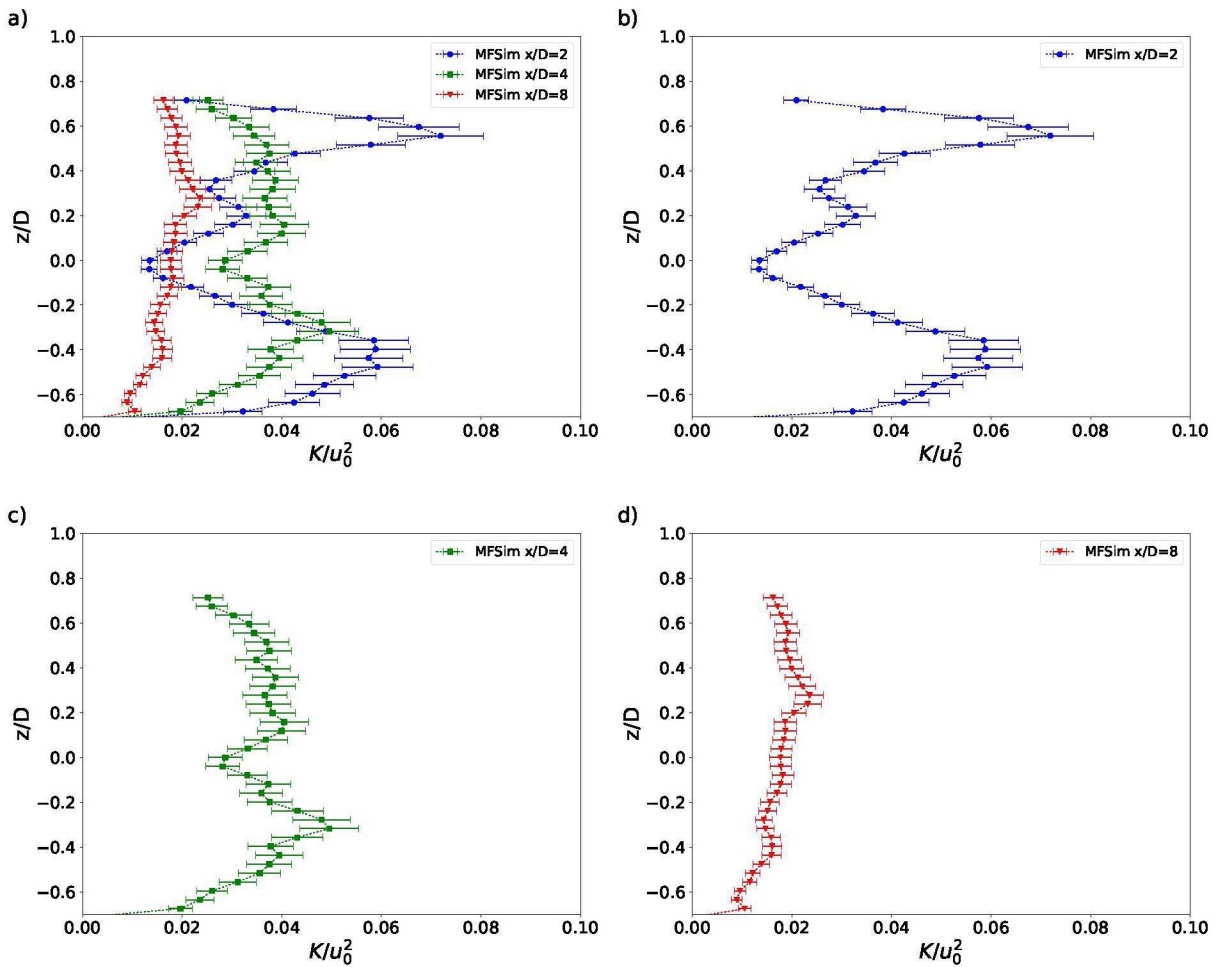
Figure 5.3.24 – Turbulent kinetic energy (k) cross-section wake profiles for the 2, 4, and 8 D downstream distances



Concerning the cross-section evaluation, the time-averaged turbulent kinetic energy (k) normalized by u_0^2 presented the highest values around 0.06 close to the blade tip for section $x/D = 2$. On the other hand, the lowest values of k/u_0^2 considering the swept area occurred at the centerline with values between 0.01 to 0.02, as depicted in Figure 5.3.24(a). The k/u_0^2 profile at section of $x/D = 2$ is shown alone in Figure 5.3.24(b), the results demonstrate two main peaks occurring on both blades tip region, where the left side peak around y/R of -1 is 0.06 while the right side peak at y/R close to 1 reached a maximum slightly over 0.04. The differences between the peaks could be attributed to the direction of the blade's rotation. The next section, at $x/D = 4$ illustrated by 5.3.24(c), representing the transition between near wake to far wake, the k/u_0^2 profile became more linear with values a little bit under and over 0.04,

between 0.03 to 0.05. Then at the furthest section, at $x/D = 8$, k/u_0^2 profile is characterized by lower values no greater than 0.03, suggesting that a larger dissipation of the turbulent kinetic energy has taken place.

Figure 5.3.25 – Turbulent kinetic energy (k) vertical wake profiles for the 2, 4, and 8 D downstream distances



Representing the similar sections as the previous analysis, but seeking to evaluate the behavior of k/u_0^2 in terms of vertical profiles is shown in Figure 5.3.25. Once again, it can be observed that higher value of k/u_0^2 occurred in the near wake, more specific around the top tip of the blade at $x/D = 2$, with values that can reach close to 0.08. Followed by values around 0.06 at the bottom tip of blade at the same downstream distance section. However, the lowest values around the swept area also occurred the $x/D = 2$ over the hub height ($z/D=0$) with values slightly above 0.01 k/u_0^2 . Moreover, at heights between -0.2 to 0.3 z/D , which is around the hub height, the k/u_0^2 values of $x/D = 4$ section produced the higher numbers, while $x/D = 8$ section depicted a virtually stable profile in the downstream direction to the far wake region.

Similar to Figure 5.3.24(a), Figure 5.3.25 (a), representing the vertical profile at the downstream distance $x/D = 2$, also shows two peaks around the blade's tip over its profile, where the top tip values are higher than the bottom tip. This can be attributed to the wind velocity ABL distribution implemented in the simulation and also due the fact that the bottom tip peak are in the tower shading area. In contrast, the transition section between near to far

wake, at $x/D = 4$ represented by Figure 5.3.25(b), there is a considerable reduced of k/u_0^2 at the top tip of the blade, ($z/D=0.5$), compared with the previous section. Meanwhile, at the hub height the k/u_0^2 still low, slightly over 0.02, but its highest values had occurred a little bit over the bottom tip of the blade height, close to $z/D=-0.4$, with values that can reach 0.05. Lastly, Figure 5.3.25(c) depicts the vertical profile of k/u_0^2 at the $x/D = 8$ downstream section, with values lower than 0.025 for its whole profile, and also characterized by its very linear profile due the larger dissipation of the turbulent kinetic energy at this further location in the far wake.

5.3.4.2 Turbulence Intensity

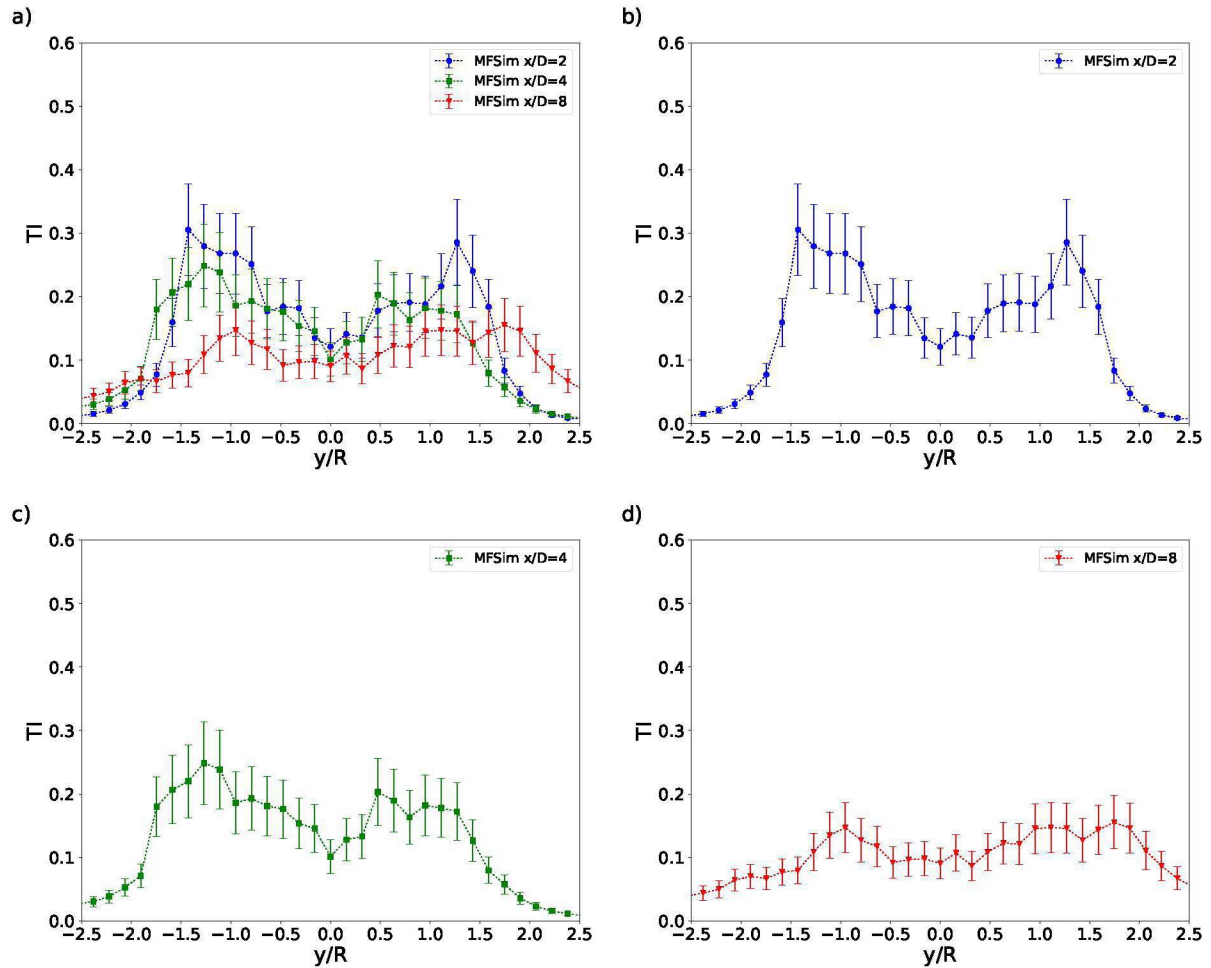
The following parameter to be analyzed is the turbulence intensity, aiming to determine its behavior in the wake downstream. It is significant to assess this parameter because turbulence developed from the upstream turbines impacts the power performance of the downstream turbines whenever the wind direction aligns with the correspondent wind turbines. Therefore, Figure 5.3.26 displays the cross-sections profiles of the time-averaged turbulence intensity (TI) with standard deviation, from 2, 4, and 8 x/D versus the transversal value y normalized by the blade radius R , from -2.5 to 2.5, considering the five levels of refinement region simulation. Meanwhile, Figure 5.3.27 also presents TI comparisons for the same downstream section, however illustrating vertical profiles from -0.7 to 0.7 z/D at the centerline of the downstream wake ($y=0$).

The results of Figure 5.3.26 demonstrate a greater predominance of TI occurring in the near wake of the flow as expected, with more significant values occurring in the section $x/D = 2$, as shown in Figure 5.3.26 (a), where values of TI reach levels close to 0.3 with deviations almost reaching 0.4, near outside the blade's tip area, $y/R = \pm 1.5$. This behavior is also produced by section $x/D = 4$, but in a lower scale, where its highest value reached a TI close to 0.25, while the furthest section downstream, $x/D=8$, did not express TI numbers over 0.2.

From Figure 5.3.26(b), section $x/D = 2$, it is worth noting that the TI values at the point of $y/R = 0$ are pretty low compared to the produced TI around $y/R = \pm 1$ to ± 1.5 , which might be due to the shading caused by the nacelle's geometry positioned in this region. Then, TI values decrease quickly in the direction of $y/R = \pm 2.5$ until they reach values close to zero, because no inflow turbulence occurs previously in the flow.

The section $x/D = 4$, the transition section between near to far wake displayed in Figure 5.3.26(c), demonstrates a larger distribution of TI over the swept area, in terms of width in y/R , while it showed a reduction in the TI values for the profile. Reaching maximum deviation values slightly greater than 0.3, and lower values close to 0.1 at the centerline. Finally, as expected, when the flow advances to far wake, the results of TI show quite small values, as can be seen in Figure C.4.5(d) displaying the $x/D = 8$ section. In this section, the TI values do not exceed 0.2 in the three simulation profiles. It also demonstrates greater uniformity and distribution of TI among profiles regarding the width y/R .

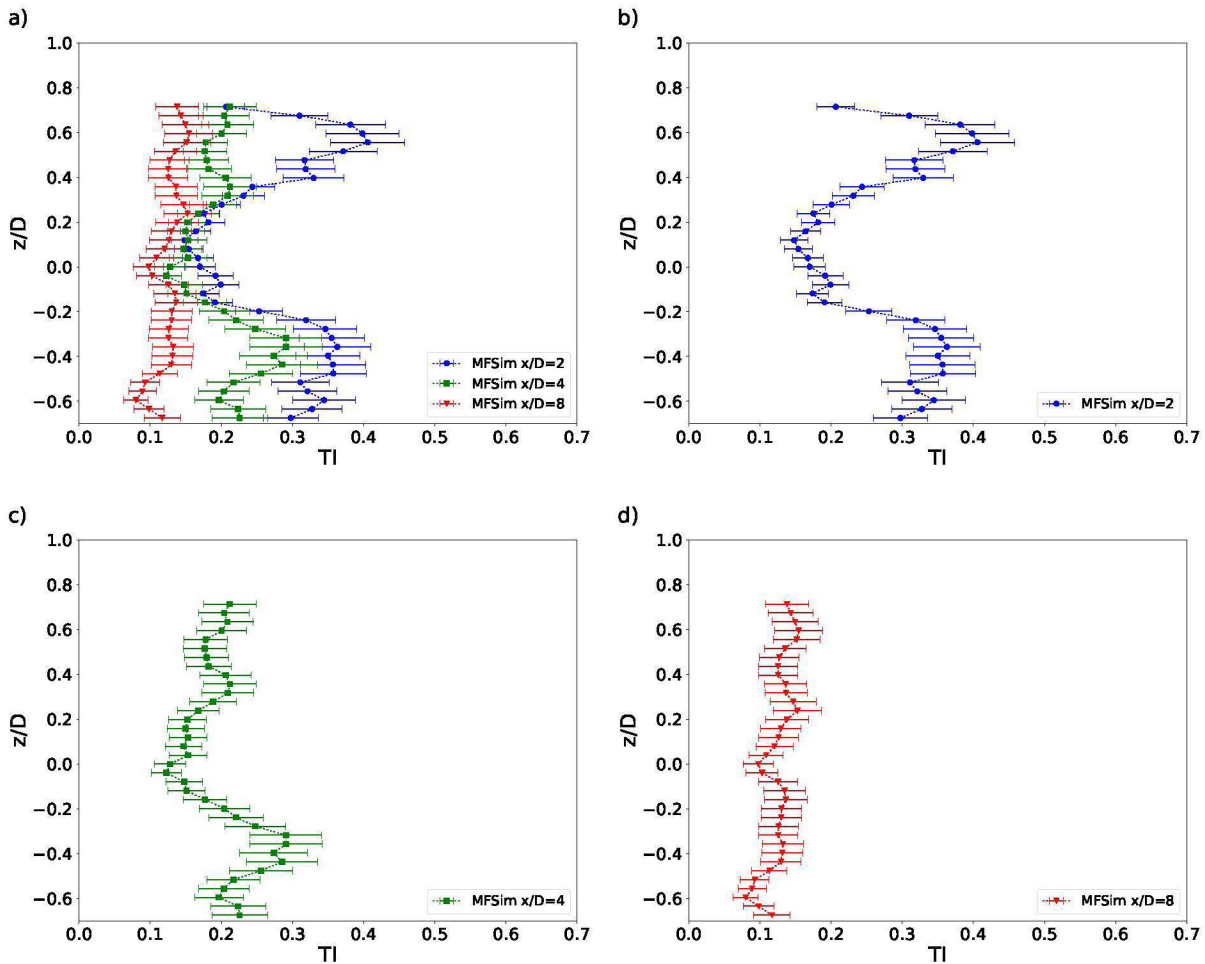
In terms of vertical profiles, depicted in Figure 5.3.27, the results also restate what it was inferred before concerning the high TI values occurring in the near wake of the wind turbine. Figure 5.3.27(a) shows the vertical profile for the section $x/D=2$ located in the near wake region

Figure 5.3.26 – Turbulence intensity cross-section wake profiles for the 2, 4 and 8 D downstream distances

where the turbine stands installed. It can be seen that the highest values occur just above the blade's top tip height, z/D around 0.5, with values of TI between 0.4 to 0.45 for $x/D=2$ section. Moreover, it is noticeable another peak of vertical TI distribution around the bottom tip of the blade with lower TI compared with the top tip region, with values close to 0.35 with deviations that can reach 0.4. This region around the blade's bottom tip ($-0.5 < z/D < -0.3$) had also presented the highest values of TI regarding the $x/D=4$ section, reaching values very close to 0.3. Meanwhile, at section $x/D=8$, the TI values occurred to be low due the larger dissipation at this far in the wake region, ranging between $0.8 < TI < 1.5$.

Figure 5.3.27(b) shows the first section downstream, $x/D = 2$, only by itself, demonstrates a lower TI distribution around the hub height compared to another regions of the profile, reaching values between 0.15 to 0.2, which is due the fact that the section is really close to the turbine then the nacelle's influence still high. In contrast to the previous section, the $x/D = 4$, represented by 5.3.27(c), presents lower values of TI around the top tip of the blade, region close to $0.5 z/D$, which indicates that the dissipation highly took place at this height. Meanwhile, the the blade's bottom tip region, the dissipation is lower due the closeness to the ground, which lead to the highest values of TI of its profile, close to 0.3 with deviations that could reach 0.35. As the flow develops away from the turbine, the values of TI tend to decrease considerably in

Figure 5.3.27 – Turbulence intensity vertical wake profiles for the 2, 4 and 8 D downstream distances



the far wake as shown in Figure 5.3.27(d) illustrating the results of $x/D = 8$ section. The profile shows that dissipation also retracted the results in the bottom region as well, and TI results not exceeded 0.2, even with the deviations for the whole profile.

5.3.4.3 Reynolds Stress Tensor Streamwise Component

Figure 5.3.28 shows the distribution Streamwise Reynolds Stress, $\sqrt{u'u'}/u_0$ with standard deviation, for downstream wake profiles of the turbine. The results were compared to the EllipSys3D and Sns code results from Laan et al. (2014), described in chapter 2, section 2.3.3. Both codes are based on LES, applying a Smagorinsky model with symmetry boundary conditions. However, the main difference from MFSim are: (i) no immersed boundary methodology, (ii) they apply an actuator disk method instead of fully resolving the wind turbine, and (iii) the turbulence is modeled with the Smagorinsky model over the Dynamic Smagorinsky. The authors also simulated an NREL 5MW, where they set a uniform mean velocity of 8 m/s at the inlet. The wind turbine is modeled as an actuator disk, representing the geometry of the rotor as a disk of 126 m.

The first analysis, Figure 5.3.28 (a), consisted of plotting three downstream sections with

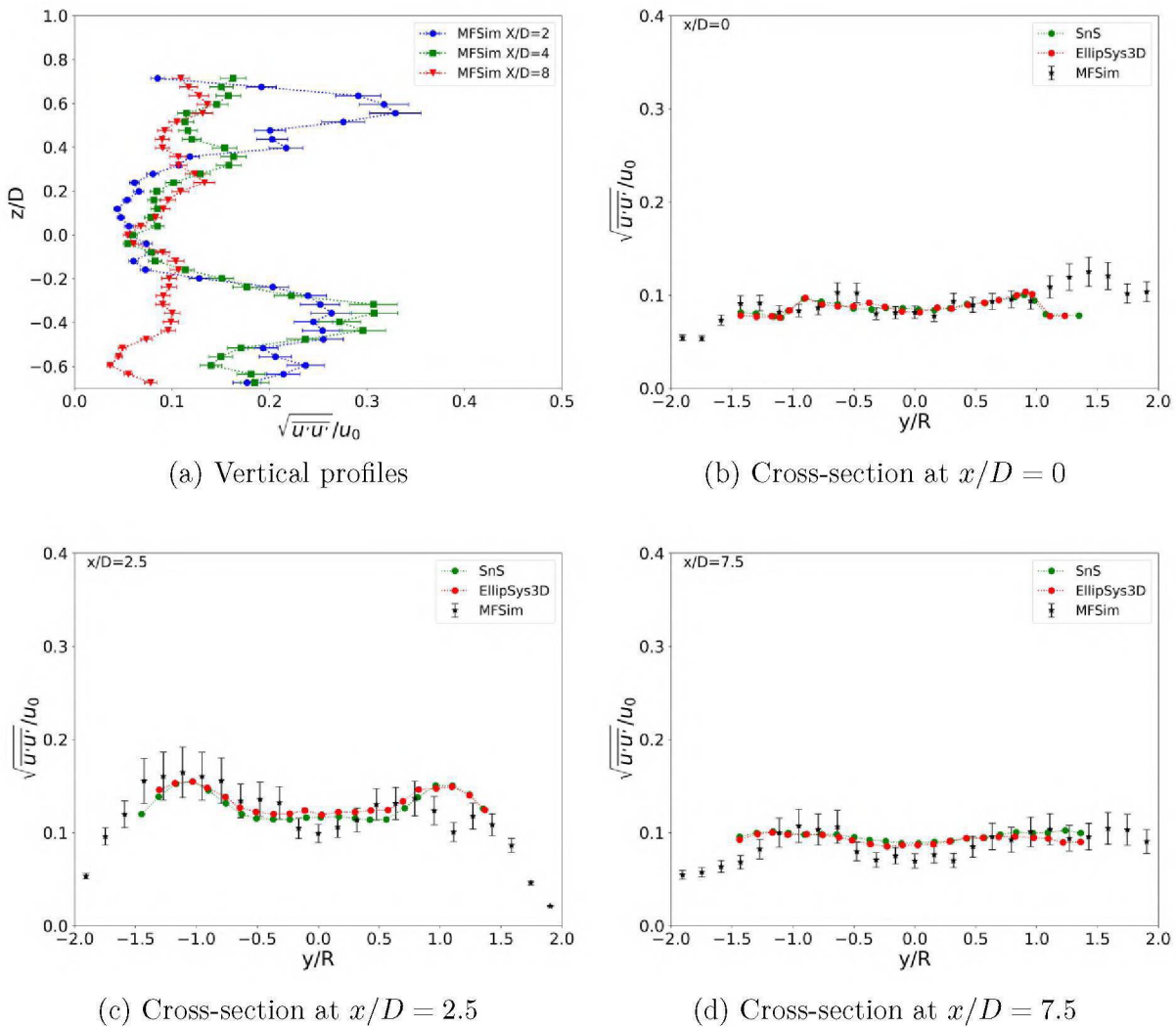
vertical profiles of MFSim results in order to represent the $\sqrt{u'u'}/u_0$ distribution over different heights. Unfortunately, no data was available from EllipSys3D and Sns code considering vertical profiles. The vertical MFSim results demonstrates lower values of $\sqrt{u'u'}/u_0$ occurring around the hub height, $-0.2 < z/D < 0.2$, ranging from 0.07 to 0.12. In the region close to the bottom tip of the blade, around $-0.6 < z/D < -0.3$, it is large the difference between near and far wake regarding the $\sqrt{u'u'}/u_0$ results. While, profiles $x/D = 2$ and $x/D = 4$ present higher values close to 0.27 and 0.32, respectively, the far wake represented by $x/D = 8$ profile did not exceeded 0.1. However, on the other side of the blade tip, in the top between $0.4 < z/D < 0.6$, only the $x/D = 2$ profile presented high numbers of $\sqrt{u'u'}/u_0$, reaching close to 0.35, the maximum value of the analysis. Meanwhile, profiles $x/D = 4$ and $x/D = 8$ ranged between 0.1 to 0.2 at this height, which restates that the dissipation happens earlier over the wake downstream for higher heights.

In terms of the comparison with EllipSys3D and Sns results, the $\sqrt{u'u'}/u_0$ is plotted versus the transversal value y normalized by the blade radius R , from -2.5 to 2.5, considering cross-sections profiles of 0, 2.5 and 7.5 x/D , illustrated in Figures 5.3.28 (b), (c), and (d). Section $x/D = 0$, depicted in Figure 5.3.28 (b), represents the location where the wind turbine was placed. The MFSim results performed well compared to EllipSys3D and Sns, with differences lower than 10% for all points among the codes over the swept area, from $-1 < y/R < 1$, where $\sqrt{u'u'}/u_0$ ranged around 0.1 with small variations of ± 0.01 . The highest difference occurred outside the right blade's tip, where MFSim results reached values close to 0.12. At the same time, EllipSys3D and Sns decreased to approximately 0.08, which might be explained due to the direction of the blade's rotation. Likewise, the other two codes did not account for the real turbine design, in which the turbine is modeled using an actuator disk.

For the section $x/D = 2.5$, relative to the near wake as shown in Figure 5.3.28(c), the results show values of $\sqrt{u'u'}/u_0$ for EllipSys3D and Sns ranging from 0.1 to 0.16, with two small peaks occurring on both blade's tip area, where their maximum values are 0.16. Meanwhile, MFSim results presented $\sqrt{u'u'}/u_0$ values from 0.09 to 0.17 over the same area covered by EllipSys3D and Sns codes, $-1.5 < y/R < 1.5$. In this region, most of the points produced differences among the profiles lower than 10%, except in the right blade's tip region (around $y/R=1$), where the difference between the results reached close to 30% that might be caused, once again, by the direction of rotation of the turbine, and also could be attributed to the inflow turbulence introduced at the inlet of the EllipSys3D and Sns codes. On the other hand, the MFSim results demonstrated great performance in both blade's tip region compared to the EllipSys3D and Sns results in the far wake section ($x/D = 7.5$), illustrated in Figure 5.3.28(d), where both references are inside MFSim deviations, ranging from 0.09 to 0.125, and also produced differences lower than 5% around $y/R \pm 1$. Over the centerline region, close to the blade root, the results presented a higher difference but did not exceed 15%, where $\sqrt{u'u'}/u_0$ values range from 0.085 to 0.1 among the profiles.

5.3.4.4 Spectrum of Turbulent Kinetic Energy

According to the Pope (1999), approximately 80% of the turbulent kinetic energy needs to be resolved in a well resolved LES. In order to have at least a qualitative idea, a partial

Figure 5.3.28 – Streamwise Reynolds Stress ($\sqrt{u'u'}/u_0$) analysis for downstream sections

verification of the numerical results can be performed by computing power spectral density of the turbulent kinetic energy (CHEN; LIANG; LI, 2022). The following section describes the power spectral density (PSD) of the turbulent kinetic energy, $E(f)$, for the LES simulations within the wind turbine wake to quantitatively study the wake instability. The $E(f)$ time series of distinct points in the wake region were recorded and used to analyze the PSD distribution, and the power law decay $k^{-5/3}$ were added for better comparison.

Figure 5.3.29 presents the turbulent kinetic energy spectrum, $E(f)$, for the LES simulations. The probes were chosen in order to represent one section upstream of the wind turbine, located at 1D upstream, and five downstream distances from the wind turbine, located at 1, 2, 4, 6, and 8 D. The probes are located at the hub height and the centerline location of the control volume. As it can be seen, the results for all analyzed sections present a broad and continuous spectrum characterizing turbulent flow regime.

The closest sections of the turbine, -1D and 1D, show a spectrum with greater amplitude, at frequencies from 10^2 to 10^3 . Figure 5.3.29(a) presents a uniform spectrum for lower frequencies due to the non-insertion of turbulence at the entrance of the domain, without introducing a

turbulence intensity condition in the inlet boundary condition. Meanwhile, in Figure 5.3.29(b), the decay of the energy spectrum starts from a frequency of 3 to 4 Hz , also showing a decaying trend beginning closer to $-5/3$, which may indicate that turbulence is developing in this region.

Figures 5.3.29 (c) and (d) show the sections between the near wake to far wake of 2D and 4D, respectively, where the highest amplitudes occur around the frequency of 10 to 25 Hz . Also from 4D to further, the spectrum indicated the presence of secondary vortex and the spectrum turned to be closer to the $-5/3$ logarithmic decay curve compared to the previous ones. With similar behavior, the Figures 5.3.29 (e) and (f) representing the far wake with sections in 6D and 8D, respectively, present their higher amplitudes between frequencies from 20 to 30 Hz . Further, most of the sharp peaks in the PSD spectrum at 6D and 8D vanished, thus suggesting a complete turbulence wake state.

Figure 5.3.30 presents the turbulent kinetic energy spectrum, $E(f)$, for near wake representations over the centerline. The probes were chosen in order to represent the induction region upstream of the wind turbine, located at 0.2D and 0.1D upstream, and four near wake downstream distances from the wind turbine, located at 0.1, 0.2, 0.4, 0.6. The probes are located at the hub height and the centerline location of the control volume.

For the induction region upstream of the wind turbine, Figure 5.3.30 (a) and (b), the density spectrum presents a small perturbation with very well captured power-law decay of $-5/3$. Moreover, these figures show a lower noise distribution in comparison with the first two downstream sections at $x = 0.1D$ and $x = 0.2D$, represented by Figure 5.3.30 (c) and (d), which is characterized by high noise density and the wake consists of an unstable hub bluff body like vortex, with the first distinguished frequency amplitude occurring around 50 Hz . Figures 5.3.30 (e) and (f) representing 0.4 and 0.6D, respectively, the density spectrum visible presents less noise than the previous ones. The initial interaction starts near 10 to 20 Hz at this downstream distance, further downstream from hub height there is an increasing, and inducing of generation, and evolution of the secondary vortex warping around the hub vortices.

In order to exemplify the tip vortex around wind turbine blades, Figure 5.3.31 presents the turbulent kinetic energy spectrum, $E(f)$, of the blade tip and near wake tip vortex points. The probes were chosen based on the blade's passage at $x = 0D$, and near wake at $x = 0.5$, and $x = 1D$ downstream of the wind turbine, over the spanwise direction of $y = \pm 1R$.

Further, the density spectrum at $x = 0D$, Figures 5.3.31 (a) and (b), exhibited sharp peaks over the blade region and at all its second and third multiples, indicating a stable tip vortex for probes 461 and 467 ($Y = -1R, X = 0D$ and $Y = 1R, X = 0D$). Additionally, the magnitude of the entire spectrum further increased and no tonal component could characterize it after 300 Hz .

At $x = 0.5D$, Figures 5.3.31 (c) and (d) the density spectrum is characterized by the presence of secondary vortex besides blade frequency and its harmonics, which appears to be in transition from stable to unstable tip vortex for probes 465 and 471 ($Y = -1R, X = 0.5D$ and $Y = 1R, X = 0.5D$), since the peaks are not very sharp anymore and emerging pairing between the tip vortices. Meanwhile, for probes 462 and 468 ($Y = -1R, X = 1D$ and $Y = 1R, X = 1D$) representing $x=1D$, Figures 5.3.31 (e) and (f), the density spectrum is visible less noise than the

Figure 5.3.29 – Spectrum of Turbulent Kinetic Energy from upstream 1D to downstream 8D in the longitudinal centerline

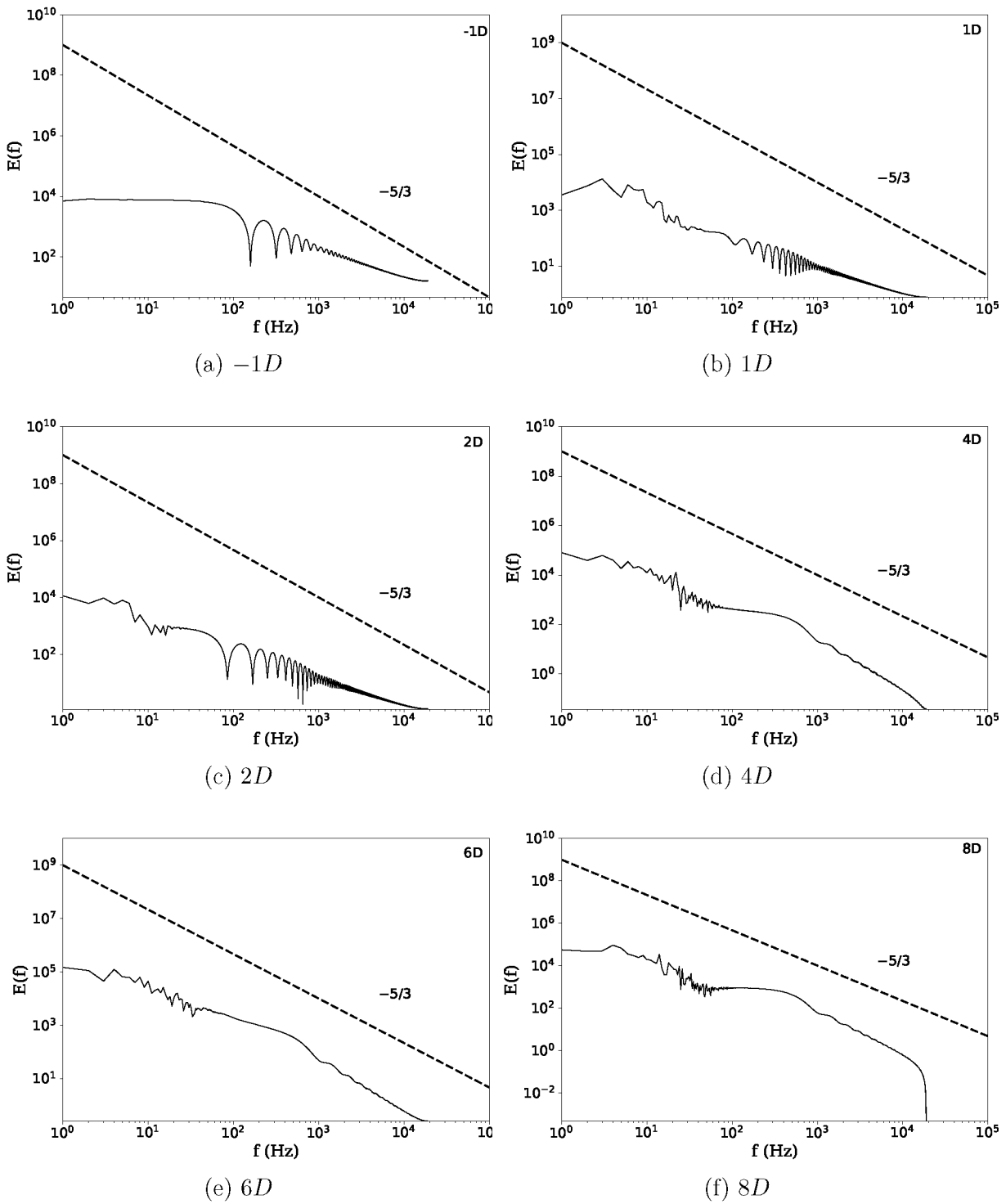


Figure 5.3.30 – Spectrum of Turbulent Kinetic Energy around the induction region and near downstream wake

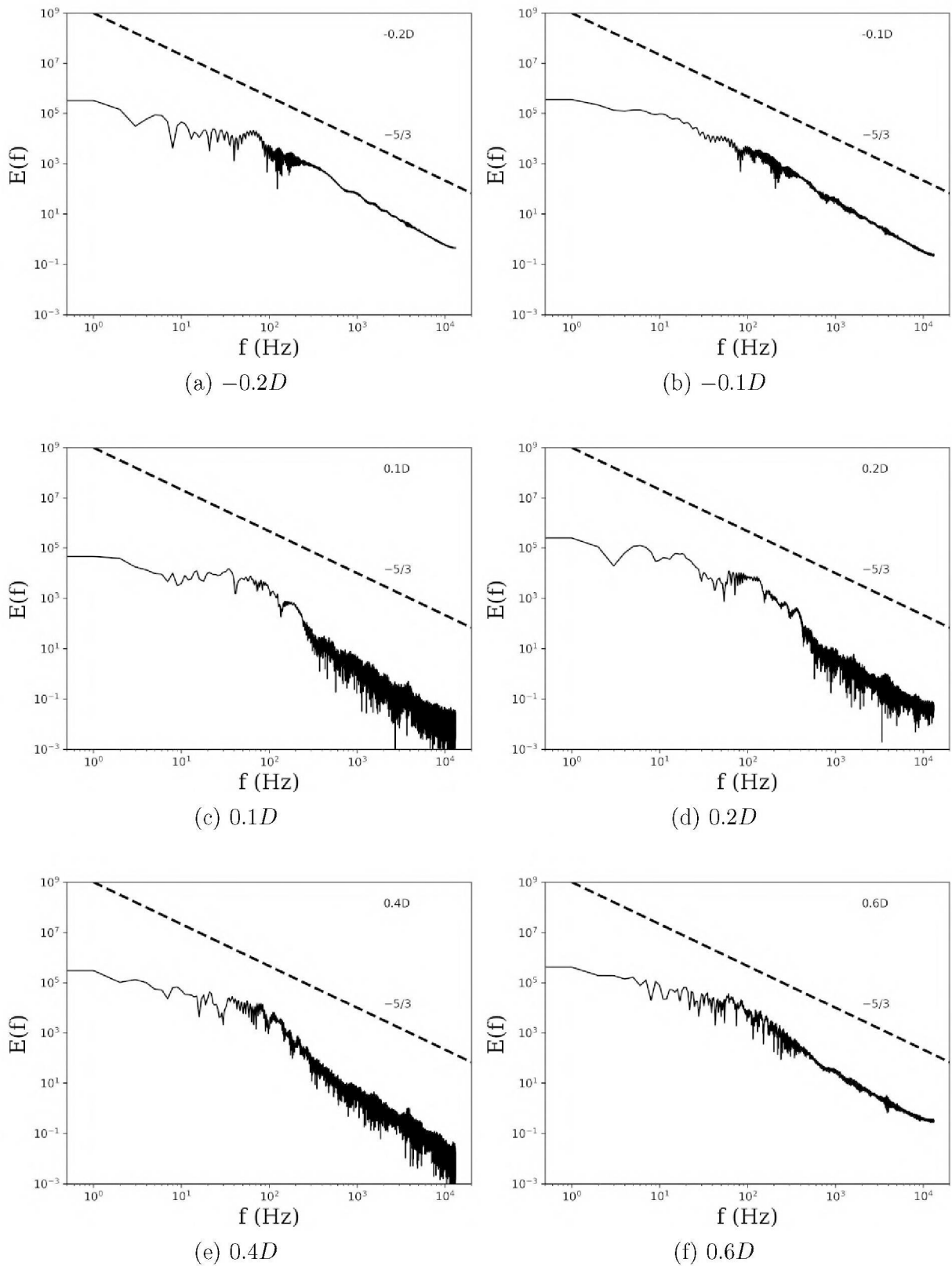
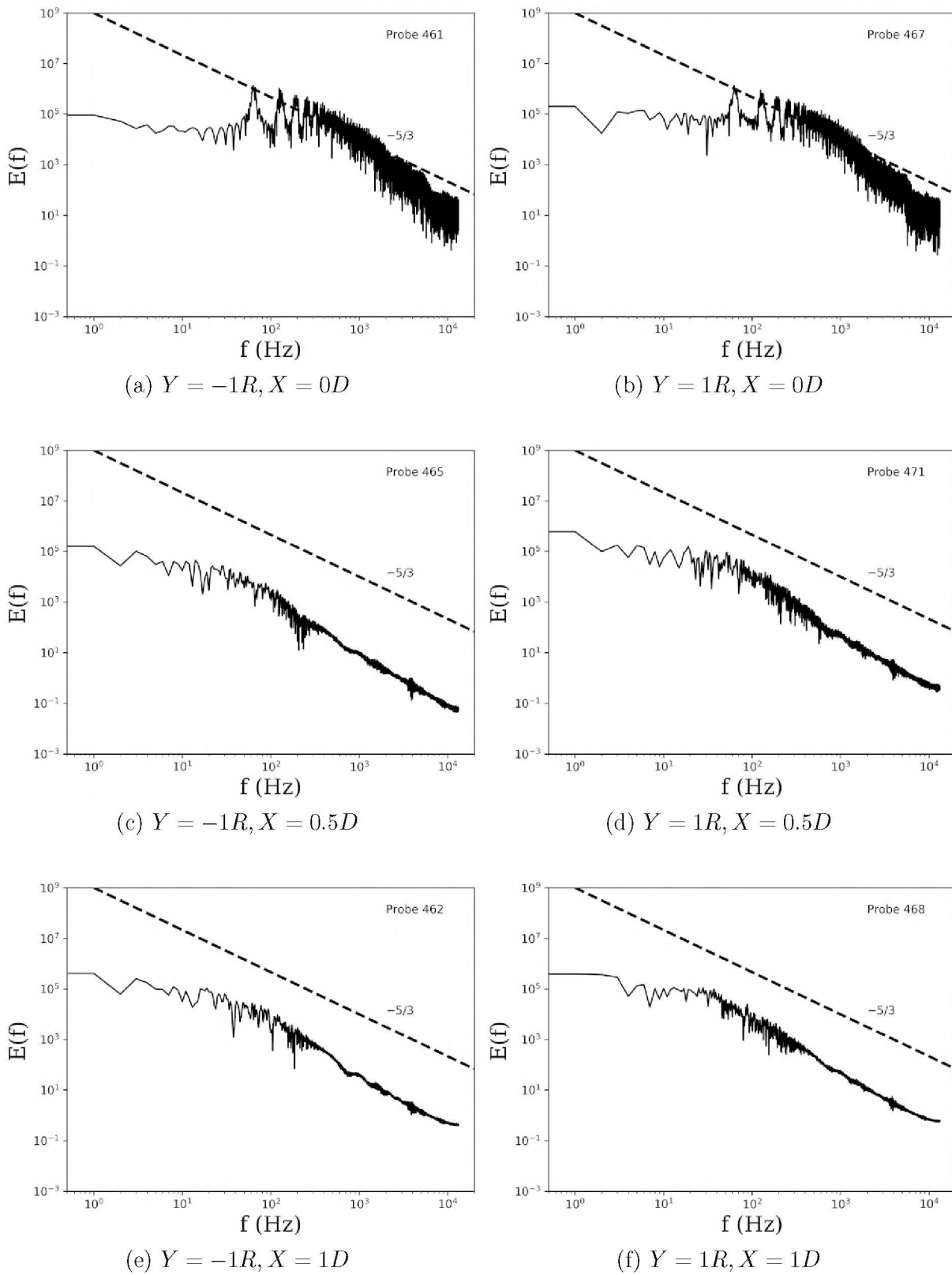


Figure 5.3.31 – Spectrum of Turbulent Kinetic Energy around blade's region



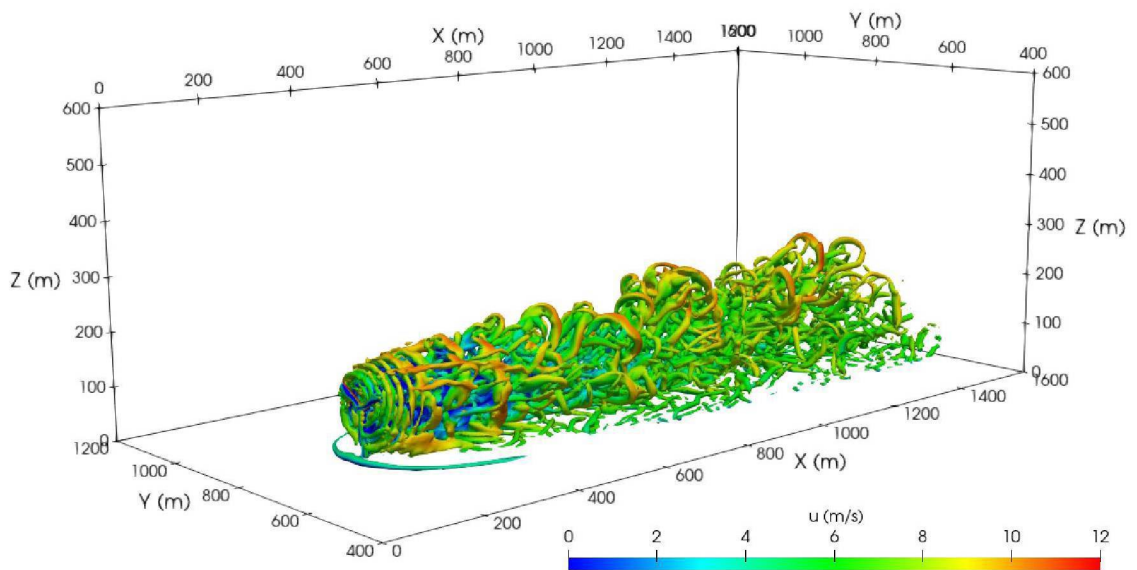
previous ones. Further, although under the influence of ABL flow the wake became slowly to be unstable, as most of the sharp peaks in the PSD spectrum are vanished in parts.

In regions where the energy spectrum has greater amplitude, the flow is consequently more turbulent, indicating higher velocity gradients on those regions. However, this results analysis is still a preliminary evaluation of the energy spectrum from the NREL 5 MW simulations. Future studies on this topic will be important in order of achieving even more refined mesh simulations, which enables capturing smaller turbulent structures, thus solving a higher part of the flow instead of modelling. These would be possible by decreasing the control volume for regions closer to the turbine and further refining the mesh, increasing as low as possible the computational cost.

5.3.5 Qualitative Analysis of the Flow Turbulent Structures

This section presents analyses to demonstrate that the LES-IB methodology is capable of simulating the interaction within the NREL 5 MW wind turbine and flow structures. Figure 5.3.32 shows a dynamic representation of the iso-surfaces colored by streamwise velocity, in order to provide important visualization of eddies occurring over the turbulent flow. Vortex structures occur in the region close to the blade's tip, which is transported over the flow forming helical shaped structures. These structures originate due to centrifugal flow acceleration, in which the fluid moves from the root towards the tip of the blade (DASARI et al., 2019; REGODESEVES; MORROS, 2021). Therefore, the vortices structure patterns are straight connected to the turbine's operational parameters.

Figure 5.3.32 – Dynamic iso-surfaces colored by velocity over flow around the wind turbine



Moreover, in order to restate the qualitative analysis, Figure 5.3.33 display instantaneous iso-surfaces colored by vorticity magnitude with a 3D visualization. Figure 5.3.33 (a) shows that higher values of vorticities, over 1 (1/s), are occurring in the near wake close to the turbine, while Figure 5.3.33 (b) demonstrated a decrease on the vorticity intensity as the flows develops around

the transition region from near to far wake, with values around 0.5 (1/s). In addition, Figure 5.3.33 (c) displays that lower values of vorticity are predominant over the far wake, therefore the vortices are carried over the flow, but reducing its intensity as the downstream development.

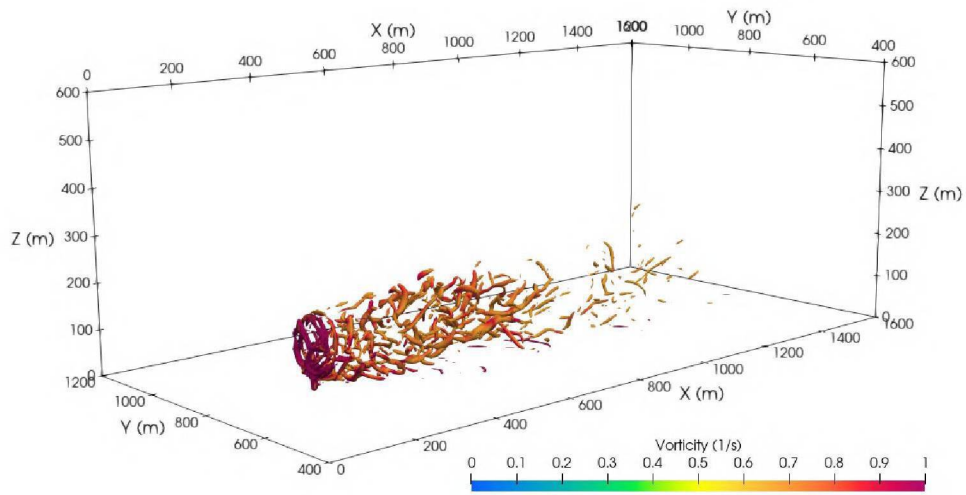
Contours of the magnitude of the instantaneous gradients are plotted in Figure 5.3.34 to highlight the flow structures around the wind turbine. Figure 5.3.34 shows instantaneous velocity contours in an xy plane at the hub height, while Figure 5.3.34 displays the wind velocity on an xz plane at the centerline. It is possible to observe the development of different flow structures in the wake, depending on the distance and height analyzed, decreasing the intensity of the magnitude of the gradients transported to the far wake concerning the near wake while the size of the larger structures predominant in the far wake. The highest magnitude of the gradients above 4 (1/s) also occurs in the rotor region. Therefore, reaffirming the previous vorticity analysis that demonstrated high vorticity values were found over the same region.

As the most elevated vorticity and gradient intensities arose near the turbine, screenshots of instantaneous vorticity contours are shown to analyze this region of the turbine. Figure 5.3.35 shows the vorticity magnitude for the xz plane, at $x/D = 0$ around the turbine, where the highest vorticity values are densely scaled over the flow field. Therefore, it is possible to see that the highest vorticity densities occur mainly over the blade's area. More specifically, as shown in Figure 5.3.36, the vorticity values tend to increase from the blade's root to the blade's tip direction.

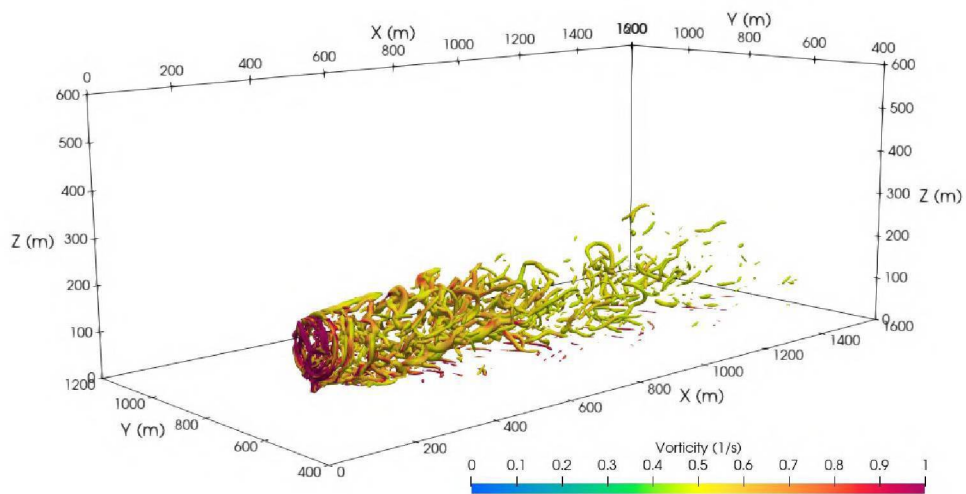
With that said, it was aimed to comprehend which gradient had the most contribution over this area. And following the mathematical definition of vorticity, as a curl of the velocity vector, $\nabla \times \vec{u} = \left(\frac{\partial w}{\partial x} - \frac{\partial v}{\partial z}\right)\vec{i} + \left(\frac{\partial u}{\partial z} - \frac{\partial w}{\partial x}\right)\vec{j} + \left(\frac{\partial v}{\partial x} - \frac{\partial u}{\partial y}\right)\vec{k}$. As the vector field is a velocity field in a flow, this measure indicates the rotation existing in the flow.

Figure 5.3.37 depicts the instantaneous gradient components contours around the swept area, where the most significant contributions come from the velocity gradients $\partial v/\partial x$ and $\partial w/\partial x$ concerning the spatial variation in the flow direction (x), primarily responsible for the downstream tip vortices structures (AKAY et al., 2014). Meanwhile, the sum of the contributions of $\partial w/\partial y$ and $\partial v/\partial z$, are accountable for the streamwise component of the vorticity, presenting the highest contribution on the leading edge of the blade's tip.

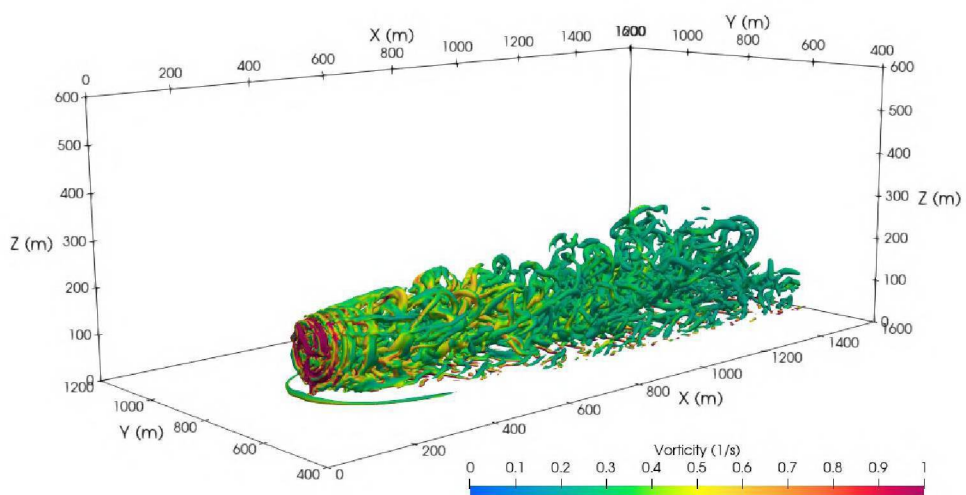
Figure 5.3.33 – Iso-surface colored by vorticity over and downstream of the NREL 5MW, where a) captures vorticity above 0.7, b) over 0.5, and c) all the vorticity range



(a)



(b)



(c)

Figure 5.3.34 – Contours of gradients over flow around the wind turbine, for (a) xy-plane, and (b) xz-plane

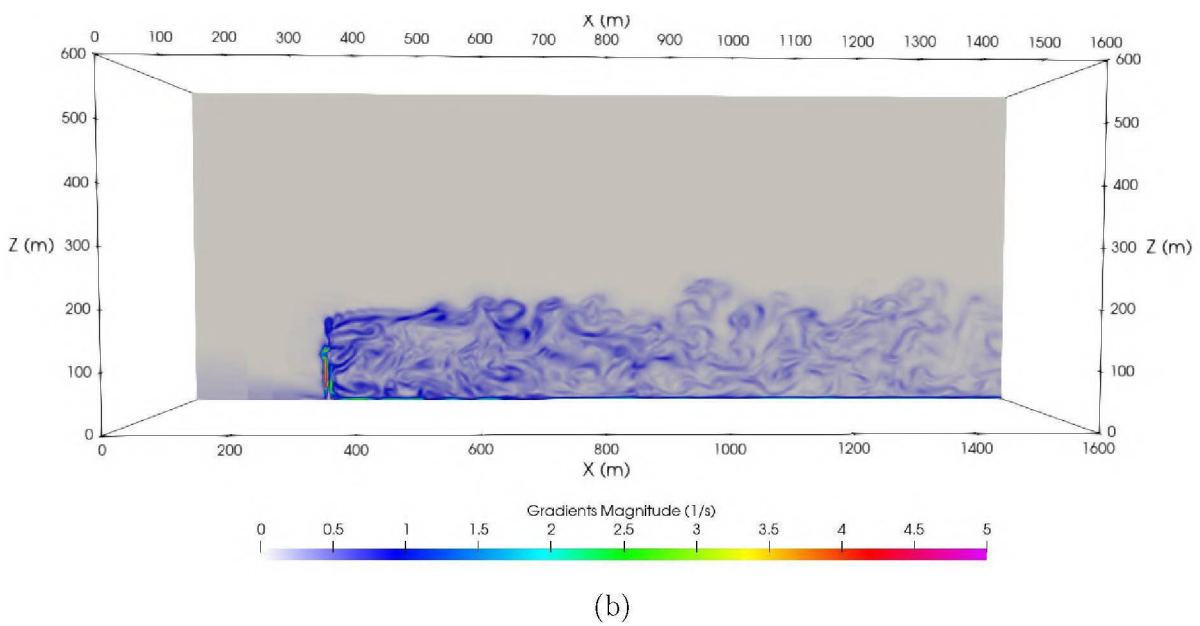
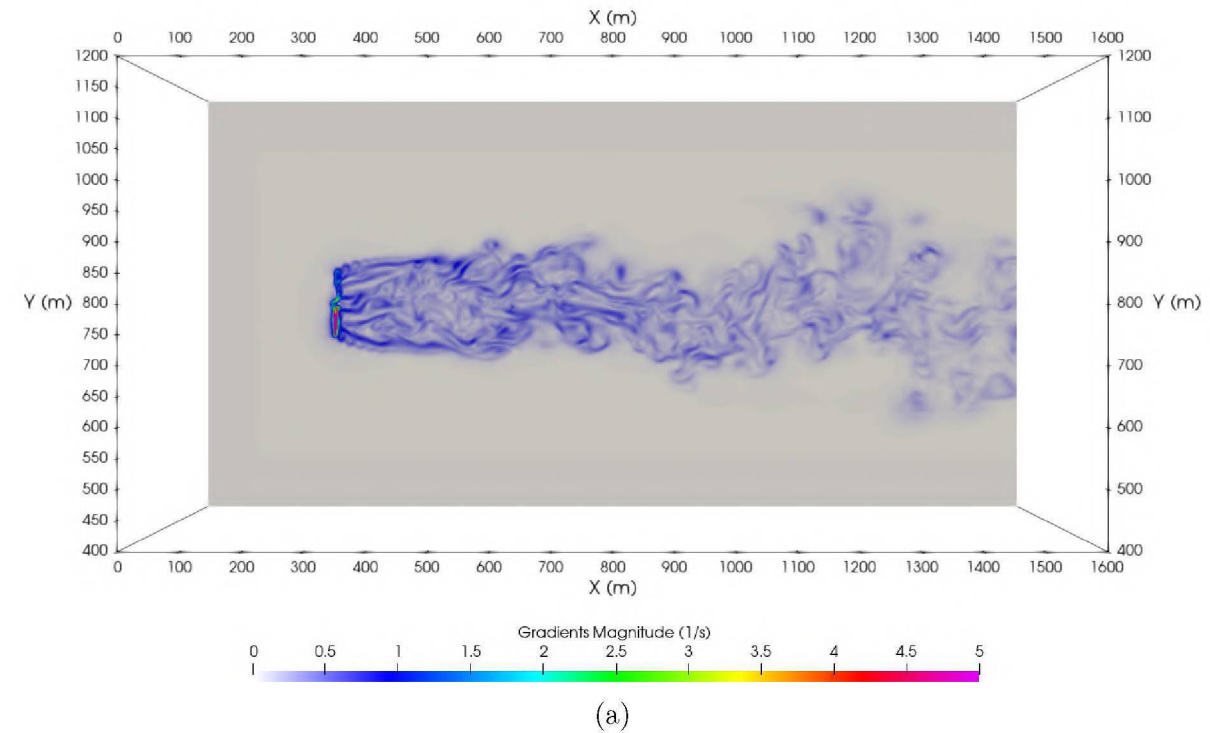


Figure 5.3.35 – Vectors of vorticity magnitude in the downstream position of the wind turbine

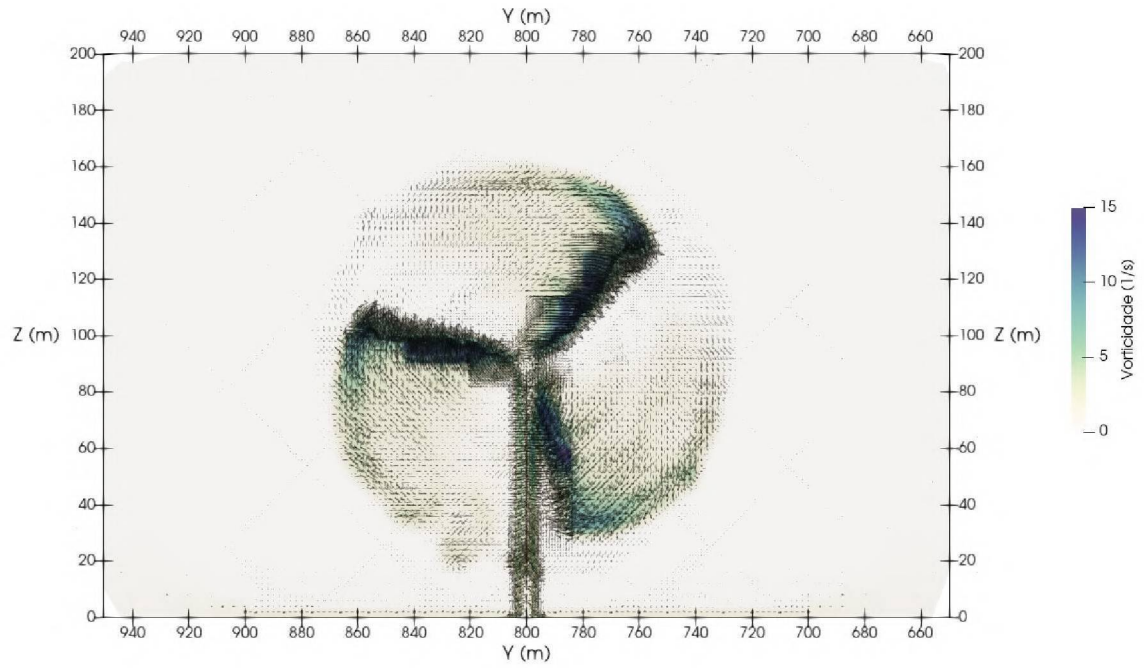


Figure 5.3.36 – Contours vorticity magnitude in the downstream position of the wind turbine

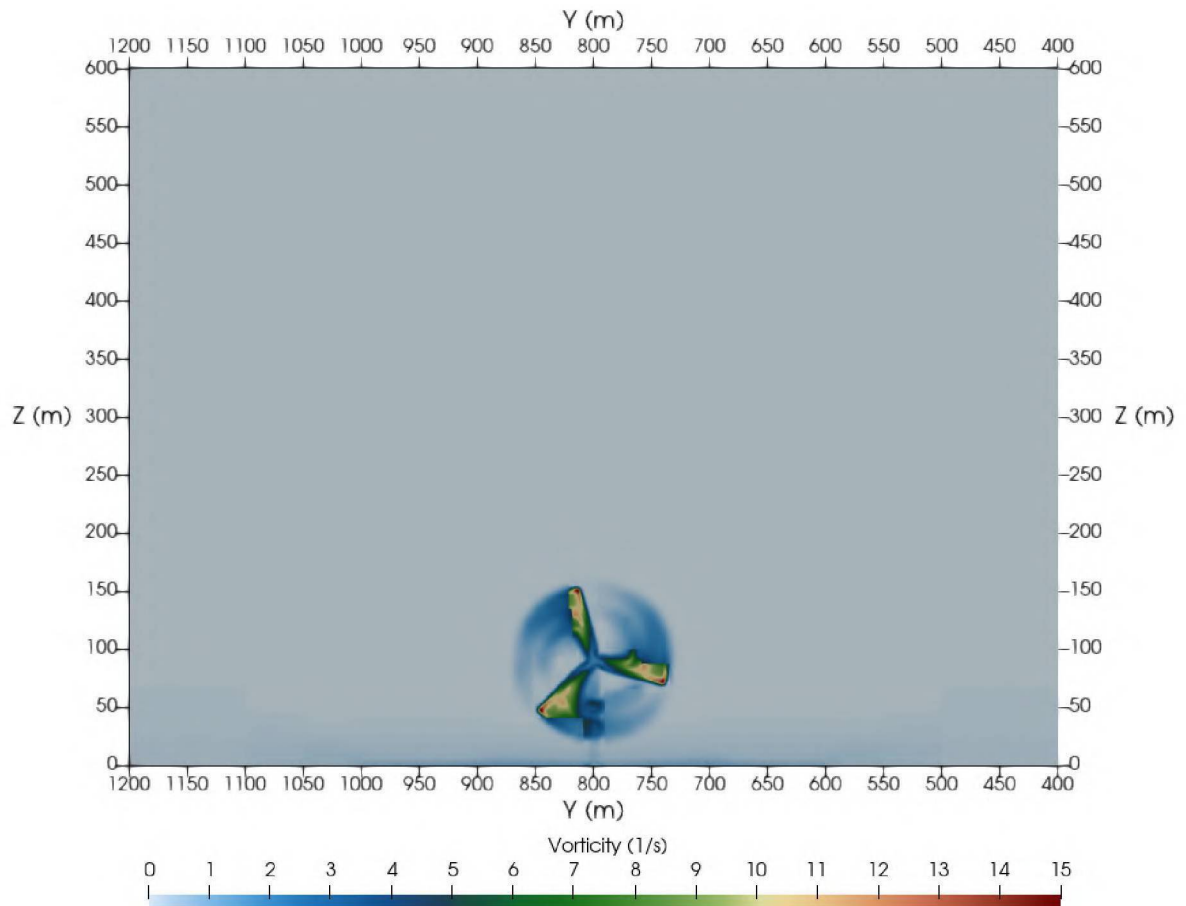
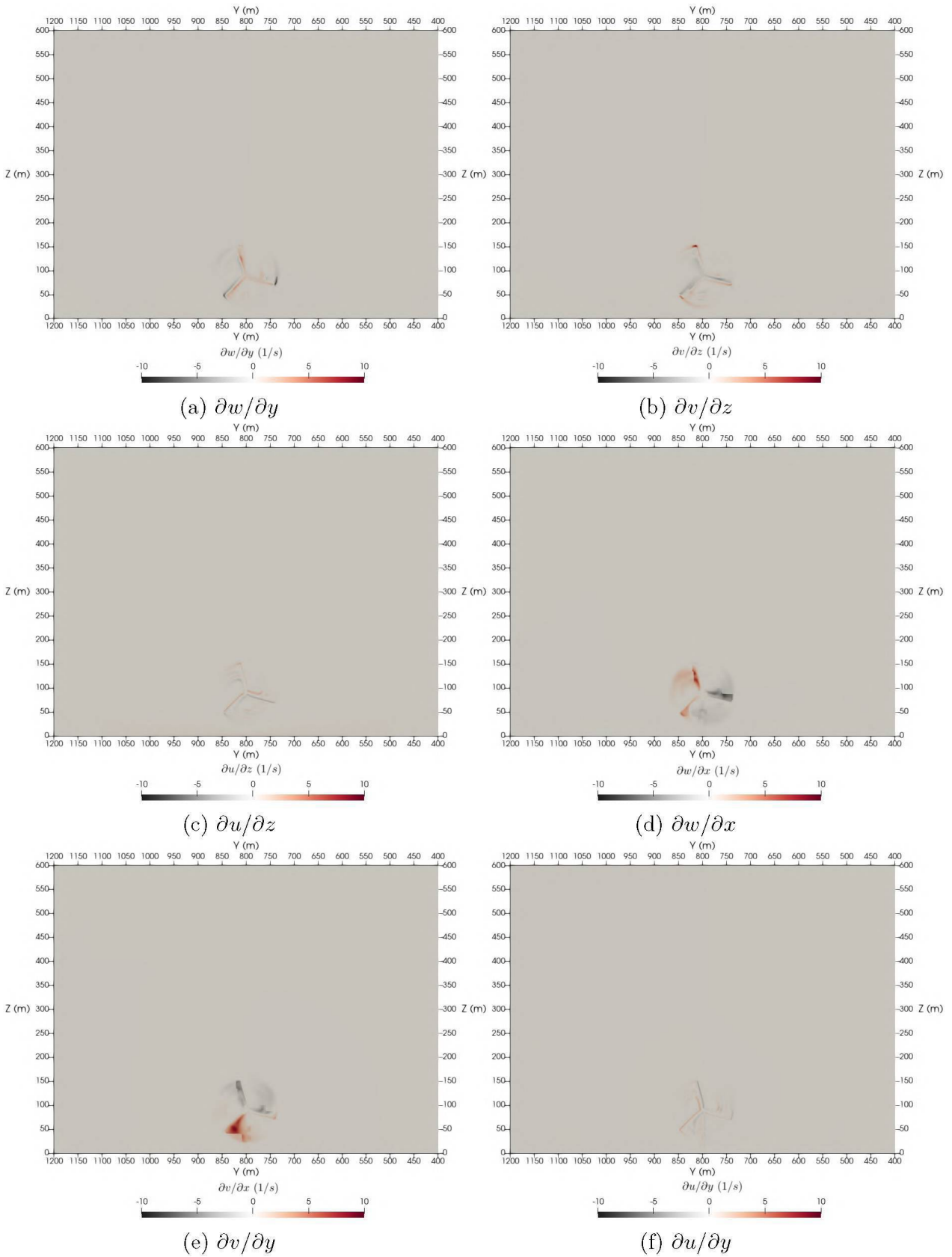


Figure 5.3.37 – Contours of the gradient components around the swept area



5.3.6 Evaluation of the Analytical Wake Models Coefficients

The analytical models used by the wind energy industry are harsh in the physical representation of the phenomena compared to most of the advanced methods based on CFD models. An advantage of the analytical models is the lower cost compared to the more computationally expensive models. The goal of analytical wake models employed for the energy yield estimation procedure is to represent the wind velocity deficits influenced by the wind turbine and the restoration ratio to the free stream velocity.

Three different analytical wake models, Park, Frandsen, and Larsen models were compared with MFSim results. In this section, the idea is to calculate what would be the best-fit parameter values for the coefficients used in each wake model based on the high fidelity LES simulation by MFSim.

The Park model simplifies the reality, assuming a top-hat shape for the velocity deficit in the wake, it considers a gradually developing longitudinal wake with a velocity deficit that is only relative to the distance behind the rotor. The Frandsen model was developed initially to represent wake for offshore wind turbines, which use could be extended for onshore conditions if they were similar to offshore, that is, very low roughness. Meanwhile, Larsen's model considers the wake expansion in terms of wake radius and wind velocity profile. The model is based on a simplified form of the Prandtl boundary layer equation, where the wind flow is presumed to be incompressible, stationary, and axisymmetric. The models were better described at Section 2.3.1

First of all, in order to evaluate the coefficients applied for the analytical wake models through the results obtained via LES simulations, it was necessary to acquire the wake diameter of the simulation for each downstream distance from the wind turbine. The approach to obtain the wake diameter was based on the methodology developed by Barthelmie et al. (2006), and also recently presented in Duda, Uruba and Yanovych (2021), which consists of specifying a threshold or wind velocity ratio. In short, it is the ratio between the wind velocity at a point inside the wake by the freestream velocity. For a single wake where the wake form is well depicted, and there are no overlapping side wakes, the ratio can be set relatively elevated around 0.95 to 0.99. However, the value has to be slightly lower for multiple and broader wake cases, varying from 0.8 to 0.9. Unfortunately, the wake diameter is highly susceptible to the selected threshold value. Because of that, it was decided to apply two ratio values, 0.95 and 0.9, to represent a single wake and the possibility of multiple wakes, respectively. Thus, the average was later taken to have the results in a mix of the range pointed by the literature.

This ratio was computed and evaluated for all probes shown in Figure 5.3.11, for plane xy at the hub height. Thus, the ratio values that are lower than the threshold values will be considered within the wake diameter. Therefore, the wake diameter is given by the distance between the points on both sides, where the ratios are higher than the threshold. The results for the wake diameter calculation are presented in the Table 4 for both thresholds and also for the average of all diameters.

From table 4 it is possible to observe that the limit of 0.9 is more restrictive than the one of 0.95, thus producing a trend of a narrower/thinner wake diameter. The next step

Table 4 – Wake diameter calculated from MFSim simulation

Threshold	0.95	0.9
Downstream (D)	Wake Diameter (D)	
1	1.270	1.190
2	1.429	1.429
3	1.508	1.270
4	1.429	1.270
5	1.429	1.270
6	1.508	1.190
7	1.349	1.190
8	1.587	1.270
9	1.667	1.270
10	1.825	1.429
Average	1.500	1.278

Table 5 – Best-fit coefficients for the simplified wake models

Model	Parameter	Threshold		
		0.90	0.95	Average
Park	K	0.039	0.061	0.050
	C_t	0.604	0.820	0.712
Frandsen	β	1.340	1.720	1.530
	γ	0.381	0.576	0.479
Larsen	c_1	0.013	0.009	0.011
	x_0	205.365	330.486	267.926
	D_e	143.370	163.290	153.330
	R_w	80.500	94.500	87.500

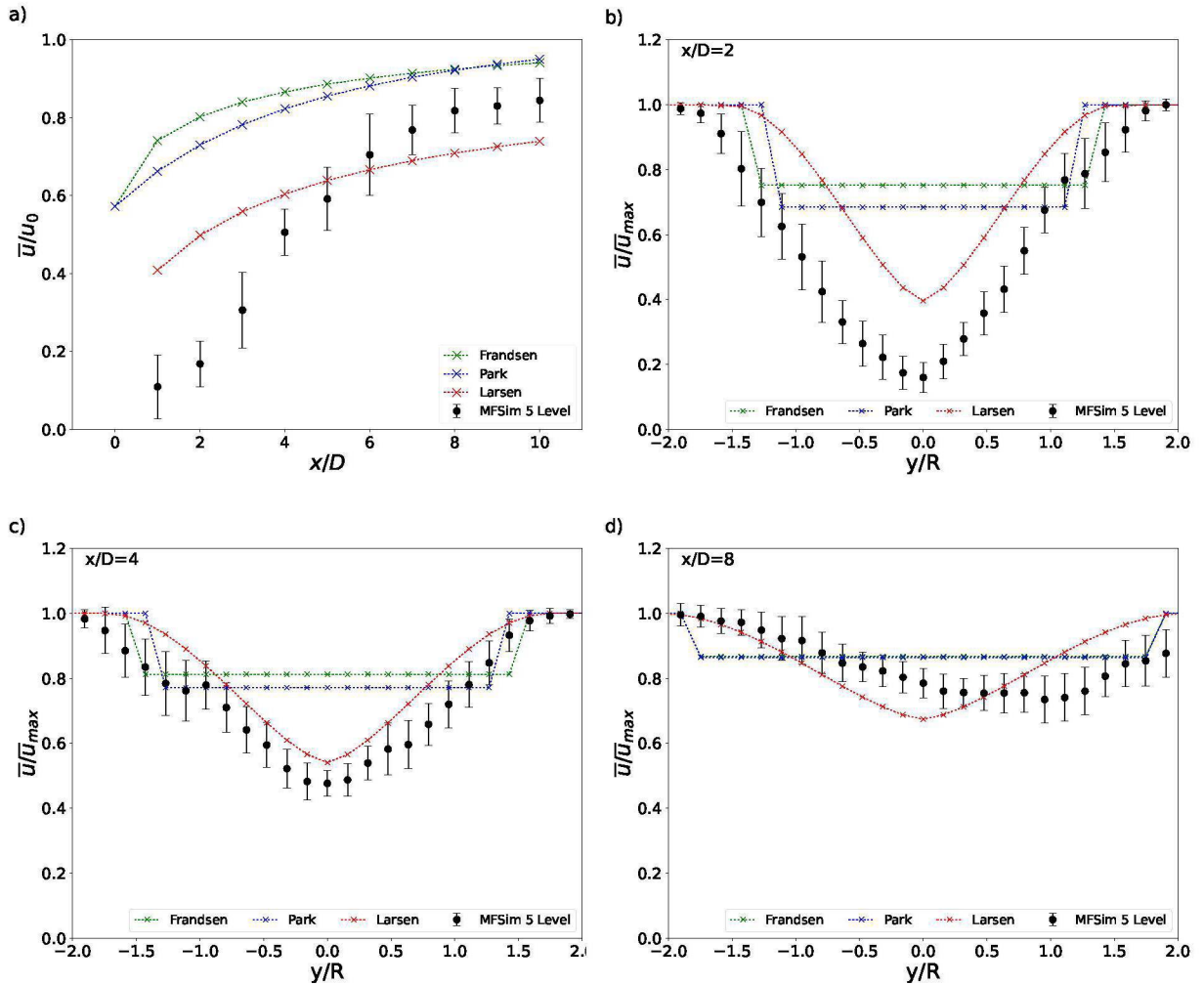
consisted of calculating the best-fit K coefficient for Park model, using the equation 5.1.7. For Frandsen model, thrust force data was obtained on the turbine through the Lagrangian mesh, and then applied to Frandsen model equation 2.14 to calculate C_t , which is also the same applied for Larsen wake model. Following the calculated C_t in the Frandsen and Larsen models, their respective coefficients (i.e. γ and β for Larsen, and c_1 , x_0 , D_e , and R_w for Larsen model) are obtained. The best-fit model's coefficients are presented in Table 5:

In terms of K , the wake decay constant of the Park model, which represents the dissipation of the wake as the wake width increases, the average results seem to fit the literature review for offshore values, from 0.04 – 0.05, while for onshore, the values tend to be adopted around 0.075 (STIVAL; GUETTER; ANDRADE, 2017; STIVAL, 2017; JENSEN, 1983; BARTHELMIE et al., 2009; ABKAR; PORTÉ-AGEL, 2015).

Frandsen and Larsen models coefficients are, basically, based on C_t and would change depending on which turbine it is working. In order to compare how the analytical wake models would behave with their best-fit coefficients that was computed from the MFSim analyses, an analysis is performed using Figure 5.3.38. In this figure, the abscissa axis is plotted the scaled velocity normalized by the maximum velocity \bar{u}/\bar{u}_{max} in the section with standard deviation, plotted against the transversal value y normalized by the radius of the blade R . Figure 5.3.38

presents the comparison in terms of longitudinal (Figure 5.3.38 (a)) and cross-sectional values in sections 2, 4 and 8 of x/D , (Figure 5.3.38 (b) to (d), respectively).

Figure 5.3.38 – Comparison of the best-fit calculated coefficients and MFSim results



It can be observed from Figure 5.3.38 that visibly the near wake is not well represented by the analytical models, where their best characterization occurred when representing the far wake. For the longitudinal analysis, the Park and Frandsen models overestimate the MFSim results throughout the centerline profile, which also occurred in the 2 and 4 D near wake cross-sections between $y/R = \pm 0.5$, with the maximum difference of \bar{u}/\bar{u}_{max} , 0.63, 0.59, and 0.29 for at longitudinal centerline, cross-section of $x/D=2$ and $x/D=4$, respectively, all three for the Frandsen model profile compared to MFSim. Only in section $x/D=8$, the two models present satisfactory results with the average difference of \bar{u}/\bar{u}_{max} between both models and MFSim is 0.063 ± 0.044 considering all profile points, which represents a range of 5 to 10% difference from MFSim results.

Meanwhile, Larsen model also overestimates the results for near wake up to about 3D in the longitudinal and visibly in $x/D=2$ in the transverse analysis, reaching maximum difference of \bar{u}/\bar{u}_{max} around 0.35. In contrast, in the centerline region of the far wake, Larsen model underestimates the results from 7D to 10D, also seen in the region close to $y/R=0$ in section

$x/D=8$ of the cross-section analysis. However, the model well represented the MFSim results for the transition sections between near wake and far wake, as can be seen in Figure 5.3.38 (a) at points of x/D equal to 5 and 6, with differences of 0.05 and 0.04 respectively, which represents around 5% difference compared to MFSim, as well as in the profile distribution of the section $x/D=4$ of the cross-section analysis, represented by Figure 5.3.38 (c), where the model presented average difference for all points of 0.049 ± 0.040 representing a range of 2 to 8% difference from MFSim results. Meanwhile, for the far wake section of $x/D=8$, Larsen model presented similar overall average difference compared to MFSim, as the other two models, with value of 0.062 ± 0.048 , which also represents a range of 5 to 10% difference from MFSim results, but visually with a better profile representation. Therefore, Larsen model was the one that best represented the flow also because it is the most sophisticated of the three analytical models.

5.3.7 Evaluation of Power Generation for Single Turbine

This section presents the results obtained from the temporal evolution of the torque and power of the stand alone wind turbine adopted in the present Scenario 3. Since, the geometry is incorporated into the fluid domain by a force term in the Navier-Stokes equations, by the immersed boundary method, an advantage is to obtain, with post-processing, the torque and power generated by the turbine over a structure immersed in the flow. This approach basically consisted of implementing lines in the code in order to improve *immersedboundary.f90* file in the MFSim code with the turbine in motion, thus enabling the calculation of torque and power generated. The steps of this implementation consisted of:

1. To calculate the distance from the wind turbine rotation reference position to the center position of each Lagrangian cell:

$$r_x = x_c - \tilde{x}_k, \quad (5.3)$$

$$r_y = y_c - \tilde{y}_k, \quad (5.4)$$

$$r_z = z_c - \tilde{z}_k, \quad (5.5)$$

where x_c, y_c, z_c are the rotation reference positions of the immersed boundary defined in the file *input/ib.amr3d* and $\tilde{x}_k, \tilde{y}_k, \tilde{z}_k$ are the center positions of each Lagrangian cell in each direction.

2. To calculate the Torque through the summation in the Lagrangian space of the cross product of force and distance in x, y and z .

$$T = \sum_{\Gamma} r \times F, \quad (5.6)$$

where F represents the force magnitude of the Lagrangian field that promotes the immersed boundary rotation.

$$r \times F = \begin{vmatrix} i & j & k \\ r_x & r_y & r_z \\ F_x & F_y & F_z \end{vmatrix} \quad (5.7)$$

3. Calculating mechanical Torque, the mechanical Power generation is obtained using the following equation:

$$Power = T\omega_x \frac{\pi}{30000}, \quad (5.8)$$

where ω_x stands for angular velocity rotation (*rad/s*).

Figure 5.3.39 (a) illustrates the original signals from the temporal evolution of torque, while Figure 5.3.39 (b) depicts the original signals from the temporal evolution of power. On the abscissa axis, the scaled Torque and Power are plotted against the normalized number of iterations for a sample of about 10000 iterations after the flow is fully developed, exhibiting that the signal is periodic, thus, statistically reliable for acquiring the average of the torque and power.

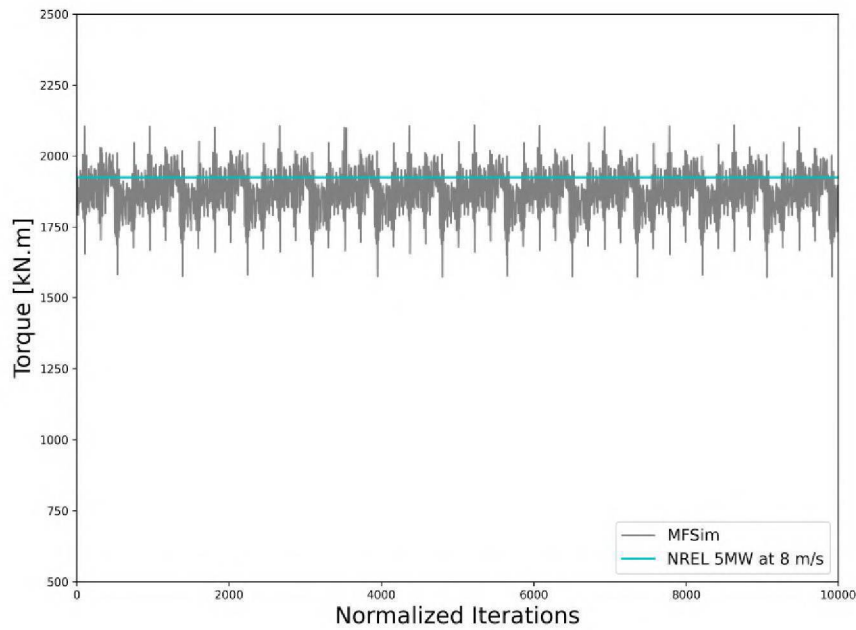
Hence, in terms of torque represented by Figure 5.3.39(a), MFSim results presented a mean and standard deviation of 1873.89 ± 73.90 (*kNm*), while the experimental study of the NREL 5MW (JONKMAN et al., 2009) showed a mean torque value of 1914.00 (*kNm*) for the same conditions, thus the mean difference corresponds to 40.11 (*kNm*), representing about a 2% difference between both results. In the case of power generation showed by Figure 5.3.39(b), mean values and standard deviation for the MFSim simulation corresponds to 1741.75 ± 69.96 (*kW*). In contrast, NREL 5MW (JONKMAN et al., 2009) presented value of 1805.00 (*kW*), which results in a difference in generating power of 63.25 (*kW*). Therefore, a difference in power generation between both results is about 3.5%, which is a pretty low difference when take into consideration the size of the wind turbine that was applied in this work.

Scenario 3 Remarks

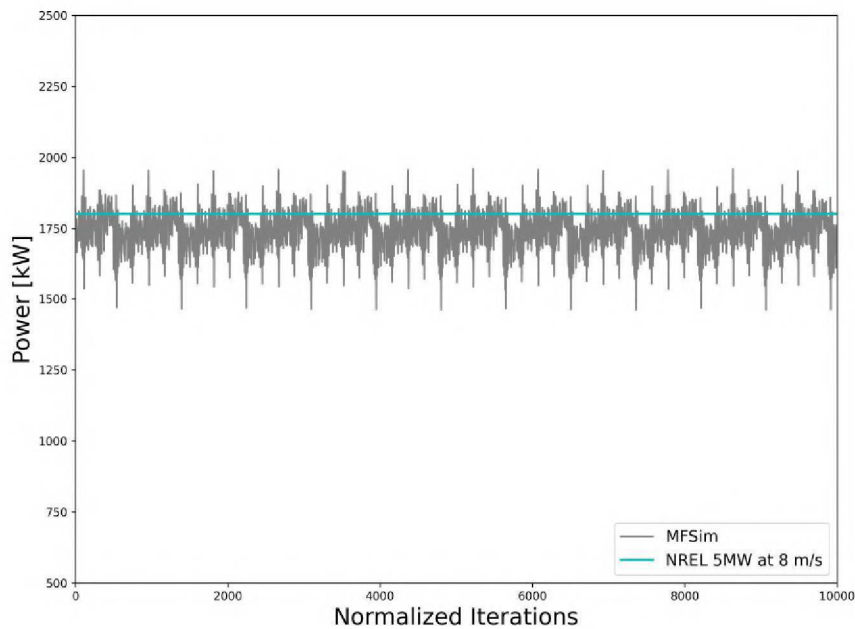
In conclusion of the third simulation scenario developed that it was based in a real scale case of an offshore wind turbine called NREL 5 MW. Firstly, it was decided to simulate the flow around the wind turbine with a control volume of 1600 *m* longitudinal, 800 *m* width, and 600 *m* height, reaching a blockage ratio around 3.42%. Then, simulations with five refinement levels over the wake was chosen in order to compare with the provided results. Regarding velocities evaluations, it was likely to distinguish high-velocity deficits in the near wake area immediately downstream from the wind turbine. Moreover, from qualitative analysis pointed out high velocities occurring around the blade tip around the swept area.

In terms of the comparison with the data provided from UBC, SOWFA and both MARBLLES overestimate the results from MFSim in the near wake centerline for cross-sectional analysis, which could be attributed to the tower and nacelle shading effecting occurring in the near wake. In the transition wake region, the profiles are similar among each other where most of the results has lower than 10% for the whole wake width. Further downstream in the far wake region, the centerline area produced similar results among the profiles with differences lower than 7% in this region. Concerning the vertical evaluation, it was presented lower recovery velocities of MFSim around the hub height in the near wake compared to other profiles, which restates the simplification blade resolving geometry applied in MARBLLES and SOWFA. Further downstream, in the transition wake region, the best correlation occurred between SOWFA

Figure 5.3.39 – Torque and Power of the NREL 5 MW



(a) Torque



(b) Power

and MFSim, from blade's bottom tip up to hub height, with extremely low variations that did not exceed 3% between the profiles. Meanwhile, in heights above hub height, both MARBLLES showed better representation of the profile in comparison with MFSim results, where the differences were lower than 9% among them. In the vertical far wake analysis the best performance

occurred around the hub area with differences, among both MARBLLES and MFSim, that can reach values lower than 1% variation among them.

From turbulence properties, the higher values of turbulent kinetic energy and turbulence intensity occur around the blade's tip in the near wake region, with values that can reach 0.06 for TKE, and 0.45 for TI, in both vertical and cross-sectional profiles. In addition, the results suggest a more significant dissipation of the turbulent kinetic energy occurs as the wake develops toward to far wake from the transition region of the wake ($x/D=4$). Moreover, the streamwise Reynolds stress from MFSim was evaluated against the results from SnS and EllipSys3D, demonstrating great performance over the wind turbine location, where the differences were lower than 10% along the swept area. Similar variations were found in the near and far wake region, excepted in the right side of the profile over near wake, even though such a difference could be attributed to geometry limitation from SnS and EllipSys3D, which the turbine is modeled using an actuator disk only. For turbulent kinetic energy spectrum analysis, in regions where the energy spectrum has greater amplitude, the flow is consequently more turbulent, indicating higher velocity gradients in those regions. However, this results analysis is still a preliminary evaluation, future studies on this topic will be essential to achieve more sophisticated mesh simulations allowing the spectrum analysis to estimate the vortices structures sizes over the wake.

Evaluation of the coefficients for the selected analytical wake models demonstrated that the average coefficient determined for Park model was consistent with the literature review. Frandsen and Larsen models are primarily based on thrust coefficient, which depends on the applied turbine characteristics of the manufacturer. Therefore, Larsen's model stood as the model that satisfactorily characterized the flow because it is the most sophisticated of the three analytical models.

Lastly, the power production analysis demonstrated that low difference between the experimental results from NREL and MFSim, leading to a lower than 3.5% difference for both torque and power generation, considering the turbine's size applied in the simulation.

5.4 SCENARIO 4: BACK TO BACK WIND TURBINES

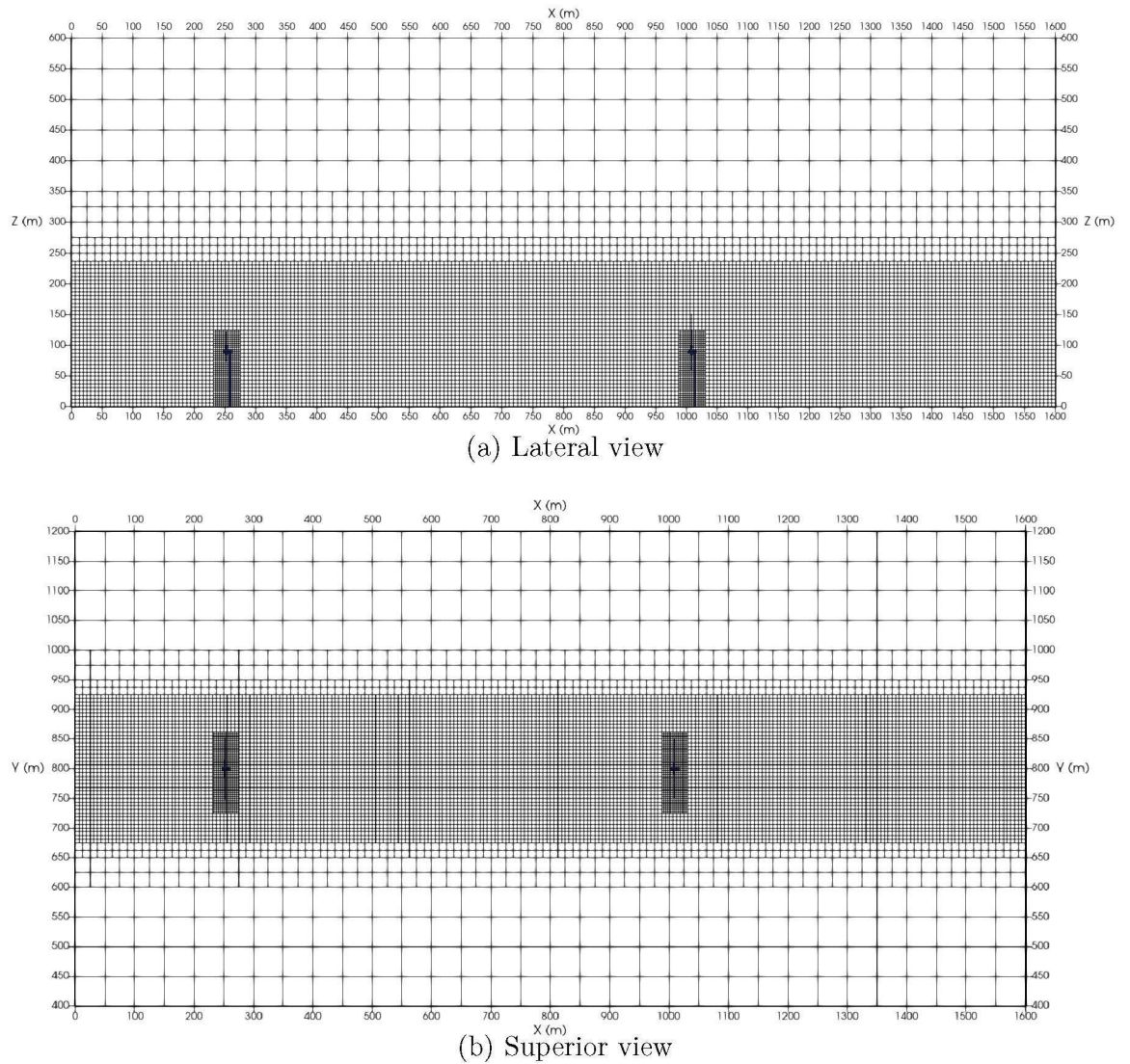
The last simulation scenario developed in this thesis was based on back to back NREL 5 MW wind turbines in a real scale case in order to represent what occurs in a wind farm power plant. The reference case from Jonkman et al. (2009) presents data in terms of aerodynamics coefficients and parameters, but it does not contain measurements of the downstream wake. Because of that, it was aimed to create this scenario which comprehends two back to back real scale turbines where wake effects, properties of the flow, and power generation is analyzed and discussed. Table 2 on Scenario 3 (5.3) already provided the main details the dimensions and operating conditions of the NREL 5MW.

5.4.1 Geometry, Computational Mesh and Boundary Conditions

The simulations on MFSim were performed with the same geometry of the NREL 5MW wind turbine that was presented in the Scenario 3 (5.3). The biggest difference in this section was placing the second wind turbine into the wake of the upstream turbine. The downstream distance between both turbines were set to $6D$, which is a reasonable number applied in the wind energy industry when wind farm power plant is developed. The work of Frandsen (2007) studied a wind farm with distance between the turbines in each row of $8.5D$, because of that it is interesting applied $6D$ difference to take into account the wake effects. Figure 5.4.1 illustrates the main displacement of the back to back 5MW NREL wind turbines. Four levels of refinement were applied in order to understand how the behavior of the results would be relative to finer mesh, without compromising the computational cost that is allowed in the MFSim code. Both wind turbines meshes, representing the lagrangian domain, contain a total of 134500 triangular cells, as shown in Figure 5.4.2. Figure 5.4.1(a) displays the xz -plane at centerline, $y=0$ m, where left side of z represents the inlet while right side is the outlet. Meanwhile, Figure 5.4.1(b) shows the xy -plane at the hub height, $z=90$ m.

The inflow wind velocity profile was similar to the previous chapter, Scenario 3 (5.3), where it was characterized the inlet with a hub height velocity of $u=8$, $v=0$ and $w=0$ m/s, being u , v , and w , the velocity vector components. The boundary conditions for the lateral planes (xz -planes) were characterized as symmetry, this condition was also applied in the top plane (xy -plane). The bottom plane (xy -plane) sets a no-slip condition in order to represent the ground where the turbine was placed in the wind tunnel. A Neumann boundary condition was used for pressure matters, meanwhile an advective condition was employed at the outflow condition, which is time varying to allow for vortical structures to cleanly exit the computational domain without reflecting back into the domain or disturbing the solution in the inner domain. The initial conditions of the simulations for velocities profiles at the hub height, $u=8$, $v=0$ and $w=0$ m/s. In these simulations, the fluid properties were $\rho=1.225$ kg/m³, $\mu=0.0000182$ kg/(m s) and setting a Reynolds number ($Re \approx 2.46 \times 10^6$) around the blade. It was adopted variable numerical time steps in the range of 10^{-4} to 10^{-5} s, maintained a CFL criteria of 0.5. The final simulation time was 800 s. All statistics were calculated based on the last 300 s of simulation, period along which the flow presented approximately steady state conditions. The computational resource was based on two nodes of Intel Xeon E5650 2.67GHz 24-core machine utilizing approximately

Figure 5.4.1 – Mesh illustration for (a) lateral, at centerline, and (b) superior, at hub height, view of four levels of refinement



32 GB RAM, the simulations required approximately 230 hours.

5.4.2 Probes Location

The same probes distribution as Scenario 5.3 was applied in the back to back simulations, in order to keep the same configuration of the post-processing. Figure 5.4.3 illustrates the probes installed in the numerical domain to retain the results in order to capture the statistics of the variables of interest. Those probes were positioned from $1D$ upstream to $10D$ downstream distances from the first NREL 5 MW wind turbine, called turbine 1, in the longitudinal direction, which is the x -direction. In consequence of that, the second turbine, called turbine 2, has probes positioned up to a downstream distance of $4D$.

The cross-sectional probes to capture the wake diameter had an implementation of 33 probes for each chosen section varying from -160 m to 160 m in the y -direction, spaced by 10

Figure 5.4.2 – Lagrangian mesh detailed for the NREL 5MW simulation

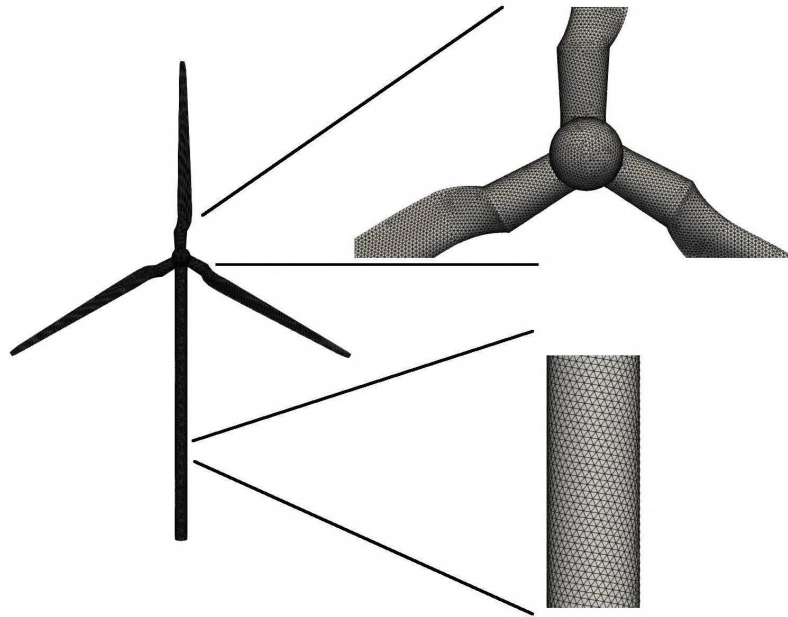
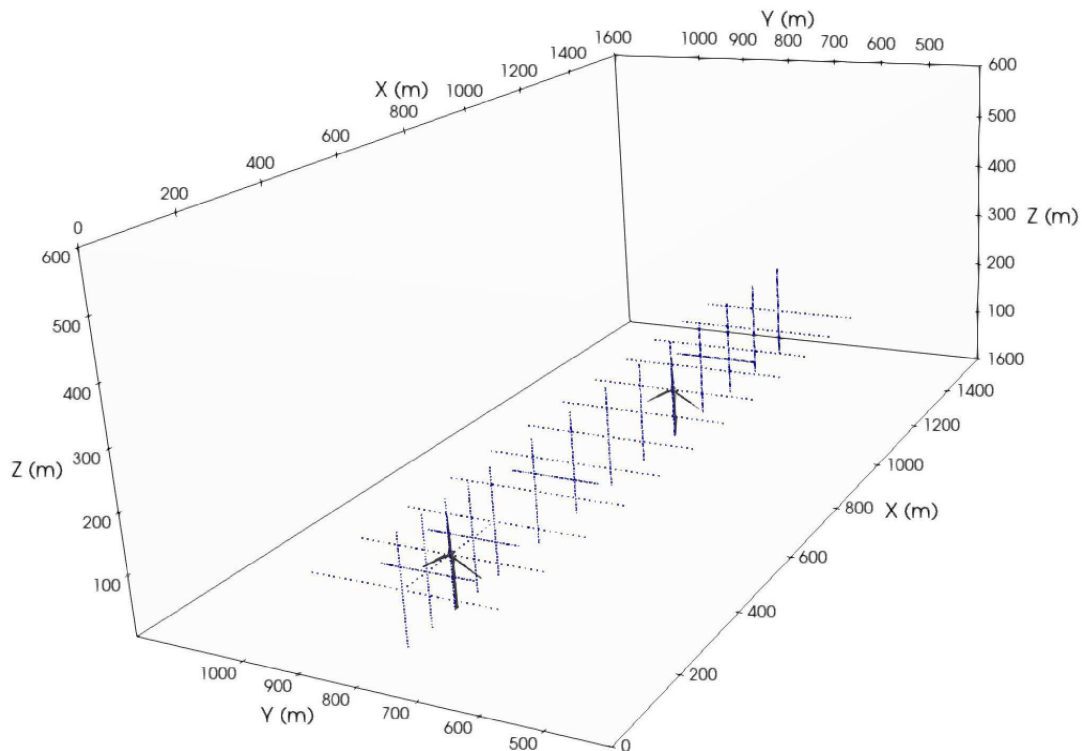


Figure 5.4.3 – Position of the installed probes in the Scenario 4



m . The chosen sections are $1D$ upstream, and end at $10D$ downstream from the wind turbine. Additionally, seeking to visualize the wake behavior downstream of the turbine, vertical profiles were established before and after the wind turbine represented by 37 probes, from 0 to $180 m$, for each section, where the sections begin at $1 D$ upstream and end at $10D$ downstream of the

wind turbine.

5.4.3 Profiles of Time-average Streamwise Velocity

The streamwise component of time-average velocity with standard deviation was analyzed downstream from the back to back wind turbines. At first, focusing on the longitudinal wind velocity recovery for chosen sections behind each turbine, Figure 5.4.4 presents the time-averaged streamwise velocity normalized by the freestream velocity (\bar{u}/u_0) at the centerline as a function of the normalized downstream distance (x/D) in a longitudinal centerline at the hub height. Figure 5.4.4 also represents the streamwise velocity for the whole domain in the same velocity profile. It is possible to observe that two main gradients of velocity occurs in the section where the turbine are positioned, 0D and 6D. The velocity recovery downstream of the turbine 2 is quicker than the turbine 1, as it can be seen in Figure 5.4.4. This might be due the turbulence that is hitting the turbine 2, because it is positioned in the wake of turbine 1, meanwhile turbine wake receives freestream wind velocity without inlet turbulence. Moreover, while the wind velocity recovery for turbine reaches approximately $\bar{u}/u_0 = 1$ at the section 5D, the velocity recovery for turbine 2 reaches the same point at 9D, which is only 3D downstream of the turbine 2.

Figure 5.4.5 presents observations of velocity recovery for the back to back wind turbines, but separately in two profiles of streamwise velocity, in order to compare the wake development of both turbines. It is possible to observe that the upstream centerline streamwise velocity of turbine 1 is a little bit higher than the turbine 2, around $\bar{u}/u_0 = 1$. Although in the first section downstream at 1D, both profiles presented similar values of \bar{u}/u_0 around 0.2, from section 3D, and further, the centerline velocity recovery of turbine 2 profile increases faster and higher than turbine 2. The highest difference of $0.33 \bar{u}/u_0$ occurred at section $x/D=4$, followed by section $x/D=3$ with 0.27 difference between both profiles. However, it is important to point out that this is representative of the centerline of the wake only.

The next step consisted on analyzing the streamwise component of time-average velocity in terms of cross-sectional perspective. Comparisons of velocity recovery over the wake cross-section have been analyzed for four cross-section locations, corresponding to downstream distances of 0, 1, 2, and $4D$, presenting the simulations for the application of the back to back turbine simulation scenario, which is represented by Figures 5.4.6 (a), (c) and (e). For all cross-sections, 33 points have been chosen and separated into 16 points on each side of the centerline. The cross-section points were equally spaced, with 5 m between adjacent points. The total represented cross-section width corresponds to 160 m . Besides that, the analysis considers the xy plane, where the height is at the wind turbine's hub. On the abscissa axis, the scaled velocity is normalized by the maximum velocity \bar{u}/\bar{u}_{max} in the section plotted against the transversal value y normalized by the radius of the blade R . Meanwhile, Figures 5.4.6 (b), (d) and (f) present time-averaged streamwise velocity recovery for vertical profiles along the centerline of the wake downstream distance, where four sections have been analyzed corresponding to downstream distances of 1, 2, 3, and $4D$. On the abscissa axis, the scaled component z is represented, which corresponds to the height, plotted against the normalized velocity \bar{u}/u_0 . The investigation illustrates two different profiles results standing for each turbine of the simulation. The analysis

Figure 5.4.4 – Time-average streamwise velocity centerline recovery for the back to back NREL 5MW wind turbines

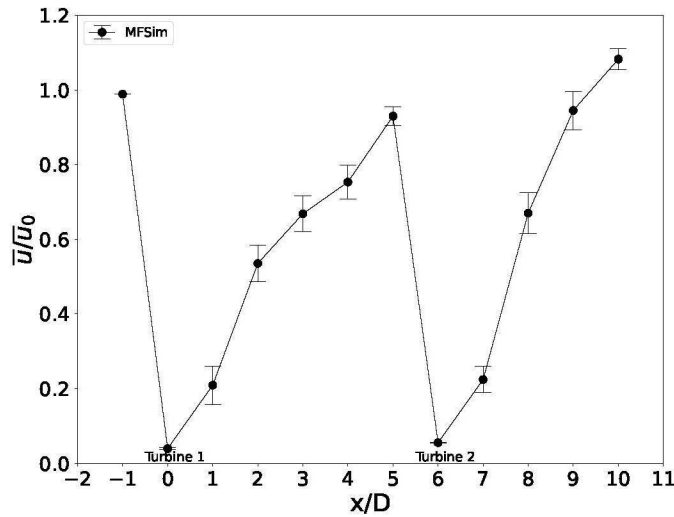
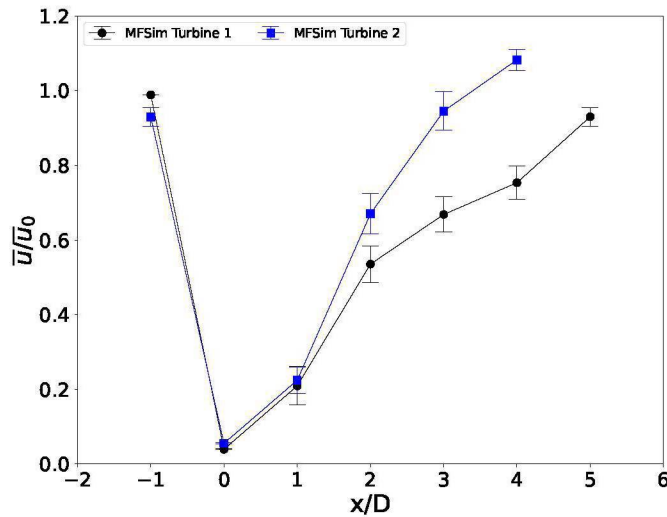


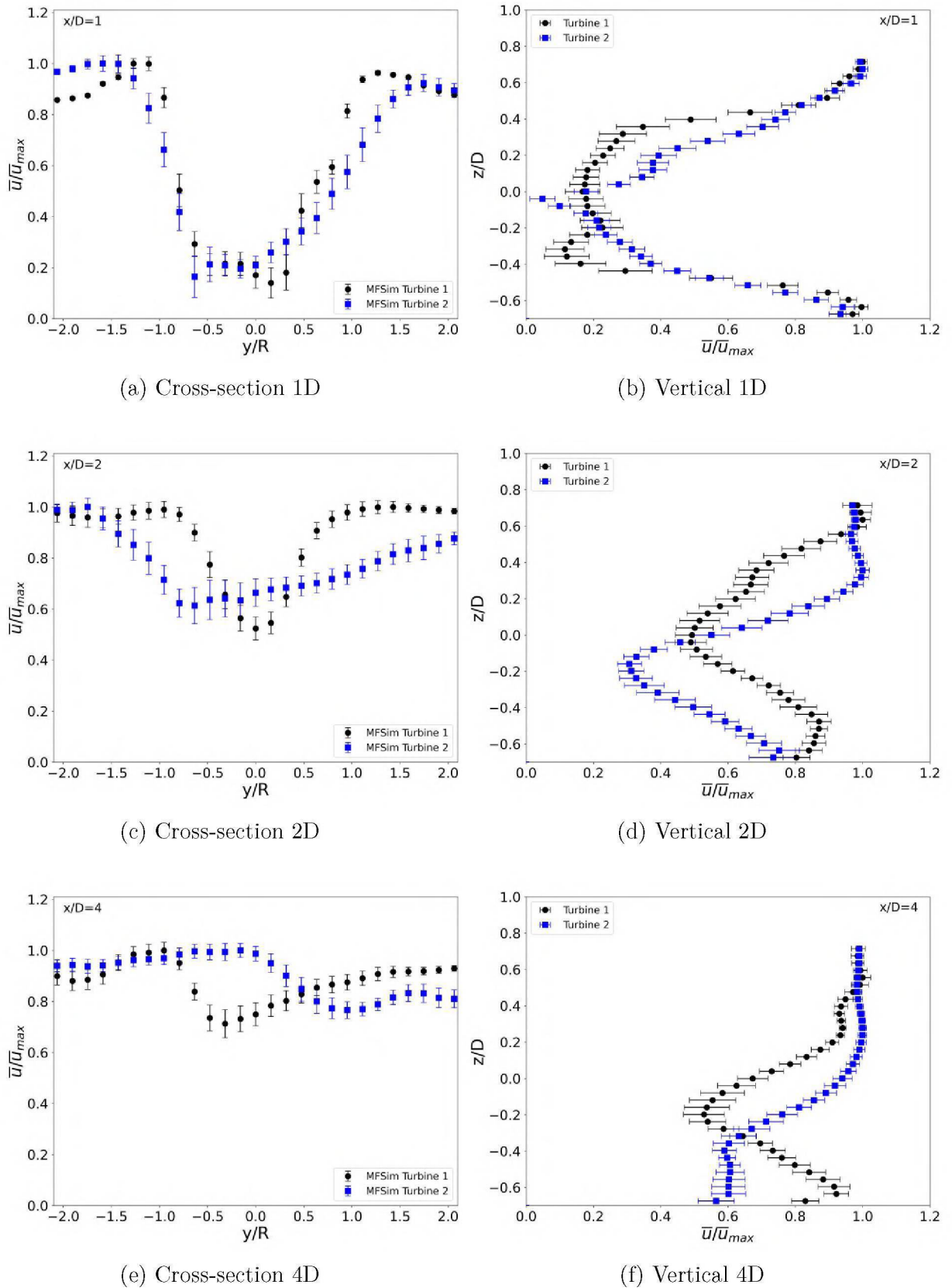
Figure 5.4.5 – Time-average streamwise velocity centerline recovery comparison between both turbines



assumes the xz plane at the centerline of the simulation ($y = 0$). Thirty-seven points have been chosen and equally spaced with 5 m between adjacent points for all vertical profiles, reaching a maximum height of 180 m.

In section $x/D=1$, Figure 5.4.6 (a), represents the first section in the region close to the wake. The lowest velocity recovery also occurred close to the wake centerline, around $0.2 y/R$ and $-0.6 y/R$, for turbines 1 and 2, respectively, with \bar{u}/\bar{u}_{max} values slightly below 0.2 for both profiles. Meanwhile, the highest velocity values occurred near the blade tip region, which is $y/R = \pm 1$, for turbine 1. However, for turbine 2, the highest velocity values occurred close to $y/R = \pm 1.5$, indicating a wake diameter greater than the one presented for the turbine 1 profile. This happens because turbine 2 is positioned downstream of turbine 1, which can be reaffirmed by

Figure 5.4.6 – Time-average streamwise velocity recovery comparison between both turbines for cross-sectional and vertical sections



analyzing the main differences between the two profiles, in this case occurring in the turbine blade tip region, $y/R = \pm 1$, with values of \bar{u}/\bar{u}_{max} varying from 20 to 25% between profiles. For the vertical analysis of the same section, Figure 5.4.6 (b), the lowest velocity recovery of the turbine 2 profile occurred close to the hub height, $z/D = 0$, with value near $0.5 \bar{u}/\bar{u}_{max}$. While turbine 1 profile presented similar values over the swept area, from -0.4 to $0.4 z/D$, varying between 0.1 to $0.3 \bar{u}/\bar{u}_{max}$. The biggest difference vertically between the profiles occurred around $z/D = \pm 0.3$ with variation of 25 to 30%.

The next section $x/D=2$, represented by Figure 5.4.6 (c), shows a large increase in velocity recovery compared to the previous section, where centerline velocity recovery increased near to $0.5 \bar{u}/\bar{u}_{max}$ for turbine 1, and about 0.65 for turbine 2. Despite the fact of turbine 1 profile shows a lower velocity recovery in the centerline than turbine 2, as shown previously in Figure 5.4.5 as well at section $x/D=2$, turbine 1 has a narrower wake profile, hence a smaller wake diameter than the turbine 2 profile, which can be attributed once again of the fact that turbine 2 is located in the wake of turbine 1. Therefore, the biggest differences between both profiles occur over sections from ± 0.75 to $\pm 1 y/R$ with variations around 25 to 35% between both profiles. The vertical profiles for the section $x/D=2$, displayed at Figure 5.4.6 (d), demonstrate the lowest velocity recovery for turbine 2 occurred in a lower height than turbine 1 profile, at $z/D -0.2$ and 0.0 respectively, thus the lowest \bar{u}/\bar{u}_{max} of 0.3 occurs below the hub height, while turbine 1 presents its lowest value around 0.5 at hub height, this results might be caused by the influence of shadowing of back to back towers.

The last section illustrated by Figure 5.4.6 (e) represents $x/D=4$, the furthest section of turbine 2, where its profile is characterized by a flatter distribution with the highest values occurring in the region between -0.5 at $0 y/R$. In contrast, the smallest values reach a velocity recovery around $0.75 \bar{u}/\bar{u}_{max}$, shifting the points of lower velocity further to the right of the profile, a characteristic that might be caused by the greater amplitude of the wake in this region of far wake and due to the large turbulent structures that are predominant in the far wake. The lowest velocity recovery of the turbine 1 profile is around $0.7 \bar{u}/\bar{u}_{max}$ and is more centralized than the turbine 2 profile. The velocity recovery difference between the two profiles occurs at around $-0.3 y/R$ with about 30% variation. At section $x/D=4$, the vertical profiles presented the highest difference near to the ground level, as depicted in Figure 5.4.6 (f), with variation of 30 to 35% between both profiles at this region. It is also the region where the turbine 2 profile hit its lowest velocity recovery with \bar{u}/\bar{u}_{max} of 0.6 , from ground level up to the bottom tip of the blade, presenting the region with mix of fluctuations at this area. Thus the velocity recovery of the turbine 2 profile in the hub height region almost reach the highest velocity of the profile.

Moreover, as an attempt of embodiment, instantaneous illustrations of velocity u and gradient of velocity contours are represented by Figures 5.4.7 and 5.4.8, respectively, displaying the upstream to downstream flow structures around the wind turbines 1 and 2. Figure 5.4.7 shows instantaneous velocity contours with vectors scale by vorticity on zx -plane at the centerline, while Figure 5.4.8 displays the gradient magnitude of velocity on xy -plane at the hub height. It is possible to observe different flow structures in the wake, depending on the distance and height development. Furthermore, the wind velocity deficit in the near wake for both turbines, showed in Figure 5.4.7, is in agreement with the presented time-averaged profile presented by

Figure 5.4.6 (b) previously, where the vertically wake diameter is higher for turbine 1 profile compared to turbine 2. The scaled vectors presented in Figure 5.4.7 indicates that the high vorticity occurred around the rotor rotation and tower shadow. This is also restated in Figure 5.4.8, where the highest gradients occurred in region around the swept area.

Figure 5.4.7 – Instantaneous velocity contours with vectors scale by vorticity on zx -plane

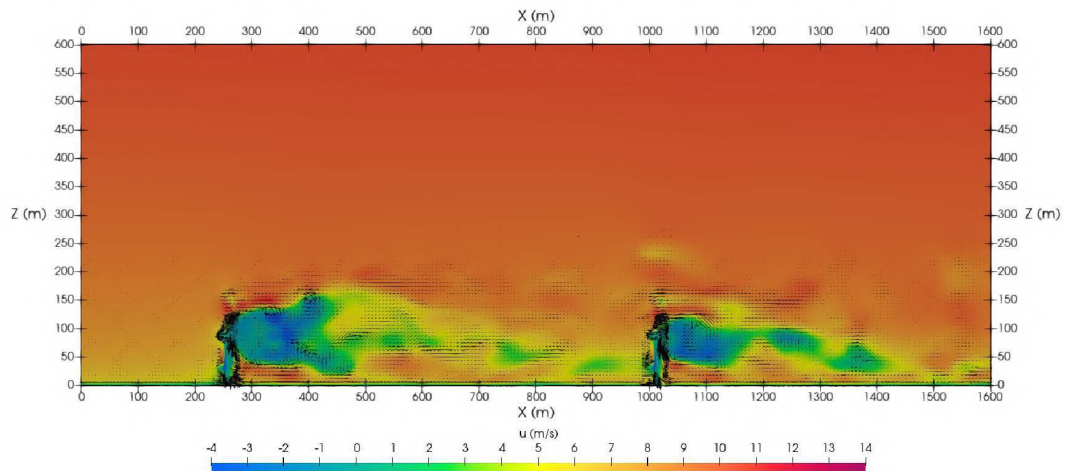
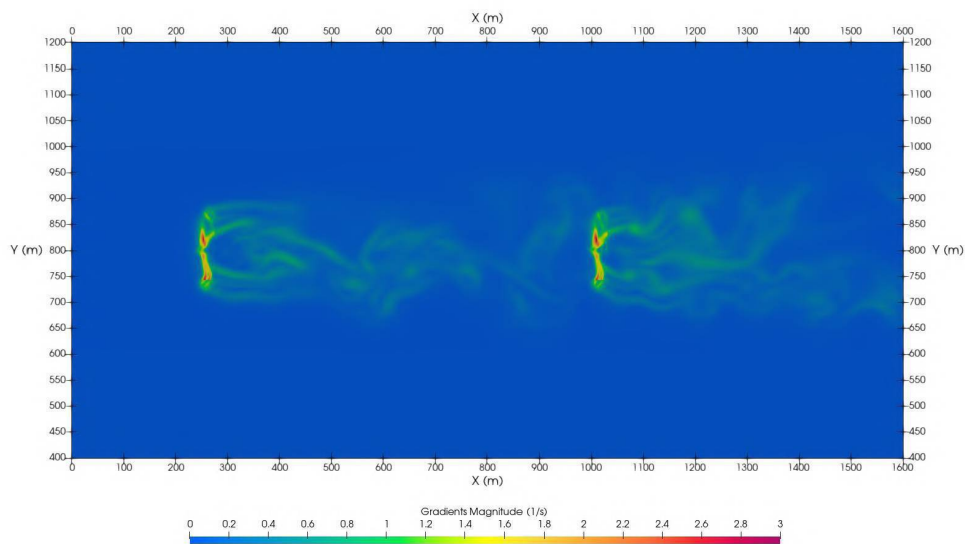


Figure 5.4.8 – Instantaneous gradient magnitude contours on xy -plane at the hub height

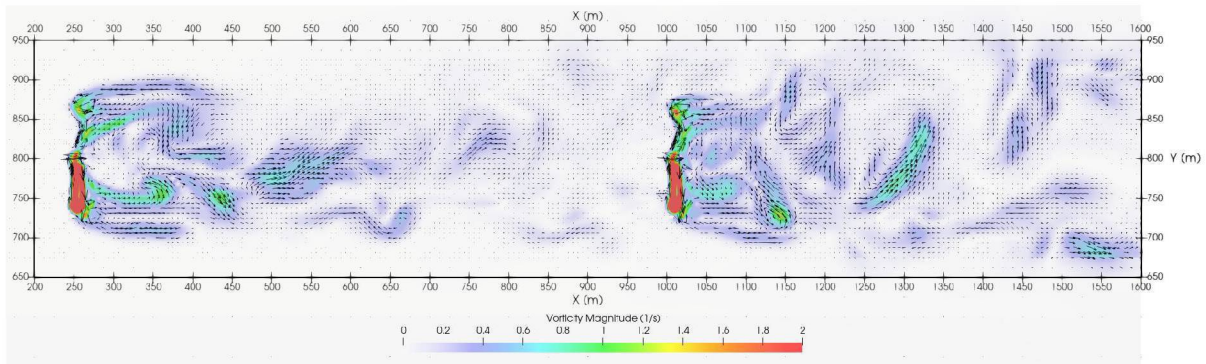


Moreover, in order to restate the qualitative analysis, Figure 5.4.9 displays an illustration of instantaneous vorticity magnitude with a dynamically visualization on the xy -plane, showing the vortices carried over the flow. Similar to stated in Scenario 5.3, most part of vortices are produced by the blade's tip motion and conveyed over the flow, reaffirming that the wind velocity recovery is linked with the flow structures in the wake. And most important, these vortex structures tend to produce extended structural loading and divergences from predicted turbine performance, increasing the cost and uncertainty of wind power plant operation (ABRAHAM; HONG, 2022).

5.4.4 Evaluation of Power Generation for Back to Back Turbines

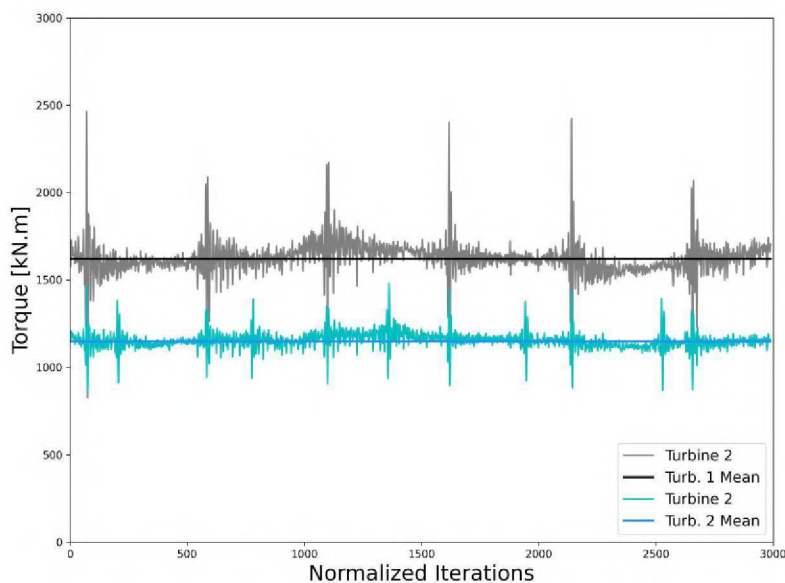
This section presents the results obtained from the temporal evolution of the torque and generated power of the back to back wind turbines adopted in the present work. Figure 5.4.10

Figure 5.4.9 – Animated longitudinal profiles and countours of streamwise velocity over time



shows the original signals from the temporal evolution of torque, while Figure 5.4.11 presents the original signals from the temporal evolution of power. This graphical and post-processing analysis were performed for a sample of about 4000 iterations after the flow is fully developed, showing that the signal is periodic and, therefore, statistically reliable for obtaining the mean and standard deviation values of torque and power generation.

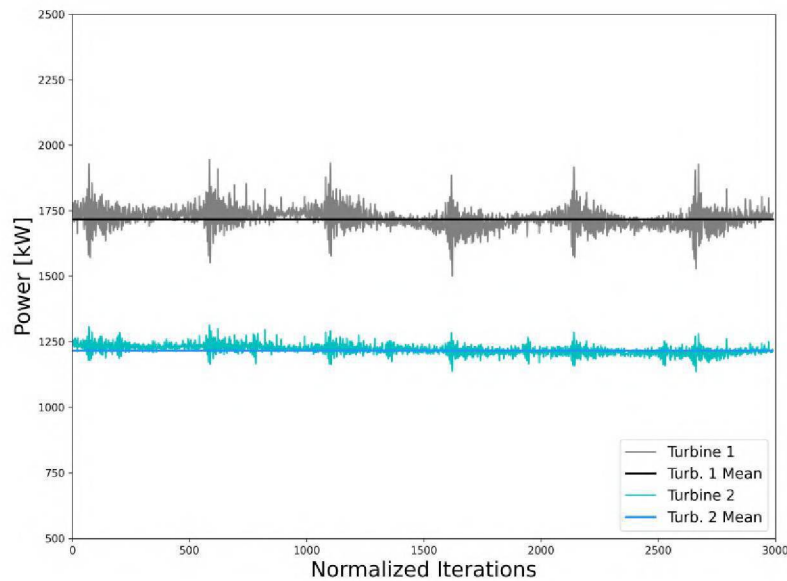
Figure 5.4.10 – Torque of the back to back NREL 5 MW wind turbines



Hence, in terms of torque represented by Figure 5.4.10, turbine 1 has a mean and standard deviation of 1630.71 ± 97.05 (kNm), while turbine 2, located downstream of turbine 1, has a mean and standard deviation 1158.95 ± 51.30 (kNm). The average difference between the two turbines reached a value of 471.73 ± 64.47 (kNm), representing about a 25 to 32% decrease from turbine 1 to turbine 2.

In the case of power generation showed by Figure 5.4.11, mean values and standard deviation for turbine 1 are equal to 1727.15 ± 43.78 (kW). In contrast, turbine 2 presents values of 1158.95 ± 51.31 (kW), which results in a difference in generating power of 501.73 ± 26.01 (kW). Therefore, a decrease in energy production of about 28 to 30% in the turbine located

Figure 5.4.11 – Power generation of the back to back NREL 5 MW wind turbines



downstream of the first turbine demonstrates that the wake effect certainly affects the power output of subsequent turbines if inadequately positioned in the wind farm layout. Even more important nowadays, since there is an assumption that the first offshore wind auction in Brazil will be held in 2023, according to [GWEC \(2022\)](#) and [ABEEÓlica \(2022\)](#).

Scenario 4 Remarks

Concluding the last scenario of this thesis, scenario 4, considers a back to back wind NREL 5 MW wind turbines. From longitudinal streamwise velocity analysis it is possible to identify that the wake recovery from turbine 2 is faster than turbine 1 in terms of the hub height centerline over the wake region. However, the tower shading influence in the wake recovery for turbine 2 is higher than turbine 1, demonstrating lower velocity recoveries in the bottom of the profile, where the highest differences between turbines could reach over 20%. It is possible to observe different flow structures in the wake, depending on the distance and height development regarding the flow visualization. Furthermore, the vertical wake height is higher for turbine 1 profile than turbine 2. The dynamical visualization shows that the vortices are carried over the flow, indicating that the wind velocity recovery and the flow structures in the wake are hardly connected. In addition, quantitative analysis of power production between both wind turbines was elaborated in order to assess the deficit in power production by the wake turbine. Therefore, a decrease in energy production could reach around 30% difference between the turbines. Demonstrating the importance of high-fidelity wind flow assessment and layout evaluation on wind energy projects.

6 CONCLUSIONS

The numerical results obtained from this work contribute to a deeper understanding of the unsteady flow around horizontal-axis wind turbines and blades. The main goal of this study was to conduct a large eddy simulation of a resolved wind turbine using a novel methodological framework that combines large eddy simulations coupling immersed boundary method with adaptive mesh refinement in order to accurately resolve the turbine aerodynamics, and especially the kinetic energy transfer and wake development. Therefore, simulations aimed at describing the dynamics of the turbulent flows in detail and the interactions between the wind with the structures of the turbine.

In terms of the flow over a wind turbine blade, the downstream wake centerline velocity analysis for different angles presented a quick recovery for small angles of attack. In contrast, in greater angles, the recovery was a bit slower. The drag and lift coefficient results showed satisfactory agreement compared to the experimental data from NREL. The vorticity parameter is the criteria applied for the first couple of scenarios with the adaptive mesh refinement, allowing the vortical structures to be accurately resolved with reasonable computational cost. The Phase VI NREL experimental turbine scenario showed a higher loss of kinetic energy in the near wake region, but achieves very similar results to literature in the far-wake region. The results were also characterized by smaller turbulent structures occurring primarily in the near wake, while larger eddies dominate the far wake. The wake velocity deficit has mostly self-similar properties in the rotor area behind the wind turbine, reducing the similarity near the edges.

From a 5MW NREL stand alone turbine perspective, it was presented lower recovery velocities of MFSim around the hub height centerline in the near wake compared to other profiles, which could be attributed to the simplification blade resolving geometry applied in MARBLLES and SOWFA. Despite that, most results presented differences lower than 10% among the profiles. Moreover, the power generation is validated with NREL experimental results with a difference of around 3.5%. Meanwhile, the back to back scenario demonstrated that waked turbine produces quicker recovery than the upstream wind turbine. However, it is more affected by the tower shading and indicates that the power performance may decrease by 30% in the downstream turbine. Demonstrating the importance of high-fidelity wind flow assessment and layout evaluation on wind energy projects.

The main contribution of the present work is to present a numerical approach in which advanced CFD techniques are deployed to accurately capture the interaction between the blades and the tower and the subsequent evolution of the near-wake flow with a reasonable computational cost. Developing such a simulation framework is essential to improving the current wake models used in wind farm design. Therefore, this study is an innovative numerical approach as a tool to enhance the design and operation of wind farms, additionally in the current scenario where the wind power has reached in Brazil.

The future perspectives from the thesis in terms of research and development are significant. These developments are presented in the next section.

7 RECOMMENDATIONS AND FUTURE WORK

The following perspectives of research, which are presently under development, consider introducing atmospheric turbulence at the inlet to enhance conditions that more closely resemble real-world conditions.

It is recommended to use vorticity criteria as refinement criteria with the flow away from the ground. Then it is suggested to overlap the vorticity criteria inside the previously determined refinement region to decrease computational cost. Therefore, there will not have remeshing areas by the vorticity criteria outside the pre-determined refinement region.

Develop fluid-structure interaction in the simulations in order to have the aeroelastic response of airfoil, the vibration of wind turbine blades, and a better understanding of wind turbine interactions over the wind farm. Moreover, to keep developing, the implementation of the generator counter-torque will also be continued. Thus, allowing variations of rotation throughout the simulation.

Implementation of metamodeling, since the optimization assisted by metamodels, is an important resource for optimizing problems whose computational complexity is high. Formed by a set of simplified equations capable of accurately and efficiently representing the original code, the metamodel should be the most representative and have as low as possible computational cost, enabling its use in optimization and sensitivity analysis, among others.

The modeling of complex geometries will also be improved using other immersed boundary methods that can better capture sharp interface geometries.

REFERENCES

- ABDELSALAM, A. M. et al. Experimental and numerical studies on the wake behavior of a horizontal axis wind turbine. *Journal of Wind Engineering and Industrial Aerodynamics*, v. 128, p. 54 – 65, 2014. ISSN 0167-6105. Available at: <<http://www.sciencedirect.com/science/article/pii/S0167610514000464>>. 42
- ABDELSALAM, A. M.; RAMALINGAM, V. Wake prediction of horizontal-axis wind turbine using full-rotor modeling. *Journal of Wind Engineering and Industrial Aerodynamics*, v. 124, p. 7 – 19, 2014. ISSN 0167-6105. Available at: <<http://www.sciencedirect.com/science/article/pii/S0167610513002511>>. 42
- ABEEÓLICA. Abeeólica muda marca para oficializar atuação em eólica offshore e hidrogênio verde. *ABEEólica*, 2022. Available at: <<https://abeeolica.org.br/>>. 21, 169
- ABKAR, M.; DABIRI, J. Self-similarity and flow characteristics of vertical-axis wind turbine wakes: an LES study. *Journal of Turbulence*, v. 18, p. 373–389, 01 2017. 111
- ABKAR, M.; PORTÉ-AGEL, F. The effect of free-atmosphere stratification on boundary-layer flow and power output from very large wind farms. *Energies*, v. 6, n. 5, p. 2338–2361, 2013. 51
- ABKAR, M.; PORTÉ-AGEL, F. Influence of atmospheric stability on wind-turbine wakes: A large-eddy simulation study. *Physics of Fluids*, v. 27, p. 035104, 03 2015. 110, 154
- ABRAHAM, A.; HONG, J. Characterization of atmospheric coherent structures and their impact on a utility-scale wind turbine. *Flow*, Cambridge University Press, v. 2, p. E5, 2022. 167
- ADARAMOLA, M.; KROGSTAD, P.- Experimental investigation of wake effects on wind turbine performance. *Renewable Energy*, v. 36, n. 8, p. 2078 – 2086, 2011. ISSN 0960-1481. Available at: <<http://www.sciencedirect.com/science/article/pii/S0960148111000462>>. 32
- AHMED, S.; CHAURASIYA, P. K. Application of remote sensing in wind resource assessment. Elsevier, 2019. 31
- AITKEN, M. L. et al. Quantifying wind turbine wake characteristics from scanning remote sensor data. *Journal of Atmospheric and Oceanic Technology*, v. 31, n. 4, p. 765–787, 2014. 32
- AKAY, B. et al. Experimental investigation of the root flow in a horizontal axis wind turbine. *Wind Energy*, v. 17, n. 7, p. 1093–1109, 2014. 148
- ALAIMO, A. et al. 3d cfd analysis of a vertical axis wind turbine. *Energies*, v. 8, p. 3013–3033, 04 2015. 42
- ANDRADE, F. O. *Contribuição à Simulação das Grandes Escalas de uma Chama Turbulenta Pré-Misturada Estabilizada em um Escoamento a Alta Velocidade*. Tese (Doutorado) — Pontifícia Universidade Católica do Rio de Janeiro, Rio de Janeiro, 2019. 54
- ANGELIDIS, D.; CHAUDHARY, S.; SOTIROPOULOS, F. Unstructured cartesian refinement with sharp interface immersed boundary method for 3d unsteady incompressible flows. *Journal of Computational Physics*, v. 325, p. 272 – 300, 2016. 49
- ARANAKE, A. C.; LAKSHMINARAYAN, V. K.; DURAISAMY, K. Computational analysis of shrouded wind turbine configurations using a 3-dimensional rans solver. *Renewable Energy*, v. 75, p. 818 – 832, 2015. ISSN 0960-1481. Available at: <<http://www.sciencedirect.com/science/article/pii/S0960148114006764>>. 40

- BAI, C.-J.; WANG, W.-C. Review of computational and experimental approaches to analysis of aerodynamic performance in horizontal-axis wind turbines (hawts). *Renewable and Sustainable Energy Reviews*, v. 63, p. 506 – 519, 2016. ISSN 1364-0321. Available at: <<http://www.sciencedirect.com/science/article/pii/S1364032116301903>>. 38
- BALDWIN, B. S.; BARTH, T. J. A one-equation turbulence transport model for high reynolds number wall-bounded flows [microform] / barrett s. baldwin and timothy j. barth. National Aeronautics and Space Administration, Ames Research Center ; For sale by the National Technical Information Service Moffett Field, Calif. : [Springfield, Va, p. 1 v., 1990. 39
- BALDWIN, B. S.; LOMAX, H. Thin layer approximation and algebraic model for separated turbulent flow. *AIAA Paper*, v. 78, 02 1978. 39
- Barbi, F. *Experimentação numérica de bolhas em ascensão*. Tese (Doutorado) — Universidade Federal de Uberlândia, Uberlândia, Brasil, 2016. 72
- BARBI, F. et al. Numerical experiments of ascending bubbles for fluid dynamic force calculations. *Journal of the Brazilian Society of Mechanical Sciences and Engineering*, v. 40, n. 11, p. 519, Oct 2018. ISSN 1806-3691. Available at: <<https://doi.org/10.1007/s40430-018-1435-7>>. 65
- BARTHELMIE, R.; FRANDBSEN, S.; RÉTHORÉ, P.-E. Modelling and measurements of offshore wakes. p. 45–53, 01 2006. 97
- BARTHELMIE, R. et al. Endow: Efficient development of offshore windfarms: Modelling wake and boundary-layer interactions. 06 2003. 110
- BARTHELMIE, R. J. et al. Modelling and measurements of power losses and turbulence intensity in wind turbine wakes at middelgrunden offshore wind farm. *Wind Energy*, v. 10, n. 6, p. 517–528, 2007. 32
- BARTHELMIE, R. J. et al. Modelling and measuring flow and wind turbine wakes in large wind farms offshore. *Wind Energy*, v. 12, n. 5, p. 431–444, 2009. 32, 154
- BARTHELMIE, R. J. et al. Comparison of wake model simulations with offshore wind turbine wake profiles measured by sodar. *Journal of Atmospheric and Oceanic Technology*, v. 23, n. 7, p. 888–901, 2006. 51, 153
- BINGÖL, F.; MANN, J.; LARSEN, G. C. Light detection and ranging measurements of wake dynamics part i: one-dimensional scanning. *Wind Energy*, v. 13, n. 1, p. 51–61, 2010. 32
- BORAZJANI, I.; GE, L.; SOTIROPOULOS, F. Curvilinear immersed boundary method for simulating fluid structure interaction with complex 3d rigid bodies. *Journal of computational physics*, v. 227, p. 7587–7620, 08 2008. 51
- BOSE, S.; MOIN, P.; YOU, D. Grid-independent large-eddy simulation using explicit filtering. *Physics of Fluids*, v. 22, n. 10, p. 105103, 2010. 58
- BOU-ZEID, E.; MENEVEAU, C.; PARLANGE, M. A scale-dependent lagrangian dynamic model for large eddy simulation of complex turbulent flows. *Physics of Fluids*, v. 17, n. 2, p. 025105, 2005. 47
- BOUSSINESQ, J. Essai sur la théorie des eaux courantes (in french). *Mémoires présentés par divers savants à l'Académie des Sciences*, v. 23, n. 1, p. 1–680, 1877. 33

- BRETON, S. et al. A survey of modelling methods for high-fidelity wind farm simulations using large eddy simulation. *Philosophical Transactions of The Royal Society A Mathematical Physical and Engineering Sciences*, v. 375, p. 20160097, 04 2017. 47
- BROWN, G. L.; ROSHKO, A. On density effects and large structure in turbulent mixing layers. *Journal of Fluid Mechanics*, Cambridge University Press, v. 64, n. 4, p. 775–816, 1974. 44
- BURTON, T. et al. Wind energy handbook. Wiley, 2011. 29
- CALAF, M.; MENEVEAU, C.; MEYERS, J. Large eddy simulation study of fully developed wind-turbine array boundary layers. *Physics of Fluids*, v. 22, n. 1, p. 015110, 2010. 46, 47, 51
- CAMPREGHER, R. B. *Modelagem matemática tridimensional para problemas de interação fluido-estrutura*. Tese (Doutorado) — Universidade Federal de Uberlândia, Uberlândia, 2005. 49, 50, 66
- CEBECI, T.; SMITH, A. Analysis of turbulent boundary layers. *NASA STI/Recon Technical Report A*, v. 75, 1974. 39
- ÇENGEL, Y. *Fluid Mechanics*. Tata McGraw Hill Education Private, 2010. (Çengel series in engineering thermal-fluid sciences). ISBN 9780070700345. Available at: <<https://books.google.com.br/books?id=c8ATbn9ChB8C>>. 25
- CHAURASIYA, P. K.; AHMED, S.; WARUDKAR, V. Wind characteristics observation using doppler-sodar for wind energy applications. *Resource-Efficient Technologies*, v. 3, n. 4, p. 495 – 505, 2017. 31
- CHEHOURI, A. et al. Review of performance optimization techniques applied to wind turbines. *Applied Energy*, v. 142, p. 361–388, 2015. 29
- CHEN, G.; LIANG, X.-F.; LI, X.-B. Modelling of wake dynamics and instabilities of a floating horizontal-axis wind turbine under surge motion. *Energy*, v. 239, p. 122110, 2022. ISSN 0360-5442. Available at: <<https://www.sciencedirect.com/science/article/pii/S0360544221023586>>. 136, 142
- CHOI, C.-K.; KWON, D. K. Wind tunnel blockage effects on aerodynamic behavior of bluff body. *Wind and Structures An International Journal*, v. 1, p. 351–364, 09 1998. 120
- CHORIN, A. J. Numerical solution of the navier-stokes equations. *Mathematics of Computation*, v. 22, p. 745–762, 1968. 69
- CLIVE, P. Remote sensing best practice. *European Wind Energy Offshore Conference, Copenhagen, DK*, 2012. 31
- CLIVE, P. Offshore power performance assessment for onshore costs. *SgurrEnergy*, 2016. 31
- COUNCIL, G. W. E. Available at:< <http://www.gwec.net/>>. *GWEC*, v. 20, 2016. 26
- CRESPO, A.; HERNÁNDEZ, J.; FRANDBSEN, S. Survey of modelling methods for wakes and wind farms. *Wind Energy*, v. 2, p. 1–24, 01 1999. 51
- DAMASCENO, M.; VEDOVOTO, J.; SILVEIRA-NETO, A. Turbulent inlet conditions modeling using large-eddy simulations. *CMES - Computer Modeling in Engineering and Sciences*, v. 104, p. 105–132, 01 2015. 65

- DAMASCENO, M. M. R.; SANTOS, J. G. de F.; VEDOVOTO, J. M. Simulation of turbulent reactive flows using a fdf methodology – advances in particle density control for normalized variables. *Computers Fluids*, v. 170, p. 128 – 140, 2018. ISSN 0045-7930. Available at: <<http://www.sciencedirect.com/science/article/pii/S0045793018302494>>. 65
- DAR, A. et al. On the self-similarity of wind turbine wakes in complex terrain using large-eddy simulation. *Wind Energy Science Discussions*, 05 2019. 110
- DASARI, T. et al. Near-wake behaviour of a utility-scale wind turbine. *Journal of Fluid Mechanics*, Cambridge University Press, v. 859, p. 204–246, 2019. 147
- DAVIDSON, L. et al. *LESFOIL: Large Eddy Simulation of Flow Around a High Lift Airfoil: Results of the Project LESFOIL Supported by the European Union 1998 - 2001*. Springer, 2003. (Community research in aeronautics, 1). ISBN 9783540005339. Available at: <<https://books.google.com.br/books?id=kPZGLiVln5wC>>. 47
- DEAVES, D. Computations of wind flow over changes in surface roughness. *Journal of Wind Engineering and Industrial Aerodynamics*, v. 7, n. 1, p. 65 – 94, 1981. 51
- DEAVES, D.; HARRIS, R. A mathematical model of the structure of strong winds. Construction Industry Research and Information Association, CIRA Report 76, 1978. 51
- DELORME, Y.; FRANKEL, S. Performance assessment of high-order large eddy simulation and immersed boundary method for rotorcraft hover. *55th AIAA Aerospace Sciences Meeting, Grapevine, Texas, USA*, 2017. 50
- DUDA, D.; URUBA, V.; YANOVYCH, V. Wake width: Discussion of several methods how to estimate it by using measured experimental data. *Energies*, v. 14, n. 15, 2021. ISSN 1996-1073. Available at: <<https://www.mdpi.com/1996-1073/14/15/4712>>. 153
- EDELENBOSCH, O. et al. Comparing projections of industrial energy demand and greenhouse gas emissions in long-term energy models. *Energy*, v. 122, p. 701 – 710, 2017. ISSN 0360-5442. Available at: <<http://www.sciencedirect.com/science/article/pii/S0360544217300178>>. 21
- EISENBACH, S.; FRIEDRICH, R. Large-eddy simulation of flow separation on an airfoil at a high angle of attack and $re = 105$ using cartesian grids. *Theoretical and Computational Fluid Dynamics*, v. 22, n. 3, p. 213–225, May 2008. 51
- FERZIGER, J.; PERIC, M. *Computational methods for fluid dynamics*. 3. ed. Institute of Physical Problems, Academy of Sciences: Springer Verlag, 2002. 67
- FRANDBSEN, S. On the wind speed reduction in the center of large clusters of wind turbines. *Journal of Wind Engineering and Industrial Aerodynamics*, v. 39, n. 1, p. 251 – 265, 1992. 34
- FRANDBSEN, S. Turbulence and turbulence-generated structural loading in wind turbine clusters. 01 2007. 160
- FRANDBSEN, S. et al. Analytical modelling of wind speed deficit in large offshore wind farms. *Wind Energy*, v. 9, n. 1-2, p. 39–53, 2006. 34, 35, 110
- GE, L.; SOTIROPOULOS, F. A numerical method for solving the 3d unsteady incompressible navier-stokes equations in curvilinear domains with complex immersed boundaries. *Journal of computational physics*, v. 225, p. 1782–1809, 09 2007. 49
- GERMANO, M. et al. A dynamic subgrid-scale eddy viscosity model. *Physics of Fluids A: Fluid Dynamics*, v. 3, p. 1760–1765, 07 1991. 45, 57

- GILMANOV, A.; ACHARYA, S. A hybrid immersed boundary and material point method for simulating 3d fluid–structure interaction problems. *International Journal for Numerical Methods in Fluids*, v. 56, n. 12, p. 2151–2177, 2008. 48
- GOTTSCHALL, J.; PEINKE, J. How to improve the estimation of power curves for wind turbines. *Environmental Research Letters*, v. 3, n. 1, 2008. 30
- GUALTIERI, G. A comprehensive review on wind resource extrapolation models applied in wind energy. *Renewable and Sustainable Energy Reviews*, v. 102, p. 215 – 233, 2019. 51
- GWEC. Global wind energy outlook 2014. *Global Wind Energy Council*, 2014. Available at: <http://www.gwec.net/wp-content/uploads/2014/10/GWEO2014_WEB.pdf>. 21
- GWEC. Global wind energy report 2022. *Global Wind Energy Council*, 2022. Available at: <<https://gwec.net/wp-content/uploads/2022/03/GWEC-GLOBAL-WIND-REPORT-2022.pdf>>. 169
- HAN, D.; LIU, G.; ABDALLAH, S. An eulerian–lagrangian–lagrangian method for solving thin moving rigid body immersed in the fluid. *Computers Fluids*, v. 179, p. 687 – 701, 2019. ISSN 0045-7930. Available at: <<http://www.sciencedirect.com/science/article/pii/S0045793018309332>>. 48
- HAND, M. M. et al. Unsteady aerodynamics experiment phase vi: Wind tunnel test configurations and available data campaigns. 12 2001. 30, 31, 77, 79, 91
- HANSEN, M. Aerodynamics of wind turbines. p. 1, 01 2008. 21, 81
- HANSEN, M.; SØRENSEN, N.; MICHELSEN, J. Extraction of lift, drag and angle of attack from computed 3-d viscous flow around a rotating blade. 1997. 1997 European Wind Energy Conference , EWEC '97 ; Conference date: 06-10-1997 Through 09-10-1997. 43
- HONRUBIA, A. et al. The influence of wind shear in wind turbine power estimation. *European Energy Conference*, 2010. 29
- HU, B. *Design of a Simple Wake Model for the Wind Farm Layout Optimization Considering the Wake Meandering Effect*. Dissertação (Mestrado), 2016. 37
- IACCARINO, G.; VERZICCO, R. Immersed boundary technique for turbulent flow simulations. *Appl. Mech. Rev.*, v. 56, n. 3, p. 331–347, 2003. 48, 49
- IVANELL, S. et al. Analysis of numerically generated wake structures. *Wind Energy*, v. 12, n. 1, p. 63–80, 2009. 46
- JENSEN, N. A note on wind generator interaction. *Risø-M-2411*, v. 1, 1983. 34, 35, 154
- JIMENEZ, A. et al. Advances in large-eddy simulation of a wind turbine wake. IOP Publishing, v. 75, p. 012041, jul 2007. 46
- JONKMAN, J. et al. Definition of a 5-mw reference wind turbine for offshore system development. 2009. 77, 116, 157, 160
- KAISER, K. et al. Turbulence correction for power curves. *Wind Energy*, 2004. 30
- KAJISHIMA, T.; TAIRA, K. *Computational fluid dynamics: Incompressible turbulent flows*. Springer, 2016. 51

- KÄSLER, Y. et al. Wake measurements of a multi-mw wind turbine with coherent long-range pulsed doppler wind lidar. *Journal of Atmospheric and Oceanic Technology*, v. 27, n. 9, p. 1529–1532, 2010. 32
- KATIC, I.; HØJSTRUP, J.; JENSEN, N. A simple model for cluster efficiency. A. Raguzzi, p. 407–410, 1987. 34
- KECK, R.-E. et al. Synthetic atmospheric turbulence and wind shear in large eddy simulations of wind turbine wakes. *Wind Energy*, v. 17, n. 8, p. 1247–1267, 2013. 50
- KILKIS, S. et al. Advancements in sustainable development of energy, water and environment systems. *Energy Conversion and Management*, v. 176, p. 164 – 183, 2018. ISSN 0196-8904. Available at: <<http://www.sciencedirect.com/science/article/pii/S0196890418310100>>. 21
- KIM, S.-H. et al. A study of the wake effects on the wind characteristics and fatigue loads for the turbines in a wind farm. *Renewable Energy*, v. 74, p. 536 – 543, 2015. ISSN 0960-1481. Available at: <<http://www.sciencedirect.com/science/article/pii/S0960148114005242>>. 32, 86
- KIM, W.; CHOI, H. Immersed boundary methods for fluid-structure interaction: A review. *International Journal of Heat and Fluid Flow*, v. 75, p. 301 – 309, 2019. ISSN 0142-727X. Available at: <<http://www.sciencedirect.com/science/article/pii/S0142727X1830691X>>. 48
- KIM, W.; MENON, S. Application of the localized dynamic subgrid-scale model to turbulent wall-bounded flows. *35th Aerospace Sciences Meeting and Exhibit. Reno, NV, U.S.A.*, 1997. 51
- KOLMOGOROV, A. Equations of turbulent motion of an incompressible fluid. *Izv. Akad. Nauk. SSSR ser. Fiz.*, v. 6, p. 56–58, 1942. 41
- LAAN, M. P. van der et al. A CFD code comparison of wind turbine wakes. *Journal of Physics: Conference Series*, IOP Publishing, v. 524, p. 012140, jun 2014. Available at: <<https://doi.org/10.1088/1742-6596/524/1/012140>>. 50, 140
- LANZAFAME, R.; MAURO, S.; MESSINA, M. Numerical and experimental analysis of micro hawts designed for wind tunnel applications. *International Journal of Energy and Environmental Engineering*, v. 7, n. 2, p. 199–210, Jun 2016. 44
- LARSEN, G. A simple wake calculation procedure. 1988. 34, 35
- LAUNDER, B.; SHARMA, B. Application of the energy-dissipation model of flow near a spinning disc. *Lett. Heat Mass Transfer*, p. 131–138, 01 1974. 41
- LEUNG, D.; YANG, Y. Wind energy development and its environmental impact: A review. *Renewable and Sustainable Energy Reviews*, Elsevier, v. 16, p. 1031–1039, 01/12 2012. Available at: <<https://www.sciencedirect.com/science/article/pii/S1364032111004746>>. 21
- LEVI, E. A universal strouhal law. *Journal of Engineering Mechanics*, v. 109, n. 3, p. 718–727, 1983. 190
- LILLY, D. K. A proposed modification of the germano subgrid-scale closure method. *Physics of Fluids A: Fluid Dynamics*, v. 4, n. 3, p. 633–635, 1992. 45, 57
- LIMA, R. S. de. *Desenvolvimento e implementação de malhas adaptativas bloco-estruturadas para computação paralela em mecânica dos fluidos*. Tese (Doutorado) — Universidade Federal de Uberlândia, Uberlândia, 2012. 73, 74
- LISSAMAN, P. B. S. Energy effectiveness of arbitrary arrays of wind turbines. *Journal of Energy*, -1, 12 1978. 51

- LUND, H. Renewable energy strategies for sustainable development. *Energy*, v. 32, n. 6, p. 912 – 919, 2007. ISSN 0360-5442. Third Dubrovnik Conference on Sustainable Development of Energy, Water and Environment Systems. Available at: <<http://www.sciencedirect.com/science/article/pii/S036054420600301X>>. 21
- MAGALHÃES, G. B. et al. Computational simulation of a plane channel with $k - \epsilon$ and multi-direct forcing method. *11th International Symposium on Turbulence and Shear Flow Phenomena Southampton, UK*, 2019. 65
- MALISKA, C. *Transferência de calor e mecânica dos fluidos computacional: fundamentos e coordenadas generalizadas*. Livros Técnicos e Científicos, 1995. Available at: <<https://books.google.com.br/books?id=lfo\MwEACAAJ>>. 30
- MANWELL, J.; MCGOWAN, J.; ROGERS, A. Wind energy explained: Theory, design and application. Wiley, 2010. 26, 27, 29, 30
- MARK, A.; WACHEM, B. van. Derivation and validation of a novel implicit second-order accurate immersed boundary method. *J. Comput. Phys.*, v. 227, p. 6660–6680, 2008. 50
- MCTAVISH, S.; FESZTY, D.; SANKAR, T. Steady and rotating computational fluid dynamics simulations of a novel vertical axis wind turbine for small-scale power generation. *Renewable Energy*, v. 41, p. 171 – 179, 2012. ISSN 0960-1481. Available at: <<http://www.sciencedirect.com/science/article/pii/S0960148111005945>>. 51
- MEDICI, D.; ALFREDSSON, P. H. Measurements on a wind turbine wake: 3d effects and bluff body vortex shedding. *Wind Energy*, v. 9, n. 3, p. 219–236, 2006. 190
- MEHTA, D. et al. Large eddy simulation of wind farm aerodynamics: A review. *Journal of Wind Engineering and Industrial Aerodynamics*, v. 133, p. 1 – 17, 2014. ISSN 0167-6105. Available at: <<http://www.sciencedirect.com/science/article/pii/S0167610514001391>>. 47
- MEHTA, D. et al. Large eddy simulation of wind farm aerodynamics: A review. *Journal of Wind Engineering and Industrial Aerodynamics*, v. 133, p. 1 – 17, 2014. ISSN 0167-6105. Available at: <<http://www.sciencedirect.com/science/article/pii/S0167610514001391>>. 54
- MELLEN, C.; FRÖHLICH, J.; RODI, W. Lessons from lesfoil project on large-eddy simulation of flow around an airfoil. *Aiaa Journal - AIAA J*, v. 41, p. 573–581, 04 2003. 51
- MELO, R. R. da S. *Formulações Integral e Diferencial Aplicadas à Análise de Escoamentos Sobre Rotores Eólicos*. Dissertação (Mestrado) — Universidade Federal de Uberlândia, Uberlândia, 2012. 62
- MELO, R. R. da S. *Modelagem e Simulação de Escoamentos Turbulentos com Efeitos Térmicos, Utilizando a Metodologia da Fronteira Imersa e Malha Adaptativa*. Tese (Doutorado) — Universidade Federal de Uberlândia, Uberlândia, 2017. 41, 48, 57, 58, 61, 62, 67, 73, 74, 75
- MENTER, F. Two-equation eddy-viscosity transport turbulence model for engineering applications. *aiaa journal* 32(8), 1598-1605. *AIAA Journal*, v. 32, 09 1994. 43
- MENTER, F.; KUNTZ, M.; LANGTRY, R. Ten years of industrial experience with the sst turbulence model. *Heat and Mass Transfer*, v. 4, 01 2003. 43
- MÉTAIS, O.; LESIEUR, M. Spectral large-eddy simulation of isotropic and stably stratified turbulence. *Journal of Fluid Mechanics*, Cambridge University Press, v. 239, p. 157–194, 1992. 51

- MIKKELSEN, R. F. *Actuator Disc Methods Applied to Wind Turbines*. Tese (Doutorado), 1 2003. 46
- MILEY, S. Catalog of low-reynolds-number airfoil data for wind-turbine applications. 2 1982. 28
- MITTAL, R.; IACCARINO, G. Immersed boundary methods. *Annual Review of Fluid Mechanics*, v. 37, n. 1, p. 239–261, 2005. 48
- MO, J. O. et al. Effects of wind speed changes on wake instability of a wind turbine in a virtual wind tunnel using large eddy simulation. *Journal of Wind Engineering and Industrial Aerodynamics*, v. 117, p. 38–56, 2013. 21
- MO, J.-O. et al. Effects of wind speed changes on wake instability of a wind turbine in a virtual wind tunnel using large eddy simulation. *Journal of Wind Engineering and Industrial Aerodynamics*, v. 117, p. 38 – 56, 2013. ISSN 0167-6105. Available at: <<http://www.sciencedirect.com/science/article/pii/S0167610513000718>>. 50, 91, 95, 96, 100, 101, 102, 103, 104, 105, 106, 114
- MOHD-YUSOF, J. Combined immersed-boundary/b-spline methods for simulations of flow in complex geometries. *Technical report, Center for Turbulence Research, Annual Research Briefs*, 1997. 49
- MOSHFEGHI, M.; SONG, Y. J.; XIE, Y. H. Effects of near-wall grid spacing on $sst - k - \omega$ model using nrel phase vi horizontal axis wind turbine. *Journal of Wind Engineering and Industrial Aerodynamics*, v. 107-108, p. 94 – 105, 2012. ISSN 0167-6105. Available at: <<http://www.sciencedirect.com/science/article/pii/S016761051200089X>>. 51
- NETO, A. S. Escoamentos turbulentos - análise física e modelagem teórica. Composer - Uberlândia, v. 1, 2020. 33
- NETO, H. R. et al. Influence of seabed proximity on the vibration responses of a pipeline accounting for fluid-structure interaction. *Mechanical Systems and Signal Processing*, Elsevier, v. 114, p. 224–238, 2019. 65
- NINI, M. et al. Three-dimensional simulation of a complete vertical axis wind turbine using overlapping grids. *Journal of Computational and Applied Mathematics*, v. 270, p. 78 – 87, 2014. ISSN 0377-0427. Fourth International Conference on Finite Element Methods in Engineering and Sciences (FEMTEC 2013). Available at: <<http://www.sciencedirect.com/science/article/pii/S037704271400106X>>. 40
- NOBARI, M.; MIRZAEI, E.; NOSRATOLLAHI, M. Improvement of wind turbine performance using a novel tip plate structure. *Energy Conversion and Management*, v. 123, p. 592 – 609, 2016. ISSN 0196-8904. Available at: <<http://www.sciencedirect.com/science/article/pii/S0196890416305672>>. 43
- OLIVEIRA, S. et al. Numerical simulation of high reynolds numbers flows over circular cylinders using the immersed boundary method. *18th International Congress of Mechanical Engineering, Ouro Preto, Brasil*, 2005. 50
- PATANKAR, S. V. Numerical heat transfer and fluid flow. Hemisphere Publishing Corporation, 1980. 65
- PENA, A.; RETHORE, P.-E.; LAAN, M. P. van der. On the application of the jensen wake model using a turbulence-dependent wake decay coefficient: the sexbierum case. *Wind Energy*, v. 19, n. 4, p. 763–776, 2016. Available at: <<https://onlinelibrary.wiley.com/doi/abs/10.1002/we.1863>>. 34

- PESKIN, C. Flow patterns around heart valves: A numerical method. *Journal of Computational Physics*, v. 10, n. 2, p. 252 – 271, 1972. ISSN 0021-9991. Available at: <<http://www.sciencedirect.com/science/article/pii/0021999172900654>>. 48, 49
- PESKIN, C. Numerical analysis of blood flow in the heart. *Journal of Computational Physics*, v. 25, n. 3, p. 220 – 252, 1977. ISSN 0021-9991. Available at: <<http://www.sciencedirect.com/science/article/pii/0021999177901000>>. 48
- PESKIN, C. The immersed boundary method. Cambridge University Press, v. 11, p. 479–518, 2002. 48
- PIOMELLI, U. Large-eddy and direct simulation of turbulent flows. *Department of Mechanical Engineering, University of Maryland College Park, Maryland, USA*, 2001. 45, 46
- PLAZA, B.; BARDERA, R.; VISIEDO, S. Comparison of bem and cfd results for mexico rotor aerodynamics. *Journal of Wind Engineering and Industrial Aerodynamics*, v. 145, p. 115 – 122, 2015. 44
- POINSOT, T. et al. Simulation tools for 3d reacting flows. *Combustion Energy Frontier Research Center, Princeton, USA*, 2015. 45
- POPE, S. B. A perspective on turbulence modeling. Springer Netherlands, Dordrecht, p. 53–67, 1999. Available at: <https://doi.org/10.1007/978-94-011-4724-8_5>. 141
- POPE, S. B. Turbulent flows. Cambridge University Press, 2000. 54, 110
- PORTÉ-AGEL, F. et al. Large-eddy simulation of atmospheric boundary layer flow through wind turbines and wind farms. *Journal of Wind Engineering and Industrial Aerodynamics*, v. 99, n. 4, p. 154 – 168, 2011. ISSN 0167-6105. The Fifth International Symposium on Computational Wind Engineering. Available at: <<http://www.sciencedirect.com/science/article/pii/S0167610511000134>>. 47
- PORTÉ-AGEL, F.; BASTANKHAH, M.; SHAMSODDIN, S. Wind-turbine and wind-farm flows: A review. *Boundary-Layer Meteorology*, v. 174, 01 2020. 29
- PRANDTL, L. 7. bericht über untersuchungen zur ausgebildeten turbulenz. *ZAMM - Journal of Applied Mathematics and Mechanics / Zeitschrift für Angewandte Mathematik und Mechanik*, v. 5, n. 2, p. 136–139, 1925. Available at: <[https://onlinelibrary.wiley.com/doi/abs/10.1002-zamm.19250050212](https://onlinelibrary.wiley.com/doi/abs/10.1002/zamm.19250050212)>. 39
- PRANDTL, L. On a new representation of fully developed turbulence. *Jet Propulsion Lab. Pub.*, v. 13, 1945. 39
- RABI, J. A.; LEMOS, M. J. S. Optimization of convergence acceleration in multigrid numerical solutions of conductive–convective problems. *Applied Mathematics and Computation*, v. 124, n. 2, p. 215 – 226, 2001. ISSN 0096-3003. 74
- RABI, J. A.; LEMOS, M. J. S. Multigrid correction-storage formulation applied to the numerical solution of incompressible laminar recirculating flows. *Applied Mathematical Modelling*, v. 27, n. 9, p. 717 – 732, 2003. ISSN 0307-904X. 74
- RAHIMI, H. et al. Navier-stokes-based predictions of the aerodynamic behaviour of stall regulated wind turbines using openfoam. *Progress in Computational Fluid Dynamics, An International Journal*, v. 16, p. 339, 01 2016. 44
- RAMSAY, R.; HOFFMAN, M.; GREGOREK, G. Effects of grit roughness and pitch oscillations on the s809 airfoil. 12 1995. 30

- RAPAKA, N. R.; SARKAR, S. An immersed boundary method for direct and large eddy simulation of stratified flows in complex geometry. *Journal of Computational Physics*, v. 322, p. 511 – 534, 2016. ISSN 0021-9991. Available at: <<http://www.sciencedirect.com/science/article/pii/S0021999116302613>>. 22, 33
- REGODESEVES, P. G.; MORROS, C. S. Numerical study on the aerodynamics of an experimental wind turbine: Influence of nacelle and tower on the blades and near-wake. *Energy Conversion and Management*, v. 237, p. 114110, 2021. ISSN 0196-8904. Available at: <<https://www.sciencedirect.com/science/article/pii/S0196890421002867>>. 147
- REYNOLDS, O. On the dynamical theory of incompressible viscous fluids and the determination of the criterion. *Philosophical Transactions of the Royal Society of London. A*, The Royal Society, v. 186, p. 123–164, 1895. ISSN 02643820. Available at: <<http://www.jstor.org/stable/90643>>. 33
- ROCHA, P. C. et al. k^ω sst (shear stress transport) turbulence model calibration: A case study on a small scale horizontal axis wind turbine. *Energy*, v. 65, p. 412 – 418, 2014. 44
- ROHATGI, J.; BARBEZIER, G. Wind turbulence and atmospheric stability — their effect on wind turbine output. *Renewable Energy*, v. 16, n. 1, p. 908 – 911, 1999. ISSN 0960-1481. Renewable Energy Energy Efficiency, Policy and the Environment. Available at: <<http://www.sciencedirect.com/science/article/pii/S0960148198003085>>. 29
- ROMA, A.; PESKIN, C.; BERGER, M. An adaptive version of the immersed boundary method. *Journal of Computational Physics*, v. 153, n. 2, p. 509 – 534, 1999. ISSN 0021-9991. Available at: <<http://www.sciencedirect.com/science/article/pii/S0021999199962939>>. 51
- ROY, S. B.; SHARP, J. Why atmospheric stability matters in wind assessment. *North American Wind Power*, v. 9, n. 12, 2013. 30, 86
- SANDERSE, B. Aerodynamics of wind turbine wakes literature review. 01 2009. 53
- SANTOS, J. G. de F. *Modelagem matemática e computacional de escoamentos gás-sólido em malha adaptativa dinâmica*. Dissertação (Mestrado) — Universidade Federal de Uberlândia, Uberlândia, 2019. 65, 66, 70, 71
- SATHE, A. et al. Influence of atmospheric stability on wind turbine loads. *Wind Energy*, 2013. 30, 86
- SEDAGHATIZADEH, N. et al. Modelling of wind turbine wake using large eddy simulation. *Renewable Energy*, v. 115, p. 1166 – 1176, 2018. ISSN 0960-1481. Available at: <<http://www.sciencedirect.com/science/article/pii/S0960148117308790>>. 28, 50, 91, 100, 102, 103, 105, 106
- SHEINMAN, Y.; ROSEN, A. A dynamic model of the influence of turbulence on the power output of a wind turbine. *Journal of Wind Engineering and Industrial Aerodynamics*, v. 39, n. 1, p. 329 – 341, 1992. 30
- SHIH, T.-H. et al. A new $k - \varepsilon$ eddy viscosity model for high reynolds number turbulent flows. *Computers Fluids*, v. 24, n. 3, p. 227 – 238, 1995. ISSN 0045-7930. Available at: <<http://www.sciencedirect.com/science/article/pii/004579309400032T>>. 41
- SILVA, A. L. E.; SILVEIRA-NETO, A.; DAMASCENO, J. Numerical simulation of two-dimensional flows over a circular cylinder using the immersed boundary method. *Journal of Computational Physics*, v. 189, n. 2, p. 351 – 370, 2003. ISSN 0021-9991. Available at: <<http://www.sciencedirect.com/science/article/pii/S0021999103002146>>. 49

- SILVEIRA, F. S. V. et al. Modelo integrado para avaliação de projetos de investimento no setor elétrico. Florianópolis, SC, 2001. 40
- SIMMS, D. et al. Nrel unsteady aerodynamics experiment in the nasa-ames wind tunnel: A comparison of predictions to measurements. 6 2001. 30, 77, 91
- SMAGORINSKY, J. General circulation experiments with the primitive equations. *Monthly Weather Review*, v. 91, n. 3, p. 99–164, 1963. 44
- SMALIKHO, I. N. et al. Lidar investigation of atmosphere effect on a wind turbine wake. *Journal of Atmospheric and Oceanic Technology*, v. 30, n. 11, p. 2554–2570, 2013. 32
- SNEL, H. Review of aerodynamics for wind turbines. *Wind Energy*, v. 6, n. 3, p. 203–211, 2003. 53
- SOMERS, D. Design and experimental results for the s809 airfoil. 01 1997. 30
- SONG, Y.; PEROT, J. Cfd simulation of the nrel phase vi rotor. *Wind Engineering*, v. 39, 04 2014. 40
- SØRENSEN, J.; SHEN, W. Z. Numerical modeling of wind turbine wakes. *Journal of Fluids Engineering*, v. 124, p. 393, 01 2002. 43
- SØRENSEN, J. N. Aerodynamic aspects of wind energy conversion. *Annual Review of Fluid Mechanics*, v. 43, n. 1, p. 427–448, 2011. 46
- SØRENSEN, N.; HANSEN, M. Rotor performance predictions using a navier-stokes method. American Institute of Aeronautics and Astronautics, p. 52–59, 1998. 38, 43
- SOTIROPOULOS, F.; YANG, X. Immersed boundary methods for simulating fluid–structure interaction. *Progress in Aerospace Sciences*, v. 65, p. 1 – 21, 2014. ISSN 0376-0421. Available at: <<http://www.sciencedirect.com/science/article/pii/S0376042113000870>>. 22, 48
- SOUZA, J. F. A. et al. Uma revisão sobre a turbulência e sua modelagem. *Revista Brasileira de Geofísica*, sciELO, v. 29, p. 21 – 41, 03 2011. 51
- SPALART, P.; ALLMARAS, S. A one-equation turbulence model for aerodynamic flows. *AIAA*, v. 439, 01 1992. 39, 40
- STERGIANNIS, N.; BEECK, J. van; RUNACRES, M. C. Full hawt rotor cfd simulations using different rans turbulence models compared with actuator disk and experimental measurements. *Wind Energy Science Discussions*, v. 2017, p. 1–20, 2017. 42
- STIVAL, L. *A study on wind assessment on the wind power performance : wind shear and turbulence intensity effects besides the wake modeling for a single wind turbine*. Dissertação (Mestrado), 2017. 37, 38, 154
- STIVAL, L. J. L.; GUETTER, A. K.; ANDRADE, F. O. The impact of wind shear and turbulence intensity on wind turbine power performance. *Espaço Energia*, v. 27, p. 11–20, 2017. 30, 34, 86, 154
- STOREY, R.; CATER, J.; NORRIS, S. Large eddy simulation of turbine loading and performance in a wind farm. *Renewable Energy*, v. 95, p. 31 – 42, 2016. ISSN 0960-1481. Available at: <<http://www.sciencedirect.com/science/article/pii/S0960148116302518>>. 46, 47
- SUMNER, J.; WATTERS, C.; MASSON, C. Cfd in wind energy: The virtual, multiscale wind tunnel. *Energies*, n. 3, p. 989–1013, 2010. 32

- Syed Ahmed Kabir, I. F.; NG, E. Effect of different atmospheric boundary layers on the wake characteristics of nrel phase vi wind turbine. *Renewable Energy*, v. 130, p. 1185–1197, 2019. ISSN 0960-1481. Available at: <<https://www.sciencedirect.com/science/article/pii/S0960148118310334>>. 50, 91, 100, 101, 102, 103, 104, 105, 106
- TACHOS, N.; FILIOS, A.; MARGARIS, D. A comparative numerical study of four turbulence models for the prediction of horizontal axis wind turbine flow. *Proceedings of the Institution of Mechanical Engineers, Part C: Journal of Mechanical Engineering Science*, v. 224, n. 9, p. 1973–1979, 2010. 43
- THÉ, J.; YU, H. A critical review on the simulations of wind turbine aerodynamics focusing on hybrid rans-les methods. *Energy*, v. 138, p. 257 – 289, 2017. ISSN 0360-5442. Available at: <<http://www.sciencedirect.com/science/article/pii/S0360544217312033>>. 40, 43, 51
- TIELEMAN, H. W. Strong wind observations in the atmospheric surface layer. *Journal of Wind Engineering and Industrial Aerodynamics*, v. 96, p. 41–77, 01 2008. 33
- TROLDBORG, N.; SØRENSEN, J. N.; MIKKELSEN, R. Actuator line simulation of wake of wind turbine operating in turbulent inflow. *Journal of Physics: Conference Series*, IOP Publishing, v. 75, p. 012063, jul 2007. 46
- TROLDBORG, N. et al. A simple atmospheric boundary layer model applied to large eddy simulations of wind turbine wakes. *Wind Energy*, v. 17, n. 4, p. 657–669, 2014. 50
- TROLDBORG, N. et al. Comparison of wind turbine wake properties in non-sheared inflow predicted by different computational fluid dynamics rotor models. *Wind Energy*, v. 18, n. 7, p. 1239–1250, 2015. 51
- TROTTEBERG, U.; SCHULLER, A. *Multigrid*. USA: Academic Press, Inc., 2000. ISBN 012701070X. 73
- TRUJILLO, J.-J. et al. Light detection and ranging measurements of wake dynamics. part ii: two-dimensional scanning. *Wind Energy*, v. 14, n. 1, p. 61–75, 2011. 32
- TSALICOGLU, C. et al. Rans computations of mexico rotor in uniform and yawed inflow. *Journal of Engineering for Gas Turbines and Power*, v. 136, p. 011202, 10 2013. 51
- URANGA, A. et al. Implicit large eddy simulation of transitional flows over airfoils and wings. *19th AIAA Computational Fluid Dynamics*, 06 2009. 51
- VAN-DRIEST, E. On turbulent flow near a wall. *Journal of the Aeronautical Sciences*, v. 23, n. 11, p. 1007–1011, 1956. 45
- VEDOVOTO, J. M. *Mathematical and Numerical Modeling of Turbulent Reactive Flows using a Hybrid LES / PDF Methodology*. Tese (Doutorado) — Universidade Federal de Uberlândia, Uberlândia, 2011. 61, 67, 68
- VEDOVOTO, J. M.; SERFATY, R.; NETO, A. S. Mathematical and Numerical Modeling of Turbulent Flows. *Anais da Academia Brasileira de Ciências*, sciELO, v. 87, p. 1195 – 1232, 06 2015. ISSN 0001-3765. Available at: <http://www.scielo.br/scielo.php?script=sci_arttext&pid=S0001-37652015000201195&nrm=iso>. 48, 49, 61
- VERMEER, L.; SØRENSEN, J.; CRESPO, A. Wind turbine wake aerodynamics. *Progress in Aerospace Sciences*, v. 39, n. 6, p. 467 – 510, 2003. 37, 46
- VERMEER, L.; SØRENSEN, J.; CRESPO, A. Wind turbine wake aerodynamics. *Progress in Aerospace Sciences*, v. 39, p. 467–510, 2003. 21

- VERSTEEG, H.; MALALASEKERA, W. *An Introduction to Computational Fluid Dynamics: The Finite Volume Method*. New York, 1995. ISBN 9780470235157. Available at: <<https://books.google.com.br/books?id=uZBpQgAACAAJ>>. 32
- VILLAR, M. *Análise numérica detalhada de escoamentos multifásicos bidimensionais*. Tese (Doutorado) — Universidade Federal de Uberlândia, Uberlândia, 2007. 65, 67, 70, 74, 75
- VOGT, S.; THOMAS, P. Sodar — a useful remote sounder to measure wind and turbulence. *Journal of Wind Engineering and Industrial Aerodynamics*, v. 54-55, p. 163 – 172, 1995. 51
- WANG, X.; LIU, W. Extended immersed boundary method using fem and rkpm. *Computer Methods in Applied Mechanics and Engineering*, v. 193, n. 12, p. 1305 – 1321, 2004. ISSN 0045-7825. Meshfree Methods: Recent Advances and New Applications. Available at: <<http://www.sciencedirect.com/science/article/pii/S0045782504000258>>. 49
- WANG, X.; ZHANG, L. T. Interpolation functions in the immersed boundary and finite element methods. *Computational Mechanics*, v. 45, n. 4, p. 321, Dec 2009. 48
- WANG, Z.; FAN, J.; LUO, K. Combined multi-direct forcing and immersed boundary method for simulating flows with moving particles. *International Journal of Multiphase Flow - INT J MULTIPHASE FLOW*, v. 34, p. 283–302, 03 2008. 50
- WHARTON, S.; LUNDQUIST, J. Atmospheric stability affects wind turbine power collection. *Environmental Research Letter*, v. 7, p. 014005, 2012. 30
- WILCOX, D. Reassessment of the scale-determining equation for advanced turbulence models. *AIAA Journal*, v. 26, p. 1299–1310, 11 1988. 43
- WILCOX, D. Formulation of the $k - \omega$ turbulence model revisited. *Aiaa Journal - AIAA J*, v. 46, p. 2823–2838, 11 2008. 43
- WILSON, W. et al. Noaa’s recent field testing of current and wave measurement systems – part ii. p. 1–8, 2015. 44
- WU, Y.; PORTÉ-AGEL, F. Atmospheric turbulence effects on wind-turbine wakes: An les study. *Energies*, v. 5, p. 5340–5362, 12 2012. 30
- XIE, S.; ARCHER, C. Self-similarity and turbulence characteristics of wind turbine wakes via large-eddy simulation. *Wind Energy*, v. 18, 08 2014. 110, 111
- YAKHOT, V.; ORSZAG, S. A. Renormalization group analysis of turbulence. i. basic theory. *Journal of Scientific Computing*, v. 1, n. 1, p. 3–51, Mar 1986. 51
- YAKHOT, V. et al. Development of turbulence models for shear flows by a double expansion technique. *Physics of Fluids A: Fluid Dynamics*, v. 4, n. 7, p. 1510–152, 1992. 41
- YILDIRIM, B. et al. A parallel implementation of fluid–solid interaction solver using an immersed boundary method. *Computers Fluids*, v. 86, p. 251 – 274, 2013. ISSN 0045-7930. Available at: <<http://www.sciencedirect.com/science/article/pii/S0045793013002697>>. 22, 33
- YOU, J. Y.; YU, D. O.; KWON, O. J. Effect of turbulence models on predicting hawt rotor blade performances. *Journal of Mechanical Science and Technology*, v. 27, n. 12, p. 3703–3711, Dec 2013. 40
- ZHANG, L. et al. Immersed finite element method. *Computer Methods in Applied Mechanics and Engineering*, v. 193, n. 21, p. 2051 – 2067, 2004. ISSN 0045-7825. Flow Simulation and Modeling. Available at: <<http://www.sciencedirect.com/science/article/pii/S0045782504000672>>. 49

ZHANG, L. X. et al. Aerodynamic performance prediction of straight-bladed vertical axis wind turbine based on cfd. *Advances in Mechanical Engineering*, v. 5, p. 905379, 2013. 42

ZHONG, W. et al. Global pattern of the international fossil fuel trade: The evolution of communities. *Energy*, v. 123, p. 260 – 270, 2017. ISSN 0360-5442. Available at: <<http://www.sciencedirect.com/science/article/pii/S0360544217302074>>. 21

APPENDIX A – SCENARIO 1: ANALYSIS OF CROSS-SECTION VELOCITY AND TURBULENCE PROPERTIES

A.1 CROSS-SECTION VELOCITY

Figure A.1.1 depicts the time-averaged streamwise velocity distribution for cross-sections located at 3c and 9c downstream from the blade, and for angles of attack varying from 0° to 20° in increments of 5° . Figure A.1.1(a) shows that the highest extraction of kinetic energy occurs in the near wake downstream from the blade, where the velocity recovery reaches values around 2 to 2.5 m/s . For angles of attack of 0° and 5° , the percentage of energy extraction was 20% to 40%, reaching velocities around 6 to 8 m/s . For all angles of attack, it was observed wake width of about 1 m and the velocity distributions appeared to be a little asymmetric due to the design of the wind blade profile.

Figure A.1.1 – Comparison of two downstream cross-sections of the time-averaged streamwise velocity \bar{U} (m/s) for different angles of attack

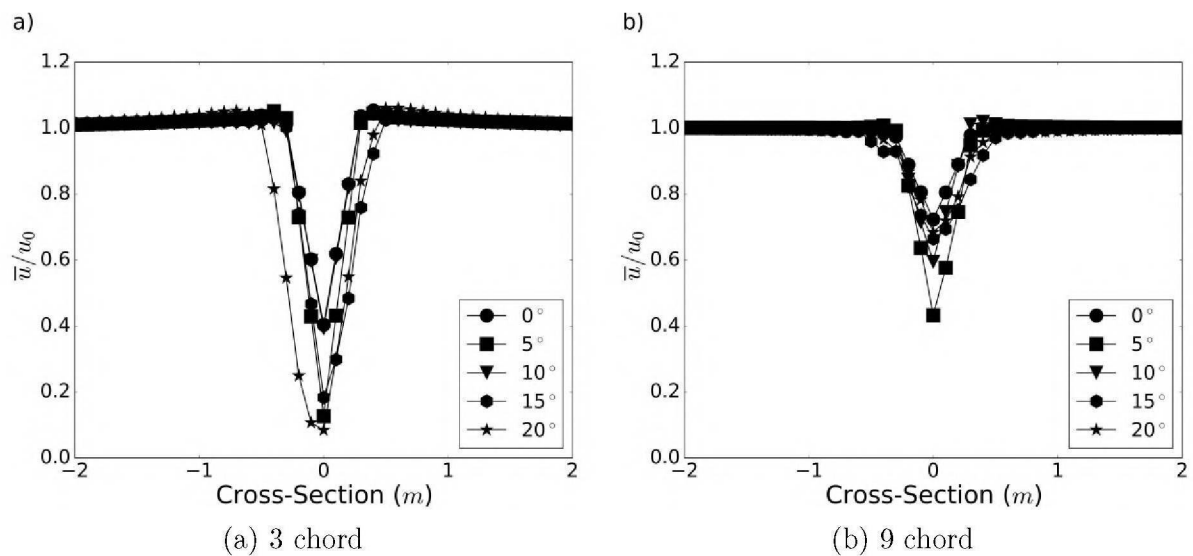
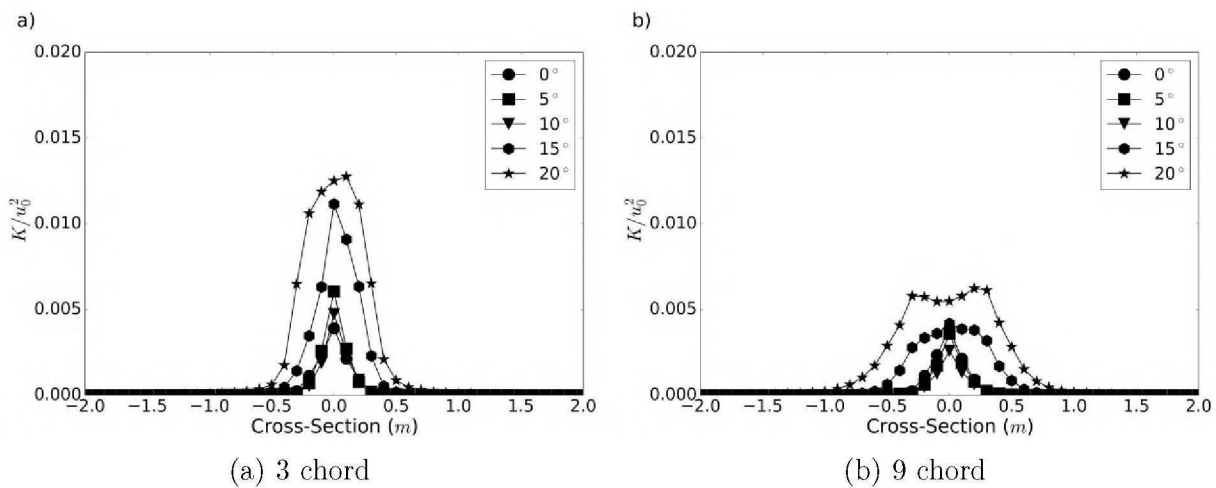


Figure A.1.1(b) displays profiles with lower kinetic energy extraction due to the larger distance downstream of the blade. The higher energy extraction occurs for angles of attack greater than 5° with velocities reaching 7 m/s . The 5° profile presents a minimum velocity of 8 m/s , while the 0° profile gets a little bit higher than 8 m/s . For lower angles of attack, the wake width decrease to 0.6 to 0.7 m . However, for 15° and 20° the wake width continues close to 1 m . The only angle of attack that has asymmetry is the 0° , which may be caused by recirculations that still could occur at 9 chords.

A.2 TURBULENCE PROPERTIES

Figure A.2.1 presents the turbulent kinetic energy distribution for cross-sections located at $x = 3c$ and $x = 9c$ downstream of the wind blade. Figure A.2.1(a) shows the high level of turbulent kinetic energy in the near wake, where the energy reaches maximum values close to 0.15 covering the angles of attack greater than 5° . Figure A.2.1(b) presents a lower level of turbulent kinetic energy in comparison to the previous one, due to the transition for far wake considered at the position of 9 chords downstream from the blade. Turbulent kinetic energy values reach maximum values slightly higher than 0.5 for angles of attack greater than 5° .

Figure A.2.1 – Comparison of two downstream cross-sections, (a) at 3 chord and (b) at 9 chord (9), of the time-averaged kinetic turbulent energy k normalized by u_0^2 for different angles of attack



Besides that, it is worth mentioning that Strouhal number (St) has been calculated in order to characterize the vortex shedding presented in the vorticity results. The Strouhal number is defined as:

$$St = \frac{fl}{u_0}, \quad (\text{A.1})$$

where f , l , and u_0 are respectively the appropriate frequency, length, and velocity scales. From this equation, assuming an inflow velocity of 10 m/s and a chord-based length scale (c) of 0.483 m, results in a Strouhal number of the order of 0.06. This is a little bit lower than the general valuable reported by Levi (1983), who formulated a valuable and straightforward mechanical model based on the hypothesis that an oscillating fluid body of width scale, triggered by an external flow, can yield a St of approximately 0.16. Also, Medici and Alfredsson (2006) measured St ordered $0.12 < St < 0.20$ for the large-scale eddies downstream a two-bladed HAWT in wind tunnel experiments. Therefore, it demonstrates that the results of St from our simulations are in the same order as the literature presented.

APPENDIX B – SCENARIO 2: EXTRA ANALYSIS OF TURBULENCE PROPERTIES

B.1 TURBULENCE PROPERTIES

Figure B.1.1 shows the turbulent kinetic energy k distribution along with the downstream distance at the hub height of the NREL Phase VI.

Figure B.1.1 – Comparison of normalized turbulent kinetic energy deficits along the downstream distance for different section of the blade

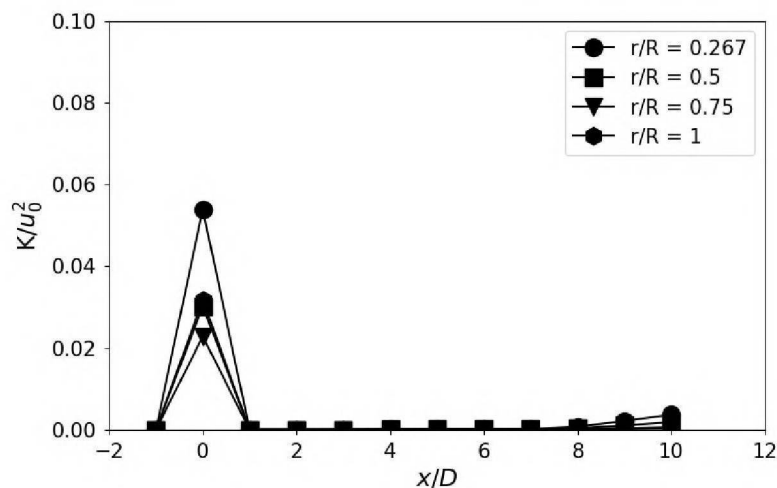
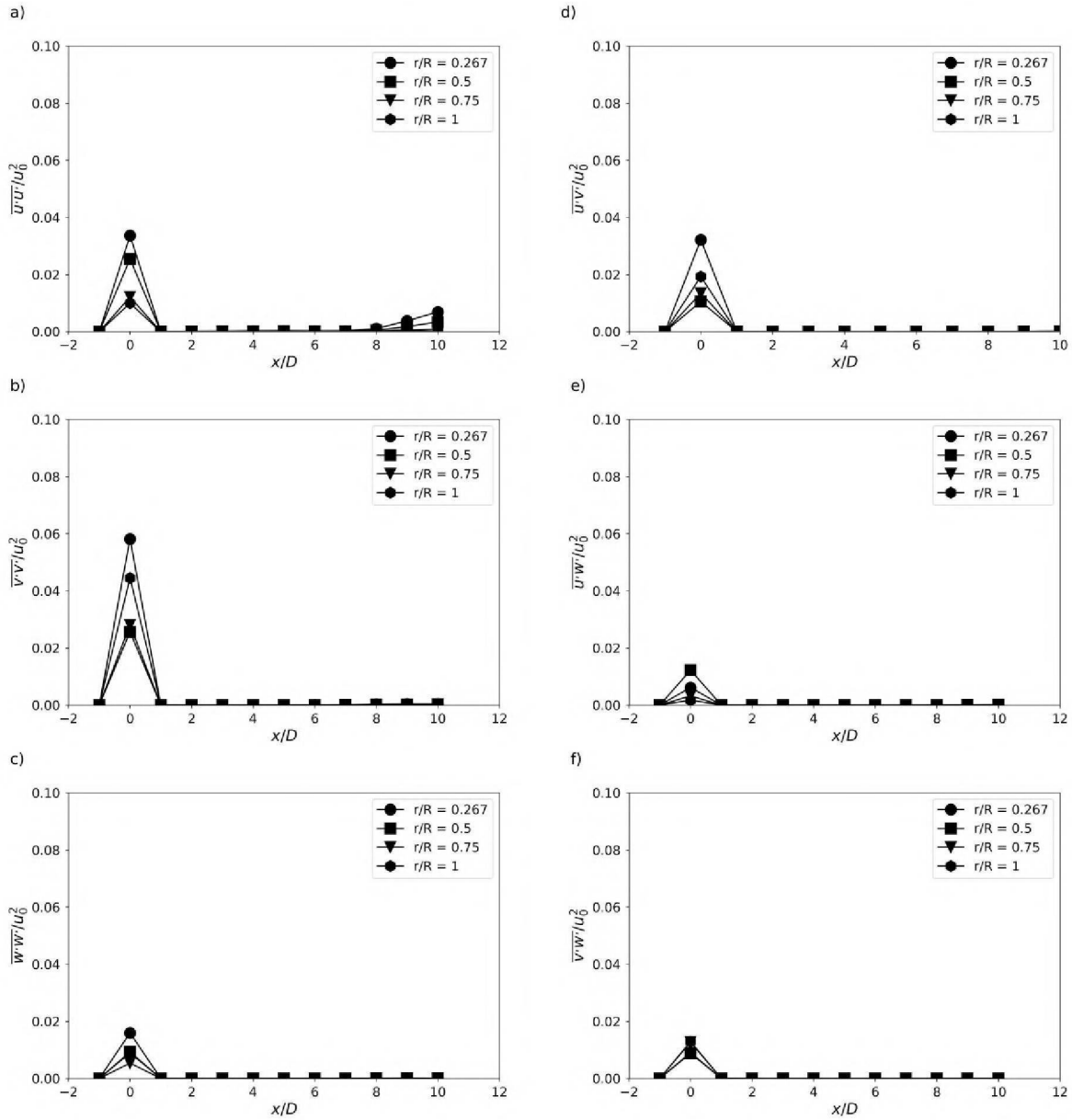


Figure B.1.1 demonstrates that the higher values of turbulent kinetic energy occur in the closest region near the wind turbine, high density of vortices occurring in this area. The profile section close to the root of the blade ($r/R = 0.267$) presented the highest value of k/u_0^2 , close to 0.06. Meanwhile, the others sections had a small variation among each other, varying between 0.25 and 0.3. Then, for downstream distances from 1 to 10 x/D , the kinetic turbulent energy profiles went flat with values close to 0. This suggests that, the majority of the turbulent kinetic energy dissipation occurs between the wind turbine location and the first section at $x/D=1$.

Figure B.1.2 shows the distribution of the Reynolds stress components downstream of the wind turbine in four different sections of the blade. Figure B.1.2(a) illustrates the normal component $\overline{u'^2}$, which reaffirms the behavior presented by the previous figure (Figure B.1.1) on the highest values of the tensor occurring in the section where the turbine is located. The same behavior can be seen in the normal component $\overline{v'^2}$ in the section closest to the turbine. Furthermore, this component is characterized as the main contribution term of turbulent kinetic energy, as depicted in Figure B.1.2(b). This fact is due to the rotating movement of the blades in the transverse flow direction, which would generate high levels of the component in this section. Figure B.1.2(c) presents the normal component $\overline{w'^2}$ of the tensor, which is characterized by being the term with the least influence on the amount of turbulent kinetic energy presented throughout

Figure B.1.2 – Reynolds stress tensor components profiles downstream the NREL Phase VI for different sections of the blade



all transverse distance. Therefore, it has been seen a solid production of these components close to the wind turbine section at $x/D=0$, and followed by a quick dissipation occurring right after the flow passed this area. This behavior most likely occurs due to the rotation of the blades in this section, which leads to increasing velocity fluctuations in the cross-flow direction around the wind turbine region.

Figures B.1.2(d), B.1.2(e) and B.1.2(f) depict the shear components of the Reynolds stress tensor for the four sections of the blade. The components $\overline{u'v'}$ presented bigger values when compared to $\overline{u'w'}$ and $\overline{v'w'}$ at the wind turbine section downstream, this is mainly due to the direction of the flow in the x -direction meanwhile velocity at y -direction is emphasized due to the rotation of the blades. As expected the bigger values of this component occur at the tip of the blade $r/R=1$, with a value that closely reaches 0.04. The $r/R=0.5$ section obtained

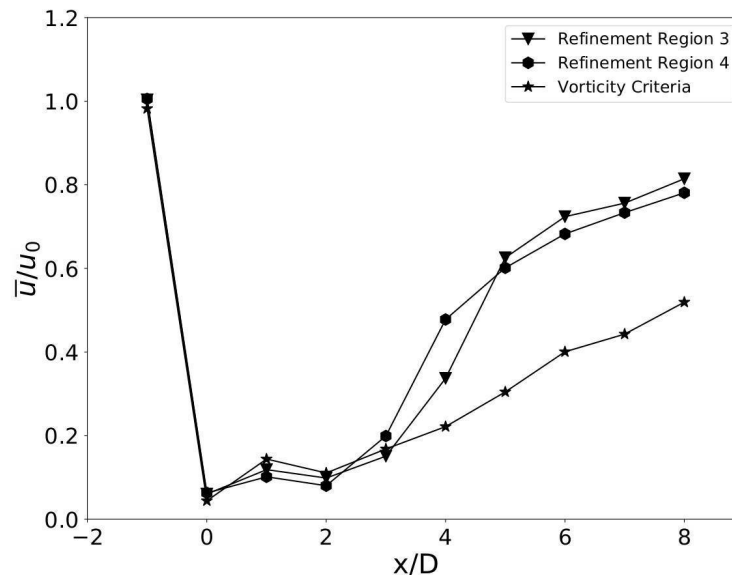
the highest value, 0.15, for the $\overline{u'w'}$ component, while $\overline{v'w'}$ component showed that all sections performed similar values around 0.15 as well.

APPENDIX C – SCENARIO 3: NREL 5MW ANALYSIS FROM PREVIOUS MESHES

C.1 LONGITUDINAL PROFILES

Figure C.1.1 shows the centerline velocity recoveries behind the turbine for three different simulations run in MFSim: (i) simulation using the vorticity criteria for remeshing in the region with the more significant amount of vortices downstream of the turbine; the other two simulations consist of applying a region and a specific level of refinement, with the mesh adaptivity occurring around the turbine, the first uses (ii) three levels of refinement while the second (iii) applies four levels of refinement in the specified region.

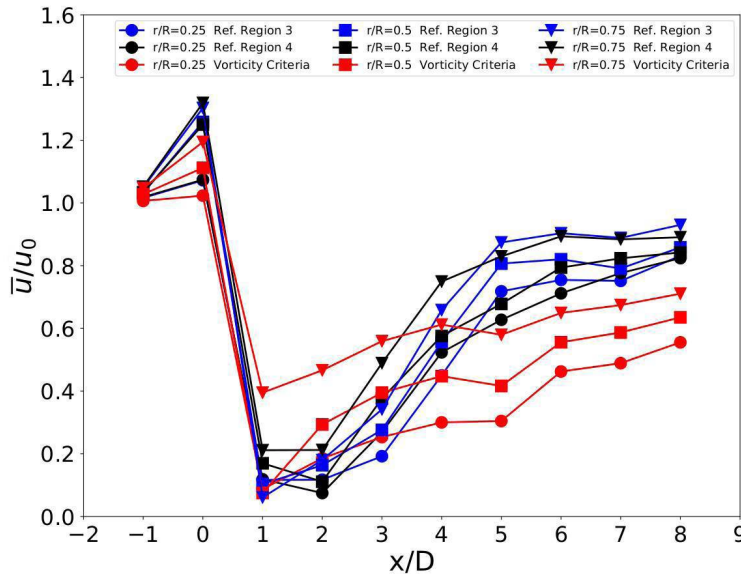
Figure C.1.1 – Longitudinal centerline profiles of time-average streamwise velocity



Based on the results presented in Figure C.1.1 it is possible to affirm that the simulations elaborated with a specific refinement region presented a greater velocity recovery, in far wake, when compared to the simulation with the vorticity criteria. For near wake region, up to $x/D = 3$, both profiles showed similar results with velocity recovery around \bar{u}/u_0 0.1 to 0.2. However, from $x/D = 4$, the vorticity criteria simulation did not obtain a velocity recovery as strong as the simulations with the refinement region, getting the highest recovery at $x/D = 8$ with \bar{u}/u_0 close to 0.5. Meanwhile, the refinement region simulations reached values of \bar{u}/u_0 close to 0.75 to 0.8 at $x/D = 8$. This difference may have been caused by the excess of refinement imposed by the vorticity criteria, further prolonging the velocity deficit generated in the wake region, thus having a lower dissipation of turbulent kinetic energy.

Figure C.1.2 presents velocity recoveries in three annular blade sections, sections at r/R of 0.25, 0.5 and 0.75, for the three distinct simulations presented above. From the results, it is possible to observe similar behavior for the simulations with the refinement region, where the highest velocity values occur for the $r/R=0.75$ section of the wind turbine blade, reaching out \bar{u}/u_0 values close to 0.9 from $x/D = 5$. Meanwhile, the r/R profiles of 0.25 and 0.5 make \bar{u}/u_0 values close to 0.8. Refinement region simulations also show the lowest values obtained close to the turbine, in the near wake region, in the downstream sections of $x/D = 1$ and $x/D = 2$ with values of \bar{u}/u_0 between 0.1 to 0.2.

Figure C.1.2 – Longitudinal annular velocity recovery profiles by ratio of r/R



C.2 CROSS-SECTIONS PROFILES

Comparisons of the time-average streamwise velocity recovery over the wake cross-section have been analyzed for four cross-section locations, corresponding to downstream distances of $1D$, $2D$, $4D$, $6D$, and $8D$, presenting the simulations for the application of the vorticity criteria, refinement region with three and four levels of refinement, which are represented by Figure C.2.1, Figure C.2.2 and Figure C.2.3, respectively. On the abscissa axis, we have the scaled velocity normalized by the maximum velocity \bar{u}/\bar{u}_{max} in the section plotted against the transversal value y normalized by the radius of the blade R .

Figure C.2.1 demonstrates that the velocity recovery, \bar{u}/\bar{u}_{max} , is lower in the near wake when compared to the far wake for the wind turbine downstream. The velocities represented for the $x/D = 1$, $x/D = 2$, and $x/D = 4$ profiles reached velocity deficit close to 20% of the maximum velocity in a region around the wake centerline. Meanwhile, the $x/D = 6$ profile showed a velocity recovery close to 40% of its maximum, and the $x/D = 8$ profile presented a

Figure C.2.1 – Cross-section wake profiles for the 1, 2, 4, 6 and 8 D downstream distances for the vorticity criteria

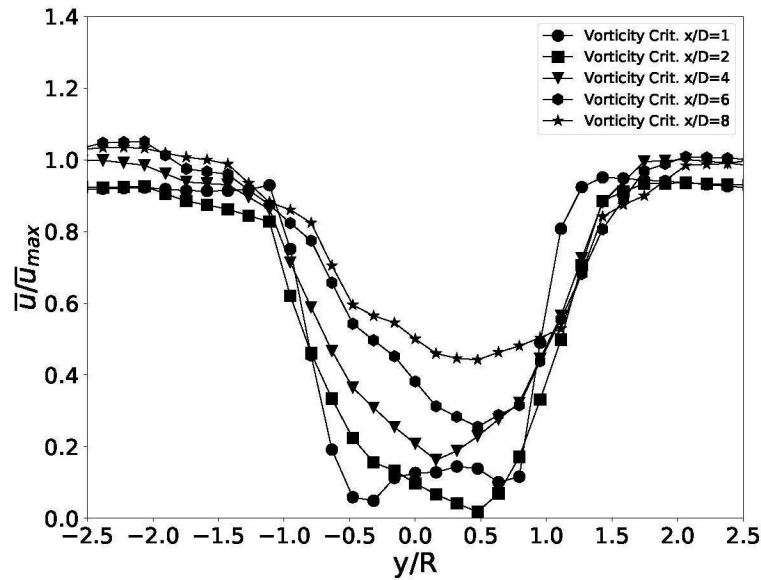
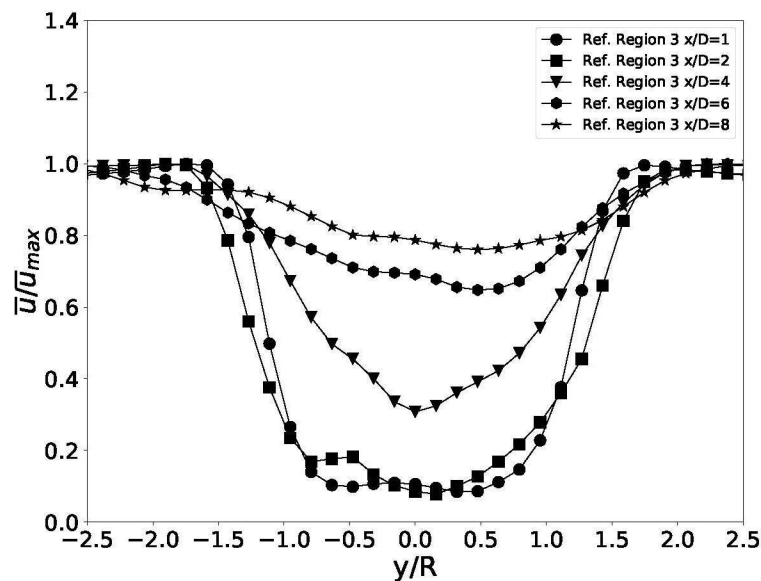


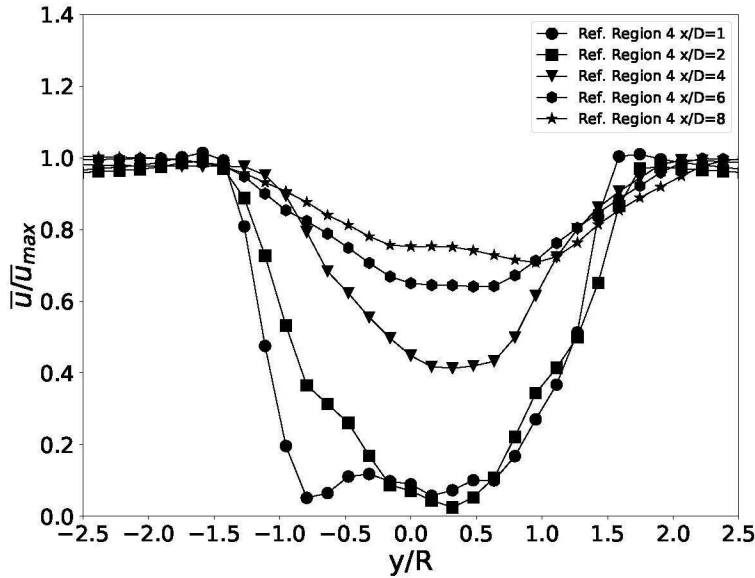
Figure C.2.2 – Cross-section wake profiles for the 1, 2, 4, 6 and 8 D downstream distances for the refinement region with 3 levels



recovery slightly below the 60% at the centerline. In terms of wake width the profiles presented to have close to 160 m of width, which would be around 2.5 R .

Figure C.2.2 shows that the velocity recovery, \bar{u}/\bar{u}_{max} , for the refinement region simulation with three levels of refinement in the whole wake region. The velocities expressed by

Figure C.2.3 – Cross-section wake profiles for the 1, 2, 4, 6 and 8 D downstream distances for the refinement region with 4 levels



the $x/D = 1$ and $x/D = 2$ profiles have reached a velocity deficit of around 20% of the maximum velocity. The $x/D = 4$ profile has almost achieved a 40% recovery on the wake centerline. The $x/D = 6$ profiles showed velocity recovery slightly below 80% while the $x/D = 8$ profile presented a velocity slightly above 80% of its maximum. Comparing the wake width with the previous simulation, the width of the refinement region of three levels reached almost $3R$, close to 183 m.

The Figure C.2.3 shows that the velocity recovery, \bar{u}/\bar{u}_{max} , for the refinement region simulation with four levels of refinement, with similar behavior, compared to the previous one since it is the same simulations with one more level of refinement. The main differences occur in the near wake where the speeds of the profiles $x/D = 1$ and $x/D = 2$ decrease to 10% velocity recovery, and in the $x/D = 4$ profile where the recovery reached values close to 50% at the centerline. Meanwhile, wake width continues around $3R$.

C.3 VERTICAL PROFILES

The time-averaged streamwise velocity recovery behavior is considered for vertical profiles along the centerline of the wake downstream distance where six sections have been analyzed corresponding to downstream distances of $-1D$, $1D$, $2D$, $4D$, $6D$, and $8D$. On the abscissa axis, we have the scaled component z , which corresponds to the height, plotted against the velocity normalized by the inflow velocity \bar{u}/u_0 . The analysis presents three different simulations applying the vorticity criteria, refinement region with three and four levels of refinement, respectively.

It is important to point out that Figures C.3.1 and C.3.5 for vorticity criteria simulation, Figures C.3.2 and C.3.6 for 3 levels of refinement region, and Figures C.3.3 and C.3.7 for

refinement region with 4 levels, depict the same results but in different graphical representation in order to complement each order and provide to the reviewers one possible comment which one would be a better cleaner representation of the results behaviour. Therefore, Figures C.3.1, C.3.2, and C.3.3 illustrate six different vertical profiles from $x/D = -1$ upstream to $x/D = 8$ downstream distance, representing by six separate subplots while Figures C.3.5, C.3.6, and C.3.7 depict all vertical profiles downstream sections at one graph for each simulation. In addition, Figure C.3.4 also presents the velocity recovery vertical profiles, but separated into subplots by the turbine's downstream sections and showing the comparison of the three different simulations for each downstream section.

Figure C.3.1 – Vertical wind velocity profiles subplots over downstream distance normalized by rotor diameters for the vorticity criteria

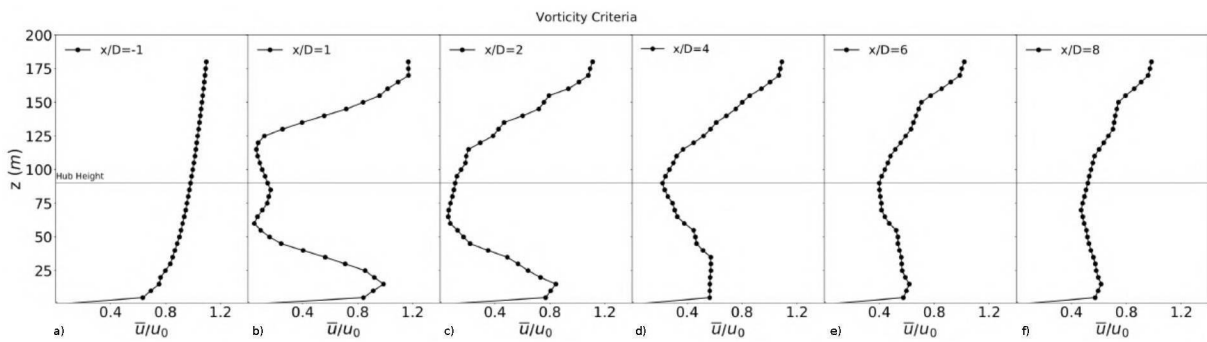
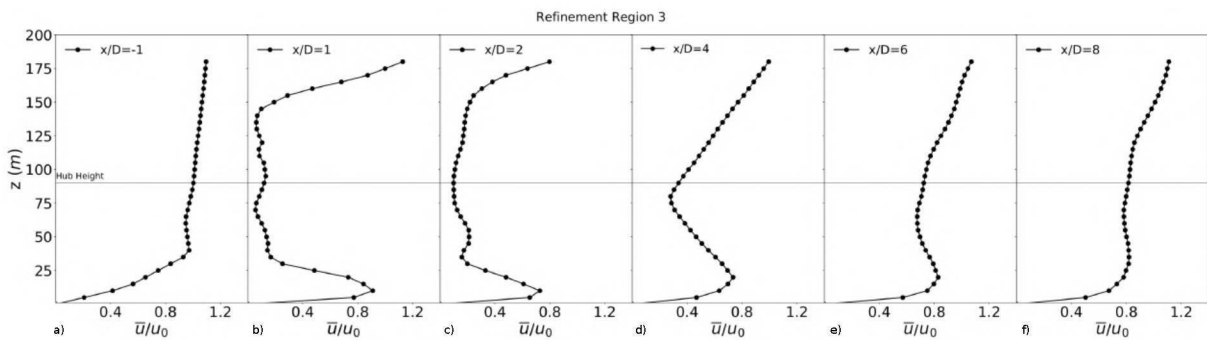


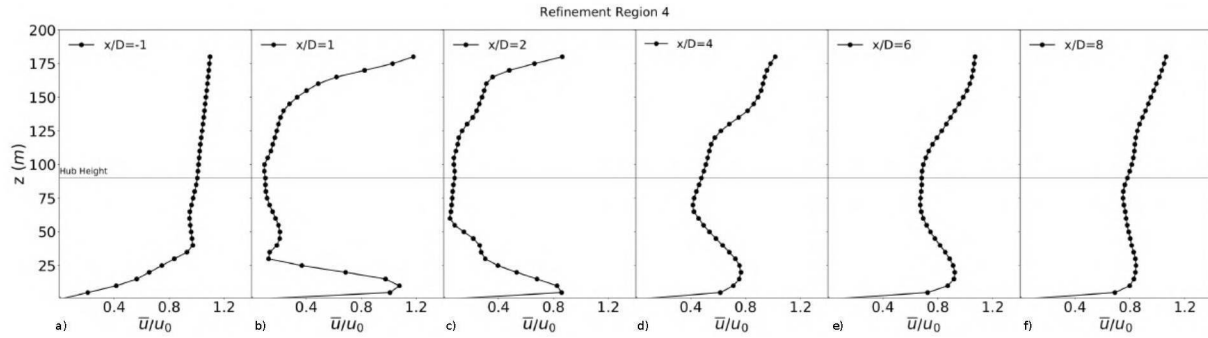
Figure C.3.2 – Vertical wind velocity profiles subplots over downstream distance normalized by rotor diameters for the refinement region with 3 levels



The first section analyzed corresponds to the upstream distance of $x/D = -1$, illustrated in the first subplot of Figures C.3.1, C.3.2, C.3.3, and also at Figure C.3.4(a) which is the inflow velocity profile chosen in the simulation. There is a small difference in the distribution between the vorticity criteria and refinement region simulations close to the 50 m height in z , which may be due to the meshing composition and size at this point.

In terms of vertical analysis, it is possible to indicate that the vorticity criteria simulation produces the lowest wake height in the near wake of the turbine when compared to the others. This is evident in the downstream sections of $x/D = 1$ and $x/D = 2$ of Figure C.3.1 and Figures C.3.4(b) and (c), where the waked region covers around 140 m total. It is even clearly seen through the number of probes with velocity recovery \bar{u}/u_0 values lower than 0.4, 40% of

Figure C.3.3 – Vertical wind velocity profiles subplots over downstream distance normalized by rotor diameters for the refinement region with 4 levels



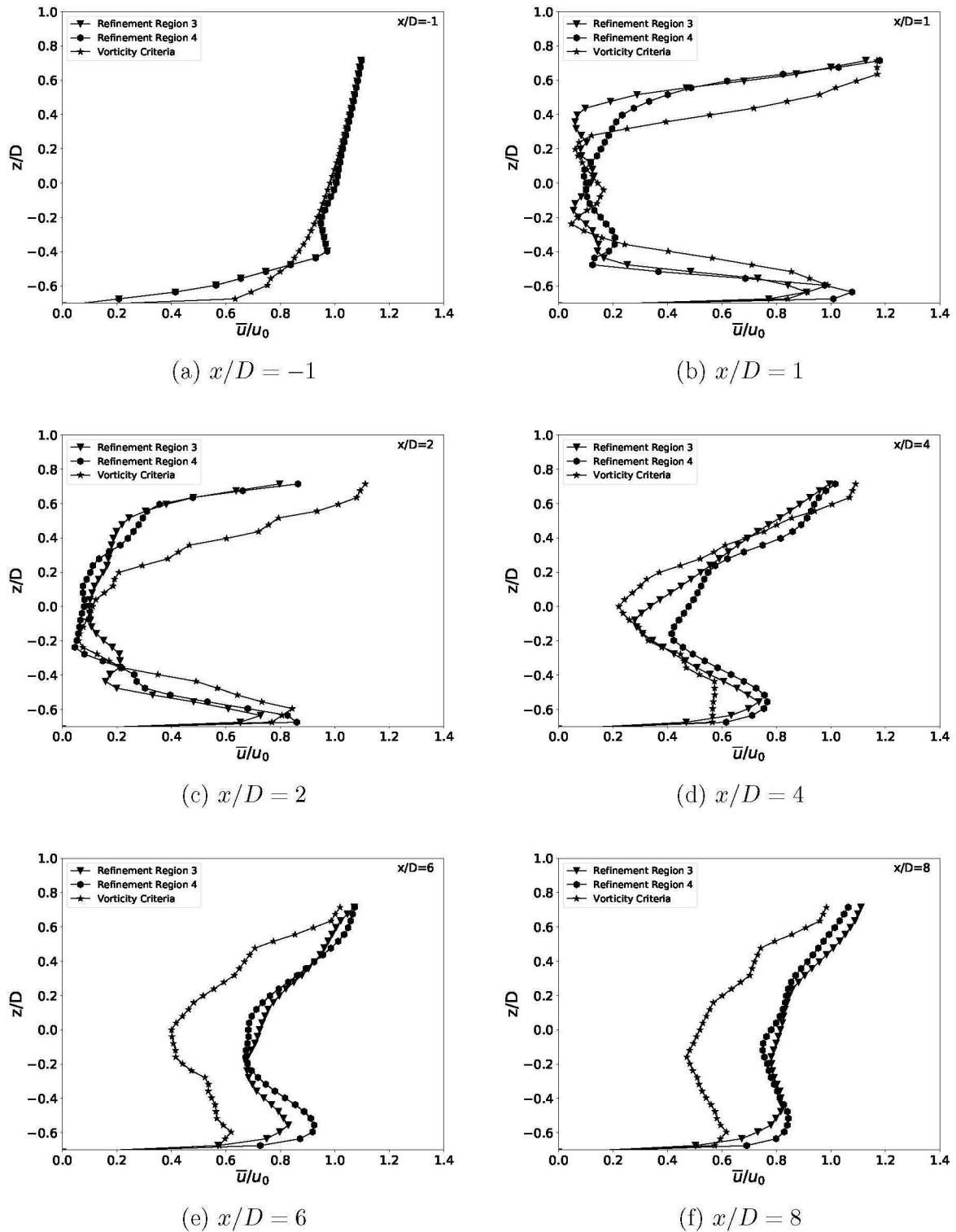
the inflow velocity, occurring from height 45 to 130 m at $x/D = 1$ and $x/D = 2$. The velocity recovery over the wake region begins to increase around the section $x/D = 4$ of Figure C.3.1 and Figure C.3.4(d), where the recovery \bar{u}/u_0 presented a value close to 0.3. The following section, $x/D = 6$ of Figure C.3.1 and Figure C.3.4(e), presents a slightly more uniform profile, with a recovery velocity that exceeds 40% of the inflow velocity in the centerline, which means \bar{u}/u_0 over 0.4. The last section composing the far wake region, at $x/D = 8$ of Figure C.3.1 and Figure C.3.4(f), has a similar distribution to the previous one, but with a higher velocity recovery where most points in the profile have a velocity recovery close to or above 0.6 for \bar{u}/u_0 .

For simulations using refinement region, represented by Figure C.3.2 for three levels, and Figure C.3.3 for four levels of refinement, the wake height is greater than the simulation of vorticity criteria for sections of $x/D = 1$ and $x/D = 2$, reaching a total value of approximately 160 m, also seen in Figures C.3.4(b) and (c).

At $x/D = 1$, the main difference between the simulations of three and four refinement levels is related to a higher velocity recovery in the upper region near the blade tip for the simulation of four levels of refinement, Figure C.3.4(b), which could be an effect of the finer mesh in this simulation. Furthermore, centerline velocity recoveries showed similar results for both levels of refinement in the sections $x/D = 1$ and $x/D = 2$, with values of \bar{u}/u_0 between 0.1 to 0.2. Meanwhile, in the $x/D = 4$ section of Figures C.3.2 and C.3.3, and also shown in Figure C.3.4(d), the simulation with four levels of refinement showed a greater velocity recovery, slightly above 40%, compared to the 3 level simulation, which was close to 30%.

In the following section, $x/D = 6$ as seen in Figure C.3.4(e), both simulations showed profile values above 0.7 for \bar{u}/u_0 , which means more than 70% of the inflow velocity recovery. The only distinction between the simulations in this section was the more symmetry profile presented by the four levels of refinement simulation, which its finer mesh may explain the behavior to be more symmetrical, showed in $x/D = 6$ of Figures C.3.2 and C.3.3. Finally, the profiles of both simulations for $x/D = 8$, Figure C.3.4(f), in far wake, showed similar behavior with most points reaching a velocity recovery close to 80% of the input velocity, \bar{u}/u_0 close to 0.8.

Figures C.3.5, C.3.6, and C.3.7 restate the information and results provided from the previous representations. An example of that can be seen in Figure C.3.5 showing that the vorticity criteria simulation has the lowest wake height concerning the other simulations. It is

Figure C.3.4 – Vertical wake profiles for the 1, 2, 4 and 8 D downstream distances

also clear from Figure C.3.5 that the simulation has a lower velocity recovery rate, reaching a \bar{u}/u_0 value close to 0.6 in the centerline of the $x/D = 8$ section, the farthest from the turbine. Meanwhile, the Figures C.3.6, and C.3.7 reaffirm a greater wake height in the near wake as well as a greater velocity recovery capacity in the far wake region. Therefore, the refinement region simulations reach recovery velocity values close to 80% of inflow velocity, \bar{u}/u_0 close to 0.8, in

the last section, $x/D = 8$, the farthest far wake.

Figure C.3.5 – Vertical wind velocity profiles over downstream distance normalized by rotor diameters for the vorticity criteria

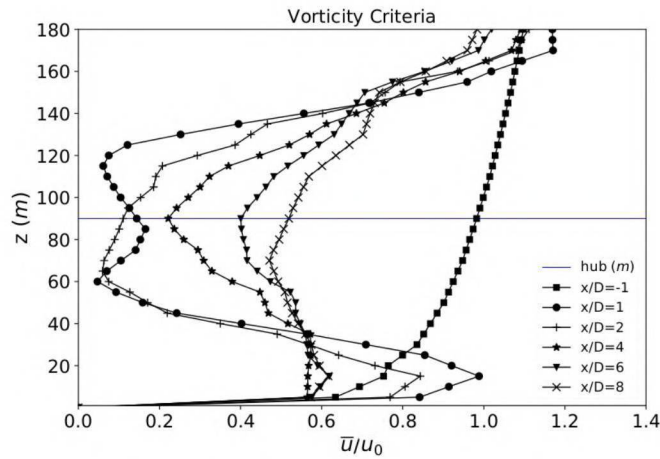


Figure C.3.6 – Vertical wind velocity profiles over downstream distance normalized by rotor diameters for the refinement region with 3 levels

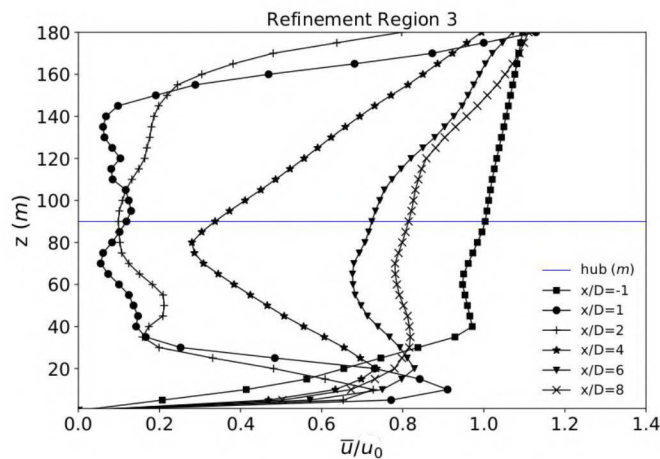
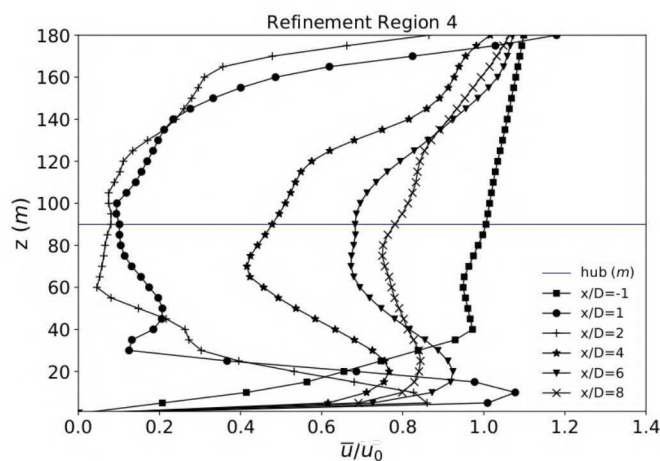


Figure C.3.7 – Vertical wind velocity profiles over downstream distance normalized by rotor diameters for the refinement region with 4 levels

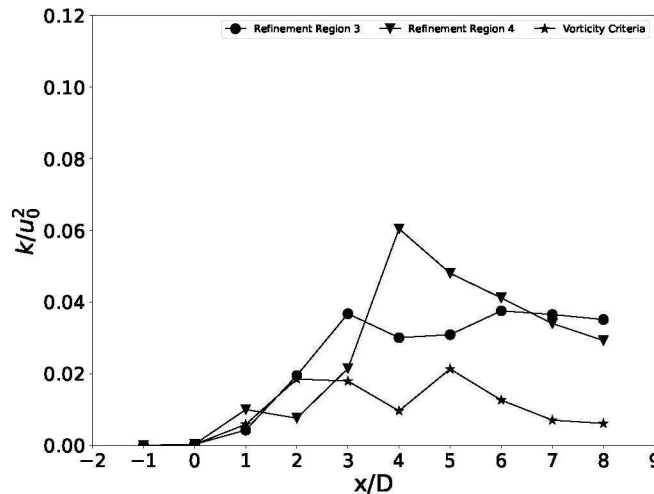


C.4 PROFILES OF TURBULENCE PROPERTIES AND SPECTRUM

C.4.1 Turbulent Kinetic Energy

Figure C.4.1 shows the turbulent kinetic energy distribution normalized by the square of the inflow velocity k/u_0^2 along with the downstream centerline distance at the hub height of the turbine, presenting the comparison among the three MFSim simulations.

Figure C.4.1 – Longitudinal centerline profiles of time-average streamwise turbulent kinetic energy (k) for the three simulations



From Figure C.4.1 it can be observed that the simulation with refinement region with four levels of refinement presented the highest value of k/u_0^2 , about 0.06, in section $x/D = 4$, after this section the k/u_0^2 profile shows a quasi-linear decrease close to 0.03 at the farthest downstream section $x/D = 8$. Meanwhile, the simulation with refinement region with three levels of refinement presented an increasing profile until the section $x/D = 3$ with a value very close to 0.04 for k/u_0^2 , followed by a virtually stable profile in the downstream direction to the far wake region. On the other hand, the vorticity criteria simulation showed the most retracted k/u_0^2 profile with the highest value being around 0.02 in sections $x/D = 2$, $x/D = 3$ and $x/D = 5$. After that, it also presented a decreasing profile to the furthest probe from $x/D = 8$ with a value lower than 0.01.

Concerning the cross-section evaluation of k/u_0^2 , Figure C.4.2, Figure C.4.3 and Figure C.4.4 present the Comparison of five downstream cross-sections of the time-averaged turbulent kinetic energy (k) normalized by u_0^2 and plotted against the transversal value y normalized by the radius of the blade R , for the vorticity criteria, three and four levels of refinement region simulation, respectively. Those figures show results from five different downstream wake sections, $1D$, $2D$, $4D$, $6D$, and $8D$.

Figure C.4.2 confirms the statement made before about the vorticity criteria simulation presents more discrete profiles in terms of k/u_0^2 even for cross-section profiles, with their maximum values occurring close to 0.04 in y/R equal to -0.5 and 0.5 in the section $x/D = 2$ downstream of the turbine. Meanwhile, Figure C.4.3 shows that the highest values for a refinement region simulation of three refinement levels reached values close to 0.06 for k/u_0^2 , in

Figure C.4.2 – Comparison of five downstream cross-sections of the time-averaged turbulent kinetic energy (k) for vorticity criteria simulation

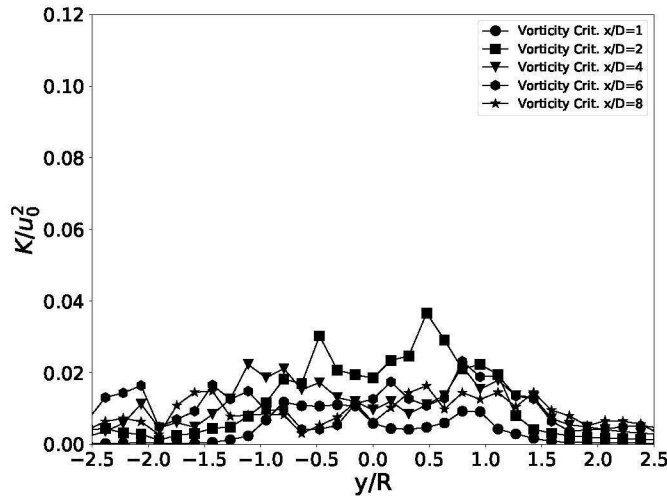
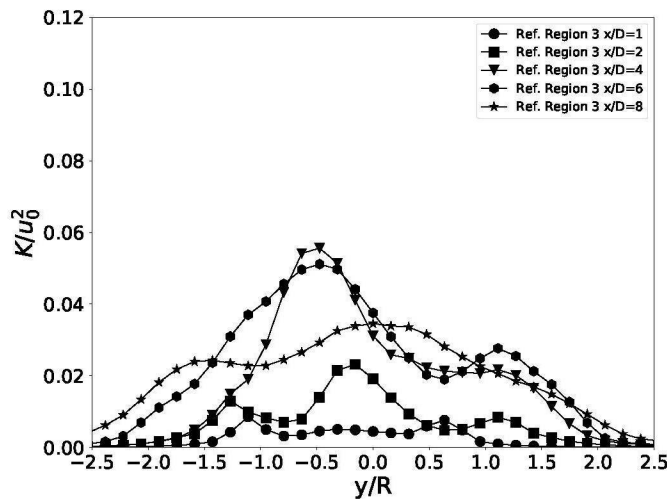


Figure C.4.3 – Comparison of five downstream cross-sections of the time-averaged turbulent kinetic energy (k) for refinement region with 3 levels

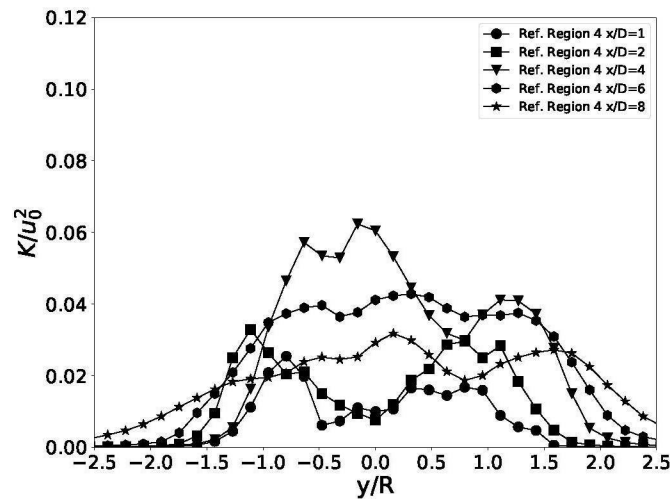


transversal points close to -0.5 of y/R on profiles of $x/D = 4$ and $x/D = 6$ downstream of the turbine. The simulation with four levels of refinement, shown in Figure C.4.4, exceeded the value 0.06 for k/u_0^2 at the centerline in the profile of $x/D = 4$, a profile that stood out for its greater predominance in the results. Furthermore, the profile of $x/D = 6$ presented consistent results, close to 0.04 , in width from -1 to 1.5 of y/R .

C.4.2 Turbulence Intensity

The following parameter to be analyzed is the turbulence intensity, aiming to determine its behavior in the wake downstream. Figure C.4.5 displays the cross-sections profiles of the time-averaged turbulence intensity (TI), from 2 , 4 , 6 , and 8 x/D versus the transversal value y normalized by the blade radius R , from -2 to 2 , for the vorticity criteria, three and four levels of

Figure C.4.4 – Comparison of five downstream cross-sections of the time-averaged turbulent kinetic energy (k) for refinement region with 4 levels

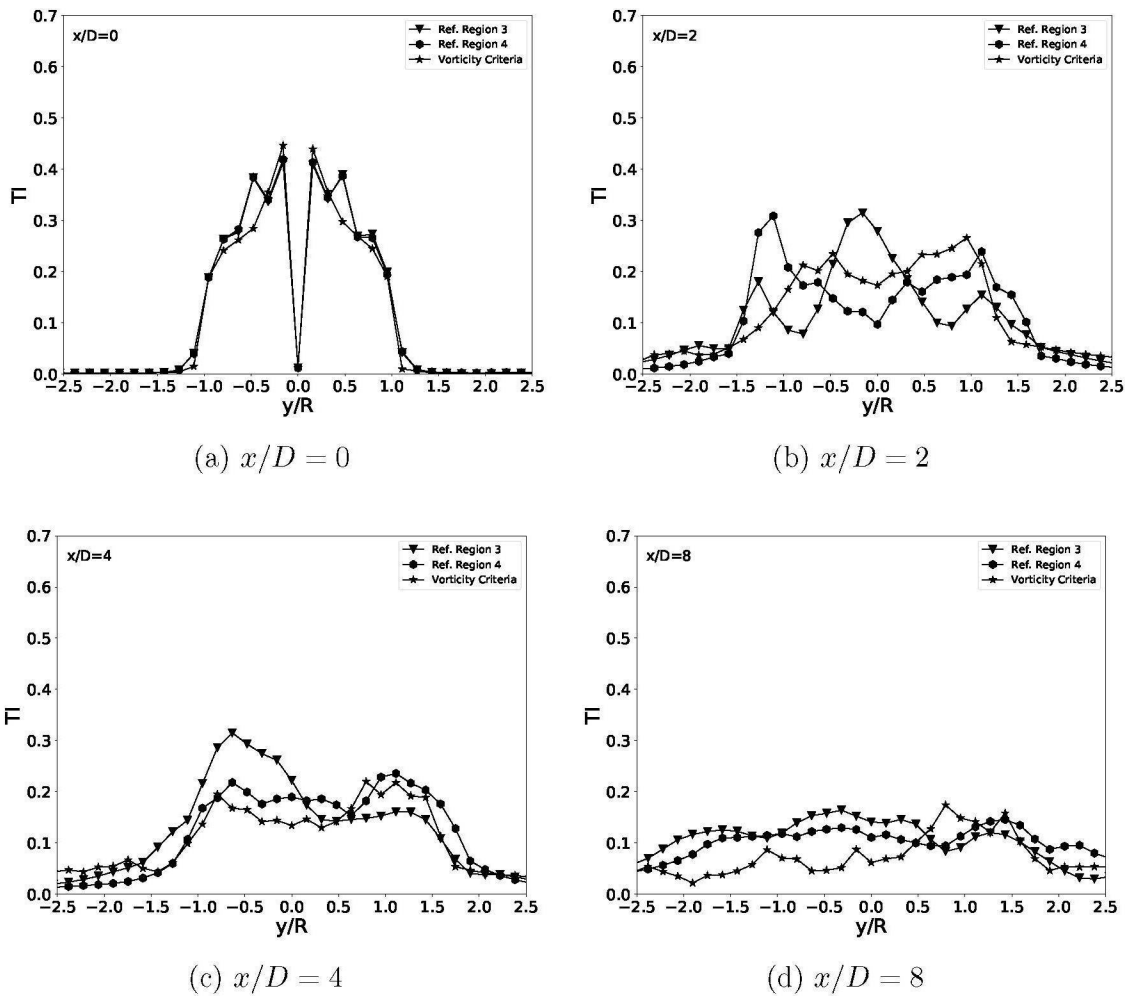


refinement region simulation, respectively. Meanwhile, Figure C.4.6 also presents TI comparisons for the three simulations but subdivided by downstream sections into 6 subplots of 0, 1, 3, 4, 6, and 8 x/D . Giving the comparison among the three simulations for the individually downstream segment of the wind turbine.

The results of Figure C.4.5 demonstrate a greater predominance of TI occurring in the near wake of the flow, with more significant values in the section $x/D = 0$, as shown in Figure C.4.5 (a), where the values of TI reach levels of 0.45 near the centerline region for the three simulations. It is worth noting that the TI values at the point of $y/R = 0$ are zero due to the geometry of the nacelle positioned in this region. The TI values decrease quickly in the direction of the blade tip until they reach values close to zero, outside the swept area, which may be occurring because no incident turbine turbulence occurs in the flow. The section $x/D = 2$, displayed in Figure C.4.5(b), demonstrates a larger distribution of TI in terms of width in y/R while it showed a reduction in the TI values for the profiles. Reaching maximum values slightly greater than 0.3 at the centerline in the refinement region simulation with three levels and y/R close to -1.25 for simulation with four levels of refinement, while the vorticity criteria simulation did not exceed values greater than 0.25 of TI .

Figure C.4.5(c) shows the results of TI for the distance downstream of $x/D = 4$, which results show a little more similarity between the simulations, with values of TI varying between 0.15 and 0.25 for most of y/R between -1 to 1.5 in the three simulations. Except the three-level refinement region simulation points in the y/R region between -0.25 to -0.75, where the values of TI reached results around 0.3. Finally, as expected, when the flow advances to far wake, the results of TI show quite small values, as can be seen in Figure C.4.5(d) displaying the $x/D = 8$ section. In this section, the TI values do not exceed 0.2 in the three simulation profiles. It also demonstrates greater uniformity among profiles, with the vorticity criteria simulation showing results slightly lower than the others.

In terms of vertical profiles, depicted in Figure C.4.6, the results also restate what it was

Figure C.4.5 – Turbulence intensity cross-section wake profiles for the 0, 2, 4 and 8 D downstream distances

inferred before concerning the high TI values occurring in the near wake of the wind turbine. Figure C.4.6(a) shows the vertical profile for the section located precisely in the region where the turbine stands installed. It can be seen that the highest values occur just above the hub height with values of TI between 0.4 to 0.5 for the three simulations. Moreover, it is noticeable that the values of the vertical distribution of TI still have a small influence on the inflow velocity profile. Once again, it can be seen that values around hub height are close to zero because of the nacelle geometry position.

The first section downstream, $x/D = 1$, represented by Figure C.4.6(b) shows a high predominance of the values of TI for the refinement region simulation with three levels of refinement, obtaining maximum TI close to 0.6 at $0.25 z/D$. In contrast, the other simulations did not show values exceeding 0.4 of TI . The three-level refinement simulation also presented the highest values for the $x/D = 3$ section, but with slightly lower results this time, slightly exceeding 0.5 of TI at z/D close to 0.4. On the other hand, the simulation of four levels of refinement showed an increase in the results of TI near the blade tips, z/D of 0.5 and -0.5, with values exceeding 0.4, as shown in Figure C.4.6(c).

The section $x/D = 4$ is characterized by the reduction of the values of TI in relation to the previous ones, where all profiles of the three simulations obtained results of TI lower than

0.35, as can be seen in Figure C.4.6(d). As the flow develops away from the turbine, the values of TI tend to decrease, Figure C.4.6(e) illustrating the results of section $x/D = 6$ shows that higher deliveries values of TI are concentrated in the 0.1 to 0.2 range for all simulations, even demonstrating a more significant agreement between the simulation profiles. A pattern that can also be seen in Figure C.4.6(f) with the section farthest from $x/D = 8$, where the values of TI show even more retracted results not exceeding the value of TI equal to 0.2 for all profiles.

Figure C.4.6 – Turbulence intensity vertical wake profiles for the 0, 1, 3, 4, 6 and 8 D downstream distances

